

学位論文

Variability and Polarization of the
Ultraviolet-optical Continuum Emission of
Quasar Accretion Disks

(クエーサー降着円盤紫外可視域連続光放射の
光度変動および偏光現象の研究)

平成 28 年 12 月 博士 (理学) 申請

東京大学大学院理学系研究科
天文学専攻
小久保 充

Variability and Polarization of the Ultraviolet-optical Continuum Emission of Quasar Accretion Disks

Mitsuru Kokubo

Department of Astronomy, the University of Tokyo

A thesis submitted in partial fulfillment of the requirements
for the degree of Doctor of Philosophy (Astronomy)

December, 2016

Abstract

The study of the physical mechanisms driving the active galactic nuclei (AGN) activity, namely the physics of the black hole accretion disks in AGNs, is essential to better understand not only the growth of the supermassive black hole (SMBH) at the center of the galaxy but also the cosmological galaxy evolution in the Universe. However, in spite of its importance, surprisingly little has been known about the true nature of the AGN accretion disks since the first proposal of standard accretion disk model as the central engine of AGNs in 1970s.

In this dissertation, we examine the ultraviolet(UV)-optical flux variability and polarization of AGNs or quasars to assess the validity of our current understandings of the quasar accretion disks and their vicinity. The flux variability and polarization are two unique observational properties of AGN/quasar UV-optical emission, enabling to disentangle the emission spectrum of the accretion disk thermal emission from the broad emission lines and the host galaxy light and consequently to examine the intrinsic accretion disk continua in AGNs/quasars.

First we review observational properties of UV-optical flux variability and polarization of AGNs/quasars from the viewpoint of standard geometrically-thin thermal accretion disk model in Chapter 1.

Then, we move on to examining the statistical properties of the spectral variability of quasars by using a large sample of multi-band light curves of quasars in the Sloan Digital Sky Survey (SDSS) Stripe82 region in Chapter 2. It is shown that the variable component spectra of the quasars, which should reflect the spectral shape of the intrinsic accretion disk emission, are much bluer ($\alpha_v \sim +1/3$) than the directly-observed spectra ($\alpha_v \sim -0.5$). We show that the accretion disk spectra of quasars revealed as the variable component spectra are too blue to be explained by existing geometrically-thin thermal accretion disk models.

In Chapter 3, we examine whether the “inhomogeneous accretion disk model” proposed by Dexter & Agol (2011) can simultaneously explain the large variability amplitude and the strong correlation of the multi-band light curves through the UV-optical wavelength range observed in the SDSS Stripe82 quasars. By comparing the intrinsic scatter σ_{int} from the linear magnitude-magnitude relation of the two-band light curves between the observational data and the inhomogeneous accretion disk model simulations, we show that the inhomogeneous accretion disk model predict systematically weaker inter-band correlation compared to the real quasars. This study demonstrates that the observed inter-band correlations in AGNs/quasars impose strong constraints on the variability models involving many localized instabilities/flares over the disk surface.

In Chapter 4, we study the relationship of the spectral shape between the variable component and the polarized flux spectra in each of the four quasars with continuum-confined polarization (B2 1208+32, Ton 202, 3C 323.1, and 4C 09.72). According to the knowledge in the previous works on the variability and polarization, both of the variable component spectra and the polarized flux spectra in these quasars should reflect the intrinsic accretion disk emission spectra. However, by comparing these two spectral components by using the archival spectro-polarimetry data and the newly obtained multi-band light curves for these quasars, we show that they have totally different spectral shape, suggesting that there are fundamental problems in the current understanding of the quasar UV-optical variability and/or polarization.

In Chapter 5, we constrain the polarization source in one of the quasars with continuum-confined polarization studied in Chapter 4, 3C 323.1, by examining the polarimetric and photometric variability of this object. It is shown that the total (\sim unpolarized) flux and the polarized flux in 3C 323.1 show strongly correlated variability during the three epochs of the polarimetric measurements, and that the polarization position angle (PA) also show evidence of time-variability. Also, multi-epoch spectro-polarimetric data reveal that the polarized flux spectra of 3C 323.1 show variability in their broad absorption features on time-scales of several years. Taking these observational facts into account, we propose a geometrical model in which the polarized flux spectra are interpreted as the accretion disk continua with additional broad absorption features induced by the equatorial absorbing region because the observed polarized light has once passed through the absorbing region. We conclude that the polarized flux spectra of quasars do not directly reflect the spectral shape of intrinsic accretion disk continua, which is the reason why the spectral shape of the polarized flux and the variable component of quasars studied in Chapter 4 does not agree with each other. This work validates the conclusions derived in Chapter 2 and Chapter 3 on the assumption that the variable component spectra of quasars is a good tracer of the spectral shape of the intrinsic accretion disk continuum emission.

Conclusions of this dissertation and future prospects are summarized in Chapter 6. These studies clarify that the observational properties of the UV-optical variability and polarization can strongly constrain models of the accretion disk and of the inner structure of AGNs/quasars. I emphasize that we should investigate models of quasar accretion disks which can naturally account for the general properties of the years time-scale AGN/quasar variability, namely, the large variability amplitude and the tight inter-band correlation within the UV-optical wavelength range, simultaneously. It is discussed in Chapter 6 that the X-ray reprocessing model may possibly explain the observed UV-optical variability of AGNs/quasars, and further simultaneous X-ray and optical monitoring observations are needed to confirm the validity of the X-ray reprocessing model. Also, we point out that the photometric and polarimetric monitoring observations for microlensing events in gravitationally lensed quasars will enable to probe the true nature of the flux variability and polarization, and consequently of the accretion disk emission in AGNs/quasars.

Table of Contents

Title	i
Abstract	iii
Table of Contents	v
1 General Introduction	1
1.1 The inner structure of AGNs	1
1.2 Standard accretion disk as the central engine of AGNs and its problems	6
1.3 Variability of the UV-optical emission of AGNs/quasars	11
1.3.1 Observational properties of AGNs/quasars UV-optical variability	11
1.3.2 The UV-optical variability of AGNs/quasars from the viewpoint of the accretion disk theory	16
1.4 Polarization of the UV-optical emission of AGNs/quasars	19
1.5 The outline of this dissertation	24
2 Spectral Variability of SDSS Stripe82 Quasars	27
2.1 Review of previous work	28
2.2 5-band quasar light curves in the SDSS Stripe 82 region	30
2.3 The flux-flux correlation method	33
2.3.1 The Color of the Flux Difference Spectrum in Flux-Flux Space	33
2.3.2 The Color of Quasars in Flux-Flux Space	35
2.3.3 The Color-Redshift Relation	36
2.3.4 Advantages of the Flux-Flux Correlation Method	37
2.3.5 Linear Regression Method and Sample Selection	39
2.4 Continuum Variability	40
2.4.1 Redshift Dependence of the Color of the Flux Difference Spectrum	41
2.4.2 Comparison with the Composite and Composite Difference Spectrum	44
2.4.3 Comparison with Standard Accretion Disk Model	47
2.4.4 Brief Summary of This Section	52
2.5 Emission line variability: The origin of the redshift dependence of the color of the flux difference spectrum	53
2.6 Variability of the Small Blue Bump	57
2.6.1 Spectral Decomposition	57

2.6.2	Mg II Emission Line Variability	59
2.6.3	Fe II Pseudo-continuum Variability	60
2.6.4	Balmer Continuum Variability	61
2.6.5	Brief Summary of This Section	61
2.7	Summary and conclusions of Chapter 2	62
3	Constraints on the Inhomogeneous Accretion Disk Model	65
3.1	Introduction to inhomogeneous accretion disk model	66
3.2	Magnitude-magnitude linear regression with LINMIX_ERR	68
3.3	Median-filtered SDSS Stripe82 quasar light curves	72
3.4	Mathematical description of the inhomogeneous accretion disk model	74
3.4.1	Dexter & Agol's formalization	74
3.4.2	Simulating the SDSS Stripe 82 quasar light curves	78
3.5	Comparison of the Inhomogeneous accretion disk Model with Observational Data . .	82
3.6	Discussion and Conclusions of Chapter 3	85
4	The Relationship between Variable and Polarized Components of Quasars	89
4.1	Contradicting results between polarimetric and variability studies ?	90
4.2	Multi-band photometric observations with the 1.05-meter Kiso Schmidt telescope . .	93
4.3	Deriving the variable component spectra from KWFC data	97
4.4	Discussion	100
4.4.1	Notes on the effect of the BLR emission variability	100
4.4.2	Possible interpretations of the relationship between variable and polarized spectral components	103
4.5	Summary and conclusions of Chapter 4	104
5	Photometric and Polarimetric Variability of 3C 323.1	107
5.1	What is the true nature of the optical polarization source in continuum-confined po- larization quasars ?	108
5.2	Polarimetric and photometric data of 3C 323.1	109
5.2.1	Observational properties of 3C 323.1: the variable component spectrum . . .	109
5.2.2	Polarimetry data	110
5.2.3	Spectro-photometric flux calibration for the Bok/SPOL and Keck/LRIS data .	115
5.3	Spectral variability of the polarimetric properties	118
5.3.1	Spectral variability of the polarization degree and the polarization position angle	118
5.3.2	Spectral variability of the polarized flux	119
5.4	V-band polarimetric and photometric variability and its interpretation	120
5.4.1	Evidence against the synchrotron origin of the optical polarization in 3C 323.1	120
5.4.2	Constraints on the geometry of the scattering region in 3C 323.1	122
5.5	Summary and conclusions of Chapter 5	127

6	Summary and prospects for future work	131
	Acknowledgments	137
A	Symbols and acronyms	141
B	Model spectra used in Section 2.5	145
C	Regression intercepts as a function of redshift	149
D	Kiso/KWFC Multi-band Quasar Light Curves	151
E	Analysis of linear polarimetry data	159
F	Correcting for the effects of the Galactic ISP	161
G	Historic white-light polarimetric measurements for 3C 323.1	163

Chapter 1

General Introduction

Currently it is widely accepted that many (or all) galaxies host central supermassive black holes (SMBHs)¹. SMBHs can efficiently acquire their mass by swallowing the surrounding gas supplied from the host galaxies (e.g., Yu & Tremaine, 2002; Alexander & Hickox, 2012). Observationally, the central SMBHs sometimes show dramatic activities in terms of their huge output of the electromagnetic luminosity at all wavelengths from radio to X-ray, and such objects are called as (radiative-mode) Active Galactic Nuclei (AGN) (e.g., Heckman & Best, 2014). The AGN central engine is believed to be the black hole accretion disk, in which the gravitational potential of the accretion matters are released as thermal radiation due to the viscous dissipation in the differentially rotating accretion disk (Lynden-Bell, 1969; Pringle & Rees, 1972; Shakura & Sunyaev, 1973; Novikov & Thorne, 1973; Balbus & Hawley, 1998). It is observationally known that the black hole mass and the host galaxy properties such the bulge mass M_{bulge} and the velocity dispersion of the bulge σ_* show strong correlation in nearby galaxies (Magorrian et al., 1998; Ferrarese & Merritt, 2000; Gebhardt et al., 2000; Kormendy & Ho, 2013), implying that the huge energy output from AGN can affect the star formation history and cosmological evolution of the host galaxy (Silk & Rees, 1998; King, 2003). Therefore, clarification of the basic physics of the central engine of AGNs has profound implications for our understanding of the galaxy formation and evolution in the Universe (e.g., Alexander & Hickox, 2012, and references therein). However, even today there is much controversy among researchers over the true nature of the AGN accretion disks. In this chapter we will briefly introduce the present understanding of the inner region of AGN and the standard model for the AGN accretion disk. Also, the previous works on the observational properties of the AGN UV-optical variability and the polarization as tools to probe the accretion disk emission are summarized.

1.1 The inner structure of AGNs

Historically, many observational subclasses of AGNs have been identified in various wavelength ranges. In the optical wavelength range, AGNs are largely divided into two subclasses referred to as type-I and type-II objects, where type-I AGNs show broad ($\gtrsim 1000$ km/s) emission lines on the

¹Acronyms and symbols used in this dissertation are summarized in Table A.1 (Appendix A).

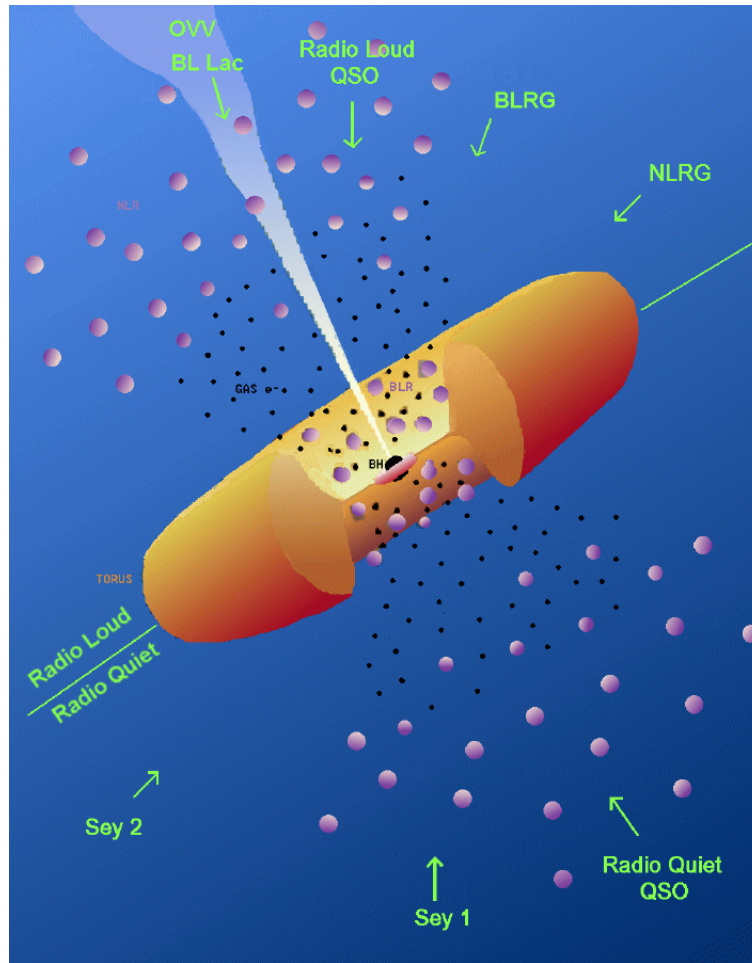


Figure 1.1: Sketch of the orientation-based unified scheme of AGN originally from Fig.1 of Urry & Padovani (1995). (The diagram is courtesy M. Polletta, ITESRE/CNR, Bologna, Italy, and appeared first at the BeppoSAX calendar 1999.)

other hand type-II AGNs shows only strong narrow emission lines at the galactic nuclear region. For historical reasons, optically faint AGNs are referred to as Seyfert galaxies, and luminous high redshift AGNs are referred to as quasars or quasi-stellar object (QSO). As well as the line-emitting AGNs, blazars, which are optically-featureless, strongly variable, point-like extragalactic objects, are also considered to be a kind of AGNs. In the radio wavelength range, galaxies associated with strong radio sources are also a class of AGNs, which are referred to as radio galaxies. Radio galaxies can also be optically divided into type-I and type-II objects.

According to the AGN unification model (Antonucci, 1993; Urry & Padovani, 1995), many subclasses of AGNs [Type-I/II objects, Seyfert galaxies, radio galaxies, blazars]² have basically the

²In this dissertation, we use the term “quasars” to refer to optically identified bright AGNs, including the radio-loud and the radio-quiet classes.

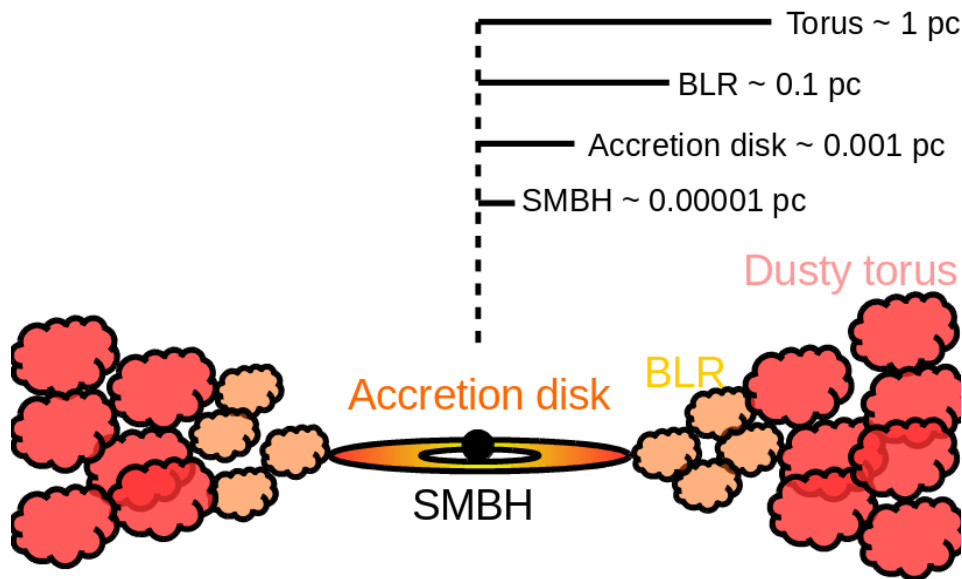


Figure 1.2: Schematic drawing of the inner structure of AGN (not to scale).

same inner structure but are viewed from different viewing angles (Figure 1.1). AGN is considered to be composed of (ordered from smallest to larger); the central SMBH (the black hole mass of $M_{BH} \sim 10^6 - 10^{10} M_{\odot}$), the black hole accretion disk, the broad emission line region (BLR), and the obscuring dusty torus (Figure 1.2). The BLR is thought to be composed of many (mostly fully ionized) clouds which have the particle density $n(H) \sim 10^{10} \text{ cm}^{-3}$ and the H-ionizing photon flux $\Phi(H) \sim 10^{18.5} \text{ cm}^{-2} \text{ s}^{-1}$ (i.e., ionization parameter $U(H) = \Phi(H)/(c \times n(H)) \sim 0.01$ (Davidson & Netzer, 1979; Baldwin et al., 1995), producing the broad permitted emission lines. More extended and lower density photo-ionized region with $n(H) \sim 10^3 \text{ cm}^{-3}$, called narrow emission line region (NLR), is usually associated with the AGN, which is responsible for producing strong narrow forbidden and permitted lines (Peterson, 1997). The dusty torus locates just outside of BLR, whose innermost radius corresponds to the dust sublimation radius defined by the UV radiation from the accretion disk (Barvainis, 1992; Suganuma et al., 2006; Koshida et al., 2014). The dust sublimation temperature is about 1500-1800 K (Barvainis, 1987; Netzer, 2015), and therefore the dusty torus emits thermal NIR-MIR radiation that dominate the total AGN luminosity at $\lambda_{rest} > 1 \mu\text{m}$ (Hernán-Caballero et al., 2016, and references therein). The radius of the BLR and the dusty torus has been observationally measured in several tens of AGNs/quasars through the reverberation mapping technique (Peterson & Horne, 2004; Suganuma et al., 2006, and references therein)³. Currently it is known that the BLR and the dusty torus radius are proportional to the square root of the AGN luminosity as is expected in the above-mentioned picture of the photo-ionized BLR and the photon-heated dusty torus (Figure 1.3).

³Because the accretion disk luminosity is time-variable (see Section 1.3 for detail), the line emission from the BLR and the NIR thermal emission from the dusty torus also vary in response to the disk continuum light curve. By measuring the time lags between the light curves of BLR/dust torus emission and the disk continuum, the flux-weighted radius of BLR/dust torus can be inferred. This is called as reverberation mapping technique.

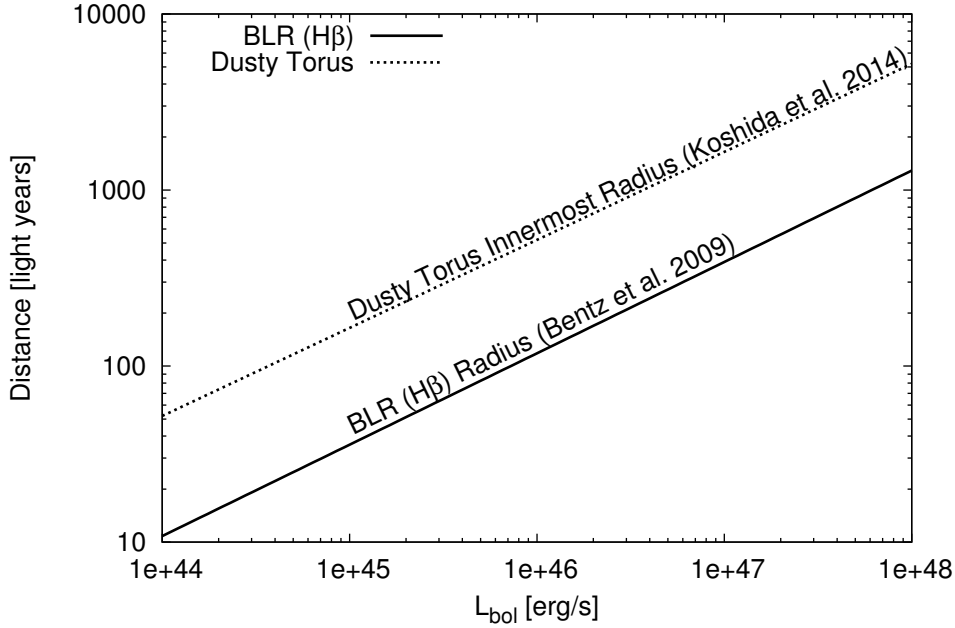


Figure 1.3: Radius-luminosity relation for the BLR (Bentz et al., 2009) and the dusty torus (Koshida et al., 2014). Both of these relationships for H β BLR and dust torus innermost radius are derived from the H β and K -band continuum reverberation mapping, respectively, therefore these are “responsivity-weighted” radius. The bolometric luminosity L_{bol} is converted from the 5100Å luminosity $L_{5100\text{Å}} = \lambda L_{\lambda}(5100\text{Å})$ by using the bolometric correction of 9.26 (Richards et al., 2006).

It should be noted that the accretion disk radius where the UV-optical photons are produced are expected to be ~ 100 times smaller than the BLR radius (i.e., typically $\lesssim 1$ light year). The physical sizes of the AGN inner structure (the accretion disk, BLR, and the dust torus) are quite small, thus it is impossible to spatially resolve these structures even with the current (and planned) largest aperture telescopes or the space telescopes (but see Rakshit et al., 2015, for details of the recent progress of the optical interferometry).

From the viewing angles close to face-on, the observer’s lines of sight do not intersect the obscuring torus and thus the observer observes the thermal continuum from the accretion disk (“Big Blue Bump”) and the BLR emission lines with $\gtrsim 1000$ km/s velocity widths at the UV-optical wavelengths (Type-I AGN). On the other hand, when an AGN is viewed from the edge-on viewing angles, the accretion disk and the BLR are hidden from the observer’s lines of sight, and thus observer cannot directly observe the disk continuum and BLR emission and can only see the NLR emission lines with < 500 km/s velocity widths (Type-II AGN). When AGNs associated with radio jet structure is viewed at the direction of the jet axis, the AGNs are observed as blazars because of the strongly Doppler-boosted optical synchrotron emission.

In this dissertation, we focus on the UV-optical emission of type I AGNs/quasars. The UV-optical emission in these objects is dominated by the accretion disk thermal continuum emission and BLR

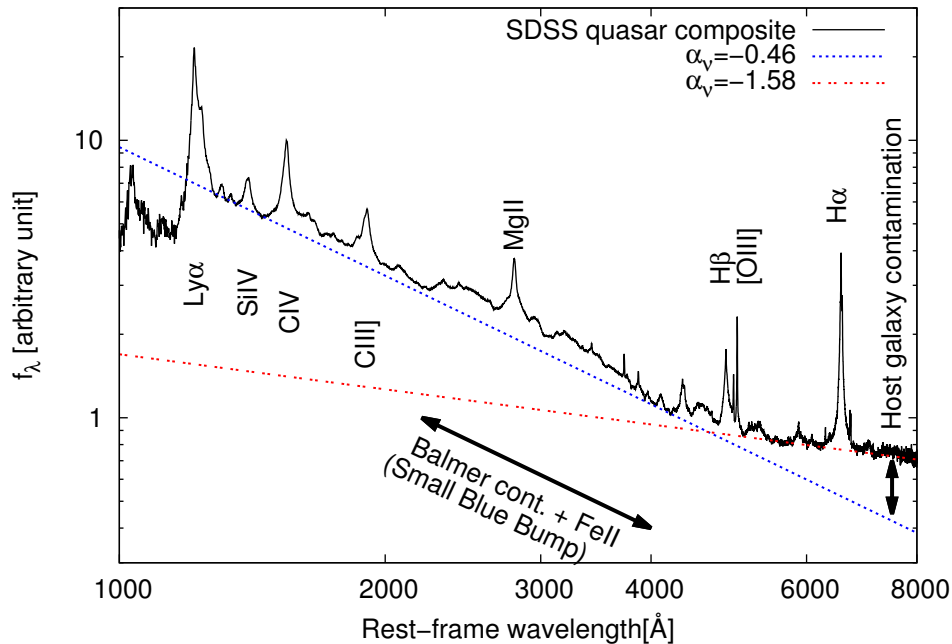


Figure 1.4: A mean quasar spectrum between 800\AA and 8555\AA presented by Vanden Berk et al. (2001), constructed from the spectra of 2200 SDSS quasars with redshifts $0.044 < z < 4.789$. Prominent BLR broad emission lines, as well as the “Small Blue Bump” (SBB) composed of the Balmer continuum and the UV Fe II pseudo-continuum from the BLR and the strong narrow [O III] $\lambda\lambda 4959, 5007$ emission lines from NLR, are labelled. On the top of the Balmer lines of H α and H β , the narrow emission line components from the NLR are also visible. The host galaxy flux contamination is stronger at redder wavelengths because the colors of galaxies are generally redder than the colors of quasars.

emission, and the host galaxy light and NLR emission also have contributions for some extent. Figure 1.4 shows the composite quasar spectrum constructed from spectra of 2200 quasars observed by the Sloan Digital Sky Survey (SDSS, York et al., 2000) with redshifts $0.044 < z < 4.789$ (Vanden Berk et al., 2001). Prominent broad emission lines of Lyman- α (Ly α at 1216\AA), Si IV $\lambda 1400$, C IV $\lambda 1549$, C III] $\lambda 1909$, Mg II $\lambda 2799$, Balmer- β and Balmer- α (H β and H α at 4863\AA and 6565\AA) are clearly seen. It should also be noted that there is an excess emission component above the underlying continuum around 2200\AA – 4000\AA . This spectral component is named “Small Blue Bump” (SBB), which is thought to be composed of a forest of UV Fe II emission lines and the Balmer recombination continuum from the BLR (e.g., Grandi, 1982; Wills et al., 1985). The spectral break of the underlying power-law like continuum indicated in Figure 1.4 is due to the observational biases; the data points used to generate the composite spectrum at longer wavelengths are dominated by the data of lower redshift, lower luminosity AGNs and therefore the host galaxy flux contribution is much stronger at longer wavelengths (Vanden Berk et al., 2001; Glikman et al., 2006). We should note that it is generally very difficult to evaluate the spectral shape of the underlying continuum in each quasar due to

the strong BLR emission and (in some cases) the host galaxy light contamination, as well as due to the limited wavelength coverage of the spectroscopic data.

1.2 Standard accretion disk as the central engine of AGNs and its problems

Soon after the first recognition of the presence of quasars (Schmidt, 1963), it was recognized that the large amount of energy emitted from quasars is only explained by the release of the gravitational energy by the collapse of matters to the SMBH, and the AGN/quasar UV-optical continua have been thought to be well represented by the optically thick, geometrically thin, thermal accretion disk around SMBH, known as α -disk model⁴ or standard accretion disk model (Lynden-Bell, 1969; Shakura & Sunyaev, 1973). In the standard accretion disk model developed by (Shakura & Sunyaev, 1973), the radial profile of the disk effective temperature $T_{\text{eff}}(R)$ is given by

$$\begin{aligned} T_{\text{eff}}(R) &= \left(\frac{3GM_{\text{BH}}\dot{M}}{8\pi\sigma_S R_{\text{in}}^3} \right)^{1/4} \left(\frac{R_{\text{in}}}{R} \right)^{3/4} \left(1 - \sqrt{\frac{R_{\text{in}}}{R}} \right)^{1/4} \\ &= T^* \left(\frac{R_{\text{in}}}{R} \right)^{3/4} \left(1 - \sqrt{\frac{R_{\text{in}}}{R}} \right)^{1/4} \\ \text{where } T^* &\equiv \left(\frac{3GM_{\text{BH}}\dot{M}}{8\pi\sigma_S R_{\text{in}}^3} \right)^{1/4} \end{aligned} \quad (1.1)$$

where M_{BH} is the black hole mass, \dot{M} [in mass per time] is the mass accretion rate, and σ_S is the Stefan-Boltzmann constant.

From the virial theorem, the accreted unit mass from $R_{\text{out}} \rightarrow \infty$ (initially has the total energy of $E = 0$) to the disk inner edge R_{in} acquires the potential energy of $U = -GM_{\text{BH}}/R_{\text{in}} = -2K$, and therefore has the total energy of $E = K + U = -GM_{\text{BH}}/2R_{\text{in}}$. This means that the energy of $GM_{\text{BH}}/2R_{\text{in}}$ is lost as radiative output from the disk surface. Since the standard accretion disk model assumes the mass accretion rate \dot{M} to be constant in time and in radius, the bolometric luminosity L_{bol} released from the disk surface corresponds to

$$L_{\text{bol}} = \dot{M} \times \frac{GM_{\text{BH}}}{2R_{\text{in}}} \quad (1.2)$$

The disk inner edge R_{in} is usually assumed to be at the inner stable circular orbit (ISCO) of the central SMBH. For non-rotating Schwarzschild black hole, ISCO is at $3R_S$, where $R_S = 2GM_{\text{BH}}/c^2$

⁴In this model, the kinematic viscosity coefficient ν is expressed as $\nu = \alpha c_s H$, where α is the viscosity parameter, c_s is the sound speed of the disk plasma, and H is the vertical height of the disk. The free parameter α does not appear in the equations describing the temperature distribution (Equation 1.1) and the emission spectrum of the disk (Equation 1.10) because of the assumption of the thermal equilibrium.

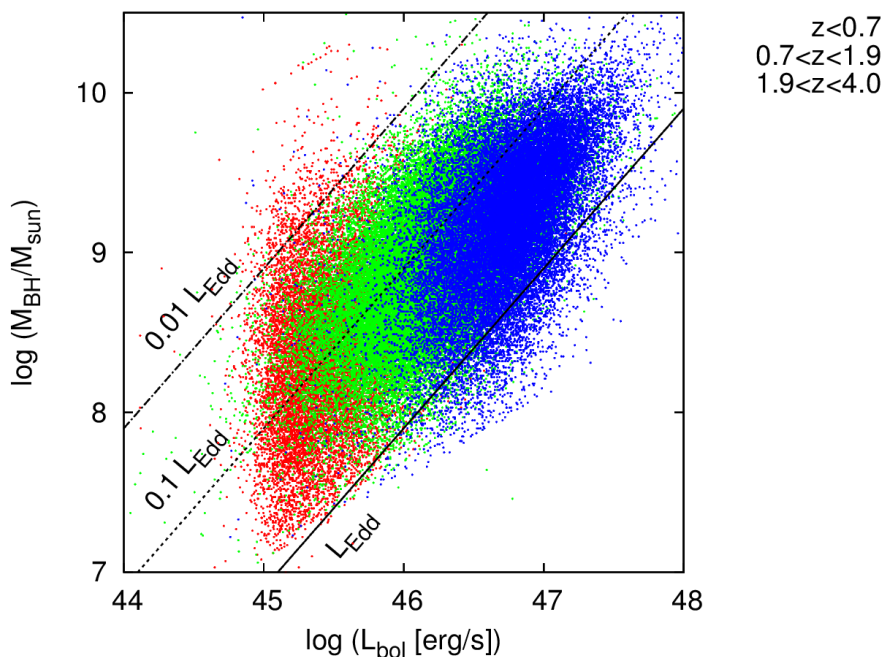


Figure 1.5: The black hole mass (M_{BH}) - the bolometric luminosity (L_{bol}) diagram of the SDSS quasars at the redshift z less than 4. The values of L_{bol} and M_{BH} are from the SDSS data release 7 catalog of quasar properties (Shen et al., 2011). Solid, dotted, and dashed dotted lines indicate the $M_{\text{BH}}-L_{\text{bol}}$ relation for the Eddington ratio η of 1, 0.1, and 0.01, respectively.

is Schwarzschild radius ⁵. With these assumption, the bolometric luminosity L_{bol} is expressed as

$$L_{\text{bol}} = \frac{1}{12} \dot{M} c^2 \quad [\text{non-rotating SMBH}]. \quad (1.3)$$

This means that the mass-to-radiation conversion efficiency ϵ of the standard accretion disk with non-rotating SMBH is $\epsilon = 1/12$ ($\sim 8.3\%$). For rotating SMBH, higher values of ϵ are achieved (Novikov & Thorne, 1973; Thorne, 1974). In this way, the mass-to-radiation conversion efficiency ϵ of the accretion disk is much higher than that of nuclear fusion ($\lesssim 1\%$), making AGNs optically luminous objects. Because ϵ for each quasar is an unknown model parameter, L_{bol} must be expressed in general as

$$L_{\text{bol}} = \epsilon \dot{M} c^2 \quad \text{with } \epsilon < 1 \quad (1.4)$$

It is convenient to express the luminosity in terms of the Eddington ratio η , which is defined as the ratio of the disk bolometric luminosity to the Eddington luminosity L_{Edd} of the SMBH. The Eddington luminosity L_{Edd} is defined as

$$L_{\text{Edd}} = \frac{4\pi G M_{\text{BH}} m_p c}{\sigma_T}, \quad (1.5)$$

⁵This corresponds to take the boundary condition for torque at the disk inner radius to be zero. Non-zero torque at the inner boundary may lead to $R_{\text{in}} < 3R_S$ (Penna et al., 2012).

where m_p is the proton mass and σ_T is the Thomson scattering cross-section. From Equation 1.5, the Eddington ratio η can be expressed as

$$\eta = \frac{L_{bol}}{L_{Edd}} \quad (1.6)$$

$$= 4.5 \times 10^8 \times \epsilon \times \frac{\dot{M} [M_\odot/\text{yr}]}{M_{BH} [M_\odot]} \quad (1.7)$$

$$\simeq 0.038 \times \left(\frac{\epsilon}{1/12} \right) \left(\frac{\dot{M}}{1M_\odot/\text{yr}} \right) \left(\frac{M_{BH}}{10^9 M_\odot} \right)^{-1}. \quad (1.8)$$

For example, typical values of the Eddington ratio of the SDSS quasars (i.e., luminous type 1 quasars) are $\eta \sim 0.01 - 1$ (Figure 1.5; e.g., Shen et al., 2011; Wu et al., 2015), indicating that the mass accretion rates are about $\dot{M} \sim 0.3 - 30M_\odot/\text{yr}$.

The characteristic temperature T^* in Equation 1.1 is the only parameter determining the spectral shape of the emitted spectrum L_ν from the standard thin accretion disk (Equation 1.11; Pereyra et al., 2006; Ruan et al., 2014). T^* roughly corresponds to the half of the peak temperature of the disk; the peak temperature of Equation 1.1 occurs at $R_{peak} = 49/36R_{in}$, and the peak temperature is $T_{peak} = 0.488T^*$. By assuming typical parameters for quasars,

$$T^* = 90600 \text{ K} \left(\frac{\epsilon}{1/12} \right)^{-1/4} \left(\frac{M_{BH}}{10^9 M_\odot} \right)^{-1/4} \left(\frac{\eta}{0.1} \right)^{1/4}. \quad (1.9)$$

The emission spectrum is given by summing up black body radiation of each annulus with the temperature of $T_{eff}(R)$:

$$L_\nu = \int \frac{2h\nu^3}{c^2} \frac{1}{e^{h\nu/k_B T_{eff}(R)} - 1} 2\pi R dR \quad (1.10)$$

Since the peak temperature of the disk $T_{peak} = 0.488T^*$ is ~ 50000 K for AGNs/quasars (Equation 1.9; see Figure 2.12), the radiative energy output of quasar accretion disks peaks at UV wavelengths, producing so called ‘‘Big Blue Bump’’ feature in their spectral energy distribution (SED).

In the long wavelength limit, by substituting $T_{eff}(R) \simeq T^*(R_{in}/R)^{3/4}$ to Equation 1.10, we obtain

$$L_\nu \propto \nu^{1/3} \quad [\text{long wavelength limit}], \quad (1.11)$$

i.e., the standard disk model predicts that the spectral index α_ν ⁶ of the disk continua at around optical-NIR wavelengths is $\alpha_\nu = 1/3$. This spectral index does not depend on any model parameters, and thus has been recognized as a primary model prediction of the standard accretion disk model, which can be used to test the validity of the standard disk model.

However, it is widely known that the observed UV-optical spectra of AGNs/quasars never show such blue spectral slope as predicted by the standard disk model (see e.g., Vanden Berk et al., 2001; Davis et al., 2007). The optical spectral indices of SDSS quasars are shown to be generally in the range from $\alpha_\nu = -1$ to 0 (Figure 1.4). Hopkins et al. (2004) showed that $\sim 98\%$ of the quasars selected by

⁶In this dissertation, α_ν is in the form of $f_\nu \propto \nu^{\alpha_\nu}$, whereas α_λ is in the form of $f_\lambda \propto \lambda^{\alpha_\lambda}$; i.e., $\alpha_\nu = -\alpha_\lambda - 2$.

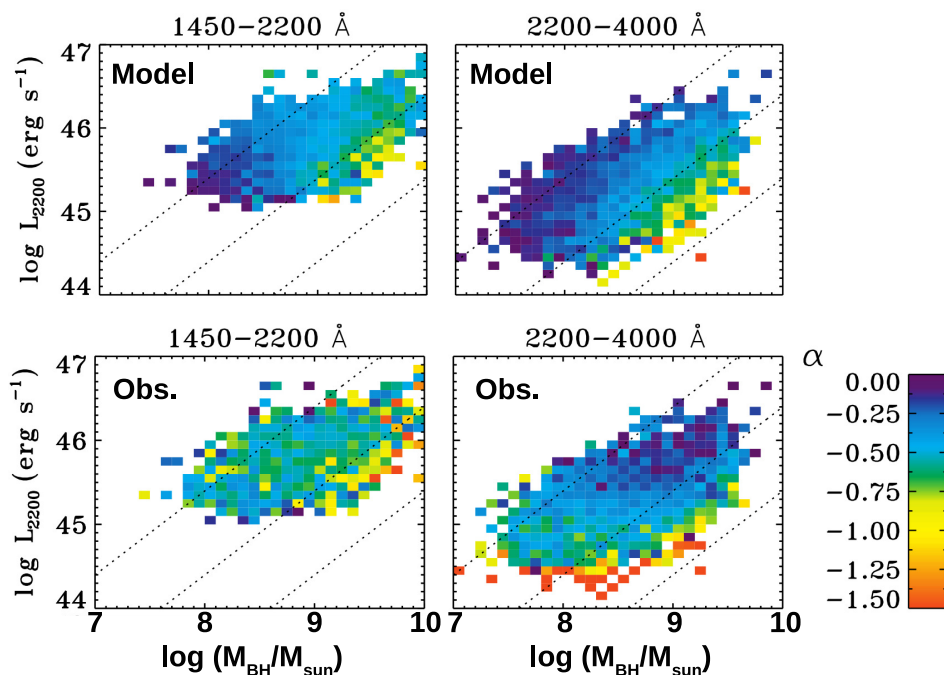


Figure 1.6: The optical spectral slopes α (in the form of $f_\nu \propto \nu^\alpha$) measured at 1450Å-2200Å and at 2200Å-4000Å (left panels and right panels, respectively) as a function of the black hole mass (M_{BH}) and the luminosity at 2200Å ($L_{2200\text{Å}}$) taken from Figures 4 and 7 of Davis et al. (2007). The upper panels are Monte Carlo calculations from the standard thin accretion disk model with non-spinning SMBH (the error on M_{BH} of 0.4 dex is assumed) and the lower panels are the SDSS quasars. Dotted lines indicate the $M_{\text{BH}}-L_{2200\text{Å}}$ relation for the Eddington ratio η of 1, 0.1, and 0.01 from the top to the bottom, respectively.

the SDSS surveys have the optical-NIR SEDs consistent with negligible extinction ($E(B - V) < 0.1$ mag) with the assumption of SMC-like reddening law (see also Krawczyk et al., 2015), and therefore the internal dust-reddening cannot be the discrepancy of the optical spectral shape between the SDSS quasars and the standard disk model. The long wavelength limit is not valid for the UV wavelengths of AGNs/quasars and thus the UV spectra are predicted to be slightly redder than $\alpha_\nu=1/3$, and more sophisticated radiative transfer calculations of the standard accretion disk by Hubeny et al. (2000) (see also Kawaguchi et al., 2001) predicted slightly lower values than $\alpha_\nu=1/3$ due to various opacity effects, but even considering them the serious discrepancy between the model predictions and the observed spectral shape still remains (Figure 1.6; Davis et al., 2007) (see also Figure 1.7). Nevertheless, we should note that the accretion disk continua in the observed AGN/quasar spectra are inevitably buried under the numerous BLR emission and also in some cases under the host galaxy (Figure 1.4). Actually, several authors have suggested that the host galaxy (and some other) flux contamination, making the observed spectra of AGNs/quasars redder, is the main cause of the discrepancy between the standard disk model predictions and the observed spectral shape (see e.g., Collier et al., 1999;

Kishimoto et al., 2008b).

In addition to this “spectral shape problem”, recently there has been growing evidence to suggest that the observed physical sizes of the AGN/quasar accretion disks measured by using the gravitational microlensing events (e.g., Pooley et al., 2007; Bachev et al., 2009; Morgan et al., 2010; Mosquera et al., 2013) or by using the X-ray-to-optical disk continuum reverberation mapping technique (see Section 1.3.2 for details; e.g., Cackett et al., 2007; Edelson et al., 2015; Noda et al., 2016; Jiang et al., 2016b) are a factor of four larger on average than that those predicted by the standard accretion disk model. This “disk size problem” also motivates several authors to propose modifications of the standard disk model (e.g., Dexter & Agol, 2011; Noda et al., 2016), but there is no consensus about the solution of this problem so far⁷.

As has already mentioned in Section 1.1, the physical size of the AGN accretion disk is too small to be spatially resolved, and therefore the observed spectra are inevitably the integrated emission from all over the accretion disk radii and from the multiple spectral components such as the host galaxy, BLR emission, and some other (possible) spectral component. In this context, the UV-optical flux variability and the polarization of AGNs/quasars are claimed to provide unique ways to probe the intrinsic accretion disk continua. The main purpose of this dissertation is to revisit the several problems of the standard accretion disk theory as a model for AGN/quasar accretion disks from the view point of the flux variability and polarization, and to examine the (in)validity of several alternative disk models proposed so far in the literature. Below subsections (Sections 1.3 and 1.4) we summarize the observational properties of the UV-optical flux variability and polarization of AGNs/quasars, and explain how these two emission properties can be used to examine the intrinsic accretion disk continua.

⁷For example, a X-ray backscattering matter above the disk (e.g., wind/warm absorber) (Bachev et al., 2009), a low radiative efficiency $\epsilon \ll 1/12$ (Morgan et al., 2010; McHardy et al., 2014), special geometrical configurations of the X-ray emitting corona region (Gardner & Done, 2016; Noda et al., 2016), and inhomogeneous disk model (Dexter & Agol, 2011, see also Section 3) have been proposed.

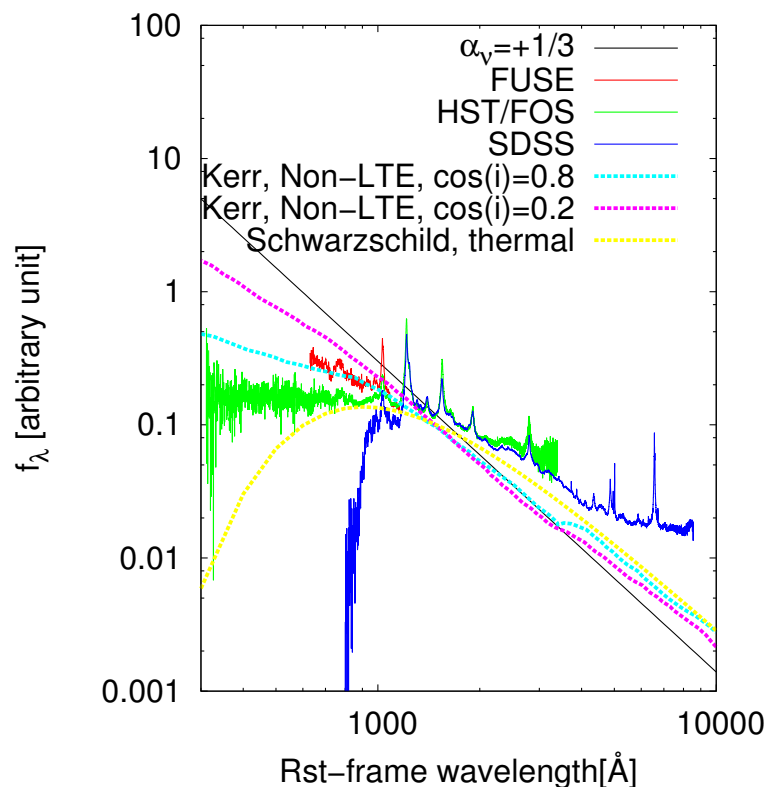


Figure 1.7: Composite spectra of type-I AGNs/quasars; red: a mean quasar spectrum from 630 Å to 1156 Å constructed from 128 FUSE observations of 85 AGNs with redshifts $z < 0.67$ (Scott et al., 2004); green: a mean quasar spectrum between 350 and 3000 Å constructed from 284 FOS observations of 101 quasars with redshifts $z > 0.33$ (Zheng et al., 1997); blue: the SDSS composite spectrum between 800 and 8555 Å from Vanden Berk et al. (2001) (shown in Figure 1.4). Composite spectra containing high redshift quasar sample are affected by Lyman α forests and damped Lyman α systems at $\lambda_{rest} < 912 \text{Å}$. Accretion disk model spectra of $\log(M_{BH}/M_{\odot}) = 9$ with $\log(\dot{M}/\dot{M}_{Edd}) = 1$ are also plotted; the standard accretion disk model spectrum for the case of Schwarzschild black hole (yellow), and non-LTE accretion disk spectral models for the case of extreme ($a_* = 0.998$) Kerr black hole Hubeny et al. (2000) (cyan and purple).

1.3 Variability of the UV-optical emission of AGNs/quasars

1.3.1 Observational properties of AGNs/quasars UV-optical variability

Soon after the discovery of the first quasar 3C 273, it was soon recognized that this quasar shows optical flux variability (Smith & Hoffleit, 1963), and currently it is widely accepted the flux variability (not only at optical but also all the other wavelength ranges) is an unique and ubiquitous property of AGNs and quasars. The short time scales of the flux variability (typically in the range from several days to years) indicate that the variability stems from the very compact region (e.g., Uttley &

Casella, 2014). In the case of “normal” type-I AGNs/quasars (i.e., excepting for blazars), the variability amplitude of the UV-optical emission is enormous (typically ~ 10 -100% from the average flux level), strongly suggesting that the flux variability must be related to the main energy source of AGN UV-optical emission, namely the accretion disk emission itself (Gaskell, 2008).

Recent studies, based on large data sets of AGNs/quasar light curves from time-domain surveys such as the SDSS Stripe82 supernova survey (Frieman et al., 2008; Sako et al., 2014), have shown that the UV-optical light curves of AGNs/quasars are mathematically well described by stationary first-order auto regressive process (AR(1)), namely damped random walk (DRW) (Rybicki & Press, 1992; Kelly et al., 2009; Kozłowski et al., 2010; MacLeod et al., 2010; Andrae et al., 2013; Zu et al., 2013; Morganson et al., 2014) (although see also Caplar et al., 2016). Continuous first-order AR process (e.g., Kelly et al., 2009; Bailer-Jones, 2012; Andrae et al., 2013) is a Markov process time series depending on a single previous signal ⁸, given as (expressed by stochastic variable s with zero mean)

$$s_i = \alpha_{AR}s_{i-1} + \varepsilon_i \quad (1.12)$$

$$\text{where } \varepsilon_i \sim G(\sigma_{AR}^2), \quad (1.13)$$

where i represents the time, and α_{AR} is an AR parameter ($|\alpha_{AR}| < 1$ for stationarity). $G(\sigma_{AR}^2)$ indicates a Gaussian distribution function with the variance σ_{AR}^2 and with zero mean, and a tilde (\sim) means that a variable on the left side is drawn from a distribution function on the right side. AR parameters of α_{AR} and σ_{AR}^2 are related to the signal covariance matrix through *the Yule-Walker equation*. By multiplying the s_i or s_{i-1} for Equation 1.12 and applying an operator $\langle \rangle$ (where $\langle s_i s_j \rangle = \sigma_{AR}^2$ (if $i = j$) or 0 (if $i \neq j$)), we obtain *the Yule-Walker equation* for AR(1) process (a special case of AR process):

$$\sigma_{AR}^2 = \langle s_i s_i \rangle - \alpha_{AR} \langle s_i s_{i-1} \rangle \quad (1.14)$$

$$\langle s_i s_{i-1} \rangle = \alpha_{AR} \langle s_i s_i \rangle \quad (1.15)$$

The DRW process is characterized by the signal covariance matrix as $\langle s_i s_i \rangle = \sigma^2$ and $\langle s_i s_{i-1} \rangle = \sigma^2 \exp(-(t_i - t_{i-1})/\tau)$, and therefore α_{AR} and σ_{AR}^2 are given as (see e.g., Kozłowski, 2016b)

$$\begin{aligned} \alpha_{AR} &= \exp\left(-\frac{t_i - t_{i-1}}{\tau}\right) \\ \sigma_{AR}^2 &= \sigma^2 \left(1 - \exp\left(-\frac{2(t_i - t_{i-1})}{\tau}\right)\right), \end{aligned} \quad (1.16)$$

where $t_i > t_{i-1}$. Structure function (SF) is a measure of the observed variability of AGNs/quasars often used in the literature, defined as $SF(\Delta t) = \sqrt{\langle \Delta m^2 \rangle}$ (Kawaguchi et al., 1998; MacLeod et al., 2012). In terms of the DRW model, the SF is expressed as

$$SF_{DRW}(\Delta t) = \sigma_{AR} = \sigma \sqrt{1 - \exp(-2\Delta t/\tau)}, \quad (1.17)$$

⁸It is “first order” in that s_n is predicted only from a single previous signal point s_{n1} , while s_{n2} etc. have no influence once s_{n1} is given, and “continuous” in that the observation times t_n are non-uniformly spaced (Andrae et al., 2013).

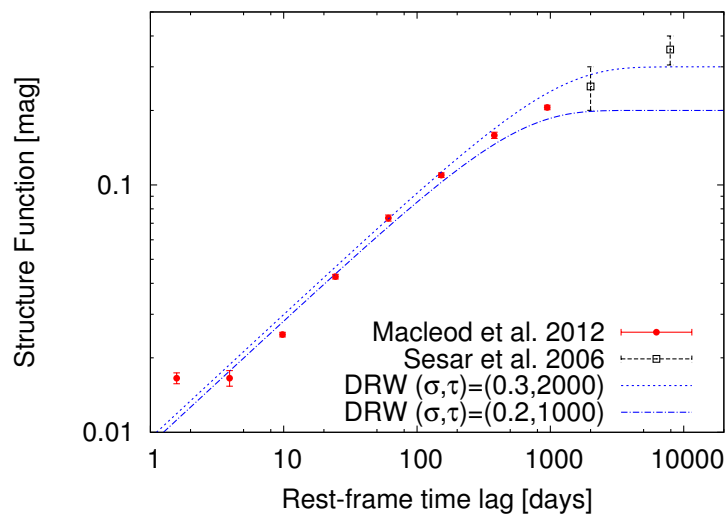


Figure 1.8: The structure function (SF) of the SDSS quasars for data with rest-frame wavelength in the range 2000-3000Å, and the DRW model SFs. The SF of the SDSS quasars at $\tau < 1000$ days is from the SDSS multi-epoch photometric observations at the Stripe82 region (MacLeod et al., 2012), and the SF at $\tau > 1000$ days is from the SDSS and the POSS-I and -II measurements derived by Sesar et al. (2006). Note that the photometric errors (at the level of ~ 0.01 mag) are dominating the SFs at the shortest time scales.

where $\Delta t = t_i - t_{i-1}$. $SF_{DRW}(\Delta t) \sim \sigma \sqrt{2\Delta t/\tau}$ at the short time scale ($\Delta t < \tau/2$), on the other hand $SF_{DRW}(\Delta t) \sim \sigma$ at the long time scale ($\Delta t > \tau/2$). According to the results of Butler & Bloom (2011) and Andrae et al. (2013) for SDSS Stripe82 quasars, the rest-frame characteristic time scale τ is ~ 1000 days and the characteristic amplitude σ is $\sim 10^{-0.5}$ mag, with ~ 2 dex scatters around the mean values. Figure 1.8 shows the SF of the SDSS quasars derived by Sesar et al. (2006) and MacLeod et al. (2012), along with the DRW model SFs. Note that the DRW model says nothing about the physical origin of the AGN/quasar flux variability; the success of the DRM model only indicates that the variability is the result of some Gaussian stochastic process in the accretion disks. There is an indication that the characteristic variability time scale is weakly anti-correlated with the mass of the SMBH (Kelly et al., 2013)⁹, but currently no strong correlation has been found between the variability time scale or amplitude and the physical properties of AGNs/quasars (e.g., Kelly et al., 2009; Caplar et al., 2016; Kozłowski, 2017, and references therein).

One important observational property of the UV-optical variability of AGNs/quasars other than the (single-band) variability time scale and amplitude is that the multi-band light curves show strong inter-band correlation through the UV-to-optical wavelengths; in other words, when plotting the two broad-band light curves in flux vs. flux plots, they show strong linear relationship (e.g., Choloniewski, 1981; Winkler et al., 1992; Sakata et al., 2010, 2011) (see Figure 1.9 for the case of NGC 4151). For

⁹The anti-correlation between the variability time scale and the SMBH mass is more clearly seen in the X-ray band (McHardy et al., 2006).

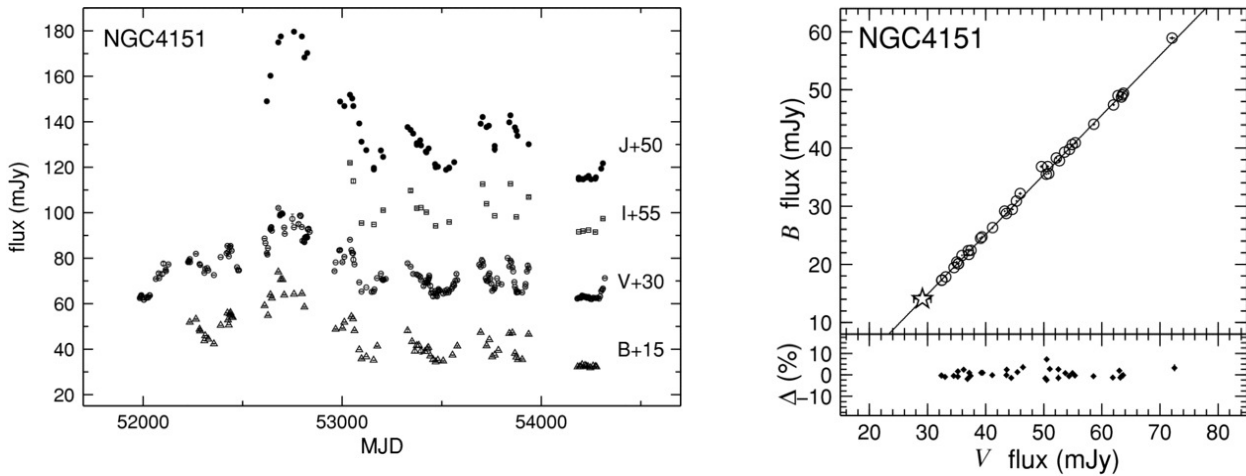


Figure 1.9: The broad-band light curves (left panel) and the B and V -band flux-flux plot (right) of NGC 4151 (figures are taken from Figures 4 and 20 of Sakata et al. 2010). Stellate symbol in the right panel represent the flux contribution from the host galaxy light and the narrow emission lines. It is clearly shown that the flux-flux plot is well represented by a best-fit regression line (the residual from the best-fit regression line is also shown in the inset of the right panel).

example, the B - and R -band light curves of 42 quasars from the Palomar-Green sample obtained by Giveon et al. (1999) show strong correlation between the two band light curves, indicating that the inter-band correlation emerges within at least less than the typical sampling interval is ~ 40 days for these quasars. Also, for nearby type I Seyfert AGNs, multi-band monitoring observations have shown almost simultaneous variability with lags of less than 1-2 days across the optical wavelengths (e.g., Cutri et al., 1985; Clavel et al., 1991; Korista et al., 1995; Wanders et al., 1997; Collier et al., 1998). Such inter-band correlation within a few days strongly suggests that there is a single, causally-connected compact variable source in AGNs/quasars (i.e., the accretion disks) or that a single physical parameter is driving the variability (Uttley & Casella, 2014).

In addition to the strong inter-band correlation, the “Bluer-When-Brighter” (BWB) color variability trend has been usually observed in multi-band light curves of the AGNs/quasars (Maoz et al., 1993; Paltani & Courvoisier, 1994; Giveon et al., 1999; Vanden Berk et al., 2004; Sakata et al., 2011; Schmidt et al., 2012; Zuo et al., 2012). In other words, the UV-optical variability amplitude is generally larger in shorter wavelengths, which makes the spectral shape of each quasar bluer when it gets brighter. Note that it has been suggested for several objects that the BWB trend is mostly due to the result of the host galaxy contamination to the intrinsically achromatic variable spectral component, where the variable component (i.e., the disk emission) is bluer than the host galaxy component. However, the BWB trend is also observed in the high luminosity SDSS quasars (e.g., Vanden Berk et al., 2004) in which the host galaxy flux contribution is negligible (e.g., Shen et al., 2011), suggesting that the BWB trend is intrinsic to the variable component.

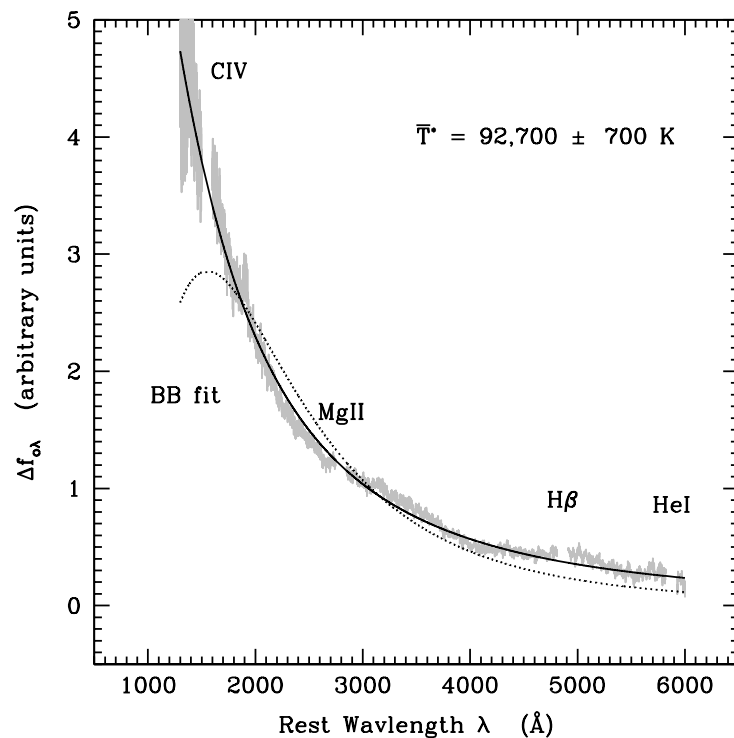


Figure 1.10: Composite flux difference spectrum derived from 315 SDSS quasars which are spectroscopically observed twice in the course of the SDSS surveys (thin gray line), constructed by Wilhite et al. (2005) (this figure is taken from Figure 7 of Pereyra et al., 2006). The best-fit model spectra for the variable mass accretion rate model with the mean characteristic temperature $\bar{T}^* = 92700 \text{ K}$ (solid line; see Equation 1.25) and the single temperature black body (dotted line) are also shown.

Because the variable source in an AGN/quasar is believed to be the accretion disk itself, it is generally assumed in previous works (Pereyra et al., 2006; Li & Cao, 2008; Schmidt et al., 2012; Ruan et al., 2014; Buisson et al., 2017) that the variable spectral component in each AGN/quasar directly reflect the spectral shape of the intrinsic accretion disk continuum emission, usually buried under the other spectral components. Figure 1.10 shows the composite flux difference spectrum, i.e., the composite variable component spectrum, derived from 315 SDSS quasars which are spectroscopically observed twice in the course of the SDSS surveys (constructed by Wilhite et al., 2005), where a flux difference spectrum of each quasar is defined as the difference between the spectrum at the brighter phase and at the fainter phase. We should note that the BLR emission (broad emission lines, Balmer continuum and the Fe II pseud continuum) is also variable in response to the changes in the disk continuum emission (c.f. the reverberation mapping; Peterson & Horne, 2004, and references therein), but it is observationally known that the variability amplitude of the BLR emission is at most 20%-30% of that of the disk continuum emission (“intrinsic Bladwin effect”; Kinney et al., 1990; Wilhite et al., 2005). Therefore, the composite variable component spectrum shown in Figure 1.10 has nearly

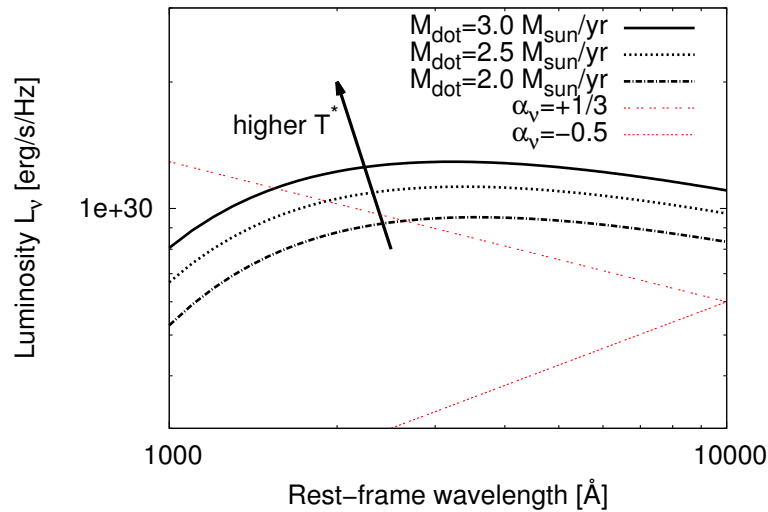


Figure 1.11: The standard disk spectra for different mass accretion rates of $\dot{M} = 2.0M_{\odot}/\text{yr}$, $\dot{M} = 2.5M_{\odot}/\text{yr}$, and $\dot{M} = 3.0M_{\odot}/\text{yr}$. The SMBH mass is fixed to $M_{BH} = 10^9M_{\odot}$. For comparison, the power-law spectra of $\alpha_v = +1/3$ (the long wavelength limit of the standard disk model; Equation 1.11) and $\alpha_v = -0.5$ (mean spectral index of SDSS quasars from Vanden Berk et al., 2001, Figure 1.4).

featureless spectral shape, and it is claimed by Pereyra et al. (2006) that this spectral shape is consistent with the theoretical prediction based on the standard accretion disk model, as shown in Figure 1.10 (see Section 1.3.2 for details). In Chapter 2, by using ~ 10 years multi-band light curves for ~ 9000 SDSS quasars available in SDSS Stripe 82 region, we will discuss the spectral shape of the variable component in these quasars and compare it with the standard accretion disk model spectra.

1.3.2 The UV-optical variability of AGNs/quasars from the viewpoint of the accretion disk theory

Because the analytic standard accretion disk theory (i.e., the steady state accretion disk model) says nothing about the time evolution of the accretion disk, additional assumptions have to be introduced to account for the UV-optical flux variability in AGNs/quasars. Historically, several models employing the external origin of the flux variability, such as starburst (Aretxaga & Terlevich, 1994; Aretxaga et al., 1997) and stellar collisions (Courvoisier et al., 1996; Torricelli-Ciamponi et al., 2000), had been proposed. However, the continued success of the BLR reverberation mapping observations for AGNs/quasars (see Barth et al., 2015; Shen et al., 2016, for recent results) and the similarity and ubiquitousness of the UV-optical variability confirmed in a large sample of AGNs/quasars essentially exclude these external source models, and it is currently accepted that some kind of changes in the accretion disks are responsible for the flux variability.

The time scales of the AGN flux variability may be directly linked to one of the characteristic accretion disk time scales (Czerny, 2006; King, 2008; Kozłowski, 2016a). The standard disk theory

states that the viscous time scale t_{visc} , defined as the diffusion time scale of the disk's surface density, is given as

$$t_{visc} \sim \frac{R_{out}^2}{\nu} = \frac{R_{out}}{\alpha c_s H} \quad (1.18)$$

$$\sim 10^{10} \left(\frac{\alpha}{0.03} \right) \left(\frac{R}{10^{18} \text{cm}} \right)^{3/2} \text{ year}. \quad (1.19)$$

Although the disk luminosity is predominantly radiated from the inner region of the disk, most of the mass accreting toward the SMBH is reserved at the outer region, thus the viscous time scale t_{visc} can be considered as the time scale of the flux variability of AGNs/quasars if the flux variability is caused by the viscous diffusion of the accreting mass (e.g., King, 2008). However this time scale is too large to explain the observed UV-optical flux variability in several months-to-years time scales. The thermal time scale t_{th} , defined as the dissipation time scale of the internal energy of the accreting mass as the thermal energy, is given as

$$t_{th} \sim \left(\frac{H}{R_{out}} \right)^2 t_{visc} \quad (1.20)$$

$$\sim 10000 \left(\frac{\alpha}{0.03} \right) \left(\frac{R_{out}}{10^{18} \text{cm}} \right)^{3/2} \text{ year}, \quad (1.21)$$

where $H/R_{out} \sim 10^{-3}$ is assumed. Again, this time scale is larger than that of the observed UV-optical flux variability in AGNs/quasars, suggesting that the thermal instability in the accretion disk may not be the cause of the observed flux variability.

For comparison, the light crossing time t_{light} is given as

$$t_{light} = \frac{R_{out}}{c} \sim \frac{v_K}{c} t_{dyn} \quad (1.22)$$

$$\sim 1 \left(\frac{R_{out}}{10^{18} \text{cm}} \right) \text{ years} \quad (1.23)$$

To account for the observed UV-optical variability amplitude and the strong inter-band correlations of AGN/quasar light curves, several authors have suggested that the changes in the mass accretion rate \dot{M} ; because the disk luminosity depend linearly on the mass accretion rate \dot{M} (Equation 1.4), changes in \dot{M} directly lead the UV-optical flux (e.g., Pereyra et al., 2006; Sakata et al., 2011; Gu & Li, 2013). Moreover, the variable \dot{M} model can naturally explain the ubiquitous BWB color variability trend in AGNs/quasars, because with this model the changes of the disk temperature due to the changes in \dot{M} ($T^* \propto \dot{M}^{1/4}$) leads to the shifts of the peak of the SED where the higher temperature makes the SED bluer (Figure 1.11; e.g., Sakata et al., 2011). By defining the variable component spectrum ΔL_ν as the difference spectrum of the two spectra with different mass accretion rate (i.e., different characteristic temperature T^*)

$$\Delta L_\nu = L_\nu(T_2^*) - L_\nu(T_1^*), \quad (1.24)$$

and assuming that the temperature difference $\Delta T^* \equiv T_2^* - T_1^*$ is small, the first order Taylor expansion of Equation 1.10 for T^* around $\bar{T}^* \equiv \frac{1}{2}(T_2^* + T_1^*)$ gives (see e.g., Pereyra et al., 2006)

$$\Delta L_\nu \simeq \frac{\Delta T^*}{\bar{T}^*} \int \frac{2h\nu^3}{c^2} \frac{h\nu}{k_B \bar{T}_{eff}} \frac{e^{h\nu/k_B \bar{T}_{eff}}}{(e^{h\nu/k_B \bar{T}_{eff}} - 1)^2} 2\pi R dR, \quad (1.25)$$

where $\bar{T}_{eff} = \bar{T}^*(R_{in}/R)^{3/4}(1 - \sqrt{R_{in}/R})^{1/4}$ (Equation 1.1). As shown in Figure 1.10, this model is claimed to well explain the spectral shape of the composite variable component spectrum derived from the SDSS quasars (Pereyra et al., 2006). As is the case for the single epoch observed spectrum in Equation 1.10, the flux difference spectrum predicted by the variable mass accretion rate model in Equation 1.25 also has the power-law index of $\alpha_\nu = +1/3$ in the long wavelength limit:

$$\Delta L_\nu \propto \nu^{1/3} \quad [\text{long wavelength limit}]. \quad (1.26)$$

This variable mass accretion rate model mathematically (algebraically) explain the strongly correlated variability throughout the UV-optical wavelengths, but as discussed above, it is theoretically difficult to change the mass accretion rate \dot{M} all over the accretion disk radius within month-to-years time scales considering the huge viscous time scale t_{visc} of the disk (Equation 1.19). In Chapter 2, we will revisit the validity of the “variable mass accretion rate model” from the viewpoint of the spectral shape of the spectral shape of the variable component spectra; the spectral shape of the variable component spectra in the SDSS quasars and that of the model variable component spectra in Equation 1.25 will be quantitative compared.

An alternative explanation for the UV-optical variability of AGNs/quasars has been proposed by Dexter & Agol (2011). In the model of Dexter & Agol (2011) (called “inhomogeneous accretion disk model”), the UV-optical variability is attributed to the localized temperature flares at the disk surface. The inhomogeneous accretion disk may be a natural consequence of a magnetorotational instability (MRI; Balbus & Hawley, 1991) driven instability (Hirose et al., 2009a), a thermal instability (Shakura & Sunyaev, 1976), an inflow instability (Lightman & Eardley, 1974), or a photon bubble instability (Turner et al., 2005) in the radiation-dominated region of the accretion disks, but it is currently unclear what kinds of instabilities are actually at work in the AGN accretion disks (note that the global radiative MHD simulations for the standard disk model, which are still in development (e.g., Hirose et al., 2009b; Sądowski, 2016)). Anyway, Dexter & Agol (2011) showed that the inhomogeneous accretion disk model with large temperature fluctuations ($\sigma_T = 0.35 - 0.50\text{dex}$ for the local effective temperature T_{eff} ; Equation 1.1) in 100-1000 independently fluctuating zones of the disk surface for every factor of two in radius can explain several observational properties of the AGN/quasar accretion disks mentioned in Section 1.2, such as the large disk size inferred from the microlensing variability in the gravitationally-lensed quasars, UV-optical variability amplitude of AGNs/quasars, and their spectral shape. However, as discussed in Chapter 3, the inhomogeneous accretion disk has difficulty in explaining the strong inter-band correlation observed in multi-band light curves of AGNs/quasars.

In addition to the “variable mass accretion rate model” and the “inhomogeneous disk model”, X-ray reprocessing model (e.g., Krolik et al., 1991) is also claimed to be a possible driver of the

UV-optical variability of AGNs/quasars. The X-ray reprocessing model assumes a variable central source of high energy photons (specifically X-ray coronas located around the innermost region of the accretion disk) illuminating the whole accretion disk surface. In this model, the disk surface temperature is heated not only by the viscous dissipation in the disk but also the X-ray or Extreme-UV (EUV) photons from the lamp-post like source (corona) located above the innermost region of the disk¹⁰. The UV-optical variability can be caused by the changes of the amount of the illuminating high energy photons, and these changes can be propagated to the outer disk region within the light travel time. Therefore, the X-ray reprocessing model can be the most straightforward interpretation of the observed short time-scale (days-to-months) variability of AGNs/quasars. Actually, for several of the nearby type I Seyfert galaxies, slight lags of several hours-to-days in the UV-optical light curves behind the X-ray light curves have been reported (disk continuum reverberation mapping; e.g., Edelson et al., 2015; Lira et al., 2015; Noda et al., 2016; Buisson et al., 2017), which are considered to be evidence of the existence of the X-ray reprocessing in these AGNs. However, one crucial counterargument for the X-ray reprocessing model for the UV-optical variability is that the total energy of the illuminating variable high energy photons is observationally much less than that of the variable UV-optical emission especially in luminous quasars (Antonucci et al., 1996; Gaskell, 2008; Edelson et al., 2014; Uttley & Casella, 2014); note that the flux ratio of the X-ray to UV emission in AGNs/quasars is anti-correlated with the UV luminosity (Vagnetti et al., 2010, and references therein). The model predictions and the potential of the X-ray reprocessing model as an AGN/quasar variability model will be discussed in Chapter 6.

1.4 Polarization of the UV-optical emission of AGNs/quasars

It has been suggested that optical spectropolarimetry can be an unique way to probe the UV-optical spectral shape of the intrinsic quasar accretion disk continua (Antonucci et al., 2004; Kishimoto et al., 2003, 2004, 2008b). In the case of type 1 quasars with prominent radio jet structure (note that the jet axis is thought to be parallel to the accretion disk's rotation axis), it is known that they generally show weak ($p \lesssim 1\%$) linear polarization parallel to the radio structure (e.g., Stockman et al., 1979; Antonucci, 1983; Stockman et al., 1984; Schmidt & Smith, 2000; Smith et al., 2002; Kishimoto et al., 2004). This “parallel” polarization is in marked contrast to the “perpendicular” polarization observed in most of the type 2 objects (Antonucci & Miller, 1985; Brindle et al., 1990; Smith et al., 2004; Zakamska et al., 2005). Even for radio-quiet quasars, high-spatial resolution imaging observations have revealed that there is a significant correlation between the direction of extended emission region (which is another good tracer of the accretion disk's rotation axis) and the polarization position angle, in that the former tends to be parallel to the latter in type 1 objects and perpendicular in type 2 objects (Zakamska et al., 2005; Borguet et al., 2008). The perpendicular polarization in type 2 objects

¹⁰The lamp-post geometry for the X-ray source in AGNs/quasars is originally suggested to account for the heavily redshifted broad spectral profile and the variability properties of the iron $K\alpha$ line at 6.4 keV in the reflection component of the X-ray spectra (e.g., Tanaka et al., 1995; Nandra et al., 1997; Miniutti & Fabian, 2004).

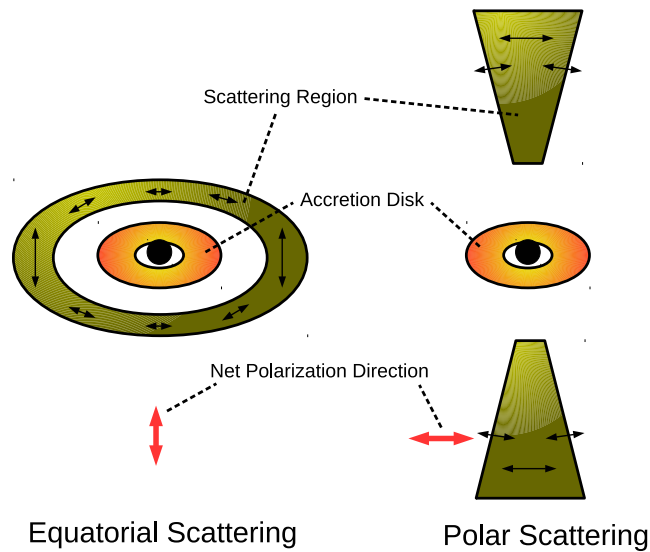


Figure 1.12: Schematic view of the optically-thin equatorial scattering geometry (left) and the polar scattering geometry (right), assuming a moderate inclination angle. The accretion disk photons are scattered toward the observer’s line of sight, producing net polarization due to the directional asymmetry of the projected surface area of the scattering region. The net polarization angle of the observed light is parallel (left; equatorial scattering) and perpendicular (right; polar scattering) to the disk’s rotation axis.

is recognized to be the results of the electron/dust scattering of the AGN nuclear emission from the polar-scattering region. However, it is generally hard to explain the parallel polarization observed in the type 1 quasars by the polar-scattering or the polarization induced within the atmosphere of plane-parallel scattering-dominated disk (e.g., Antonucci, 1988; Kishimoto et al., 2003). In addition, some authors have claimed that the intrinsic quasar accretion disk continua must be completely depolarized because of the strong Faraday depolarization with magnetic fields in the disk atmosphere (Agol & Blaes, 1996; Silant’ev et al., 2009, and references therein). Instead, The observed optical polarization properties in the type 1 quasars can be explained by assuming a geometrically- and optically-thin equatorial electron scattering region locating inside the dust torus; photons produced inside this electron-scattering region can be scattered into our line of sight, resulting in a net linear polarization “parallel” to the disk rotation axis (e.g., Stockman et al., 1979; Antonucci, 1988; Smith et al., 2004, 2005; Goosmann & Gaskell, 2007; Kishimoto et al., 2008a; Batcheldor et al., 2011; Gaskell et al., 2012; Marin & Goosmann, 2013; Hutsemékers et al., 2015; Silant’ev et al., 2016). Figure 1.12 shows the schematic view of the equatorial and polar scattering geometry around the accretion disk. As is clearly indicated in Figure 1.12, the polar scattering produces polarization perpendicular to the disk’s axis, on the other hand the equatorial scattering produces relatively weak net polarization parallel to the disk’s axis (valid in both cases of dust and electron scattering; Zubko & Laor, 2000; Marin et al., 2012; Goosmann et al., 2014).

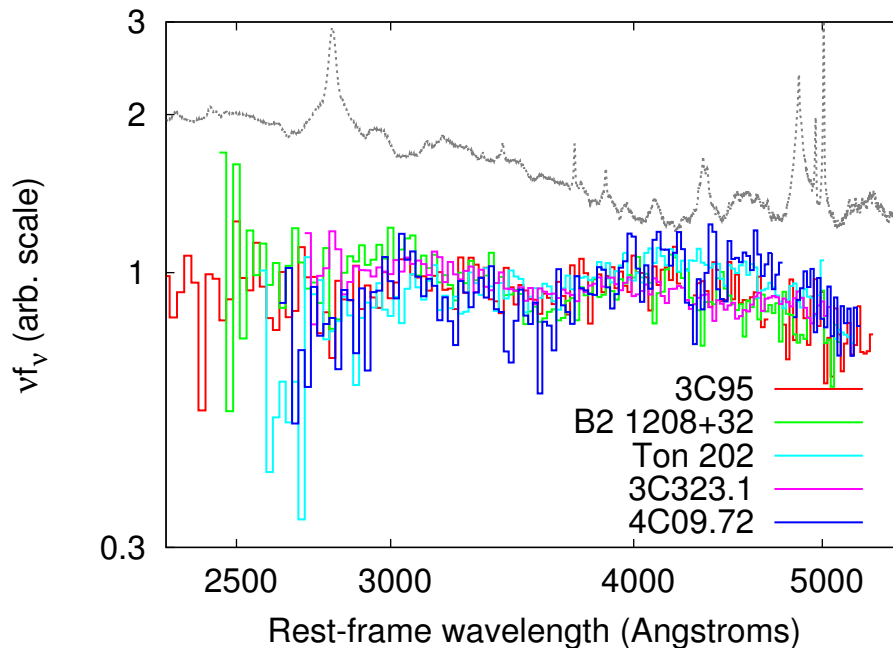


Figure 1.13: Polarized flux spectra for five quasars showing polarization decrease at $\lambda_{rest} < 4000 \text{ \AA}$ (Figure 35 of Kishimoto et al. 2004). It should be noted that the statistical errors of the data points of the polarized flux spectra are large, and the polarized flux spectra are consistent with smooth continuum spectra. Also shown is the SDSS quasar composite spectrum Vanden Berk et al. (2001) (Figure 1.4). It is clearly seen that the broad emission lines do not appear in the polarized flux spectra, meaning that the BLR emission is unpolarized.

In most of type 1 Seyfert galaxies, it is observationally known that not only the UV-optical continua but also the BLR emission lines are polarized. The polarization of the BLR emission lines are often observed to be at lower polarization degree and at different position angle than that of the continuum emission, and showing polarization angle rotation as a function of wavelength (e.g., Smith et al., 2004) This implies that the putative equatorial electron scattering region is more or less similar in size to the BLR in these AGNs (e.g., Angel & Stockman, 1980; Smith et al., 2005; Kishimoto et al., 2008a; Baldi et al., 2016). However, optical spectropolarimetry observations for luminous type 1 quasars with “parallel” optical polarization carried out by Antonucci (1988), Schmidt & Smith (2000) and Kishimoto et al. (2003, 2004, 2005, 2008b) have revealed that there is a population of quasars whose BLR emission lines are essentially unpolarized, i.e., the polarization of these quasars is confined only to the continuum¹¹. Figure 1.13 shows the polarized flux spectra (defined as $p_\lambda \times v f_v$, where p_λ represents the polarization degree as a function of wavelength) for the 5 quasars with “continuum-

¹¹Kishimoto et al. (2004) showed that 5 of the 15 quasars spectropolarimetrically observed by them have the continuum-confined polarization. However, note that Kishimoto et al. (2004)’s target selection was biased to the quasars which had already been known to be showing a hint of continuum-confined polarization by previous works. Therefore, it is currently unclear how common the continuum-confined polarization is observed in general quasar population.

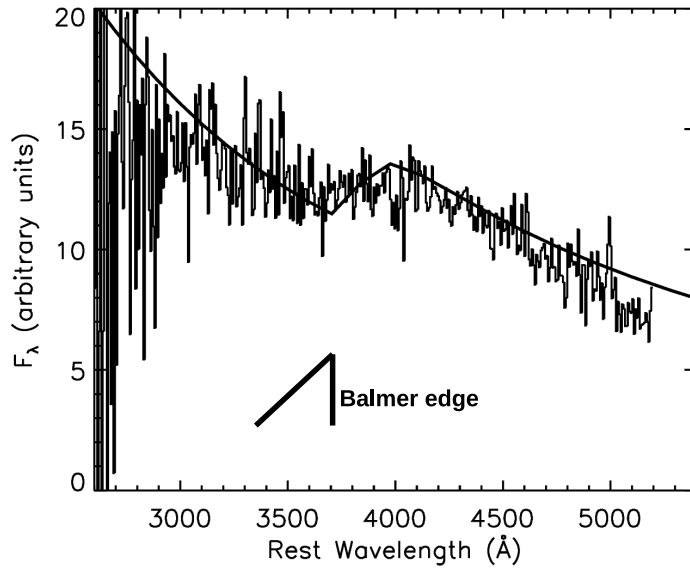


Figure 1.14: A spectrum of the Hubeny et al. (2000)’s accretion disk model for a maximally rotating Kerr ($a = 0.998$) BH of $M_{\text{BH}} = 8 \times 10^9 M_{\odot}$ and $\dot{M} = 2M_{\odot}/\text{yr}$ (thick smooth line), compared with the polarized flux spectrum of Ton 202. The model spectrum is arbitrarily scaled. This figure is taken from Figure 33 of Kishimoto et al. (2004).

confined polarization” confirmed by Kishimoto et al. (2004) (3C95, B2 1208+32, Ton 202, 3C 323.1, 4C 09.72). This figure clearly shows that the broad emission lines such as $\text{H}\beta$ are not appearing in the polarized flux spectra, meaning that the polarization degree at the wavelengths of the BLR emission is weaker than that at the wavelengths of the continuum windows. The observed null polarization of the BLR emission rules out the possibility that the optical polarization in these quasars is predominantly attributed to scattering processes outside of the BLR (e.g., Smith et al., 1993; Kishimoto et al., 2003). This also implies that the dust scattering is unlikely to be the cause of the polarization, because dust grains cannot survive inside the dust sublimation radius, which is a factor of four to five larger on average than the BLR radius (Koshida et al., 2014). The continuum polarization position angles of these quasars are mostly wavelength-independent, indicating that there is a single dominant mechanism producing the observed polarization.

Kishimoto et al. (2004) interpreted the continuum-confined polarization observed in several type 1 quasars such that the equatorial electron scattering region in these quasars is smaller in size to the BLR, but is still much larger than the UV-optical emitting regions of the accretion disk. In such geometrical configuration, the electron scattering produces no net polarization in the observed BLR emission (including Balmer continuum and Fe II pseudo-continuum) because the polarization is cancelled out when the polarized BLR flux vectors are averaged over a wide range of angles, and thus the polarization due to the equatorial electron scattering is confined only to the accretion disk continua (see also Kishimoto et al., 2008a).

One interesting consequence of the Kishimoto et al. (2003, 2004)’s interpretation is that because

the cross-section of the electron (Thomson) scattering is wavelength-independent, this interpretation implies that the polarized flux spectra in these quasars conserve the spectral shape (as a function of wavelength) of the intrinsic accretion disk continua (Antonucci, 2002; Kishimoto et al., 2003, 2004; Hu & Zhang, 2012; Marin & Goosmann, 2013). Actually, Kishimoto et al. (2004) showed that the polarized flux spectra of the quasars with the continuum-confined polarization shares the same feature of the spectral break at $\lambda_{rest} \sim 3600\text{\AA}$, which they interpreted as the Doppler-broadened hydrogen Balmer absorption edge imprinted in the accretion disk thermal emission due to the disk atmospheric opacity effect (Figure 1.14). Kishimoto et al. (2004) further claimed that the overall spectral shape of these quasars (including the Balmer edge-like spectral break) can be well described by the non-LTE radiative-transferred thermal accretion disk model of Hubeny et al. (2000) (Figure 1.14; see also Gaskell, 2009; Hu & Zhang, 2012).

However, we should note that the Kishimoto et al. (2003, 2004)'s interpretation (equatorial electron scattering inside the BLR) for the continuum-confined polarization quasars is currently based on the results for a small sample quasars and therefore has not yet been widely accepted. Schmidt & Smith (2000) suggested that the polarization in quasars with the continuum-confined polarization may be attributed to a weak optical synchrotron component from the misdirected blazar core components. Actually, all of the five quasars (3C95, Ton 202, B2 1208+32, 3C 323.1, and 4C09.72) confirmed to be showing the continuum-confined polarization both by Schmidt & Smith (2000) and Kishimoto et al. (2004) are radio-loud objects, thus it is not surprising that there is a flux contribution from the jet synchrotron component to the observed optical spectra (see e.g., Impey et al. 1989; Smith et al. 1993 and Afanasiev et al. 2015 for the cases of 3C 273 and 3C 390.3). However, in the case of Ton 202, Kishimoto et al. (2003) presented counterargument against the optical synchrotron scenario, in that the expected flux contribution from the synchrotron component in the optical wavelengths is too weak to explain the observed polarization degree. Also, as mentioned above, Kishimoto et al. (2004) claimed that the spectral break at $\lambda_{rest} \sim 3600\text{\AA}$ observed in the polarized flux spectra of the quasars with continuum-confined polarization cannot be interpreted other than the electron-scattered disk continuum with the Doppler-broadened Balmer absorption edge feature predicted by accretion disk models. It should also be noted that the subsequent work by Kishimoto et al. (2008b) has identified two radio-quiet quasars (Q0144-3938 and CTS A09.36) with continuum-confined polarization.

Anyway, although the optical spectropolarimetry for quasars is claimed to provide a new way to examine the intrinsic accretion disk continua buried under the unpolairzed BLR emission and the host galaxy light if the equatorial electron scattering (inside the BLR) scenario for the continuum-confined polarization quasars is true, careful examinations of alternative explanations for the optical sources in quasars are still needed. We will tackle this problem in Chapter 4 and in Chapter 5.

1.5 The outline of this dissertation

As mentioned above, the variability and polarization of the UV-optical emission of AGNs/quasars have been suggested to be a good tool to examine the intrinsic accretion disk emission around the SMBH. However, so far these two observational properties have been discussed separately.

Outline of the content of this dissertation is as follows (see Figure 1.15). First we examine the statistical properties of the spectral variability of quasars by using a large sample of multi-band light curves of quasars in the SDSS Stripe82 region (Chapter 2). By comparing several analysis methods which have been used to quantify the spectral/color variability of AGNs/quasars, we carefully revisit the mixed results on the quasar color variability and (in)variability of the physical models of the variability obtained in the literature. Especially, the “variable mass accretion rate model” introduced in Section 1.3.2 is tested against the observed variable component spectra in the SDSS quasars. We will show that the variable component spectra of the SDSS quasars, which should reflect the spectral shape of the accretion disk continua, generally have the spectral index of $\alpha_\nu \sim +1/3$ predicted by the standard accretion disk theory and by the variable mass accretion rate model in the long wavelength limit (Equation 1.11 and 1.26). Nevertheless, quantitative comparisons between the observed spectral shape of the variable component spectra and that of the variable mass accretion rate model reveal that the variable component spectra is systematically too blue at the rest-frame UV wavelengths to be explained by the standard accretion disk.

Next in Chapter 3, by using the same observational data used in Chapter 2, we examine the (in)validity of the “inhomogeneous accretion disk model” introduced by Dexter & Agol (2011) (Section 1.3.2) as the physical model for the quasar flux variability. We will show that the strong inter-band correlation and the 0.1-0.2 mag variability amplitude generally observed in multi-band UV-optical light curves of AGNs/quasars cannot be simultaneously achieved by the inhomogeneous accretion disk model.

In Chapter 4, the relationship between the variable and polarized spectral components in 4 quasars (B2 1208+32, Ton 202, 3C 323.1, and 4C 09.72), whose UV-optical spectropolarimetry had been carried out by Kishimoto et al. (2004) (Figure 1.13), is discussed. We obtain the multi-band (u , g , r , i , and z) light curves obtained in 2015-2016 by using 1.05-m Kiso Schmidt telescope at the Kiso observatory, and derive the spectral shape of the variable component spectra in these four quasar. The working hypothesis is that, because the spectral shape of both of the polarized and the variable components in each quasar are considered to be reflecting the spectral shape of the intrinsic accretion disk continuum emission (Section 1.3 and 1.4), these two spectral components should have the same spectral shape. However, the comparisons of the spectral shape between the polarized and the variable component spectra in these 4 quasars show that, contrary to the expectation, these two spectral components have totally different spectral shape. We will discuss the possible scenarios for this discrepancy at the end of Chapter 4.

One possible reason for the discrepancy of the spectral shape between the polarized and the variable components of the quasars discussed in Chapter 4 is that the polarized flux component spectra

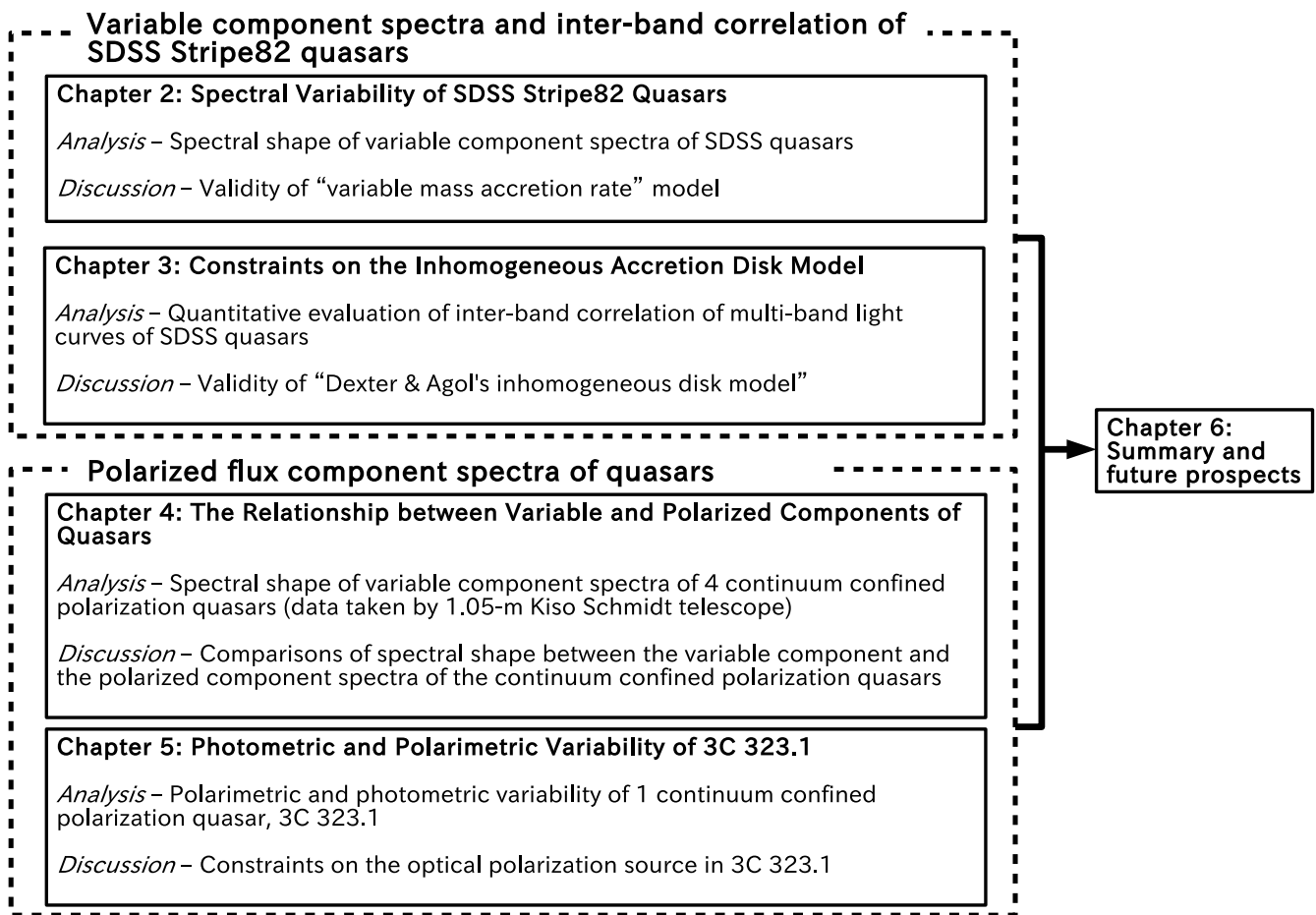


Figure 1.15: Dissertation outline.

are affected by some form of absorbing materials located at somewhere along the line of sight. To examine this scenario, the variability of the polarized flux and the total (unpolarized) flux in one of the quasar studied in Chapter 4, 3C 323.1, is studied in Chapter 5 by using archival spectro- and imaging-polarimetric data. It is shown that the observed photometric and polarimetric variability properties strongly suggest that the polarized flux component spectra of 3C 323.1 are actually the electron-scattered disk continuum emission but are affected by equatorial absorbing materials whose geometry is time-variable. This means that the spectral shape of the variable component spectra better represent the intrinsic spectral shape of the disk continua than the polarized flux component spectra, validating the conclusions in Chapter 2 and Chapter 3 derived on the assumption that the variable component spectra of quasars is a good tracer of the spectral shape of the intrinsic disk continua.

The summary of this dissertation (Figure 6.1) and prospects for future work will be given in Chapter 6.

Chapter 2

Statistical Properties of Multi-epoch Spectral Variability of SDSS Stripe82 Quasars¹

Abstract of Chapter 2

We investigate the UV–optical (longward of Ly α 1216Å) spectral variability of nearly 9000 quasars ($0 < z < 4$) using multi-epoch photometric data within the SDSS Stripe 82 region. The regression slope in the flux–flux space of a quasar light curve directly measures the color of the flux difference spectrum, then the spectral shape of the flux difference spectra can be derived by taking a careful look at the redshift dependence of the regression slopes. First, we confirm that the observed quasar spectrum becomes bluer when the quasar becomes brighter. We infer the spectral index of the composite difference spectrum as $\alpha_v^{\text{dif}} \sim +1/3$ (in the form of $f_\nu \propto \nu^{\alpha_\nu}$), which is significantly bluer than that of the composite spectrum $\alpha_v^{\text{com}} \sim -0.5$. We also show that the continuum variability cannot be explained by the accretion disk models with varying mass accretion rate, in that the power-law like spectral shape of the intrinsic accretion disk emission throughout the rest-frame UV to optical wavelengths revealed as the variable component spectra is too blue to be explained by the standard thin thermal accretion disk model. Second, we examine the effects of broad emission line variability on the color-redshift space. The variability of the "Small Blue Bump" is extensively discussed. We show that the low-ionization lines of Mg II and Fe II are less variable compared to Balmer emission lines and high-ionization lines, and the Balmer continuum is the dominant variable source around $\sim 3000\text{\AA}$. These results are compared with previous studies, and the physical mechanisms of the variability of the continuum and emission lines are discussed.

¹This Chapter 2, in full, is a reprint of the material as it appears in The Astrophysical Journal, Volume 783, Issue 1, article id. 46, 2014 (Kokubo et al., 2014). The dissertation author was the first author of this paper and did the bulk of the data analysis.

2.1 Review of previous work on the UV-optical spectral variability of AGNs/quasars

Because the spectral shape of the accretion disk continuum emission reflects the disk temperature distribution as a function of radius (Equation 1.1), studies of the spectral variability (i.e., wavelength dependence of the flux variation) of AGNs can provide important clues for underlying accretion disk physics. As has already been mentioned in Section 1.3, one of the well-known features of AGN UV–optical variability is that the color tends to become bluer when it gets brighter (“BWB” color variability trend; e.g., Maoz et al., 1993; Paltani & Courvoisier, 1994; Giveon et al., 1999; Vanden Berk et al., 2004; Sakata et al., 2011; Schmidt et al., 2012; Zuo et al., 2012; Ruan et al., 2014; Guo & Gu, 2016), which is used to constrain the accretion disk models in several previous works (e.g., Schmidt et al., 2012, and references therein). This bluer-when-brighter trend is also important for studies of the emission line formation, as a change of the spectral energy distribution of the ionizing continuum has significant effects on the physical state of the emission line region (e.g., Korista & Goad, 2004). However, as noted in Sakata et al. (2010), the “observed” bluer-when-brighter trend admits a dual interpretation: (1) the variable component, which is probably the accretion disk emission itself, becomes brighter and gets bluer (e.g., Wamsteker et al., 1990; Giveon et al., 1999; Webb & Malkan, 2000; Vanden Berk et al., 2004; Wilhite et al., 2005), and (2) the variable component of constant color becomes brighter and increasingly dominant over the non-variable components of red color, which is mainly composed of host galaxy flux (e.g., Choloniewski, 1981; Winkler et al., 1992; Winkler, 1997; Paltani & Walter, 1996; Suganuma et al., 2006). That is, the “observed” bluer-when-brighter trend does not directly imply AGN intrinsic spectral hardening. Moreover, we have to be careful of the effect of the broad emission lines (BELs) when analyzing the broad-band photometric variability, because they have large amount of flux and are variable themselves. Sakata et al. (2010) investigated the color variability of 11 nearby Seyfert galaxies, estimating the effect of non-variable components, and concluded that interpretation (2) is valid for the AGN intrinsic continuum emission in the optical region, which kept the constant spectral shape during the flux variation. The same result was obtained by Woo et al. (2007) and Walsh et al. (2009). On the other hand, Sakata et al. (2011) did the same kind of analyses as Sakata et al. (2010) for 10 Sloan Digital Sky Survey (SDSS) high redshift quasars and concluded that AGN intrinsic spectra actually became steeper as it got brighter in the UV region, which indicates that interpretation (1) is valid in the UV region. Wilhite et al. (2005) used two-epoch spectral data for ~ 300 SDSS quasars and concluded that the composite flux difference spectrum is steeper than the composite spectrum in the UV range but it has the same spectral index in the optical range. Note that the effects of the contamination from non-variable components, which are undoubtedly existing at least in part in the composite spectrum (e.g., Glikman et al., 2006; Vanden Berk et al., 2006) are not evaluated in Wilhite et al. (2005). Thus, a consensus about the properties of the color variability of AGNs has not been obtained yet (see e.g., Bian et al., 2012; Zhang, 2013).

The difficulties of variability studies have led to the uncertainties of the AGN variability model.

A number of models have been developed attempting to explain AGN variability such as X-ray re-processing (Krolik et al., 1991), instabilities in the accretion disk (Kawaguchi et al., 1998; Dexter & Agol, 2011), gravitational microlensing (Hawkins, 1993), star collisions (Torricelli-Ciamponi et al., 2000), and multiple supernovae or starbursts near the nucleus (Terlevich et al., 1992). Recently, several authors have claimed that the AGN variability is due to the changes in accretion rate (Pereyra et al., 2006; Li & Cao, 2008; Sakata et al., 2011; Zuo et al., 2012; Gu & Li, 2013), which seems to explain the larger variability in the shorter wavelengths quantitatively. Sakata et al. (2011) fitted the standard accretion disk model (Shakura & Sunyaev, 1973) with a varying accretion rate for the light curves of 10 SDSS quasars and concluded that this model could correctly explain the color variability. Gu & Li (2013) also obtained the same conclusion for eighteen steep spectrum radio quasars. However, Schmidt et al. (2012) investigated the color variability of ~ 9000 SDSS Stripe 82 quasars and concluded that the color variability of quasars cannot be described by the several accretion disk models (Davis et al., 2007) with varying accretion rate, as the color of quasars becomes bluer than the model predictions. Trèvese & Vagnetti (2002) also pointed out that the changes of accretion rate are insufficient to explain the amount of spectral variation.

In the present work, we focus on the model of Pereyra et al. (2006), which assumes that the AGN variability is caused by small changes in the mass accretion rate in the standard thermal accretion disk (Shakura & Sunyaev, 1973) and predict the flux difference spectrum between one epoch to another. We note that although we cannot directly observe the intrinsic AGN spectra or intrinsic color, we can directly observe the color of the variable portion in AGN spectra (i.e., the flux difference spectrum). This can be achieved by using the “flux–flux correlation method” described in Section 2.3, which relies on the fact that UV–optical, two-band flux to flux plots of AGN broad-band light curves show strong linear correlation (e.g., Choloniewski, 1981; Sakata et al., 2011; Lira et al., 2011, and references therein). As mentioned earlier, the flux variability occurs not only in the continuum emission, but also in the BELs. In general, the quasar variability (obtained by broad-band photometry) is dominated by continuum variability (intrinsic Baldwin effect, e.g., Wilhite et al., 2005; Shields, 2007), but we are probably able to see some amount of variable emission line components in it. We can also examine the effects of the BEL variability on the broad band photometry by taking a careful look at our result, which has not been well studied in previous works.

In this Chapter, we investigate the years-time-scale UV–optical spectral variability of large quasar samples in SDSS Stripe 82 region, attempting to derive some insight to the physical mechanisms of AGN variability. Our standpoint is summarized as below:

- Using the flux–flux correlation method, we derive the color of the flux difference spectrum for each quasar and for each band pair model-independently. Then, we investigate the rest-frame wavelength dependence of the quasar spectral variability by taking a careful look at the redshift dependence of the color of the flux difference spectrum, with the assumption that there is no redshift-dependence in the rest-frame spectral variability (e.g., Schmidt et al., 2012; Zuo et al., 2012). The derived flux difference spectrum can be directly compared with the AGN

UV–optical variability model presented in Pereyra et al. (2006).

- We do not assume any models or estimates of non-variable components such as host galaxy flux or narrow line emissions in the present work. This means that the color variability trend (bluer-when-brighter or achromatic variation) referred to in this work is actually the “observed” color variability trend, not the AGN intrinsic variation in spectral shape. However, as shown by Sakata et al. (2011) (see also Croom et al., 2009; Krawczyk et al., 2013), host galaxy flux and narrow emission lines in SDSS bandpasses are probably negligible for intermediate and high redshift quasars. Thus the “observed” color variability trend, particularly in rest-frame UV wavelengths, can be considered as the intrinsic variation in AGN continuum spectral shape, although the effects of the variability of BELs should be taken into consideration.

In Section 2.2 we describe a database of SDSS Stripe 82 multi-epoch five-band light curves from the SDSS data, and we introduce the flux–flux correlation method (Choloniewski, 1981) in Section 2.3. In Section 2.4, we show the linear regression slopes in flux–flux space for quasar light curves, which correspond to the color of the flux difference spectrum, as a function of redshift. Then, we compare our results with previous works and the standard thin-disk model. We discussed the emission line variability in Section 2.5. The variability of the Small Blue Bump (SBB) spectral region is discussed separately in Section 2.6. Finally, we summarize our conclusions in Section 2.7. The adopted models for emission lines and intergalactic medium (IGM) attenuation used in Section 2.5 are described in Appendix B, and the results of the regression intercept, which are not concerned with the main results in this work, are interpreted and shown in Appendix C.

2.2 5-band quasar light curves in the SDSS Stripe 82 region

The SDSS is an ongoing multi-band photometry and multi-object fiber spectroscopy survey carried out by using a dedicated 2.5-m SDSS telescope located at Apache Point Observatory, in south east New Mexico (Gunn et al., 1998; York et al., 2000; Gunn et al., 2006). It has progressed through several phases, commissioning phase (1998-2000), SDSS-I (2000-2005), SDSS-II (2005-2008), SDSS-III (2008-2014), and SDSS-IV (2014-). The SDSS imaging camera is an array of 30 2048×2048 pixel CCDs arranged in six columns of five CCDs each, aligned with the pixel columns of the CCDs themselves. The five CCDs in each column of the camera are filtered by the five SDSS filters respectively; *u*, *g*, *r*, *i*, and *z*-band. Figure 2.1 shows the filter response of the SDSS filter system (Doi et al., 2010). The central wavelengths of the five SDSS filters are 3551, 4686, 6165, 7481, 8931Å, respectively, covering full range of the optical wavelength range. Magnitude limits of the SDSS photometry (evaluated as 95% detection repeatability for point sources) are 22.0, 22.2, 22.2, 21.3, and 20.5 mag for *u*, *g*, *r*, *i*, and *z*-band, respectively.

The SDSS Legacy Survey (SDSS-I/-II), which is the main survey program of the SDSS survey, provided a uniform, well-calibrated map in the five SDSS filters of more than 7500 square degrees of the North Galactic Cap and three stripes in the South Galactic Cap totaling 740 square degrees,

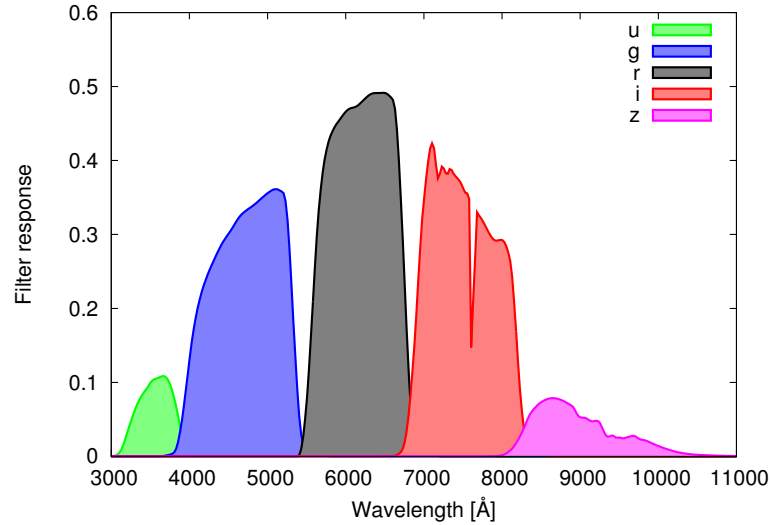


Figure 2.1: 2.5 m telescope reference response function, including extinction through an airmass of 1.3 at Apache Point Observatory (Table 4 of Doi et al., 2010).

as well as the spectroscopy data for galaxies and stars. The SDSS photometry is accurate to ~ 0.02 mag (rms scatter) for unresolved sources not limited by photon statistics (Scranton et al., 2002; Ivezić et al., 2003; Sesar et al., 2007) and with a zero-point uncertainty of ~ 0.02 mag (Ivezić et al., 2004; MacLeod et al., 2012). Within the Legacy Survey’s sky coverage, SDSS Stripe 82 region, which is located in the center of the three stripes in the South Galactic Cap, was scanned multiple times by the SDSS Legacy Survey and the SDSS Supernova Survey (Frieman et al., 2008) in order to enable a deep co-addition of the data and to find variable objects². The SDSS Stripe82 region is defined as the region spanning 8 hour in right ascension (RA) from $\alpha = 20^h$ to 4^h and $2^\circ.5$ in declination (Dec) from $\delta = -1^\circ.25$ to $1^\circ.25$, consisting of two scan regions referred to as the north and south strips (Figure 2.2). Both the north and south strips have been repeatedly imaged about 60 times on average by more than 300 nights of observations from 1998 to 2007, with about 70 percent of the imaging run obtained after 2005, when the SDSS-II Supernova Survey started. The SDSS Data Release 7 (DR7; Abazajian et al., 2009) Catalog Archive Server (CAS) contains the Stripe 82 database, distinct from the DR7 and RUNS databases, containing all imaging from SDSS Stripe 82³. There are about 37,000 quasar photometrically selected candidates in the Stripe 82 region (Richards et al., 2009), of which spectroscopic data were available for about 9,000 candidates.

We use a database of SDSS Stripe 82 multi-epoch five-band light curves for spectroscopically confirmed quasars presented by MacLeod et al. (2012). Their Southern sample catalog contains recalibrated ~ 10 yr light curves for 9258 quasars in the SDSS Data Release 7 (DR7; Abazajian et al., 2009) (Figure 2.2). SDSS magnitude is converted to flux unit. The SDSS system is nearly the AB system ($AB \text{ mag} \equiv -2.5 \log(f_\nu/f_{\nu,0})$), where zero-point flux density $f_{\nu,0} = 3631 \text{ Jy}$), but the

²Run List for Data Release Stripe 82 - SN is available in <http://www.sdss.org/dr7/coverage/sndr7.html>

³<http://cas.sdss.org/stripe82/en/>

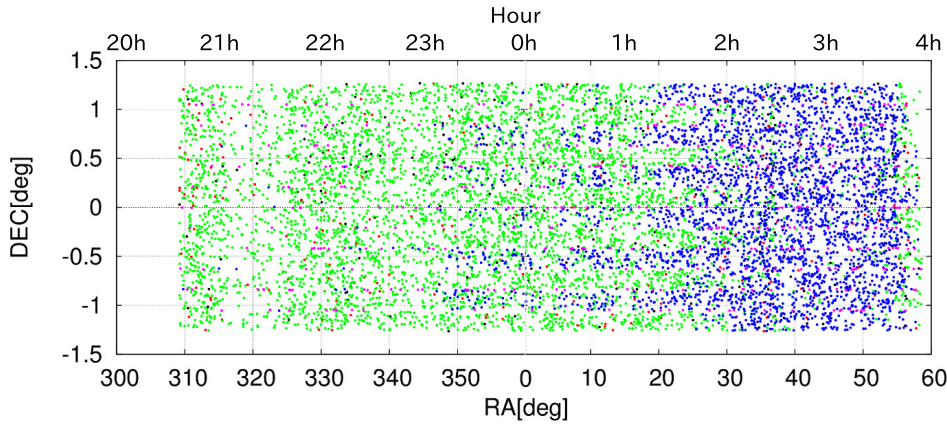


Figure 2.2: The spatial distribution of the SDSS DR7 quasars (Schneider et al., 2010) in the SDSS Stripe 82 region. Colors indicate the number of available photometry; black: less than 20 epochs; red: 20 to 40 epochs; green: 40 to 60 epochs; blue: 60 to 80 epochs; Magenta: larger than 80 epochs.

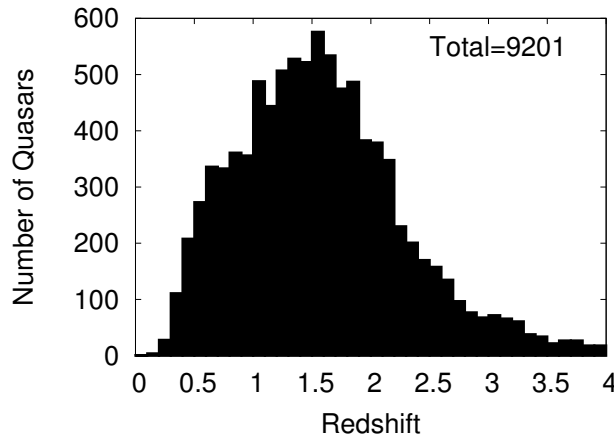


Figure 2.3: Redshift distribution ($0 < z < 4$) of the SDSS Stripe 82 quasar sample.

photometric zero-points are slightly off the AB standard. We apply the correction for the zero-point offset between the SDSS system and the AB system following the recommendations in the SDSS instructions⁴: $u_{AB} = u_{SDSS} - 0.04$, $g_{AB} = g_{SDSS}$, $r_{AB} = r_{SDSS}$, $i_{AB} = i_{SDSS}$ and $z_{AB} = z_{SDSS} + 0.02$. In this work, “Flux” means f_ν unit (i.e., Jansky unit), but we also use f_λ unit when we refer to the spectral shape. These two are related as $f_\nu = \lambda^2 f_\lambda / c$, and power-law indices are related as $\alpha_\nu = -2 - \alpha_\lambda$, where $f_\nu \propto \nu^{\alpha_\nu}$ and $f_\lambda \propto \lambda^{\alpha_\lambda}$.

We cross-match the Southern sample light curve catalog with a catalog of quasar properties from SDSS DR7 (Shen et al., 2011) (the maximum search radius is 2 arcsec). We use the improved redshift from Hewett & Wild (2010) as the redshift of each quasar. In this work, we use a sample of quasars within the redshift range from 0 to 4, in which there are 9201 quasars. The redshift distribution of the sample ($0 < z < 4$) is shown in Figure 2.3.

⁴<http://www.sdss.org/dr7/algorithms/fluxcal.html>

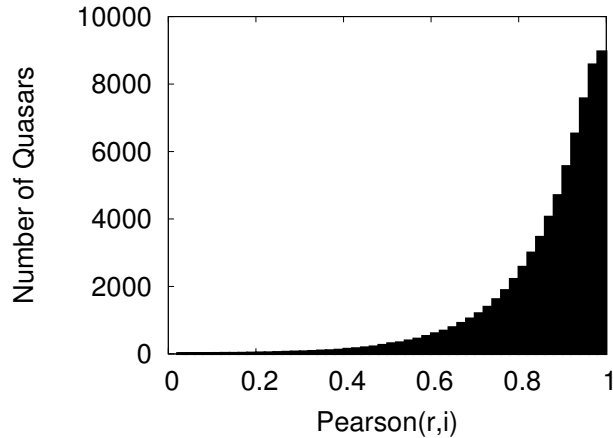


Figure 2.4: Cumulative distribution of Pearson correlation coefficient in flux–flux space (x -axis = r -band flux, and y -axis = i -band flux) for light curves of our sample ($0 < z < 4$) observed more than 20 epochs (see Section 2.3.5 for more details of our sample).

Galactic absorption is corrected using A_u [mag] tabulated in the database of MacLeod et al. (2012) for each quasar, where $A_g, A_r, A_i, A_z = 0.736, 0.534, 0.405, 0.287 \times A_u$ (Schlegel et al., 1998; MacLeod et al., 2012).

2.3 The flux-flux correlation method

In this section, we introduce the flux–flux correlation method and discuss the advantages of the use of this method.

2.3.1 The Color of the Flux Difference Spectrum in Flux-Flux Space

We introduce flux–flux correlation method (Choloniewski, 1981; Winkler et al., 1992; Lyutyi & Doroshenko, 1993; Hagen-Thorn, 1997) as an alternative to magnitude–magnitude or magnitude–color correlation analyses. Choloniewski (1981) first noticed that the quasars’ UV–optical fluxes have a linear correlation in flux–flux space, and several authors have since confirmed it (e.g., Winkler, 1997; Glass, 2004; Sakata et al., 2011; Lira et al., 2011; Gu & Li, 2013). In Figure 2.4, we show the Pearson correlation coefficient of the $f_v(r) - f_v(i)$ plot for our sample ($0 < z < 4$) observed more than 20 epochs (see Section 2.3.5 for more details of our sample). In terms of the Pearson correlation coefficient, almost all of the quasars have strong positive flux–flux correlation. The strong correlation for a quasar light curve means that the flux difference spectrum, which is defined as the flux difference of the quasar spectra of any of the two observational epochs, keeps nearly constant shape for at least several years.

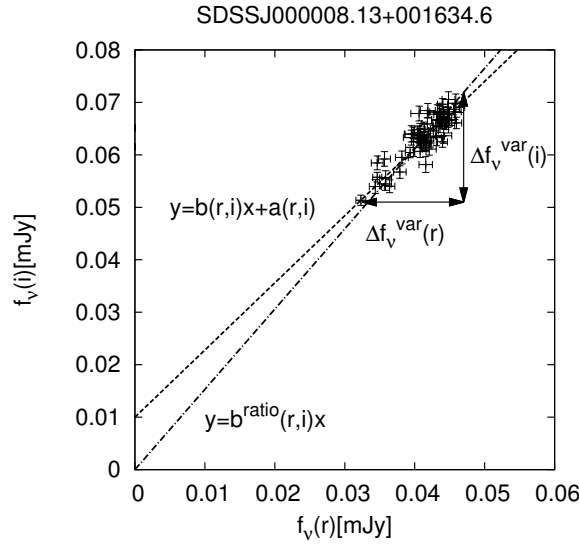


Figure 2.5: Illustration for the flux–flux correlation method. The linear regression line is $y = 1.28x + 0.01$ [mJy] (i.e., $b(r, i) = \Delta f_v^{\text{var}}(i) / \Delta f_v^{\text{var}}(r) = 1.28$). The time-averaged color is $b^{\text{ratio}}(r, i) = \bar{f}_v(i) / \bar{f}_v(r) = 1.53$, so the flux difference spectrum is bluer than the time-averaged spectrum in this object.

We express a linear regression line ($y = b \times x + a$) in flux–flux space ($f_v(s) - f_v(l)$ space) as

$$f_v(l) = b(s, l) \times f_v(s) + a(s, l) \quad (2.1)$$

$$(s = u, g, r, i; l = g, r, i, z)$$

where “s” (“short” wavelength, x -axis in flux–flux space), and “l” (“long” wavelength, y -axis in flux–flux space) indicate two of the five photometric bands, whose average wavelengths are $\lambda(s) < \lambda(l)$ (where $\lambda(u), \lambda(g), \lambda(r), \lambda(i), \lambda(z) = 3551, 4686, 6165, 7481, 8931 \text{ \AA}$)⁵. Figure 2.5 shows an illustration of our method. When we fit a regression line in flux–flux space, the regression slope $b(s, l)$ and the intercept $a(s, l)$ are expressed as

$$b(s, l) = \frac{\Delta f_v^{\text{var}}(l)}{\Delta f_v^{\text{var}}(s)} \quad (2.2)$$

$$a(s, l) = \bar{f}_v(l) - b(s, l) \bar{f}_v(s) \quad (2.3)$$

where Δf_v^{var} is the varying broad-band flux range (flux difference) during the observations, and \bar{f}_v is the baseline flux given as the mean flux of light curves for each bandpass. The effects of contaminations of baseline flux ($= \bar{f}_v$, e.g., host galaxy flux and time-averaged fluxes of emission lines) do not affect to the regression slope (they only affect to the regression intercepts), so the regression slope in the flux–flux space directly measures the ratio of the two broad-band fluxes of the flux difference spectrum of each quasar.

⁵<http://www.sdss.org/dr7/instruments/imager/>

Given the flux difference spectrum f_v^{dif} for a quasar, the regression slope in flux–flux space is expressed as (Richards et al., 2001),

$$b(s, l) = \frac{\int f_v^{\text{dif}} S_v(l) d \log \nu}{\int f_v^{\text{dif}} S_v(s) d \log \nu} \times \left(\frac{\int S_v(l) d \log \nu}{\int S_v(s) d \log \nu} \right)^{-1} \quad (2.4)$$

where S_v is the throughput of the SDSS photometric system in each bandpass (Doi et al., 2010).

From Equation (2.4), the color of the flux difference spectrum $m_s - m_l|_{\text{dif}}$ (e.g., $r - i|_{\text{dif}}$) in units of magnitude is expressed by $b(s, l)$ as,

$$m_s - m_l|_{\text{dif}} = +2.5 \log(b(s, l)). \quad (2.5)$$

This means that the bluer color indicates a smaller value of Equation (2.5), and then a smaller value of $b(s, l)$. In this way, the color of the flux difference spectrum is related directly to the observable $b(s, l)$. In the present work, we refer $b(s, l)$ simply as “the color of the flux difference spectrum” and this can be converted to the conventional definition of color through Equation (2.5).

If we assume a power-law difference spectrum ($f_v^{\text{dif}} \propto \nu^{\alpha_v^{\text{dif}}}$), we obtain (by Equation (2.4))

$$b(s, l) \sim \left(\frac{\nu(l)}{\nu(s)} \right)^{\alpha_v^{\text{dif}}} = \left(\frac{\lambda(s)}{\lambda(l)} \right)^{\alpha_v^{\text{dif}}} \quad (2.6)$$

where $\nu(s)$ and $\nu(l)$ indicate average frequencies for the SDSS photometric bands. Because we define $b(s, l)$ as $\lambda(l) > \lambda(s)$,

$$\begin{cases} b(s, l) > 1 & (\text{if } \alpha_v^{\text{dif}} < 0) \\ b(s, l) < 1 & (\text{if } \alpha_v^{\text{dif}} > 0). \end{cases} \quad (2.7)$$

When the flux difference spectra of quasars have power-law shape, the color of the flux difference spectra has no dependence on the quasar redshift because the wavelength-shift by cosmic expansion is canceled out in Equation (2.6). That is, $b(s, l)$ with a power-law difference spectrum is constant as a function of redshift if α_v^{dif} is fixed. Although the color of the difference spectrum is actually contaminated by BEL variability, we can infer α_v^{dif} by investigating the mean redshift dependence of $b(s, l)$ for sample quasars.

2.3.2 The Color of Quasars in Flux-Flux Space

In flux–flux space, the “observed” color corresponds to the slope of a straight line that passes through the origin of the coordinates and an observed point at an epoch. The “observed” color is time-dependent if $a(s, l)$ (the regression intercept in flux–flux space) is non-zero (Sakata et al., 2010, 2011, and see Appendix B).

We define the $b^{\text{ratio}}(s, l)$ by taking the time-average of light curves in any combination of five photometric bands (“baseline flux” $\bar{f}_v(j)$, $j = u, g, r, i, z$) and taking the ratio as (see Figure 2.5)

$$b^{\text{ratio}}(s, l) \equiv \frac{\bar{f}_v(l)}{\bar{f}_v(s)}. \quad (2.8)$$

Equation (2.5), which is the (time-averaged) color $m_1 - m_2$ of the quasar spectrum (e.g., $r - i$) is expressed by $b^{\text{ratio}}(s, l)$ as

$$m_s - m_l = +2.5 \log(b^{\text{ratio}}(s, l)). \quad (2.9)$$

We refer to $b^{\text{ratio}}(s, l)$ simply as “the color of the quasar spectrum” in this work, and you can always convert it to the conventional definition of color through Equation (2.9).

$b^{\text{ratio}}(s, l)$ is expressed for a quasar with a spectrum f_ν as

$$b^{\text{ratio}}(s, l) = \frac{\int f_\nu S_\nu(l) d \log \nu}{\int f_\nu S_\nu(s) d \log \nu} \times \left(\frac{\int S_\nu(l) d \log \nu}{\int S_\nu(s) d \log \nu} \right)^{-1}. \quad (2.10)$$

If we assume a power-law spectrum ($f_\nu \propto \nu^{\alpha_\nu}$), we obtain

$$b^{\text{ratio}}(s, l) \sim \left(\frac{\nu(l)}{\nu(s)} \right)^{\alpha_\nu} = \left(\frac{\lambda(s)}{\lambda(l)} \right)^{\alpha_\nu}. \quad (2.11)$$

Because we define $b^{\text{ratio}}(s, l)$ as $\lambda(l) > \lambda(s)$,

$$\begin{cases} b^{\text{ratio}}(s, l) > 1 & (\text{if } \alpha_\nu < 0) \\ b^{\text{ratio}}(s, l) < 1 & (\text{if } \alpha_\nu > 0). \end{cases} \quad (2.12)$$

2.3.3 The Color-Redshift Relation

Richards et al. (2001) investigated the causes of the observed features in the color as a function of redshift for 2625 SDSS quasars by comparing the color–redshift relation model including the effects of emission lines. They confirmed that the average of the observed color of quasars as a function of redshift is well represented by a power-law continuum using $\alpha_\nu \sim -0.5$ (similar to the result of Vanden Berk et al., 2001), and identified the effects of emission lines for the broad-band colors as deviations from power-law colors.

Because we are able to obtain the color of the flux difference spectrum for quasars using the flux–flux correlation method, the same kind of analyses as Richards et al. (2001) for the flux difference spectrum can be applied. Currently, there are only a few studies related to the flux difference spectrum (Wilhite et al., 2005; Bian et al., 2012; Guo & Gu, 2014). Among these, we refer to that of Wilhite et al. (2005) for the quasar composite flux difference spectrum in this work. They constructed the composite residual (composite flux differences spectrum) from 315 quasars observed twice by SDSS spectroscopy. Figure 2.6 shows the histogram of the rest-frame time-lag between the two spectroscopic observations in Wilhite’s sample, with a histogram of the time span of the photometric observations in our sample. The median rest-frame time-lag of the Wilhite’s sample is 123 days, which is about one-tenth of ours (median ~ 1200 days). Aside from the difference in the rest-frame time-lag, we can compare our results with the (redshifted) composite flux difference spectrum by Wilhite et al. (2005) using Equation (2.4) on the color–redshift space. Note that Wilhite et al. (2005) mainly focused on the ratio spectrum (the ratio of the composite difference spectrum to the composite

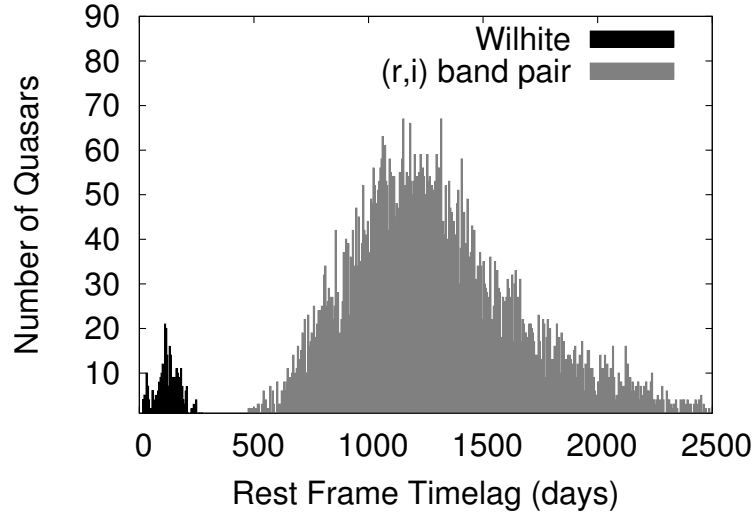


Figure 2.6: Rest-frame time-lag histograms binned for five days. The left histogram (black, median = 123 days) indicates the number of quasars with two-epoch spectra used in Wilhite et al. (2005) (time-lag is defined as the difference of the observational epochs). The right histogram (gray, median ~ 1200 days) is the rest-frame time-lag distribution of r and i -band light curves, which we used in the present work (time-lag is defined as the difference of first and last observational epochs). See the details of our sample definition in Section 2.3.5.

spectrum), so they did not apply the correction of Galactic extinction to their composite difference spectrum. We discuss the effect introduced by this non-correction in Section 2.4.2.

Here, we show the illustration of the effect of an emission line contamination for $b(s, l)$ and $b^{\text{ratio}}(s, l)$ on the redshift dependence (see also Richards et al., 2001). We can treat $b(s, l)$ and $b^{\text{ratio}}(s, l)$ in the same way, so here we show the case of $b(s, l)$. We consider the case of $s = r$ and $l = i$ (i.e., $b(r, i)$) for example. When an emission line is redshifted and enters r -band, the r -band flux becomes larger, and $b(r, i)$ becomes smaller (bluer) than the case of a single power-law flux difference spectrum. At higher z , when the emission line enters the i -band, $b(r, i)$ becomes larger (redder). This behavior is shown in Figure 2.7, assuming the continuum and line variability as

$$\begin{aligned} f_{\lambda}^{\text{dif}} &= f_{\lambda}^{\text{dif}}(\text{continuum}) + f_{\lambda}^{\text{dif}}(\text{line}) \\ &= \left(\frac{\lambda}{3000\text{\AA}} \right)^{\alpha_{\lambda}^{\text{dif}}} + \frac{1}{2} \exp\left(-\frac{(\lambda - \lambda_{\text{rest}})^2}{2\sigma_{\lambda}^2} \right) \end{aligned} \quad (2.13)$$

where σ_{λ} is the emission line width (here $\sigma_{\lambda} = 40\text{\AA}$), and λ_{rest} is the central wavelength of the line (here $\lambda_{\text{rest}} = 3000\text{\AA}$). $\alpha_{\lambda}^{\text{dif}}$ is as shown in Figure 2.7. The different power-law indices $\alpha_{\lambda}^{\text{dif}}$ lead to the different constant levels of $b(s, l)$ following Equation (2.6).

2.3.4 Advantages of the Flux-Flux Correlation Method

Schmidt et al. (2012) pointed out that previous analyses usually focused on the color variability

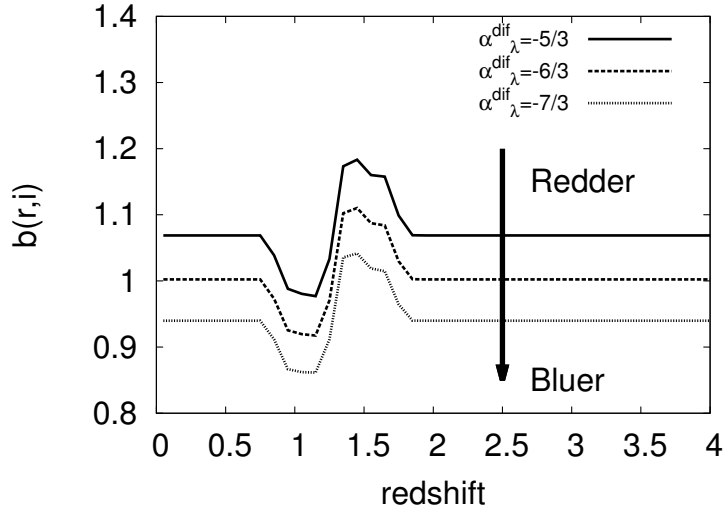


Figure 2.7: Illustration of an emission line contamination effect on the $b(r, i)$ –redshift plane. We can treat $b(s, l)$ and $b^{\text{ratio}}(s, l)$ in the same way, so here we show the case of $b(s, l)$. Curves are calculated by Equation (2.4) combined with Equation (2.13), for $\alpha_{\lambda}^{\text{dif}} = -5/3, -6/3, -7/3$. The power-law spectrum with definite spectral index means constant color at all redshift (Equation (2.6)). At $z \sim 1.1$, the emission line component of Equation (2.13) enters the r -band, and the color becomes bluer than the power-law color. At $z \sim 1.5$, the emission line component leaves the r -band and enters the i -band, and the color becomes redder than the power-law color.

of the quasar in color–magnitude space and suffered from covariance between the color and magnitude uncertainties. They avoided these error correlations by analyzing the color variability in magnitude–magnitude space, and concluded that the color variability has the bluer-when-brighter trend.

Although magnitude–magnitude correlation method can avoid error correlations, it still has another problem. Schmidt et al. (2012) fitted a straight line for each quasar’s magnitude–magnitude plot, and used the best fit slope as the indicator of color variability. Note that regression slopes on magnitude–magnitude space highly depend on the contaminations of baseline flux (e.g., host galaxy flux and time-averaged fluxes of emission lines) (e.g., Woo et al., 2007; Hawkins, 2003). The regression slope in magnitude–magnitude space can be expressed as

$$b^{\text{mag}}(s, l) \approx \frac{\log\left[\left(\bar{f}_v(l) + \Delta f_v^{\text{var}}(l)/2\right) / \left(\bar{f}_v(l) - \Delta f_v^{\text{var}}(l)/2\right)\right]}{\log\left[\left(\bar{f}_v(s) + \Delta f_v^{\text{var}}(s)/2\right) / \left(\bar{f}_v(s) - \Delta f_v^{\text{var}}(s)/2\right)\right]}$$

where the notation is the same as Equation (2.2) and (2.3). Unlike in flux–flux space (Equation (2.2)), the regression slope in magnitude–magnitude space is dependent not only on the flux difference Δf_v^{var} , but also on the time-averaged flux levels \bar{f}_v (“baseline flux”, Equation (2.8)). Thus, $b^{\text{mag}}(s, l)$ only tells whether the “observed” color variability is bluer-when-brighter ($b^{\text{mag}} < 1$), redder-when-brighter

($b^{\text{mag}} > 1$) or achromatic ($b^{\text{mag}} = 1$). To derive the flux difference spectrum from b^{mag} , one needs to employ some models or estimate the contamination \bar{f}_v . On the other hand, the flux–flux correlation method enables us not only to avoid error correlations, but also to derive the flux difference spectrum model independently (Equation (2.2)).

Another statistical method to derive the flux difference spectrum exists. Meusinger et al. (2011) investigated the rest-frame wavelength dependence of the quasar variability using the structure functions V^{mag} of five SDSS photometric bands as a function of rest-frame wavelength. However, the structure function analyses, which are done in units of magnitude, are not appropriate to study the spectral variability or the flux difference spectrum because the structure function can be expressed as

$$\begin{aligned} V^{\text{mag}} &\approx [\Delta m]^2 \\ &\approx \left[-2.5 \log \left(\frac{\bar{f}_v(s) + \Delta f_v^{\text{var}}(s)/2}{\bar{f}_v(s) - \Delta f_v^{\text{var}}(s)/2} \right) \right]^2. \end{aligned}$$

Then again, this is dependent not only on the flux difference Δf_v^{var} , but also on the time-averaged flux levels \bar{f}_v .

In summary:

1. The flux–flux correlation method can avoid the error correlations that exist in magnitude–color or flux–color correlation method as was pointed out by Schmidt et al. (2012).
2. The regression slope $b(s, l)$ derived by the flux–flux correlation of a quasar multi-band light curve is not affected by baseline fluxes (e.g., host galaxy flux or time-averaged fluxes of emission lines).
3. Regression slopes represent the color of the flux difference spectrum for each quasar, so we are able to infer the (mean) flux difference spectrum using redshift dependence of the derived regression slopes.

2.3.5 Linear Regression Method and Sample Selection

Linear regression for the data that have intrinsic scatter (σ_{int}) and error bars on both axes (e.g., flux–flux space linear regression) is complex and there are several different methods (see Park et al., 2012; Feigelson & Jogesh Babu, 2012; Cappellari et al., 2013, and references therein). We adopt the MPFITEXY IDL routine (Williams et al., 2010) to fit a linear relation to the flux–flux correlation for each quasar. According to Park et al. (2012), the FITEXY method generally provides the least-biased result compared to the other methods. The MPFITEXY routine depends on the MPFIT package (Markwardt, 2009). This routine is able to cope with intrinsic scatter, which is automatically adjusted to ensure $\chi^2/(\text{degrees of freedom}) \sim 1$ (see Tremaine et al., 2002; Novak et al., 2006; Park et al., 2012, for more detail and justifications).

We fit a straight line in flux–flux space for each band pair light curve, excluding the data points with a “Bad observations” flag (MacLeod et al., 2012) or fainter than limiting magnitudes (22.0, 22.2,

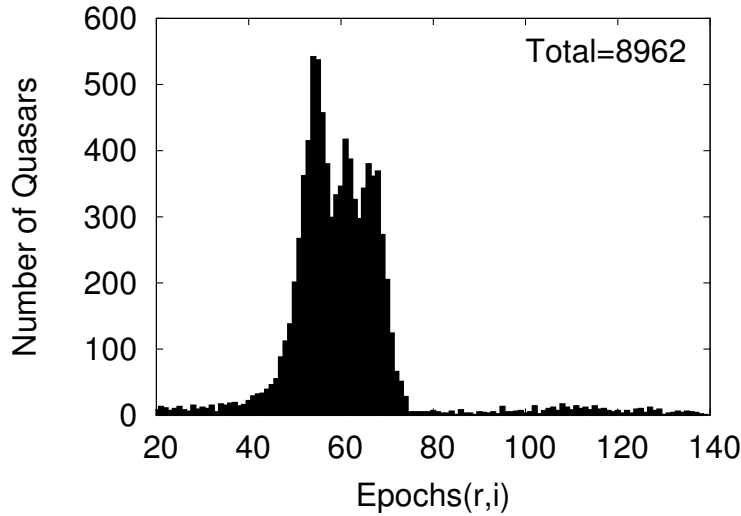


Figure 2.8: Histogram of the number of observational epochs of the (r,i) band pair light curves for our quasar sample. Observations with a “Bad observations” flag (MacLeod et al., 2012) are excluded.

22.2, 21.3, and 20.5 mag for u , g , r , i , and z -band, respectively).⁶ We focused on the properties of long-term and multi-epoch-averaged variability, so we exclude quasars that have less than 20 photometric epochs. Linear relation $y = b(x - x_0) + a'$ is assumed in the fitting procedure, where x_0 is taken to be the average of x values (i.e., $\bar{f}_i(s)$). The reference value x_0 is necessary to minimize the uncertainty in the estimate of a' and the correlation between a' and b (Tremaine et al., 2002). Regression intercept a is calculated as $a = a' - bx_0$. Linear regression for several quasars did not converge because of the low signal-to-noise ratio (S/N). Thus, we eliminated them from our sample. Furthermore, we confirmed that all of the regression slopes with a negative value were the results of a bad fitting (because of the small variability or low S/N) and we also eliminated them from our sample. In this work we examine the modal redshift trends, so these eliminations had little effect on our analyses.

As an example, we show the histogram of the number of observational epochs of the (r,i) band pair light curves without a “Bad observations” flag (MacLeod et al., 2012) for our quasar sample in Figure 2.8. Resulting sample sizes for each band pair are shown in Table 2.1. Redshift distribution is not significantly modified from Figure 2.3 by our sample selection.

2.4 Continuum Variability

In this section, we show linear regression slopes $b(s, l)$ derived in flux–flux space for quasar light curves, which correspond to the color of the flux difference spectrum as discussed in the previous section. The wide redshift range for our quasar samples and large separation of effective wavelengths of the SDSS filters enable us to investigate the continuum variability from 1216Å to about 6000Å

⁶<http://www.sdss.org/dr7/>

Table 2.1: Sample Size ($0 < z < 4$)

Band pairs (s, l)	Samples
(u, g)	8,537
(u, r)	8,523
(u, i)	8,495
(u, z)	8,213
(g, r)	8,996
(g, i)	8,949
(g, z)	8,745
(r, i)	8,962
(r, z)	8,770
(i, z)	8,761

in the rest-frame wavelength. We first check the consistency between our result and the previous spectroscopic result of the flux difference spectrum (Wilhite et al., 2005). Then, we adopt a model for the continuum flux variation in which the variability is caused by changes in mass accretion rate in the standard accretion disk (Pereyra et al., 2006) as a working hypothesis, and compare it with observed continuum variability in $b(s, l)$ –redshift space.

2.4.1 Redshift Dependence of the Color of the Flux Difference Spectrum

Figure 2.9 shows the regression slopes $b(s, l)$ as a function of redshift for each quasar (dots). The curves in Figure 2.9 are:

- Solid and dashed curves: The modal color ($b(s, l)$) of the flux difference spectrum (solid) with 1σ outer quartiles (dashed), derived by linear regression analyses in flux–flux space (i.e., mode and 1σ outer quartiles of the dots in the figure).
- Dash-dotted and double-dot-dashed curves: The modal color ($b^{\text{ratio}}(s, l)$) of the time-averaged spectrum (dash-dotted) with 1σ outer quartiles (double-dot-dashed), given by Equation (2.8).

Modal value is defined following Hopkins et al. (2004), and the bin size is taken to be 0.2 in redshift.

At high redshift, u , g , and r -band fluxes are affected by Ly α forests or damped Ly α systems, which absorb UV flux and decrease u , g , and r -band variability (i.e., regression slopes become larger at higher redshifts). This makes it difficult to estimate intrinsic quasar spectrum and spectral variability. The shortest transmission wavelengths for u , g , and r -band are 3000Å, 3700Å, and 5400Å, respectively, so the Ly α emission line (1216Å) enters in these bands at $z = 1.47, 2.04, 3.44$. The arrows with the label “Ly α ” in Figure 2.9 indicate the redshift ranges in which Ly α forests change the observed color. In the later sections, we focus on redshift range below $z = 1.47, 2.04, \text{ and } 3.44$ for band pairs containing u , g , and r -band, respectively, for clarifying the discussion about intrinsic spectral variability.

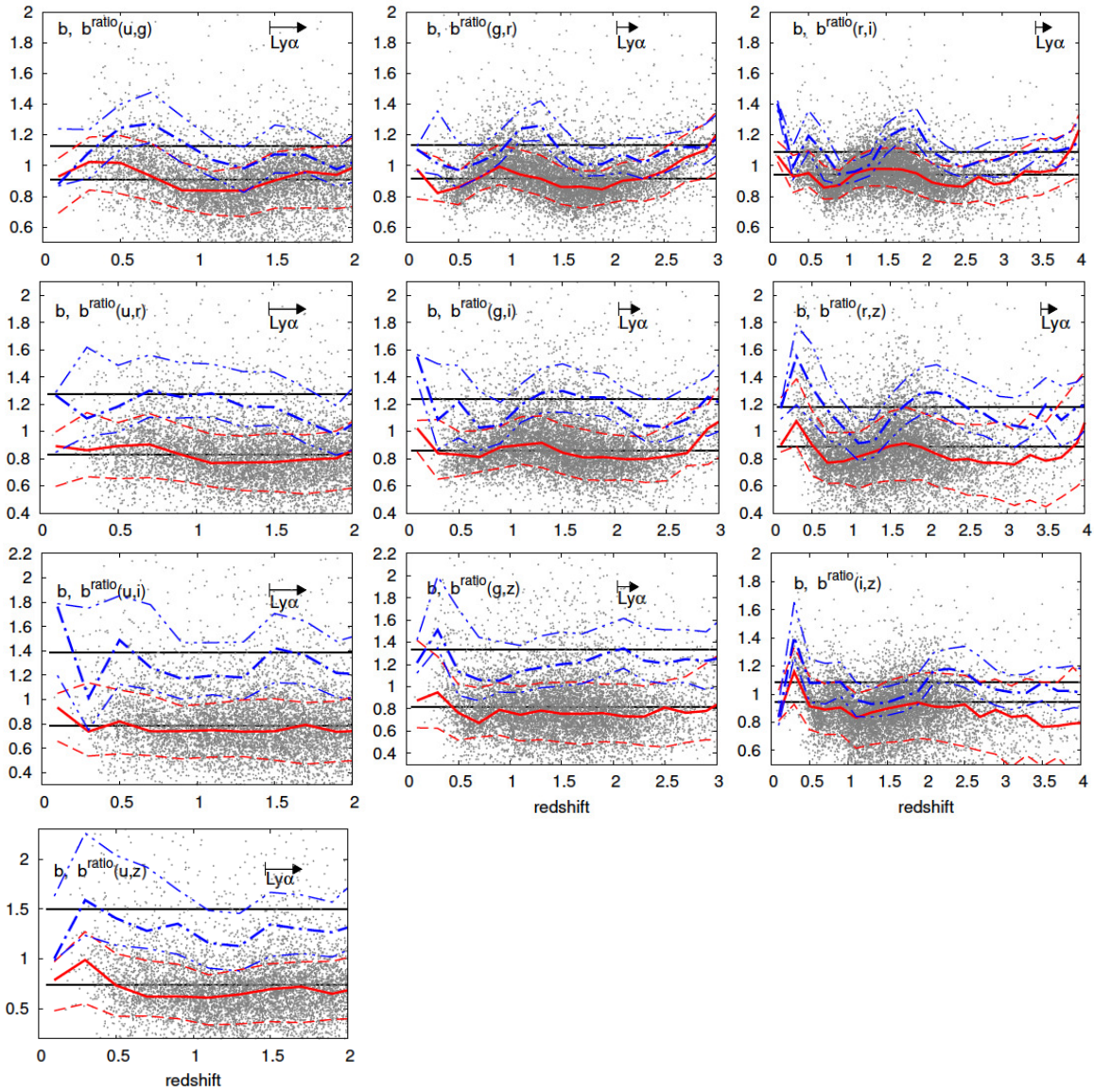


Figure 2.9: Regression slopes $b(s, l)$ as a function of redshift (dots). Solid curves with dashed outer quartiles (colored red in the electronic edition) indicate the mode and the 1σ (68%) range of the slopes for each redshift bins ($\Delta z = 0.2$), and dash-dotted curves with double-dot-dashed outer quartiles (colored blue in the electronic edition) are the mode of the ratio of fluxes $b^{\text{ratio}}(s, l)$ defined by Equation (2.8). Two thin horizontal lines (upper and bottom) indicate the case of power-law spectrum models, $\alpha_v = -0.44$ and $+1/3$ ($\alpha_\lambda = -1.56, -7/3$), respectively. $b^{\text{ratio}}(s, l)$ -redshift relation (i.e., the color of the time-averaged observed spectrum as a function of redshift) can be represented by $\alpha_v^{\text{com}} = -0.44$ (Vanden Berk et al., 2001). On the other hand, $b(s, l)$ -redshift relation (i.e., the color of the difference spectrum as a function of redshift) can be represented by $\alpha_v^{\text{dif}} = +1/3$.

The dash-dotted curves ($b^{\text{ratio}}(s, l)$) in Figure 2.9 are generally larger than 1. This is consistent with the result of the geometric mean composite spectrum for SDSS quasars presented by Vanden Berk et al. (2001); the spectral index of the composite spectrum $\alpha_v^{\text{com}} \sim -0.44 < 0$ ($\alpha_\lambda^{\text{com}} \sim -1.56$)

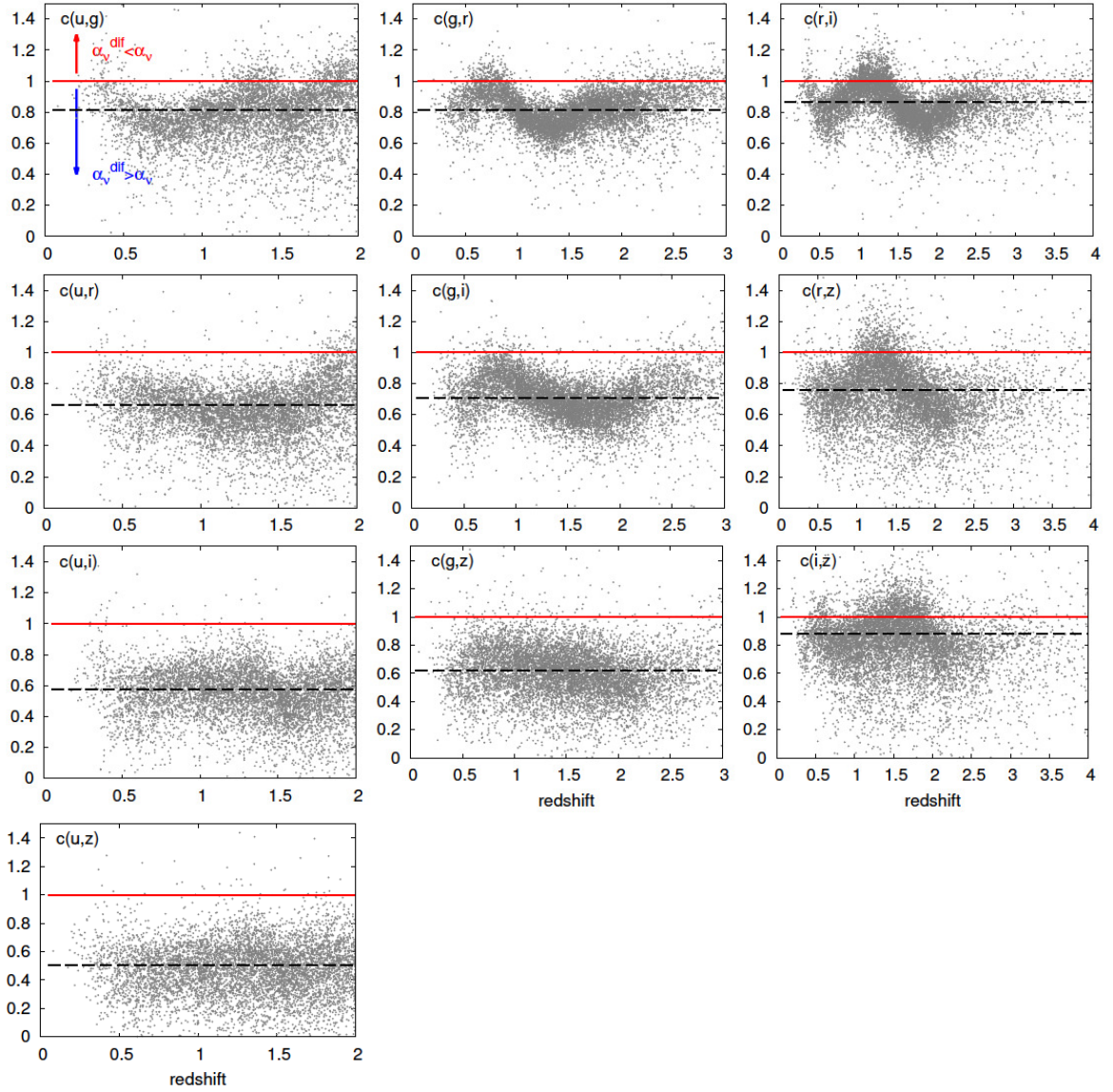


Figure 2.10: $c(s, l) \equiv b(s, l)/b^{\text{ratio}}(s, l)$ (Equation (2.14)) as a function of redshift. The dashed horizontal lines indicate $\Delta\alpha_v = \alpha_v^{\text{dif}} - \alpha_v = -\alpha_\lambda^{\text{dif}} + \alpha_\lambda = +7/3 - 1.56 \sim 0.77$ (difference of the spectral indices shown in Figure 2.9), and the solid lines (colored red in the electronic edition) indicate $\Delta\alpha_v = 0.0$. $c(s, l) > 1$ implies $\alpha_v^{\text{dif}} < \alpha_v$ (corresponds to redder-when-brighter trend in observed color), and $c(s, l) < 1$ implies $\alpha_v^{\text{dif}} > \alpha_v$ (corresponds to bluer-when-brighter trend in observed color).

indicates $b(s, l) > 1$ (Equation (2.12)). The upper thin solid horizontal line in each panel of Figure 2.9 indicates the power-law spectrum model with $\alpha_v = -0.44$ calculated by Equation (2.4).

On the other hand, the solid curves ($b(s, l)$) in Figure 2.9 are generally less than 1 and it implies $\alpha_v^{\text{dif}} > 0$ (Equation (2.7)). The composite flux difference spectrum presented by Wilhite et al. (2005) was reported to have the spectral index $\alpha_v^{\text{dif}} = 0$, and it implies $b(s, l) = 1$ (Equation (2.6)). However, the solid curves in Figure 2.9 are less than 1 within the 1σ ranges (dashed curves). We attempt to employ the spectral index $\alpha_v^{\text{dif}} = +1/3$ that is suggested by Sakata et al. (2010) (the lower thin, solid

horizontal line in each panel of Figure 2.9). This spectral index seems to reproduce the mean value of the $b(s, l)$ for all the band pairs well. This inconsistency between the result of Wilhite et al. (2005) and ours is discussed in Section 2.4.2.

$b^{\text{ratio}}(s, l) > b(s, l)$ is the general trend for quasar variability as shown in Figure 2.9 (see also Appendix B). This indicates that the quasar composite flux difference spectrum is flatter (bluer) than the composite spectrum. In other words, quasar UV–optical spectra tend to become flatter (bluer) when in brighter phase. To clarify the “observed” bluer-when-brighter trend for individual quasars, we show the ratio of $b(s, l)$ to $b^{\text{ratio}}(s, l)$ given as

$$c(s, l) \equiv \frac{b(s, l)}{b^{\text{ratio}}(s, l)} \sim \left(\frac{\lambda(s)}{\lambda(l)} \right)^{\Delta\alpha_\nu} \quad (2.14)$$

as a function of redshift in Figure 2.10, where $\Delta\alpha_\nu = \alpha_\nu^{\text{dif}} - \alpha_\nu$ (approximate value is from Equation (2.6) and (2.11)). By definition, as in Equation (2.7) and (2.12),

$$\begin{cases} c(s, l) > 1 & (\text{if } \alpha_\nu^{\text{dif}} < \alpha_\nu) \\ c(s, l) < 1 & (\text{if } \alpha_\nu^{\text{dif}} > \alpha_\nu). \end{cases} \quad (2.15)$$

Dashed horizontal lines in Figure 2.10 indicate $\Delta\alpha_\nu = \alpha_\nu^{\text{dif}} - \alpha_\nu = -\alpha_\lambda^{\text{dif}} + \alpha_\lambda = 7/3 - 1.56 \sim 0.77$ (difference of the spectral indices shown in Figure 2.9), and solid horizontal lines indicate the case of $\alpha_\nu^{\text{dif}} = \alpha_\nu$. Figure 2.10 shows that almost all of quasars have $\alpha_\nu^{\text{dif}} > \alpha_\nu$. This means the “observed” bluer-when-brighter spectral variability is a common trend in quasars.

Besides the continuum (power-law) variability, we are able to see several spectral features in Figure 2.9 and also in Figure 2.10. These features are mainly made up of the emission line contributions (e.g., Wilhite et al., 2005). It is known that the emission line variability is smaller compared with the continuum variability (intrinsic Baldwin effect, Wilhite et al., 2005). As expected by the intrinsic Baldwin effect, the solid curves in Figure 2.9 show less features compared to the dash-dotted curves. Nonetheless, we are still able to identify the coincidence and the difference of features (the redshift dependence) between the solid and dash-dotted curves. The most apparent difference between them, which corresponds to the difference between the composite and composite difference spectrum, is the bump in intermediate redshifts (e.g., the redshift range $z \sim 1.0$ -1.5 of $g - r$ band pair in Figure 2.9). This difference makes several sharp transitions on $c(s, l)$ as a function of redshift shown in Figure 2.10. The peaks of the bump of dash-dotted curves correspond to the spectral region of Mg II (2800Å) emission line and Fe II pseudo-continuum, and this peak is not seen in the solid curves. It implies that the variability of these emissions are weak. This point is discussed in Sections 2.5 and 2.6.

2.4.2 Comparison with the Composite and Composite Difference Spectrum

There have been several statistical studies about spectral shape and spectral variability for quasars selected and spectroscopically confirmed within SDSS. Here we show the consistency of these previous spectroscopic results with our photometric results.

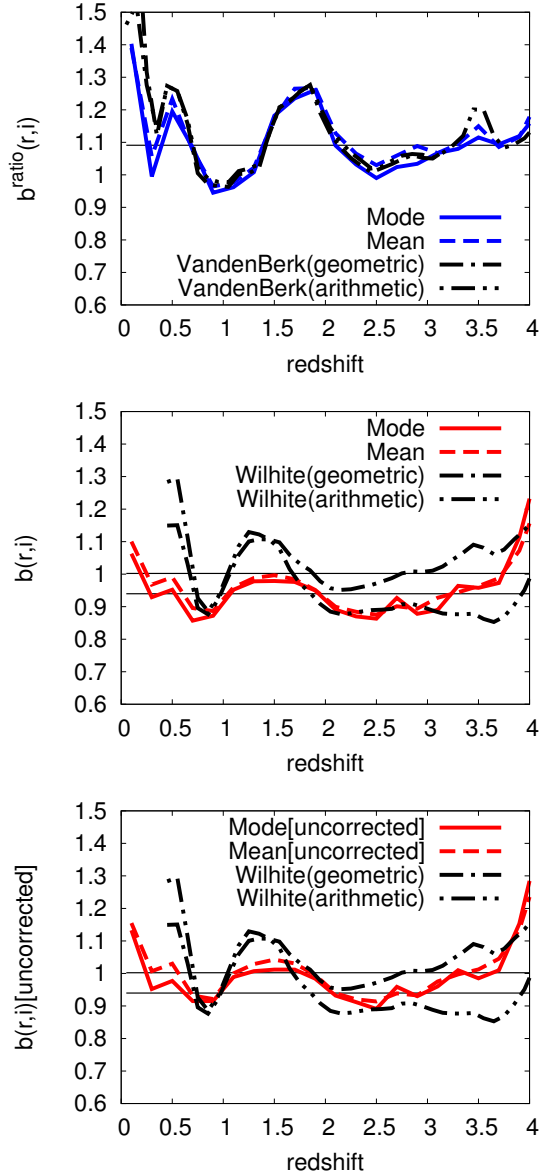


Figure 2.11: Top panel: the comparison of the modal and mean color of the time-averaged spectrum ($b^{\text{ratio}}(r, i)$) with the color of the redshifted geometric and arithmetic composite spectrum (Vanden Berk et al., 2001) calculated by Equation (2.10). The horizontal line is the color of a power-law spectrum with $\alpha_v = -0.44$ (Vanden Berk et al., 2001). Middle panel: the comparison of the modal and mean color of the difference spectrum ($b(r, i)$) with the color of the redshifted geometric and arithmetic composite difference spectrum (Wilhite et al., 2005) calculated by Equation (2.4). The two horizontal lines are the color of power-law difference spectra with $\alpha_v^{\text{dif}} = 0$ and $+1/3$ (upper and lower, respectively). Bottom panel: the same plot as middle panel, but the modal and mean color of the difference spectrum ($b(r, i)$) is not corrected for Galactic extinction.

Figure 2.11 shows the comparison of our results (modal color as a function of redshift in Figure 2.9) with the composite (Vanden Berk et al., 2001) and composite difference (Wilhite et al., 2005)

spectrum using Equation (2.10) and (2.4). In Figure 2.11 we plot not only modal value, but also (weighted) mean value as a function of redshift to check the effects of the asymmetric color distribution, which has a red wing at a given redshift due to intrinsic dust reddening (Richards et al., 2003). We are able to see in Figure 2.11 that the mean values are slightly larger (redder) than the modal value, but the difference is small. This indicates that our results are not affected heavily by this method of taking average.

The composite spectra composed by taking arithmetic or geometric means (Vanden Berk et al., 2001; Wilhite et al., 2005) are compared with our result through Equation (2.4) and (2.10). The geometric mean preserves the average power-law slope, insofar as quasar spectra can be accurately described by a power-law. On the other hand, the arithmetic mean retains the relative strength of the non-power-law features, such as emission lines (Vanden Berk et al., 2001).

As shown in the top panel of Figure 2.11, $b^{\text{ratio}}(r, i)$ of our result and of the composite spectrum (Vanden Berk et al., 2001) are generally consistent. Vanden Berk et al. (2001) presented the geometric and arithmetic composite spectra, but their difference is very small (their spectral index is $\alpha_v = -0.44$ and -0.46 , respectively, with the uncertainty ~ 0.1 due to the spectrophotometric calibration) and they have almost the same $b^{\text{ratio}}(r, i)$ -redshift relation. Power-law index $\alpha_v = -0.44$ (shown as dotted line in upper panel of Figure 2.11) is consistent with $b^{\text{ratio}}(r, i)$, and as we have shown in Figure 2.9, all $b^{\text{ratio}}(s, l)$ are also consistent with $\alpha_v = -0.44$.

On the other hand, $b(r, i)$ of the regression results and the geometric composite difference spectrum (Wilhite et al., 2005) (middle panel of Figure 2.11) seem to be inconsistent in that $b(r, i)$ of the regression results are generally lower than that of the composite difference spectrum for any redshift. This indicates that their composite geometric difference spectrum is steeper than our sample mean color of the difference spectra. We note that their difference spectra composed by taking geometric mean and arithmetic mean are largely different. The authors did not specify the reasons for this large discrepancy. They rely on the geometric composite spectrum when inferring the continuum spectral index $\alpha_v^{\text{dif}} = 0.0$, and we should compare our result with the geometric one when inferring the continuum variability. Also, we note that their spectra are not corrected for Galactic extinction (see Abazajian et al., 2004; Wilhite et al., 2005). The composite spectra with no correction for Galactic extinction obtained by Wilhite et al. (2005) has the spectral index $\alpha_\lambda^{\text{com}} = -1.35$, which is steeper (redder) than the dereddened composite spectrum by Vanden Berk et al. (2001) ($\alpha_\lambda^{\text{com}} = -1.56$). So, the composite flux difference spectrum with $\alpha_\lambda^{\text{dif}} = -2.0$ with no correction for Galactic extinction obtained by (Wilhite et al., 2005) means that the intrinsic composite flux difference spectrum should have flatter (bluer) spectral index (i.e., $\alpha_\lambda^{\text{dif}} < -2.0$), which is consistent with our result $\alpha_\lambda^{\text{dif}} \sim -7/3$ or $\alpha_v^{\text{dif}} \sim +1/3$. In the bottom panel of Figure 2.11 we show $b(r, i)$ with no correction for Galactic extinction as a function of redshift. In this plot, although bumpy features in the $b(r, i)$ -redshift relation (which correspond to the emission lines variability and are discussed in Sections 2.5 and 2.6) of the regression results are still not in good agreement with that of the geometric composite difference spectrum (Wilhite et al., 2005), it is clear that our result and that of the geometric composite difference spectrum (Wilhite et al., 2005) are approximately consistent in that they have similar average

power-law value. Thus, a large fraction of the discrepancy between our result and that of Wilhite et al. (2005) seen in the middle panel of Figure 2.11 can be attributed to a correction or no-correction for the Galactic extinction. It also indicates that the composite flux difference spectrum is not so different in spite of the large difference in time scale between ours and that of (Wilhite et al., 2005, ; see Figure 2.6).

Hereafter, we refer the approximate form of power-law continuum flux difference spectrum as

$$f_{\nu}^{\text{dif}} \propto \nu^{+1/3} \quad (2.16)$$

(i.e., $\alpha_{\nu}^{\text{dif}} \sim +1/3$). As already mentioned in Section 1.2, this power-law index is well known as the standard disk model prediction (Equation 1.11; Lynden-Bell, 1969; Shakura & Sunyaev, 1973). Tomita et al. (2006) and Lira et al. (2011) concluded that the flux difference spectra in near infrared (NIR) wavelengths for their AGN samples are well represented by a combination of the dusty torus component (Blackbody spectrum) and the accretion disk component ($\alpha_{\nu}^{\text{dif}} \sim +1/3$) on the assumption that the flux difference spectrum conserves the spectral shape (spectral index) of the underlying accretion disk spectrum (see also Paltani & Walter, 1996; Collier et al., 1999). Note that the observations of the polarized flux spectra of AGNs – which is assumed to be produced by electron scattering interior to the dust sublimation radius and is regarded as a copy of the spectrum originating in the accretion disk – also revealed the underlying continuum spectral shape consistent with $\alpha_{\nu} = +1/3$ ($\alpha_{\nu} = +0.44 \pm 0.11$, Kishimoto et al., 2008b). Our result can be considered to be the UV–optical extension of the previous results on the flux difference spectrum obtained in the optical–NIR wavelengths (Tomita et al., 2006; Lira et al., 2011), because the dust in the nuclear region cannot become higher temperature than the dust sublimation temperature ($T_{\text{sub}} \sim 1500\text{K}$) and the accretion disk component dominate in UV–optical wavelengths.

In Section 2.4.3, we discuss the validity of the accretion disk model in UV–optical wavelengths.

2.4.3 Comparison with Standard Accretion Disk Model

Pereyra et al. (2006) fitted the composite flux difference spectrum presented by Wilhite et al. (2005) with a standard thermal accretion disk model (Shakura & Sunyaev, 1973), in which the luminosity varies following the changes in accretion rate from one epoch to the next, and concluded that most of the UV–optical variability observed in quasars may be due to processes involving changes in mass accretion rates. The Pereyra et al. (2006)’s formalization of the “varying mass accretion rate model” has already been described in Equation 1.25. Sakata et al. (2011) investigated this model for 10 SDSS quasars individually, and also concluded that the model can explain the UV-optical variability quantitatively. Definitions of the model adopted by Pereyra et al. (2006) and Sakata et al. (2011) are slightly different in that the former depends on the first order Taylor expansion about the average characteristic temperature T^* (see Equation 1.25), but the predicted flux difference spectra are identical for the modest variation amplitude, which is valid for most of quasars.

As described in Equation 1.25, in the formalization of Pereyra et al. (2006), the model flux difference spectrum has two free parameters: a normalization constant ΔT^* and the average characteristic

temperature \bar{T}^* (hereinafter referred to simply as the T^*). One of the advantages of focusing on the color–redshift relation is that it does not depend on the inclination angle (including limb-darkening effect, e.g., Phillips & Meszaros, 1986). When inferring the color of the flux difference spectrum (observable $b(s, l)$ in the present work), this model requires only one parameter T^* because the normalization constant does not affect the color of the difference spectrum. T^* is defined as (Equation 1.9)

$$T^* = \left(\frac{3GM_{\text{BH}}\dot{M}}{8\pi\sigma_S(3R_S)^3} \right)^{1/4} \quad (2.17)$$

$$= 90,600 \text{ K} \left(\frac{\epsilon}{1/12} \right)^{-1/4} \left(\frac{M_{\text{BH}}}{10^9 M_\odot} \right)^{-1/4} \left(\frac{\eta}{0.1} \right)^{1/4} \quad (2.18)$$

where M_{BH} is the black hole mass, \dot{M} is the mass accretion rate, σ_S is the Stefan-Boltzmann constant, and K denotes the kelvin. The disk inner edge is assumed to be at the inner stable circular orbit ($R_{\text{in}} = 3R_S$, where R_S is Schwarzschild radius). Eddington luminosity is defined as $L_{\text{Edd}} = 4\pi GM_{\text{BH}}m_p c / \sigma_T$ (where m_p is the proton mass and σ_T is the Thomson cross section) and Eddington ratio, denoted η , is given as $\eta \equiv L_{\text{bol}} / L_{\text{Edd}}$. Radiative efficiency ϵ , defined as $L_{\text{bol}} = \epsilon \dot{M} c^2$, is fixed⁷ to $\epsilon = 1/12$. Changes in \dot{M} lead to the changes in T^* as $T^* \propto \dot{M}^{1/4}$ and then to the changes in flux. Pereyra et al. (2006) fitted their continuum variability model to the geometric mean flux difference spectrum of Wilhite et al. (2005), and obtained $T^* = 92,700$ K. The upper panel of Figure 2.12 shows the characteristic temperature of our quasar samples calculated by Equation (2.18) using the fiducial virial black hole mass and Eddington ratio listed in quasar property catalog (Shen et al., 2011). $T^* = 92,700$ K, obtained by Pereyra et al. (2006), is very reasonable for SDSS quasars.

As noted in Equation 1.26, at the long wavelength limit, the “varying mass accretion rate model” turns out to be simple scaling of the disk luminosity. Therefore, the spectral index of the flux difference spectrum predicted in this model is the same as that of the static standard Shakura & Sunyaev (1973) accretion disk model, $\alpha_v^{\text{dif}} \sim +1/3$, at the long wavelength limit. Because we obtained $\alpha_v^{\text{dif}} \sim +1/3$ as shown in Figure 2.9, this model is approximately valid. However, we should be careful because:

- The long wavelength limit approximation is not valid for the wavelength range of SDSS photometry for high-redshift quasars. In UV wavelengths, f_v^{dif} predicted by this model becomes gradually steeper (redder) because the UV spectral range corresponds to the turnover spectral region of the blackbody radiation from the accretion disk inner boundary at the inner stable circular orbit (i.e., the hottest part of the disk), as seen in the lower panel of Figure 2.12.
- Pereyra et al. (2006) used the composite difference spectrum not corrected for Galactic extinction (Wilhite et al., 2005), and the effect of the non-correction is not investigated in their paper. The same is true for Sakata et al. (2011), in which the correction for the Galactic extinction was

⁷In the (non-relativistic) standard disk model, the radially integrated disk luminosity is $L_{\text{bol}} = (GM_{\text{BH}}\dot{M}) / (2R_{\text{in}}) = (1/12)\dot{M}c^2$, then $\epsilon = 1/12$ (Kato et al., 2008).

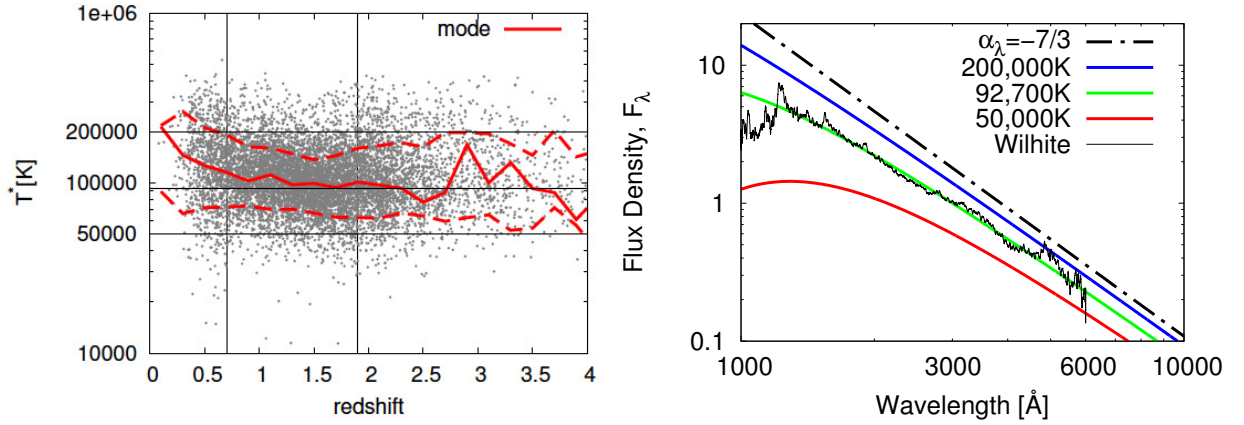


Figure 2.12: **Left panel:** characteristic temperature of SDSS Stripe 82 quasars calculated by Equation (2.18) with the use of a quasar property catalog (Shen et al., 2011). Vertical thin solid lines indicate redshift ranges in which bolometric luminosities are computed in different ways: from L_{5100} ($z < 0.7$), L_{3000} ($0.7 < z < 1.9$), L_{1350} ($z > 1.9$) using bolometric corrections $BC_{5100} = 9.26$, $BC_{3000} = 5.15$, and $BC_{1350} = 3.81$, respectively (Shen et al., 2011). A horizontal thin solid line indicates $T^* = 200,000$ K, 92,700 K (best-fit value obtained by Pereyra et al., 2006), 50,000 K. The solid curve with dashed outer quartiles (colored red in the electronic edition) indicate the mode and the 1σ range for each redshift bin ($\Delta z = 0.2$). **Right panel:** model flux difference spectra f_v^{dif} (Pereyra et al., 2006), calculated for $T^* = 200,000$ K (bluest), 92,700 K, and 50,000 K (reddest). A dash-dotted line is a power-law with $\alpha_\lambda = -7/3$. For comparison, the geometric composite flux difference spectrum by Wilhite et al. (2005) is shown as a thin line. Spectra are arbitrarily scaled.

not properly applied.⁸ It is possible that the non-correction for Galactic extinction leads to the wrong conclusion.

So, it is worth comparing our (Galactic-extinction corrected) result with the model prediction to clarify the validity of the standard disk model. We compare our results with the model proposed by Pereyra et al. (2006) in $b(r, i)$ –redshift space as shown in Figure 2.13. In Figure 2.13, Pereyra’s model (with their best-fit value of $T^* = 92,700$ K) is actually in agreement with the Wilhite’s composite flux difference spectrum. However, the model prediction is apparently steeper ($b(r, i)$ is larger) than our result. This discrepancy is mainly due to whether or not Galactic extinction is corrected (see middle and bottom panel in Figure 2.11). In Figure 2.13, we also plot the model prediction range in $b(s, l)$ –redshift space, which is from $T^* = 50,000$ K (upper boundary) to 200,000 K (lower boundary). The model prediction is apparently not consistent with the $b(s, l)$ –redshift region obtained in our analyses, in that the model predicts larger $b(s, l)$ values and larger spread in $b(s, l)$ –redshift space than observed values particularly in the high redshift range.

⁸Sakata et al. (2011) mentioned that they used the point-spread function magnitude corrected for Galactic extinction obtained from the SDSS database, but we found that the light curves shown in their figures are not properly corrected for it.

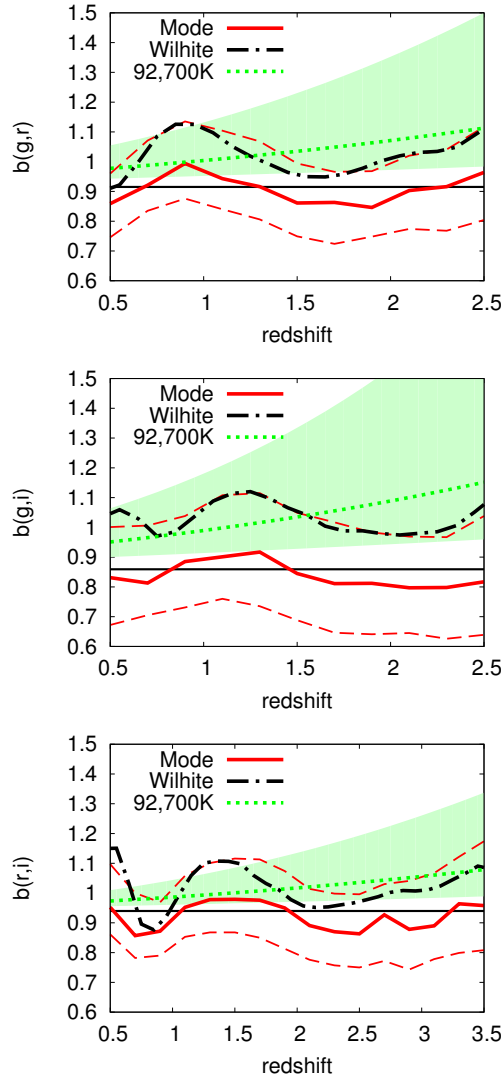


Figure 2.13: Comparison of the observed $b(s, l)$ (corrected for Galactic extinction) with prediction by a standard thermal accretion disk model (Pereyra et al., 2006) in $b(s, l)$ -redshift space. Dotted curves (colored green in the electronic edition) indicate a standard thermal accretion disk model with changing mass accretion rate, assuming that the average characteristic disk temperature is $T^* = 92,700\text{K}$ (Pereyra et al., 2006). The filled region (colored light green in the electronic edition) corresponds to the disk temperature ranges from $T^* = 50,000\text{K}$ to $200,000\text{K}$ (see Figure 2.12). The solid curves with dashed outer quantile (colored red in the electronic edition) are the same as those in Figure 2.9. The dash-dotted curves are calculated from the geometric composite flux difference spectrum (the same as those in Figure 2.11). Horizontal thin solid lines are the color of the power-law difference spectrum with $\alpha_{\nu}^{\text{dif}} = +1/3$.

These indicate that the intrinsic composite flux difference spectrum of quasars is actually flatter (bluer) than the prediction of the accretion disk model, particularly in the UV wavelength range. In other words, we cannot see the model-predicted “UV turnover” feature (e.g., Shang et al., 2005) in

the flux difference spectrum. This result is qualitatively consistent with Schmidt et al. (2012), but our method enables us to examine the difference between observed variability and the model prediction quantitatively.

We are able to make the model flux difference spectrum flatter (up to $f_v^{\text{dif}} \propto \nu^{1/3}$ at all UV–optical wavelengths) if we assume the disk characteristic temperature to be, for example, $T^* > 200,000$ K, but this is not valid for most of our quasar samples as shown in the upper panel of Figure 2.12. According to the accretion disk theory, when the mass accretion rate well exceeds the Eddington limit, the disk becomes radiation pressure-dominated state, where advection becomes important as the energy transport mechanism (Abramowicz et al., 1988; Ohsuga et al., 2002). Such a disk, which is called a “slim disk”, however, produces much redder emission spectrum than the standard thin accretion disk model because the radial profile of the disk temperature becomes flatter than that of the thin disk model due to the effect of advection energy transport at the inner disk radius (e.g., Pezzulli et al., 2016). Therefore, the flat spectrum of $f_v^{\text{dif}} \propto \nu^{1/3}$ also indicates that the accretion disks of the SDSS quasars should not be the slim disks.

Beyond the standard accretion disk model (Shakura & Sunyaev, 1973), several more sophisticated accretion disk models are proposed (see, e.g., Hubeny et al., 2000; Davis et al., 2007). However, accretion disk model spectra based on non-LTE atmosphere calculations (Davis et al., 2007) usually have redder color than the standard thermal accretion disk model because of opacity effects (e.g., Hubeny et al., 2000) and this leads to the redder color of the flux difference spectrum as shown in Schmidt et al. (2012). Although radiative transfer calculations for a disk+corona configuration (rather than those for a bare disk above) result in a weaker “UV turnover” (Kawaguchi et al., 2001), the expected spectra are redder than the long wavelength limit of the standard disk as well. In addition, the accretion disk of quasars or luminous AGNs is thought to be seen almost face-on, so the relativistic effects for the color of the observed spectrum is probably negligible (Hubeny et al., 2000). In short, it is difficult to explain the flux difference spectrum with $\alpha_v^{\text{dif}} \sim 1/3$ by any of the existing accretion disk models.

However, it is true that the reasonable range of physical parameters related to the accretion disk model (M_{BH} and Eddington ratio) can qualitatively explain the absolute continuum flux and flux variation amplitude as indicated in Sakata et al. (2011) and Gu & Li (2013), and α_v^{dif} obtained here can be naturally attributed to the well-known long wavelength limit value predicted in standard accretion disk models. Thus, we can only conclude that the continuum spectral variability in quasars cannot be explained by the accretion disk model with varying mass accretion rate, but it is probably related to thermal accretion disk itself. Finally, we note that it seems to be difficult to explain the large coherent flux variation within UV–optical wavelength range (e.g., a strong linear flux–flux correlation in each individual quasar) by the accretion disk local fluctuations or hot spot scenarios (e.g., Dexter & Agol, 2011; Schmidt et al., 2012; Meusinger & Weiss, 2013). In Chapter 3, we will quantitatively see how the strong inter-band correlation observed in UV-optical quasar light curves constrains the temperature inhomogeneity on the disk surface assumed in the Dexter & Agol (2011)’s “inhomogeneous disk model”.

2.4.4 Brief Summary of This Section

In summary, our conclusions in this section are:

1. We show that the continuum component of the flux difference spectra is (in average) well approximated by a power-law shape with $\alpha_v^{\text{dif}} \sim +1/3$, and it is bluer than the spectroscopic composite flux difference spectrum ($\alpha_v^{\text{dif}} = 0.0$) obtained by Wilhite et al. (2005). We conclude that the discrepancy is due to the Galactic extinction; the light curves used in our analyses are corrected for Galactic extinction but the spectra used in Wilhite et al. (2005) are not. If we derive the color of the flux difference spectrum without the correction, our result shows consistent color and rest-frame wavelength dependence of the flux difference spectrum with Wilhite et al. (2005), in spite of the large difference in time scale (Figure 2.6).

2. We compare the $b(s, l)$ -redshift relation with “the standard disk with varying mass accretion rate model” (Pereyra et al., 2006). One of the advantages of our method is that it is based on the direct comparison of observable color of the difference spectrum ($b(s, l)$) with the model predicted difference spectrum, and does not require additional models or assumptions for non-variable spectral components. We concluded that the flux difference spectrum is flatter (bluer) than the model prediction. In particular, we confirm that the model-predicted “UV turnover” is not seen in the flux difference spectrum. This is surprising because not only the standard accretion disk model (Shakura & Sunyaev, 1973) but also any accretion disk models cannot produce such a flat spectrum as $\alpha_v^{\text{dif}} \sim +1/3$. This result is qualitatively consistent with Schmidt et al. (2012), but our method enables us to examine the difference between observed variability and the model prediction quantitatively.

2.5 Emission line variability: The origin of the redshift dependence of the color of the flux difference spectrum

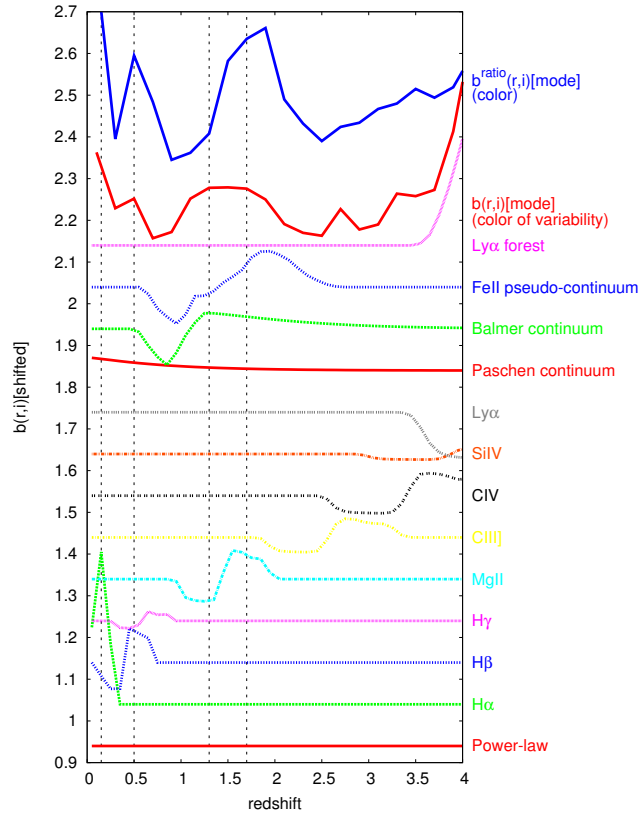


Figure 2.14: $b(r, i)$ as a function of redshift. Each curve (except for the top two curves) is calculated by Equation (2.4) assuming a difference spectrum f_v^{dif} composed of power-law continuum and one additional spectral component: the broad emission lines, Balmer and Paschen continuum, or Ly α forests (Equations (2.19) and (2.20)). The solid curve labeled “ $b^{\text{ratio}}(r, i)[\text{mode}]$ ” (colored blue in the electronic edition) is the modal color of the time-averaged spectrum $b^{\text{ratio}}(r, i)$ as a function of redshift. The solid curve labeled “ $b(r, i)[\text{mode}]$ ” (colored red in the electronic edition) is the modal color of the difference spectrum ($b(r, i)$) as a function of redshift. Curves (other than the “power-law” model) are shifted vertically, and the offset is taken to be 0.1 from adjacent curves.

The flux difference spectra are composed of the continuum component (accretion disk emission) and the BELs component. The regression slope $b(s, l)$ can be related to the difference spectrum as in Equation (2.4), and as we have seen in Section 2.3.3 (Figure 2.7), emission line variability on the power-law continuum variability makes bumpy features in $b(s, l)$ –redshift space. Many of the features in the color-redshift (i.e., $b^{\text{ratio}}(s, l)$ –redshift, or $b(s, l)$ –redshift) relations are caused by more than one feature in the quasar spectrum (Richards et al., 2001). We are able to infer the contribution of each of the emission line variability to the flux difference spectrum by examining the $b(s, l)$ –redshift relation.

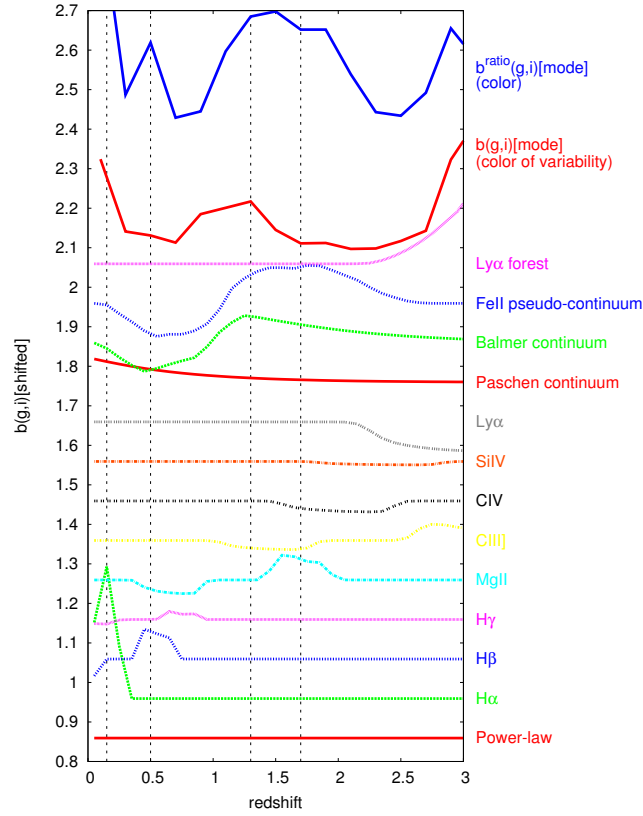


Figure 2.15: Same as Figure 2.14, but for $b(g, i)$ and $b^{\text{ratio}}(g, i)$.

We show the effects of the variability of each of the prominent BEL on $b(r, i)$ and $b(g, i)$ as a function of redshift in Figures 2.14 and 2.15, respectively. “Emission lines” contain BELs, Balmer and Paschen continuum emission (BaC and PaC), and Fe II pseudo-continuum emission. They are calculated assuming

$$f_{\lambda}^{\text{dif}} = f_{\lambda}^{\text{dif}}(\text{continuum}) + 0.05 \times f_{\lambda}^{\text{dif}}(\text{line}) \quad (2.19)$$

where $f_{\lambda}^{\text{dif}}(\text{continuum})$ is the power-law continuum variable component (Equation (2.16)) normalized to 1 at 3000\AA , and given as

$$f_{\lambda}^{\text{dif}}(\text{continuum}) = \left(\frac{\lambda}{3000\text{\AA}} \right)^{-7/3} \quad (2.20)$$

$f_{\lambda}^{\text{dif}}(\text{line})$ includes $f_{\lambda}^{\text{dif}}(\text{BEL})$, $f_{\lambda}^{\text{dif}}(\text{BaC})$, $f_{\lambda}^{\text{dif}}(\text{PaC})$, and $f_{\lambda}^{\text{dif}}(\text{Fe II})$. The factor “0.05” in Equation (2.19) is an overall normalization constant for emission line components to a power-law continuum component and is determined to approximately reproduce the amplitude of bumpy features in the observed $b(s, l)$ –redshift relation. The analytical expressions for calculating these components, and the IGM attenuation model (labeled “Ly α forest”) are summarized in Appendix A. In Figures 2.14 and 2.15, the relative strengths of these components are taken into consideration as described in Appendix A.

Here, we discuss several features of $b^{\text{ratio}}(r, i)$ –redshift relation and $b(r, i)$ –redshift relation qualitatively. We focus on the case of (r, i) band pair, but the color–redshift relation of other band pairs

2.5. Emission line variability: The origin of the redshift dependence of the color of the flux difference spectrum

can be interpreted in the same way.

By comparing $b(r, i)$ –redshift relation with $b^{\text{ratio}}(r, i)$ –redshift relation in Figure 2.14, we are able to identify several similarities and differences in the features. Features of Balmer emission lines and Balmer continuum are seen in both $b(r, i)$ and $b^{\text{ratio}}(r, i)$. The most significant difference between $b(r, i)$ and $b^{\text{ratio}}(r, i)$ exists in features of the Fe II pseudo-continuum and the Mg II emission line. As was done in Richards et al. (2001), we can identify each of the significant features in the $b^{\text{ratio}}(r, i)$ -redshift relation and $b(r, i)$ –redshift relation for each redshift range as below:

- $z \sim 0.1$ to 0.2 — $\text{H}\alpha$ is in i -band and makes $b^{\text{ratio}}(r, i)$ and $b(r, i)$ redder than the average power-law value. Also, the Paschen continuum emission possibly makes the color slightly redder (e.g., Landt et al., 2011).
- $z \sim 0.3$ — The presence of $\text{H}\beta$ in r -band drives $b^{\text{ratio}}(r, i)$ and $b(r, i)$ blueward.
- $z \sim 0.5$ — $b^{\text{ratio}}(r, i)$ and $b(r, i)$ moves back to red color while $\text{H}\beta$ is in i -band.
- $z \sim 0.7$ — Balmer continuum enters the r -band making $b^{\text{ratio}}(r, i)$ and $b(r, i)$ bluer.
- $z \sim 0.9$ — Fe II and Mg II fill the r -band making $b^{\text{ratio}}(r, i)$ bluer. However, these features seem to be absent in $b(r, i)$.
- $z \sim 1.4$ to 1.5 — $b^{\text{ratio}}(r, i)$ makes a sharp transition from blue to red as Mg II leaves r -band and enters i -band. This transition seems to be absent in $b(r, i)$
- $z \sim 1.8$ — A small hump is caused as both Mg II and Fe II push $b^{\text{ratio}}(r, i)$ redward. Again, this feature is absent in $b(r, i)$.
- $z \sim 2.0$ to 2.5 — $b^{\text{ratio}}(r, i)$ is driven back to the blue as Fe II leaves i -band. $b(r, i)$ also becomes blue, probably because of the contribution from C III] in $b(r, i)$. Note that there exist many kinds of weaker high-ionization lines between C III] and C IV that we do not show (e.g., Fe III, Al III, N III], and N IV), and they also make $b^{\text{ratio}}(r, i)$ and $b(r, i)$ bluer.
- $z \sim 2.6$ to 3.4 — C IV and C III] offset each other when the former is in r -band and the latter is in i -band, and keeps $b^{\text{ratio}}(r, i)$ and $b(r, i)$ blue.
- $z > 3.4$ — $\text{Ly}\alpha$ and C IV offset each other during the period when the former is in r -band and the latter is in i -band. At higher redshift, $b^{\text{ratio}}(r, i)$ and $b(r, i)$ rises rapidly as the $\text{Ly}\alpha$ forest or Lyman-limit systems absorb r -band flux (see Figure B.1).

In Figure 2.16, we show the comparison of the observed $b^{\text{ratio}}(r, i)$ (upper solid curve) and $b(r, i)$ (lower solid curve) with those of model spectra (dotted curves) as a function of redshift. The model spectra are the sum of a power-law component ($\alpha_v = -1.56$ and $\alpha_v^{\text{dif}} = -7/3$ for $b^{\text{ratio}}(r, i)$ and $b(r, i)$, respectively (scaled to 1 at 3000\AA , as Equation (2.20)), and several additional components as below: In the model spectrum for $b^{\text{ratio}}(r, i)$ (upper dotted curve), all the emission line components shown

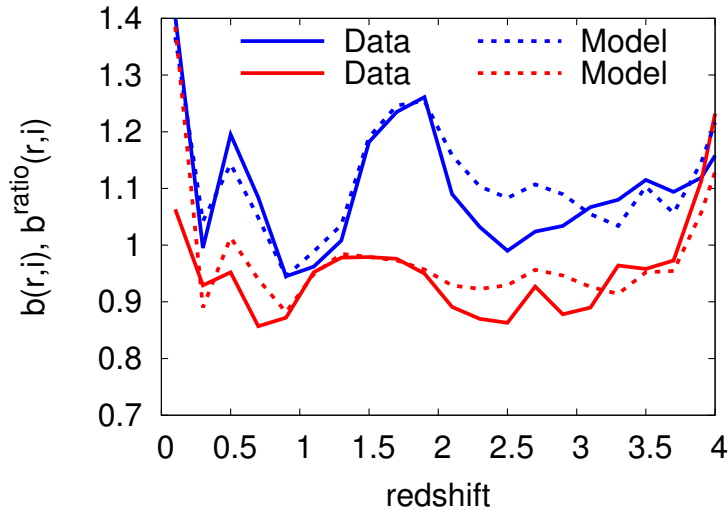


Figure 2.16: Comparison of observed $b^{\text{ratio}}(r, i)$ (upper solid line, colored blue in the electronic edition) and $b(r, i)$ (lower solid line, colored red in the electronic edition) with those of model spectra (dotted lines) as a function of redshift. The model spectra are the sum of a power-law component ($\alpha_{\lambda} = -1.56$ and $\alpha_{\lambda}^{\text{dif}} = -7/3$ for $b^{\text{ratio}}(r, i)$ and $b(r, i)$, respectively) (scaled to 1 at 3000\AA , as Equation (2.20)), and several additional components as below: In the model spectrum for $b^{\text{ratio}}(r, i)$ (upper dotted line, colored blue in the electronic edition), all the emission line components shown in Figure 2.14, Balmer and Paschen continuum emission, and Fe II pseudo-continuum emission are included and the IGM attenuation is applied (the relative strengths of each of the components are the same as Appendix A). On the other hand, in the model spectrum for $b(r, i)$ (lower dotted line, colored red in the electronic edition) we exclude Mg II emission line and Fe II pseudo-continuum emission. Note that there exist many kinds of weaker high-ionization lines between C III] and C IV that we do not show in Figure 2.14/2.15 (e.g., Fe III, Al III, N III], and N IV), so the model spectra have redder color than the observed color both in $b^{\text{ratio}}(r, i)$ and $b(r, i)$.

in Figure 2.14, Balmer and Paschen continuum emission, and Fe II pseudo-continuum emission are included, and the IGM attenuation is applied (the relative strengths of each of the components are the same as Appendix A). On the other hand, in the model spectrum for $b(r, i)$ (lower dotted curve) we exclude Mg II emission line and Fe II pseudo-continuum emission. Note that there exist many kinds of weaker high-ionization lines between C III] and C IV that we do not show in Figure 2.14/2.15 (e.g., Fe III, Al III, N III], and N IV), so the model spectra have redder color than the observed color both in $b^{\text{ratio}}(r, i)$ and $b(r, i)$. Nevertheless, it is clear that the model spectra successfully reproduce the observed bumpy feature in $b(s, l)$ –redshift and $b^{\text{ratio}}(s, l)$ –redshift relations. Moreover, it is also clearly shown that the differences between $b^{\text{ratio}}(s, l)$ and $b(s, l)$ as a function of redshift exist not only in the continuum power-law spectral index, but also in the relative significance of the emission line components; Mg II and Fe II emission line components seem not to play an important role in the $b(s, l)$ –redshift relation, although they have significant contribution in the $b^{\text{ratio}}(r, i)$ –redshift relation.

In summary:

1. Utilizing the average $b^{\text{ratio}}(s, l)$ –redshift relation, we can identify the emission line contamination in the color of the quasars (Richards et al., 2001) as bumpy features in $b^{\text{ratio}}(s, l)$ –redshift curves. Applying this method to the $b(s, l)$ –redshift relation, we identify the features due to, for instance, Balmer emission lines and Balmer continuum variability in $b(s, l)$ –redshift relation.
2. We show that several features seen in $b^{\text{ratio}}(s, l)$ –redshift and $b(s, l)$ –redshift relation are similar (e.g., the Balmer series emission), but they look significantly different around the features attributable to the broad Mg II emission line. This indicates that the variability of Mg II emission line and Fe II pseudo-continuum emission seem to be relatively weaker than other emission line components, such as Balmer series emission lines. This spectral region (referred to as “SBB”) also contains the Balmer continuum, Fe II pseudo-continuum emission, and some other (relatively weak) high-ionization lines, so detailed spectral decomposition analysis is needed to infer the variability of each component, and this is attempted in the next section.

2.6 Variability of the Small Blue Bump

In this section, we focus on the variability of the SBB spectral components. First we decompose the high resolution composite spectrum of Vanden Berk et al. (2001) into spectral components, and compose several model spectra by combining some of the components. Then, we calculate the $b(r, i)$ –redshift relation of each of the model spectrum and compare it with the observed $b(r, i)$ –redshift relation. This procedure enables us to identify the (non-)variable spectral components in the SBB.

2.6.1 Spectral Decomposition

As seen in Figure 2.9 and discussed in the previous section, the most apparent difference between $b^{\text{ratio}}(s, l)$ [color of the time-averaged spectrum] and $b(s, l)$ [color of the flux difference spectrum] exists in features of the Fe II pseudo-continuum and the Mg II emission line. The spectral region containing Fe II pseudo-continuum, Balmer continuum emission, and Mg II emission line is called SBB (Wills et al., 1985). Note that in the actual quasar spectra, higher order Balmer lines are merging to a pseudo-continuum and yielding a smooth rise to the Balmer edge (Dietrich et al., 2003), which is also contained in SBB. Here we discuss the SBB variability.

To clarify the difference between $b^{\text{ratio}}(s, l)$ and $b(s, l)$ (as a function of redshift) arising from the complex emission line composition, we decompose the SBB in the composite spectrum (Vanden Berk et al., 2001) into power-law continuum, Mg II emission line, Fe II pseudo-continuum, and Balmer continuum and investigate the color (corresponding to $b^{\text{ratio}}(s, l)$ and $b(s, l)$) as a function of redshift for the composite spectra with and without some SBB components.

Kurk et al. (2007) decomposed the Vanden Berk’s composite spectrum into a power-law continuum, Balmer continuum, and residual. They confirmed that the residual was well described by the

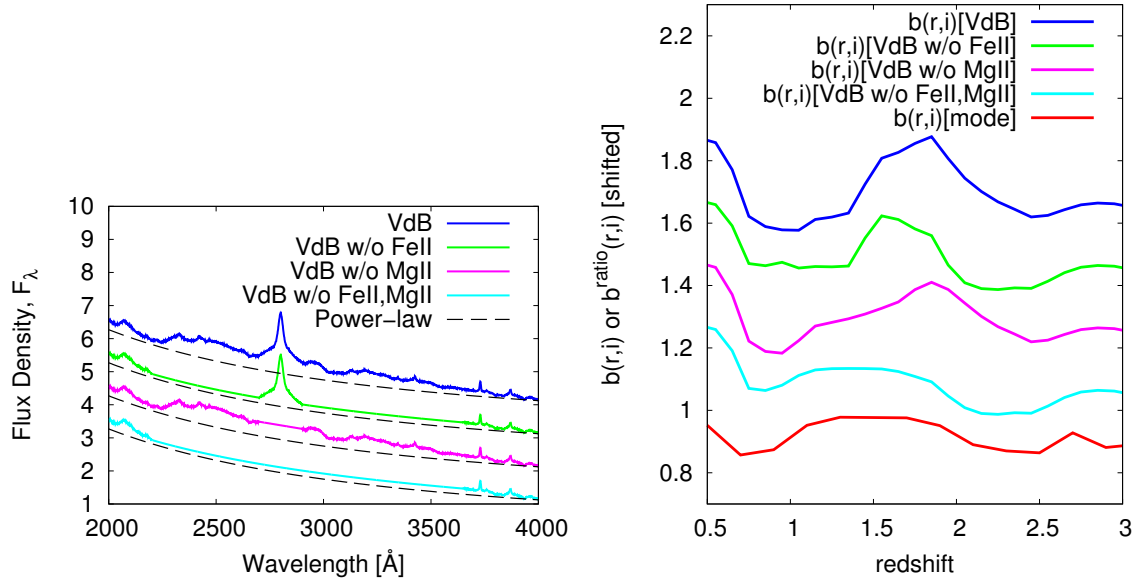


Figure 2.17: **Left panel:** decomposition of the Small Blue Bump (2200Å - 3646Å) in the composite spectrum (Vanden Berk et al., 2001) following Kurk et al. (2007). “VdB” indicate the Vanden Berk’s quasars composite spectrum. From top to bottom, solid curves indicate the raw composite spectrum (VdB), the Fe II-subtracted composite spectrum (VdB w/o Fe II), the Mg II-subtracted composite spectrum (VdB w/o Mg II), and the Fe II-Mg II-subtracted composite spectrum (VdB w/o Fe II, Mg II), respectively (colored blue, green, magenta, and cyan in the electronic edition). These spectra are shifted by +3.0, 2.0, 1.0, and 0.0 in y-axis, respectively. The continuum power-law index is $\alpha_\lambda = -1.54$ and the power-law component is normalized to the flux values in the 4200-4230Å region (dashed lines). The Balmer continuum is created by Equation (B.2) and normalized to the value at 3675Å. Mg II is decomposed by linearly interpolating the spectrum through 2700Å to 2900Å. **Right panel:** the color of the redshifted spectra in left panel as a function of redshift (upper four curves), compared with the observed modal color of the difference spectrum ($b(r, i)$) as a function of redshift (bottom solid curve, the same as Figure 2.9). From top to bottom, the upper four curves are shifted by +0.6, 0.4, 0.2 and 0.0 in the y-axis, respectively (colored blue, green, magenta, and cyan, respectively, in the electronic edition). The composite spectrum without Fe II pseudo-continuum and the Mg II emission line (VdB w/o Fe II, Mg II), which means this spectrum is composed of a power-law continuum and the Balmer continuum emission, has a similar color–redshift relation with the observed $b(r, i)$ –redshift curve. Note that the host galaxy contamination in the VdB composite spectrum is not subtracted.

Fe II emission template (Vestergaard & Wilkes, 2001) and a Mg II emission line. We follow their decomposition procedure, which is done in the 2200-3646Å region. First, the power-law continuum with $\alpha_\lambda = -1.54$ is normalized to the values in the 4200-4230Å region. Second, the Balmer continuum is created by Equation (B.2) and normalized to the value at 3675Å. The residual spectrum (the composite spectrum minus a power-law minus Balmer continuum) is composed of Fe II pseudo-continuum and a Mg II emission line. The Mg II emission line is decomposed by simply assuming the Fe II pseudo-continuum in 2700Å to 2900Å region is described by linear interpolation of the residual spectrum from 2700Å to 2900Å.

Using the decomposed components, we define four spectra of the SBB region $f_\lambda(\text{SBB})$ as below:

- VdB: the composite spectrum of Vanden Berk et al. (2001).

$$f_\lambda(\text{SBB}) = f_\lambda(\text{PL}) + f_\lambda(\text{BaC}) + f_\lambda(\text{Fe II}) + f_\lambda(\text{Mg II}) \quad (2.21)$$

where “PL” denotes a power-law component.

- VdB w/o Fe II: VdB minus Fe II pseudo-continuum.

$$f_\lambda(\text{SBB}) = f_\lambda(\text{PL}) + f_\lambda(\text{BaC}) + f_\lambda(\text{Mg II}). \quad (2.22)$$

- VdB w/o Mg II: VdB minus Mg II emission line

$$f_\lambda(\text{SBB}) = f_\lambda(\text{PL}) + f_\lambda(\text{BaC}) + f_\lambda(\text{Fe II}). \quad (2.23)$$

- VdB w/o Fe II, Mg II: VdB minus Fe II pseudo-continuum minus Mg II emission line

$$f_\lambda(\text{SBB}) = f_\lambda(\text{PL}) + f_\lambda(\text{BaC}). \quad (2.24)$$

These spectra are shown in the upper panel of Figure 2.17. Then, we calculate the color of these spectra by Equation (2.4) or (2.10) as a function of redshift. Results are shown in the bottom panel of Figure 2.17. We can see that the Balmer continuum, Fe II pseudo-continuum, and the Mg II emission line make distinguishable bump features at different redshift ranges. The peak in $b(r, i)[\text{VdB}]$ at $z \sim 1.5-1.8$ are made of a Mg II emission line ($z \sim 1.5$) and Fe II pseudo-continuum ($z \sim 1.8$) (in agreement with Richards et al., 2001), and this feature is not seen in the $b(r, i)[\text{mode}]$. The $b(r, i)[\text{mode}]$ curve resembles the case of “VdB w/o Fe II, Mg II” (i.e., $f_\lambda(\text{SBB}) = f_\lambda(\text{PL}) + f_\lambda(\text{BaC})$). This indicates that the variability of Mg II emission line and Fe II pseudo-continuum are relatively weaker compared to the Balmer continuum emission.

2.6.2 Mg II Emission Line Variability

Mg II line variability has been examined in several papers (see Woo, 2008; Hryniewicz et al., 2014; Modzelewska et al., 2014; Sredzinska et al., 2016, and references therein). Goad et al. (1999a,b)

showed that continuum flux and the broad high-ionization emission lines of Ly α , C IV, N V(1240Å), He II(1640Å), and the semi-forbidden lines of the Si III]+C III] blend varied significantly (a factor of 5 at 1365Å and 3 at 2230Å for continuum, and a factor of 2 for Ly α and C IV), while the low-ionization lines of Mg II and Fe II do not vary significantly (less than 7%) during 11 months of observations for the Seyfert 1 galaxy NGC 3516. Goad et al. (1999a) listed three possible physical reasons explaining an absence of response in the Mg II emission line: (1) the continuum band responsible for the Mg II emission line (i.e., 600 to 800 eV, Krolik & Kallman, 1988) is invariant; (2) the emission line is insensitive to continuum variations; and (3) the line-emitting region is physically extended and thus has yet to respond to the observed continuum variations. (1) was denied in Goad et al. (1999a) by observational evidence that showed that the amplitude of the continuum variations generally increase toward shorter wavelengths at least up to EUV wavelength range for several AGNs (e.g., Marshall et al., 1997; Cagnoni et al., 1999; Halpern et al., 2003). Strong soft X-ray variability has been observed in many AGNs, so (1) is definitely not true. (3) is not true, especially in our sample, with three to four years (in quasar rest-frame) observational duration. Thus, we are able to expect situation (2) to be responsible for an absence of variability in the Mg II emission line. Goad et al. (1993) defined the line responsivity as a linear coefficient relating line emissivity with ionization parameter, assuming that locally the emission-line gas responds linearly to continuum variations (Goad et al., 1999a; Korista & Goad, 2004; Goad et al., 2012). The larger the line responsivity is, the more responsive the line is to continuum variations. Although the line responsivity is model dependent, high-ionization emission lines generally have the line responsivity of ~ 1 ; Balmer lines have ~ 0.6 ; and Mg II emission line has ~ 0.2 (Goad et al., 1999a; Korista & Goad, 2004). We are able to interpret our result with respect to the weak variability of Mg II as the consequence of the small line responsivity for the low-ionization lines.

2.6.3 Fe II Pseudo-continuum Variability

The Fe II emission line is also a member of the low-ionization lines. In the same way as the Mg II emission line, the weak variability of Fe II can be the consequence of the small line responsivity. However, the situation may be more complicated in regards to the Fe II.

The origin of Fe II emissions is still controversial (e.g., Dong et al., 2011). Baldwin et al. (2004) showed that Fe II emissions from photoionized broad emission line region (BELR) cannot explain all the Fe II emission features, and suggested that a large amount of Fe II emission originates in either a separate collisionally ionized component or BELR with considerable velocity structure (microturbulence). The collisionally ionized component would not vary in response to continuum variations, thus Fe II pseudo-continuum variability would be weak as a whole. On the other hand, several authors suggest that Fe II is emitted in infalling photoionized gas (Hu et al., 2008; Ferland et al., 2009), and several recent observational evidences support this picture (Barth et al., 2013, and references therein). When this is the case, the small amplitude of Fe II variability can be explained as the consequence of the different origin of Fe II, (i.e., Fe II emission does not come from usual BELR, so it cannot vary in

the same way as other BELs). However, more detailed investigation of the Fe II emission is beyond the scope of this work.

2.6.4 Balmer Continuum Variability

Figure 2.17 indicates that the Balmer continuum is a dominant variable component in SBB region. We can expect that the Balmer continuum and Balmer emission lines are formed coherently by some photoionization processes in the broad line region, as we can see in the fourth global eigenspectrum presented by Yip et al. (2004). There is no wonder that the Balmer continuum is variable like the Balmer emission lines (e.g., $H\alpha$ and $H\beta$). The variability of the Balmer continuum has been discussed observationally in Wamsteker et al. (1990), Maoz et al. (1993), and Edelson et al. (2015), and theoretically in Korista & Goad (2001). Our result is the first study clearly showing the variability of the Balmer continuum emission in large quasar samples.

Wilhite et al. (2005) showed that the ratio spectrum of the composite difference spectrum to the composite spectrum was depressed around 3000\AA (see also Bian et al., 2012). Photometric variability using structure function formalization (Vanden Berk et al., 2004; MacLeod et al., 2012) also shows the depression around 3000\AA . This behavior can be interpreted by our result about the variability and non-variability of SBB components. Because the Fe II pseudo-continuum ($\sim 2200\text{-}3000\text{\AA}$) and Mg II emission line ($\sim 2800\text{\AA}$) exist in the composite spectrum although not in the composite difference spectrum, the ratio is significantly depressed. Moreover, as discussed in Bian et al. (2012), the Balmer continuum should obey the intrinsic Baldwin effect in the same way as Balmer emission lines, so the ratio spectrum around the Balmer continuum region should be slightly depressed.

2.6.5 Brief Summary of This Section

In summary, our conclusions in this section are:

1. We first decompose the SBB spectral region of the high resolution SDSS quasar composite spectrum (Vanden Berk et al., 2001) into a power-law continuum, Balmer continuum, Fe II, and Mg II following Kurk et al. (2007). Then, we investigate the color–redshift relation of the composite spectrum with and without each component. We confirm that the composite spectrum without Fe II and Mg II emission line components has similar color–redshift relations with the color of the flux difference spectrum. This indicates that Fe II and Mg II have (in average) small variability, and the Balmer continuum is variable in broad spectral region. This is the first time that the strong variability of Balmer continuum and small variability of Fe II and Mg II are confirmed as the statistical property of large quasar samples.
2. Small variability of the Mg II emission line is naturally interpreted by the small line responsivity of the low-ionization line to the ionizing continuum variation (Goad et al., 1999a).

3. Small variability of the Fe II emission line is also interpreted by the small line responsivity of the low-ionization line, but the origin of the Fe II emission is controversial, so it is possible that the small variability of Fe II is due to the different origin of Fe II from normal photoionization BELR.
4. It is no wonder that the Balmer continuum is variable like the other Balmer emission lines because we can expect that they are formed coherently by some photoionization processes in the broad line region.

2.7 Summary and conclusions of Chapter 2

We have explored the wavelength dependence of quasar long term variability. We have introduced the flux–flux correlation method, and applied it to a database of SDSS Stripe 82 multi-epoch five-band light curves for spectroscopically confirmed quasars. This method enables us to infer the spectral variability without suffering from time-averaged baseline flux, which includes time-constant quasar host galaxy flux contamination and time-averaged emission line flux contaminations.

In this work, we focused on the statistical properties of the quasar UV–optical variability, and we conclude:

1. In Section 2.4, we show that the continuum component of the flux difference spectra is (on average) well approximated by a power-law shape with $\alpha_v^{\text{dif}} \sim +1/3$. Then, we compare the $b(s, l)$ –redshift relation with “the standard disk with varying mass accretion rate model” (Pereyra et al., 2006). We concluded that the flux difference spectrum is flatter (bluer) than the model prediction. In particular, we confirm that the model-predicted “UV turnover” is not seen in the flux difference spectrum. This is surprising because not only the standard accretion disk model (Shakura & Sunyaev, 1973) but also any accretion disk models cannot produce such a flat spectrum as $\alpha_v^{\text{dif}} \sim +1/3$. We stress the importance of the correction for Galactic extinction, without which the flux difference spectrum happens to have similar spectral shape with the model spectrum.
2. In Section 2.5, we identify the features due to, for instance, Balmer emission lines and Balmer continuum variability in the $b(s, l)$ –redshift relation. We show that some of the features seen in $b^{\text{ratio}}(s, l)$ –redshift and $b(s, l)$ –redshift relation are similar (e.g., the Balmer series emission), but they look significantly different around the SBB spectral region. It indicates that the variability of Mg II emission lines and Fe II pseudo-continuum emission seem to be relatively weaker than other emission line components, such as the Balmer series emission lines.
3. In Section 2.6, we first decompose the SBB spectral region of the high resolution SDSS quasar composite spectrum (Vanden Berk et al., 2001) into a power-law continuum, Balmer continuum, Fe II, and Mg II following Kurk et al. (2007). Then, we investigate the color–redshift relation

of the composite spectrum with and without each component. We confirm that the composite spectrum without Fe II and Mg II emission line components has similar color–redshift relations with the color of the flux difference spectrum. This indicates that Fe II and Mg II have (in average) small variability, and the Balmer continuum is variable in broad spectral region. This is the first time that the strong variability of the Balmer continuum and the small variability of Fe II and Mg II are confirmed as the statistical property of large quasar samples. The small variability of the Mg II emission lines and Fe II emission lines is naturally interpreted by the small line responsivity of the low-ionization line to the ionizing continuum variation (Goad et al., 1999a). However, the origin of the Fe II emission is controversial, so it is possible that the small variability of Fe II is due to the different origin of Fe II from normal photoionization BELR. It is no wonder that the Balmer continuum is variable like the other Balmer emission lines, as we can expect that they are formed coherently by some photoionization processes in the broad line region.

In the present work, we have limited our discussion to the UV–optical variability and UV–optical data. However, it is clear that the AGN variability should be understood as multi-wavelength phenomena. The correlation between the X-ray and UV–optical variability is definitely important. The X-ray reprocessing model, which also predicts the bluer-when-brighter UV–optical color variability with $\alpha_v^{\text{dif}} \sim +1/3$ if simple geometry for the X-ray emitting region and the accretion disk is assumed, may be the alternative model for AGN UV–optical variability (“the lamppost model”; e.g., Tomita et al., 2006; Cackett et al., 2007; Lira et al., 2011; Gil-Merino et al., 2012; Chelouche, 2013). This model also explains the variability time-scale (nearly simultaneous UV-to-optical variability) as the light-crossing time of the accretion disk. However, the geometry around the accretion disk and the X-ray emitting region is not well known, and definitive conclusions about the validity of the X-ray reprocessing model have not been obtained yet. The correlation between UV–optical and X-ray variability has been observed in several AGNs (e.g., Breedt et al., 2009; Cameron et al., 2012; Edelson et al., 2015; Lira et al., 2015; Troyer et al., 2016; McHardy et al., 2016; Noda et al., 2016; Starkey et al., 2016; Pal et al., 2016; Buisson et al., 2017), but sometimes conflicting results with the X-ray reprocessing model have been obtained (e.g., Maoz et al., 2002; Shemmer et al., 2003; Marshall et al., 2008). Future multi-wavelength intensive monitoring for more AGNs will be needed to clarify the origin of the X-ray–UV–optical correlation.

Chapter 3

Constraints on the Temperature Inhomogeneity in Quasar Accretion Disks from the UV-Optical Spectral Variability¹

Abstract of Chapter 3

Recently, Dexter & Agol (2011) presented a model of quasar UV-optical variability, which assumes large local temperature fluctuations in the quasar accretion disks. This inhomogeneous accretion disk model is claimed to describe not only the single-band variability amplitude, but also microlensing size constraints and the quasar composite spectral shape. In this work, we examine the validity of the inhomogeneous accretion disk model in the light of quasar UV-optical spectral variability by using five-band multi-epoch light curves for nearly 9 000 quasars in the Sloan Digital Sky Survey (SDSS) Stripe 82 region. By comparing the values of the intrinsic scatter σ_{int} of the two-band magnitude–magnitude plots for the SDSS quasar light curves and for the simulated light curves, we show that Dexter & Agol’s inhomogeneous accretion disk model generally predicts weaker inter-band correlation compared to the actual quasar light curves. This result leads us to conclude that the local temperature fluctuations in the accretion disks are not the main driver of the several years’ UV-optical variability of quasars, and consequently, that the assumption that the quasar accretion disks have large localized temperature fluctuations is not preferred from the viewpoint of the UV-optical spectral variability.

¹This Chapter 3, in full, is a reprint of the material as it appears in Monthly Notices of the Royal Astronomical Society, volume 449, page 94, 2015 (Kokubo, 2015). The dissertation author was the primary investigator and single author of this paper.

3.1 Inhomogeneous accretion disk model as an alternative to the standard (static) disk model for AGNs/quasar accretion disks

As already discussed in Chapter 2, several authors have claimed that the AGN variability is due to changes in the global mass accretion rate in AGN accretion disks (Pereyra et al., 2006; Li & Cao, 2008; Sakata et al., 2011; Zuo et al., 2012; Gu & Li, 2013). The variable mass accretion rate model seems to explain the large variability amplitude and the bluer-when-brighter color variability trend often observed for AGNs (e.g., Cutri et al., 1985; di Clemente et al., 1996; Cristiani et al., 1997; Ulrich et al., 1997; Giveon et al., 1999; Hawkins, 2003; Vanden Berk et al., 2004; Meusinger et al., 2011; Sakata et al., 2011; Zuo et al., 2012; Schmidt et al., 2012; Gezari et al., 2013; Gallastegui-Aizpun & Sarajedini, 2014). However, as we have shown in Chapter 2 (see also Schmidt et al., 2012), the variable mass accretion rate model cannot fully account for the strong variability observed in UV wavelengths. Moreover, the variable mass accretion rate model is not preferred when the large difference between the AGN UV-optical spectral variability time-scale and the sound crossing (and the viscous) time-scale of the accretion disk, which corresponds to the time-scale required for global changes of mass accretion rate within the whole of the accretion disk, is taken into consideration (Section 1.3.2; see e.g., Courvoisier & Clavel, 1991; Uttley & Casella, 2014; LaMassa et al., 2015).

Recently, an alternative AGN variability model was presented by Dexter & Agol (2011): the strongly inhomogeneous accretion disk model, which assumes large local temperature fluctuations in the quasar accretion disks as the cause of flux variability. Dexter & Agol's inhomogeneous accretion disk model is motivated by recent numerical simulation studies of thermal or magnetorotational instabilities (e.g., Hirose et al., 2009b; Jiang et al., 2013, and references therein). This model aims to describe not only the observed amplitude of AGN UV-optical single-band variability, but also the otherwise unexplained observational properties of AGN/quasar accretion disks summarized in Section 1.2 and Section 1.3.1, i.e., the unexpectedly large size of the quasar accretion disk revealed by microlensing observations (see e.g., Pooley et al., 2007; Dai et al., 2010; Jiménez-Vicente et al., 2014; Edelson et al., 2015; Jiang et al., 2016b), the excess emission in UV wavelengths observed in a composite Hubble Space Telescope spectrum of quasars (Zheng et al., 1997; Kawaguchi et al., 2001), and the stochastic properties of quasar light curves (Kelly et al., 2009; Kozłowski et al., 2010; MacLeod et al., 2012; Zu et al., 2013; Andrae et al., 2013; Morganson et al., 2014, and references therein). The Dexter & Agol inhomogeneous accretion disk model has received much attention, and several authors have claimed that this model can reproduce several observed properties of quasar UV-optical variability (e.g., Meusinger & Weiss, 2013; Ruan et al., 2014; Sun et al., 2014). For example, Meusinger & Weiss (2013) discussed that the observed anti-correlation between the variability amplitude and the mass accretion rate of quasars could be explained by the Dexter & Agol inhomogeneous accretion disk model. Sun et al. (2014) discussed that the Dexter & Agol inhomogeneous accretion disk model seemed (at least qualitatively) to account for the timescale-dependent color variability of quasars.

Ruan et al. (2014) constructed a composite difference spectrum using two-epoch quasar spectra

(for 604 quasars) from the Sloan Digital Sky Survey (SDSS) (York et al., 2000) following the procedure of Wilhite et al. (2005), and compared it with the Dexter & Agol inhomogeneous accretion disk model. The model's composite difference spectra are calculated as follows: 5 000 model difference spectra between any two successive time steps are produced, and then the model's composite difference spectrum is produced by taking a geometric mean. In Ruan et al. (2014), they obtained a reasonable fitting of the model's geometric mean composite difference spectra to the observed composite difference spectrum, and concluded that quasar UV-optical variability is mainly caused by the large localized temperature fluctuations in the quasar accretion disks.

However, it should be noted that because the quasar accretion disks have a large physical size, temperature fluctuations occurring at different radii of the quasar accretion disks, which have different mean temperatures, must be causally unconnected. Thus, the superposition of independent flares from the localized temperature fluctuations generally means that the inter-band flux–flux correlation observed in the two-band light curve of each individual quasar becomes weaker and weaker when we take more and more separated wavelength band pairs, which contradicts a well-known feature of AGN variability: the UV-optical continua light curves of quasars in different bands are highly correlated (Chapter 2 and see, e.g., Choloniewski, 1981; Krolik et al., 1991; Courvoisier & Clavel, 1991; Korista et al., 1995; Ulrich et al., 1997; Winkler, 1997; Cackett et al., 2007; Gaskell, 2008; Sakata et al., 2010). According to this consideration, the successful fitting to the observed difference spectrum by the Dexter & Agol inhomogeneous accretion disk model obtained by Ruan et al. (2014) is expected to be obtainable only when the comparison between the model and observed difference spectra is done in a composite sense, because the model's predicted weak inter-band correlation can be smeared out when compositing the model spectra. As mentioned in Section 2.4.3, at least qualitatively, it seems to be difficult to explain the large coherent inter-band variation within the UV-optical wavelength range (i.e., the strong flux–flux correlation for each individual quasar) by localized flares in the quasar accretion disks.

In this Chapter, we give quantitative counterarguments against Dexter & Agol's inhomogeneous accretion disk model from the viewpoint of quasar UV-optical spectral variability. We calculate the intrinsic scatter (see Section 3.2 for details) of the inter-band linear correlation in magnitude–magnitude space predicted by the Dexter & Agol inhomogeneous accretion disk model and compare it with the observed scatter quantitatively. As a result of the comparison, we show that the Dexter & Agol inhomogeneous accretion disk model actually cannot explain the tight magnitude–magnitude correlation often observed in quasar UV-optical multi-band light curves. We conclude that it is suspicious that the large localized temperature fluctuations are the main driver of the quasar variability, and consequently, that the assumption of a strongly inhomogeneous accretion disk is not preferred from the viewpoint of the UV-optical spectral variability.

In Section 3.2, we introduce the statistical method we use in this work to evaluate the intrinsic scatter of the magnitude–magnitude plots of the two-band light curves. We describe the database of the SDSS Stripe 82 multi-band multi-epoch light curves of quasars, and then evaluate the variability amplitude and the intrinsic scatter of the magnitude–magnitude plots of these light curves in Sec-

tion 3.3. We describe the Dexter & Agol inhomogeneous accretion disk model in Section 3.4.1, and then show the details of the model light curve calculations in Section 3.4.2. We compare the data with the model predictions in Section 3.5. Finally, discussion and conclusions are given in Section 3.6.

3.2 Magnitude-magnitude linear regression with LINMIX_ERR

The flux–flux plots, and almost equivalently the magnitude–magnitude plots, of quasar two-band simultaneous light curves are known to be well fitted by straight lines of $y = a + bx$ (Chapter 2; see, e.g., Choloniewski, 1981; Winkler et al., 1992; Hagen-Thorn, 1997; Cackett et al., 2007; Sakata et al., 2010, 2011; Lira et al., 2011; Schmidt et al., 2012). The linear regression slope of the flux–flux plot of an AGN light curve quantifies the color of the variable component (Section 2.3.1), and the linear regression slope of the magnitude–magnitude plot can be an indicator of the color variability of AGNs (Schmidt et al., 2012). In this work, as described later, we focus on the intrinsic scatter from the regression line in magnitude–magnitude space, which can be considered as an indicator of the strength of the inter-band correlation; the larger the intrinsic scatter is, the weaker the two-band magnitude–magnitude correlation is. Since the values of the variability amplitude and the intrinsic scatter evaluated in magnitude–magnitude space do not depend on the absolute value of the flux (i.e., the magnitude unit is dimensionless), it is preferable to use the magnitude–magnitude plot because it makes the comparison with model predictions easy. Thus, in later sections we use the magnitude unit when quantifying the quasar variability.

To evaluate the intrinsic scatter from the regression line, it is needed to use a more sophisticated statistical modelling compared to the analysis in Chapter 2. The linear regression line of a magnitude–magnitude plot of a two-band quasar light curve with measurement errors on both axes and with intrinsic scatter can be modelled as [following the notation of Kelly 2007]

$$\eta_i = a + b\xi_i + \epsilon_i \quad (3.1)$$

$$x_i = \xi_i + \epsilon_{x,i} \quad (3.2)$$

$$y_i = \eta_i + \epsilon_{y,i} \quad (3.3)$$

$$\epsilon_i \sim G(\sigma_{\text{int}}^2), \quad \epsilon_{x,i} \sim G(\sigma_{x,i}^2), \quad \epsilon_{y,i} \sim G(\sigma_{y,i}^2), \quad (3.4)$$

where the measurement values of the two-band magnitudes are expressed as x_i and y_i , in which i labels the measurement epoch; $i = 1, 2, \dots$. $G(x^2)$ indicates a Gaussian distribution function with the variance x^2 and with zero mean, and a tilde (\sim) means that a variable on the left side is drawn from a distribution function on the right side. ξ_i is the independent variable and η_i is the dependent variable, representing the true values of the two-band magnitudes. $\epsilon_{x,i}$ and $\epsilon_{y,i}$ are the random measurement errors on x_i and y_i , whose variances are $\sigma_{x,i}^2$ and $\sigma_{y,i}^2$, respectively. ϵ_i represents the intrinsic scatter, whose variance is assumed to be constant and is denoted as σ_{int}^2 , which corresponds to the square of the standard error of the regression.

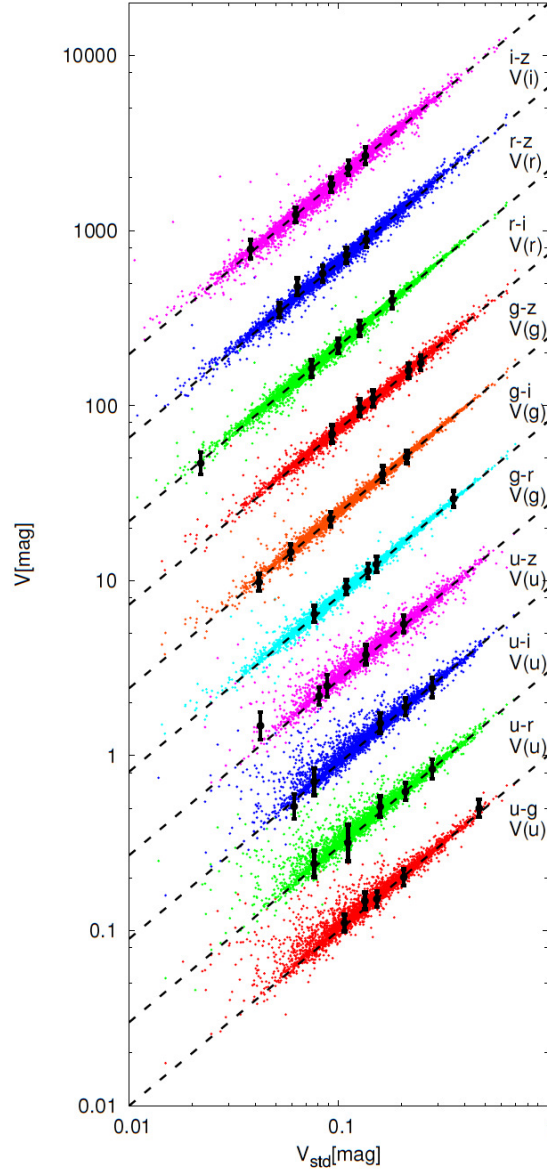


Figure 3.1: Comparison of the values of u -, g -, r -, and i -band variability amplitudes for the SDSS Stripe 82 quasars derived by the two methods. V_{std} is defined as $V_{\text{std}} = \sqrt{\Sigma^2 - \xi^2}$, where Σ is the sample standard deviation and ξ is the root mean square of the photometric error of a single-band light curve. V is the point estimate value of the variability amplitude derived by the Bayesian regression analyses from LINMIX_ERR for the magnitude–magnitude plots of the band pairs of u - g , u - r , u - i , u - z for $V(u)$, g - r , g - i , g - z for $V(g)$, r - i , r - z for $V(r)$, and i - z for $V(i)$. The values of V for adjacent band pairs are scaled by 3 for clarity. Black points with error bars are the randomly selected measurement points indicating the typical values of uncertainty in V , and straight lines indicate $V = V_{\text{std}}$.

Table 3.1: Properties of the individual filter combinations for the SDSS Stripe 82 quasar light curves.

Band pairs ($s-l$)	z	$\langle z \rangle$	N_{obj}	$\langle N_{\text{epoch}} \rangle$	$\langle \lambda_{\text{rest}} \rangle_s$	$\langle \lambda_{\text{rest}} \rangle_l$	$\Delta \langle \lambda_{\text{rest}} \rangle$
$u-g$	0.0 – 1.5	1.025	3984	53	1754	2314	560
$u-r$	0.0 – 1.5	1.025	3977	54	1754	3044	1290
$u-i$	0.0 – 1.5	1.026	3964	54	1753	3692	1939
$u-z$	0.0 – 1.5	1.010	3502	52	1767	4443	2676
$g-r$	0.0 – 2.0	1.280	6715	58	2055	2704	649
$g-i$	0.0 – 2.0	1.280	6708	58	2055	3281	1226
$g-z$	0.0 – 2.0	1.263	5787	56	2071	3947	1876
$r-i$	0.0 – 3.5	1.558	8783	60	2410	2925	515
$r-z$	0.0 – 3.5	1.517	7417	57	2449	3548	1099
$i-z$	0.0 – 4.5	1.547	7510	57	2937	3506	569

A band pair is expressed as $s-l$, where s is the band with the *shorter* effective wavelength and l indicates the other one. $\langle z \rangle$, N_{obj} , and $\langle N_{\text{epoch}} \rangle$ are the mean redshift, the number of objects and the mean number of observed epochs for the SDSS Stripe 82 light curve sample of each band pair (see Section 3.3 for the details of the sample selection). $\langle \lambda_{\text{rest}} \rangle_s$ and $\langle \lambda_{\text{rest}} \rangle_l$ are the mean rest-frame wavelengths of the bands, defined as the effective wavelengths of the bands divided by $1 + \langle z \rangle$.

$\Delta \langle \lambda_{\text{rest}} \rangle$ is their difference (in units of Å).

There are several methods for evaluating the linear regression line and the intrinsic scatter for data with measurement errors on both axes (Gull, 1989; D’Agostini, 2005; Kelly, 2007; Hogg et al., 2010; Wall & Jenkins, 2012; Feigelson & Jogesh Babu, 2012; Park et al., 2012; Sereno, 2016, and references therein). Kelly (2007) introduced a Bayesian approach to this problem. Kelly (2007)’s method assumes that the measurement errors and intrinsic scatter are Gaussian, and the probability distribution of independent variable ξ_i (true value of the i th measurement x_i), denoted as $p(\xi_i|\psi)$ where ψ is the parameter set describing the distribution, is modelled as a weighted mixture of K Gaussian functions:

$$p(\xi_i|\psi) = \sum_{k=1}^K \frac{\pi_k}{\sqrt{2\pi\tau_k^2}} \exp\left[-\frac{1}{2} \frac{(\xi_i - \mu_k)^2}{\tau_k^2}\right], \quad (3.5)$$

where $\sum_{k=1}^K \pi_k = 1$ and τ_k and μ_k ($k = 1, 2, \dots, K$) are the parameters of this model. Kelly (2007) mentioned that it was useful to model $p(\xi_i|\psi)$ using this form because it was flexible enough to adapt to a wide variety of distributions (see also Mantz, 2016; Sereno, 2016). In the particular case of the magnitude–magnitude plots for the quasar light curves, however, there is observational reasoning for adopting the Gaussian function as the probability distribution of ξ_i ; single-band quasar light curves are known to be well modelled by a first-order autoregressive Gaussian process known as a damped random walk (Section 1.3; e.g., MacLeod et al., 2012, and references therein). This implies that $p(\xi_i|\psi)$ for magnitude–magnitude linear regression of quasar light curves can be modelled as a Gaussian distribution ($K = 1$), if the light curve is sampled for a sufficiently long duration of time [i.e.,

longer than the damping timescale of the time series, which is known to be ~ 200 d in the rest frame for quasar variability, (e.g., Butler & Bloom, 2011; Andrae et al., 2013)]. Therefore, in the following analyses, we assume $K = 1$, although the choice of the exact value of K actually does not significantly affect the results obtained. For $K = 1$, $p(\xi_i|\psi)$ can be expressed as:

$$p(\xi_i|\psi) = \frac{1}{\sqrt{2\pi\tau^2}} \exp\left(-\frac{1}{2} \frac{(\xi_i - \mu)^2}{\tau^2}\right), \quad (3.6)$$

where τ and μ are the parameters of this model. This informative prior [equation (3.6)] for sample positions enables Bayesian data analyses for linear regression of data with measurement errors on both axes (Gull, 1989; Kelly, 2007; Mantz, 2016). The IDL routine for the Bayesian linear regression analysis discussed in Kelly (2007) (LINMIX_ERR) has been made available in the IDL Astronomy Users Library². The prior density distributions of the model parameters and the data likelihood function assumed in LINMIX_ERR can be found in Kelly (2007).

The LINMIX_ERR estimator has an advantage over other non-Bayesian methods in that it calculates the posterior distribution of the parameters for the given data using a Markov Chain Monte Carlo (MCMC) method, and hence provides well-defined and reliable parameter uncertainties (see, e.g., Park et al., 2012). Therefore, we can estimate the intrinsic scatter in the magnitude–magnitude plot, denoted as $\sigma_{\text{int}}(\text{data})$ for the observation data (Section 3.3) and as $\sigma_{\text{int}}(\text{model})$ for the model light curves (Section 3.4.2), with their uncertainties, using LINMIX_ERR.

In addition to σ_{int} , we can also derive the single-band variability amplitude of the light curve plotted on the x -axis and its uncertainty by way of the model parameter τ appearing in equation (3.6). By definition, τ is basically the same as the often-used variability amplitude indicator V_{std} , defined as $V_{\text{std}} = \sqrt{\Sigma^2 - \xi^2}$, where Σ is the sample standard deviation and ξ is the root mean square of the photometric error of a single-band light curve (e.g., Vaughan et al., 2003; Sesar et al., 2007; Ai et al., 2010; Zuo et al., 2012). In this work, we denote τ in Equation 3.6 as $V(x)$:

$$V(x) = \tau, \quad (3.7)$$

where x indicates the photometric band corresponding to the x -axis of a magnitude–magnitude plot (e.g., $x = u$ for u - g , u - r , u - i and u - z plots), and refer to $V(x)$ as the variability amplitude. Figure 3.1 compares the variability amplitude of g -, r -, i - and z -band light curves of SDSS Stripe 82 quasars (see Section 3.3 for details) derived by the two methods described above, i.e., V_{std} and V . In Figure 3.1, the values of V are in good agreement with those of V_{std} . This result validates the use of LINMIX_ERR as a reliable tool to quantify the quasar variability amplitude, and eventually its magnitude–magnitude correlation.

It should be noted that the broad-band photometric light curves contain the flux variability not only of the accretion disk continuum emission but also of the broad emission lines and the Balmer continuum emission (Section 2.5 and Section 2.6; e.g., Blandford & McKee, 1982; O’Brien et al., 1995; Baldwin et al., 1995; Korista & Goad, 2001; Peterson & Horne, 2004; Korista & Goad, 2004; Wilhite

²<http://idlastro.gsfc.nasa.gov/>

et al., 2005; Czerny et al., 2013; Chelouche et al., 2014; Hernitschek et al., 2015; Edelson et al., 2015). However, contamination of emission line variability only makes the scatter in magnitude–magnitude space $\sigma_{\text{int}}(\text{data})$ larger because of the reverberation nature of the emission line variability (e.g., Sakata et al., 2011; Schmidt et al., 2012). In other words, we should consider $\sigma_{\text{int}}(\text{data})$ evaluated by the broad-band quasar light curves as an upper bound of the intrinsic scatter of the magnitude–magnitude correlation of the pure accretion disk continuum emission. Therefore, even when the broad emission line variability dilutes the coherent variation of the pure accretion disk continuum emission to some extent, we can assess the invalidity of the Dexter & Agol inhomogeneous accretion disk model by confirming the relation $\sigma_{\text{int}}(\text{model}) > \sigma_{\text{int}}(\text{data})$.

3.3 Median-filtered SDSS Stripe82 quasar light curves

Quantifying the intrinsic scatter in magnitude–magnitude space requires simultaneous multi-epoch multi-band photometric light curves for quasars. Hence, as in Chapter 2, we again use a database of the SDSS Stripe 82 multi-epoch five-band light curves for spectroscopically confirmed quasars from the fifth SDSS quasar catalogue (Schneider et al., 2010) presented by MacLeod et al. (2012) (see Section 2.2 for details). The average wavelengths for the u -, g -, r -, i - and z -bands are 3551, 4686, 6165, 7481 and 8931Å, respectively³. We cross-match the Stripe 82 light curve catalogue of MacLeod et al. (2012) with a catalogue of quasar properties from SDSS DR7 (Shen et al., 2011), and use the improved red shift estimates (Hewett & Wild, 2010) listed in Shen et al. (2011)’s catalogue as the redshift of each quasar.

For completeness, we use all the five-band light curves. The x -axis of the two-band magnitude–magnitude plot (x - y space) is always chosen to be the shorter wavelength band of the two. This results in a total of 10 band pairs: u - g , u - r , u - i , u - z , g - r , g - i , g - z , r - i , r - z and i - z magnitude–magnitude plots. To avoid the Lyman α absorption (<1216 Å) entering into the u -, g -, r - and i -bands, we focus only on the redshift range below $z = 1.5, 2.0, 3.5$ and 4.5 for the regression analyses of band pairs containing the u -, g -, r - and i -bands, respectively (as listed in Table 3.1).

It is known that the SDSS Stripe 82 light curves contain some outlying photometric points that are several magnitudes fainter (or brighter) than adjacent values, most of which must have a non-physical origin (e.g., Schmidt et al., 2010; MacLeod et al., 2010; Meusinger et al., 2011; Palanque-Delabrouille et al., 2011; Zuo et al., 2012). Since the values of the intrinsic scatter σ_{int} described in Section 3.2 may be sensitive to these outlying photometric points, in this Chapter a more careful selection of clean data compared to Chapter 2 is applied; to eliminate the outlying measurements, a medianized light curve was generated by applying a seven-point median filter to each of the light curves of the five bands, and then the measurements with a residual between the medianized light curve and the photometric data larger than 0.25 mag were removed (following the procedures of Schmidt et al., 2010). Then, we exclude quasar light curves that show no variability, i.e., whose sample variance is smaller than

³<http://www.sdss.org/dr7/>

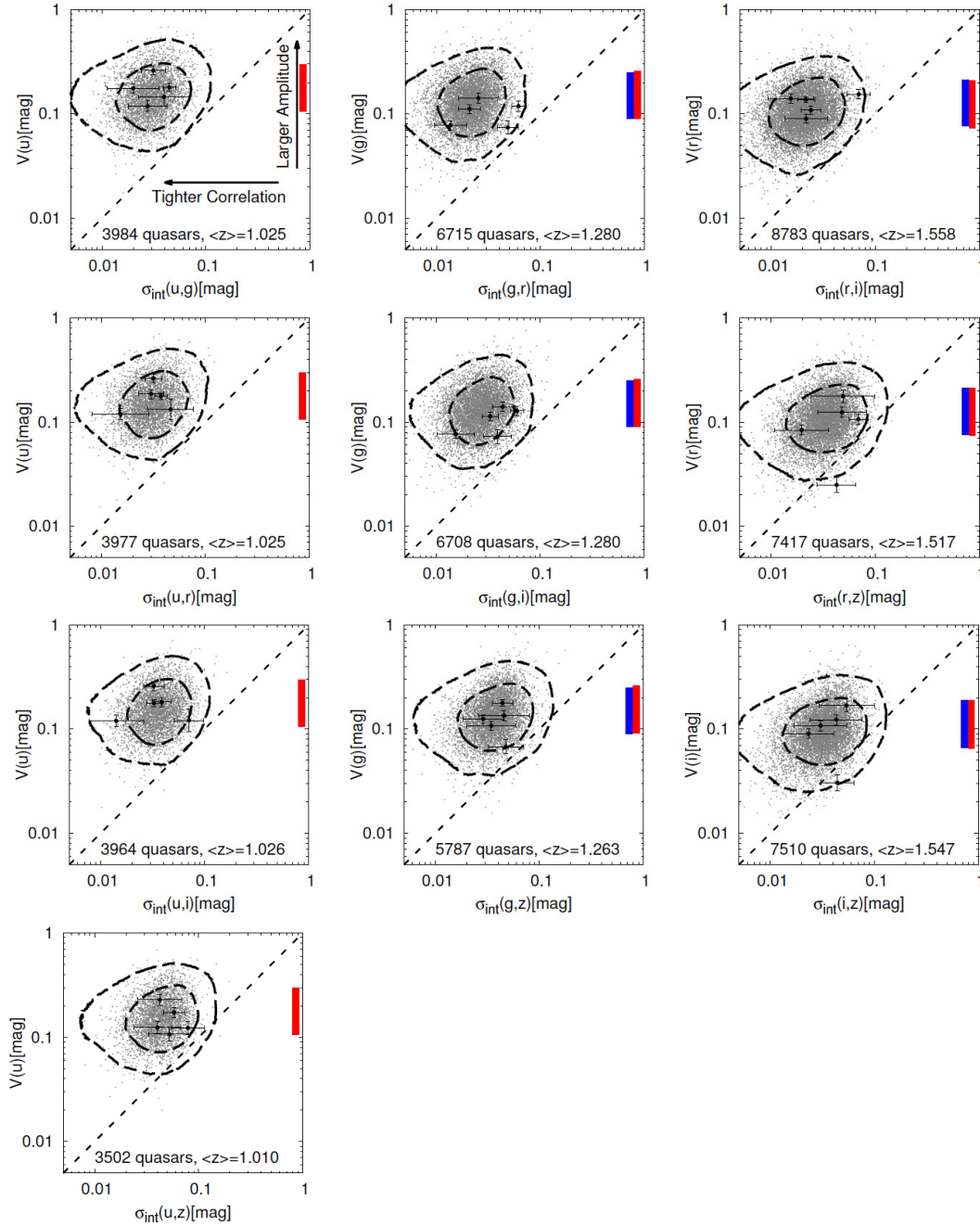


Figure 3.2: Intrinsic scatter σ_{int} versus variability amplitude V for the SDSS Stripe 82 quasars obtained by the regression analyses in magnitude–magnitude space for all 10 band pairs (Section 3.3). Gray dots are the point estimates of the values of σ_{int} and V . Black points with error bars are the randomly selected points of σ_{int} and V to indicate the typical values of uncertainty in the point estimates. 1σ (68.2 per cent, inner dashed line) and 2σ (95.4 per cent, outer dashed line) contours, which are calculated from a composite $\sigma_{\text{int}}-V$ posterior distribution constructed by summing each individual posterior distribution of the sample, are also shown in each of the panel. We show the range of median \pm median absolute deviation of V as red vertical bars on the right-hand side of the panels, and for comparison, we also show the median values of the variability amplitude (corresponding to V_{std}) derived by Zuo et al. 2012 for the g -, r - and i -band light curves of the SDSS Stripe 82 quasars as blue vertical bars on the left of the red vertical bars in the panels for $V(g)$, $V(r)$ and $V(i)$. A thin dashed straight line in each of the panel indicates $V = \sigma_{\text{int}}$. The number of objects and the mean redshift $\langle z \rangle$ for the sample of each band pair are indicated at the bottom of each panel.

the mean measurement error variance (e.g., Zuo et al., 2012). In addition, since we are attempting to focus on the properties of long-term and multi-epoch variability, we exclude from our sample quasar light curves that have less than 20 photometric epochs. The mean total photometric points $\langle N_{\text{epoch}} \rangle$ in the resulting two-band light curves are listed in Table 3.1. Then, linear regression analyses in magnitude–magnitude space for these two-band light curves are conducted using LINMIX_ERR. The potential scale reduction factor \hat{R} (Gelman & Rubin, 1992) is used in LINMIX_ERR to monitor the convergence of the MCMC to the posterior, and we do not use data for which the condition $\hat{R} < 1.1$ is not satisfied within 10 000 iterations of MCMC. The final quasar sample size N_{obj} is listed in Table 3.1.

In Figure 3.2, we plot the results of the regression analyses for the SDSS Stripe 82 data in magnitude–magnitude space; i.e., the intrinsic scatter σ_{int} versus variability amplitude V for all 10 band pairs. Point estimates of the values of σ_{int} and V for each individual quasar are defined as the mean and the standard deviation of the posterior distributions of these parameters. 1σ (68.2 per cent) and 2σ (95.4 per cent) contours of the $\sigma_{\text{int}}-V$ relation for the SDSS Stripe 82 data, which we use as the observational constraint in later sections, are calculated from a composite $\sigma_{\text{int}}-V$ posterior distribution constructed by summing each individual posterior distribution of the sample quasars.

A red vertical bar on the right-hand side in each of the panels of Figure 3.2 shows the range of the median \pm median absolute deviation of V . And for comparison, we also show the median values of the variability amplitude (corresponding to V_{std}) derived by Zuo et al. (2012) for the g -, r - and i -band light curves of the SDSS Stripe 82 quasars as blue vertical bars on the left of the red vertical bars in the panels for $V(g)$, $V(r)$ and $V(i)$. In Figure 3.2, we can see that the values of the variability amplitude V_{std} derived by Zuo et al. (2012) are consistent with those of V derived by LINMIX_ERR. Again (as already mentioned in Section 3.2), this consistency validates the use of LINMIX_ERR as a reliable tool for quantifying the quasar magnitude–magnitude correlation.

As indicated in Figure 3.2, smaller values of σ_{int} indicate tighter linear correlation in magnitude–magnitude space, and larger values of V indicate a larger variability amplitude. The 1σ and 2σ contours generally satisfy $V \gg \sigma_{\text{int}}$, which means that the two-band light curves of quasars are highly correlated.

3.4 Mathematical description of the inhomogeneous accretion disk model

3.4.1 Dexter & Agol’s formalization

Steady-state black hole accretion disks residing in luminous AGNs or quasars are thought to be well described by the standard thin accretion disk model (Shakura & Sunyaev, 1973; Novikov & Thorne, 1973). The emitted spectrum from the standard thin accretion disk can be written as a sum of black-body spectra from the surface elements of the disk (Equation 1.1; e.g., Frank et al., 1992; Kato et al.,

Table 3.2: Assumed photometric errors in the model five-band light curves (in magnitude unit).

Group	1	2	3	4	5	6	7	8	9
σ_u	0.018	0.021	0.028	0.037	0.051	0.071	0.097	0.14	0.20
σ_g	0.011	0.012	0.014	0.016	0.021	0.027	0.035	0.048	0.068
σ_r	0.0099	0.011	0.013	0.015	0.019	0.025	0.034	0.047	0.066
σ_i	0.011	0.012	0.014	0.017	0.022	0.029	0.040	0.057	0.081
σ_z	0.016	0.020	0.027	0.037	0.054	0.079	0.11	0.16	0.25
Per cent	1	2	4	10	18	28	28	8	1

2008):

$$F_\nu(\nu_{\text{obs}}) \propto \nu^3 \int \frac{1}{e^{h\nu/k_B T_{\text{eff}}(R)} - 1} dS \quad (3.8)$$

$$\begin{aligned} T_{\text{eff}}(R) &= \left(\frac{3GM_{\text{BH}}\dot{M}}{8\pi\sigma_S R_{\text{in}}^3} \right)^{1/4} \left(\frac{R_{\text{in}}}{R} \right)^{3/4} \left(1 - \sqrt{\frac{R_{\text{in}}}{R}} \right)^{1/4} \\ &= T^* \left(\frac{1}{x} \right)^{3/4} \left(1 - \sqrt{\frac{1}{x}} \right)^{1/4}, \end{aligned} \quad (3.9)$$

where h , k_B , G , and σ_S are Planck constant, Boltzmann constant, gravitational constant and the Stefan-Boltzmann constant, respectively. ν_{obs} is the observed-frame frequency, which is related to the rest-frame frequency ν as $\nu_{\text{obs}} = \nu/(1+z)$. M_{BH} and \dot{M} represent the black hole mass and the mass accretion rate, respectively. $dS = R d\phi dR$ is the surface element of the accretion disk, where R and ϕ are the radial and azimuthal coordinates on the disk plane, respectively. The disk inner radius R_{in} is taken to be $R_{\text{in}} = 3R_S$ where R_S is the Schwarzschild radius $R_S = 2GM_{\text{BH}}/c^2$. $3R_S$ corresponds to the innermost stable circular orbit of a non-spinning Schwarzschild black hole. The dimensionless radial coordinate x is defined as $x = R/R_{\text{in}}$, which means the disk inner radius is $x_{\text{in}} = 1$.

$$T^* = \left(\frac{3GM_{\text{BH}}\dot{M}}{8\pi\sigma_S R_{\text{in}}^3} \right)^{1/4} \quad (3.10)$$

is the disk characteristic temperature (Equation 1.1), which is the only parameter determining the spectral shape of the emitted spectrum L_ν from the standard thin accretion disk (Section 2.4.3; Pereyra et al., 2006; Ruan et al., 2014). For the SDSS quasars, T^* ranges from 50000 to 200000 K if the Newtonian value of radiative efficiency ($\epsilon = 1/12$) is adopted (Section 2.4.3).

It should be noted that there are several pieces of evidence from the studies of hot-dust-poor AGNs, dust reverberation mapping and infrared polarimetry, suggesting that emission from quasar accretion disks extends well into near-infrared wavelengths, which means that an accretion disk does not truncate even at a few thousands of R_S (e.g., Kishimoto et al., 2005; Tomita et al., 2006; Kishimoto et al., 2007, 2008b; Hönig & Kishimoto, 2010; Hao et al., 2010; Lira et al., 2011; Koshida et al., 2014; Oknyansky et al., 2014, and references therein). Therefore, we fix the disk outer radius as $x_{\text{out}} = 2^{16}$ for convenience of the model calculations. Since emissions from the outer region of the

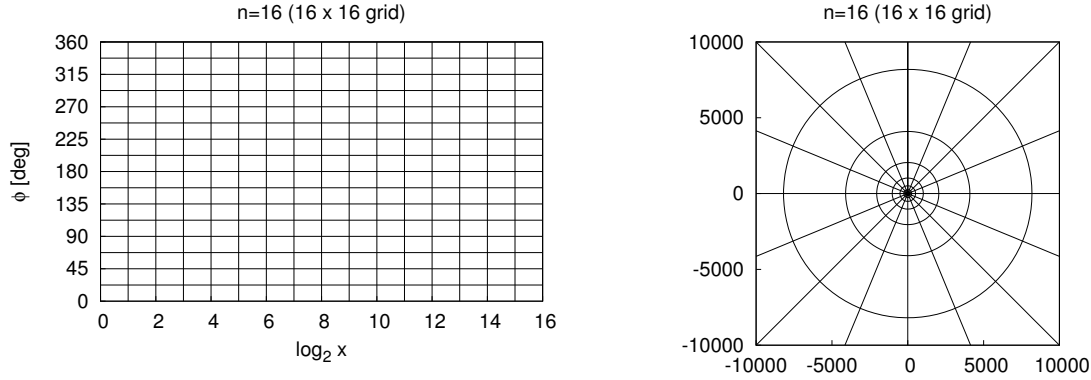


Figure 3.3: An examine of grid of the inhomogeneous disk model in the case of $n = 16$ (i.e., 16×16 grid). The disk with inner and outer radii of $x_{\text{in}} = 1$ and $x_{\text{out}} = 2^{16}$ is divided into $n = 16$ (1×16) zones per factor of 2 in radius (left panel). Right panel shows the grid of the left panel in linear spatial scale.

quasar accretion disk (e.g., $x > 10000$) are negligible in the UV-optical wavelength range, the exact choice of the disk outer radius has little effect on the resulting UV-optical spectra.

Dexter & Agol (2011) and Ruan et al. (2014) calculated inhomogeneous accretion disk model spectra by dividing the disk into n zones per factor of 2 in radius. The zones are log-spaced in r and evenly spaced in ϕ (see Figure 3.3). From an $N \times N$ grid with inner and outer radii of $x_{\text{in}} = 1$ and $x_{\text{out}} = 2^{16}$, the parameter n is given by

$$n = N \frac{\log(2)}{\log(2^{16})} \times N = \frac{N^2}{16}.$$

To cover the whole range of the parameter space suggested by Dexter & Agol (2011) sufficiently (Figure 3.4; i.e., $n = 10-1\ 000$), in this work we consider the cases $n = 16, 64, 144, 256, 400, 576, 784, 1024, 1296, 1600, 1936, 2304, 2704, 3136, 3600$ and 4096 .

In Dexter & Agol's inhomogeneous accretion disk model, disk inhomogeneity is given by adding temperature fluctuations to the effective temperature profile [equation (3.9)] for each zone independently. The common logarithm of the effective temperature of each zone $T_{\text{eff}}(x)$ is assumed to undergo a damped random walk (DRW) (Equation 1.12; e.g., Kelly et al., 2009; Kozłowski et al., 2010; MacLeod et al., 2010; Hernitschek et al., 2015) with an amplitude σ_T (in the unit of $\log T_{\text{eff}}$); Based on Equation 1.12, the DRW of the effective temperature ($\log T_{\text{eff}}^{\text{DRW}}(x, \phi)_i$) is expressed as

$$\log T_{\text{eff}}^{\text{DRW}}(x, \phi)_i - \mu(x) = \alpha_{\text{AR}} \left(\log T_{\text{eff}}^{\text{DRW}}(x, \phi)_{i-1} - \mu(x) \right) + \varepsilon_i, \quad (3.11)$$

where

$$\varepsilon_i \sim G(\sigma_{\text{AR}}^2) \quad (3.12)$$

$$\sigma_{\text{AR}}^2 = \sigma^2 \left(1 - \exp \left(-\frac{2(t_i - t_{i-1})}{\tau_{\text{damp}}} \right) \right). \quad (3.13)$$

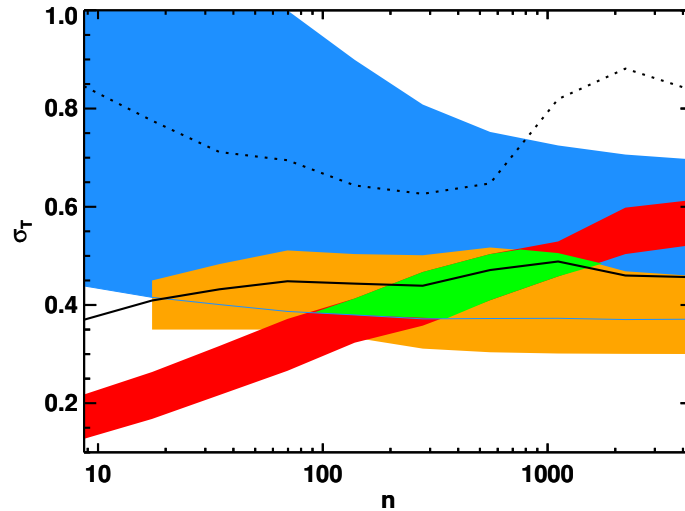


Figure 3.4: Observational constraints (68% regions) on the inhomogeneous disk model parameters σ_T and n ; the constraints are from microlensing (blue), variability (red), and spectral (orange) observations. The combined constraint is coloured green. Solid and dotted lines represent the parameter values with which the rms deviations between the inhomogeneous disk model and best-fit power-law disk model microlensing light curves at 2500\AA become 1% and 2%, respectively (the inhomogeneous disk model predicts short timescale deviations from smooth power-law disk models in microlensing light curves). This figure is taken directly from Figure 5 of Dexter & Agol (2011).

$\mu(x)$ represents the common logarithm of the mean effective temperature at x . In the limit $n \rightarrow \infty$, the damped random walk model becomes time independent with a log-normal distribution of disk temperatures in each annulus whose variance is $(\ln 10 \sigma_T)^2/2$ [equation (2) of (Dexter & Agol, 2011)]. The definition of σ_T in Dexter & Agol (2011) (see also Dexter & Quataert, 2012) is related to σ as $\sigma \equiv \sigma_T/\sqrt{2}$. It should also be noted that $\mu(x)$ is taken not to be the stationary disk value $\log T_{eff}(x)$ given in Equation 3.9) but to be

$$\mu(x) \equiv \ln T_{eff}(x) - \frac{(\ln 10 \sigma_T)^2}{2} \quad (3.14)$$

to correct for the shift of the mean temperature of the log-normal temperature distribution of T_{eff}^{DRW} . As assumed in Dexter & Agol (2011) and Ruan et al. (2014), the characteristic decay timescale of the temperature fluctuations τ_{damp} is fixed to be 200 d, although the results are insensitive to the choice of τ_{damp} (Dexter & Agol, 2011).

We tested our own simulation code of the inhomogeneous disk model against the relative variability $\sigma_{L_v}/\langle L_v \rangle$ vs. σ_T relation given in Figure 2 of Dexter & Agol (2011). As shown in Figure 3.5, the $\sigma_{L_v}/\langle L_v \rangle$ vs. σ_T relation obtained by our code and that presented by Dexter & Agol (2011) are in good agreement⁴.

⁴There is a typo in Equation 1 of Dexter & Agol (2011); the correct form of the fitting formulas for the $\sigma_{L_v}/\langle L_v \rangle$

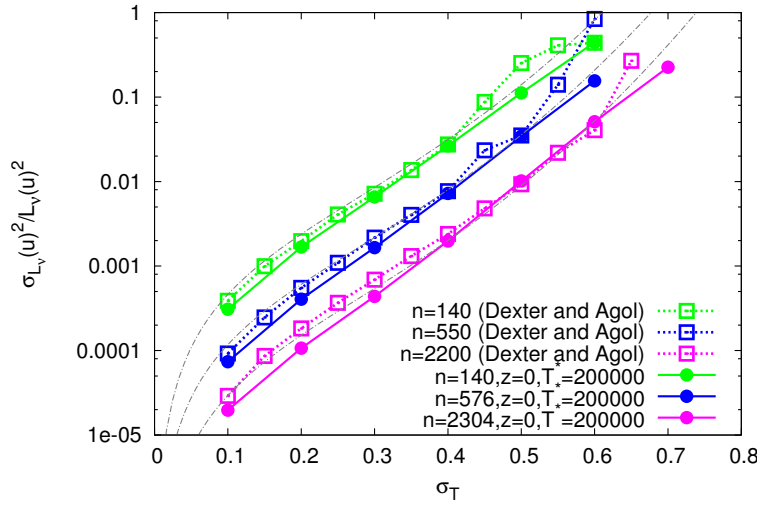


Figure 3.5: Comparisons of the $\sigma_{L_v} / \langle L_v \rangle$ vs. σ_T relation obtained by our own code and that presented by Dexter & Agol (2011) for the purpose of testing of our code. Empty squares are the data from Figure 2 of Dexter & Agol (2011), and the filled circles are calculated from our own simulation code (u -band, redshift=0, $T^* = 200000$ K). The gray dash-dot lines indicate the fitting formulas for the $\sigma_{L_v} / \langle L_v \rangle$ vs. σ_T relation presented in Equation 1 of Dexter & Quataert (2012).

3.4.2 Simulating the SDSS Stripe 82 quasar light curves

The Dexter & Agol inhomogeneous accretion disk model is characterized by two model parameters, n and σ_T , which represent the number of separated zones in an annulus of the disk and the amplitude of temperature fluctuations, respectively. In addition to these two parameters, the spectral shape depends on a physical parameter, T^* (Chapter 2). The quasar redshift z determines which of the rest-frame wavelengths fall on to the broad-band filters. In summary, there are four model parameters in our model calculations: n , σ_T , T^* , and redshift z . Dexter & Agol (2011) concluded that, for quasar accretion disks, the two parameters n and σ_T should be in the range of $n = 100$ – $1\,000$ and $\sigma_T = 0.35$ – 0.50 to fit several observational constraints, including microlensing accretion disk size measurements, quasar UV spectral shape and the UV-optical variability amplitude (see Section 3.1). Ruan et al. (2014) showed that the composite difference spectrum of the SDSS quasars can be fitted by the Dexter & Agol inhomogeneous accretion disk model with the same parameter ranges as Dexter & Agol (2011). We decide to explore the parameter space of $16 \leq n \leq 4096$ and $0.1 \leq \sigma_T \leq 0.6$, which sufficiently covers the whole range of the parameter space suggested by Dexter & Agol (2011).

The parameters T^* and z are taken to represent the SDSS Stripe 82 data. For the SDSS quasars, the parameter T^* ranges from 50 000 K to 200 000 K (Figure 2.12; see also Ruan et al., 2014). The redshift z is taken to be $z < 1.5$ for u - g , u - r , u - i and u - z band pairs; $z < 2.0$ for g - r , g - i and g - z band

vs. σ_T relation is $\frac{\sigma_{L_v}^2}{\langle L_v \rangle^2} \simeq \frac{3}{8n} (e^{3(\ln 10 \sigma_T)^2} - 1) \sim \frac{3}{8n} (e^{16\sigma_T^2} - 1)$ (J. Dexter, private communication). This typo is corrected in Dexter & Quataert (2012), and Figure 3.5 shows the corrected formulas.

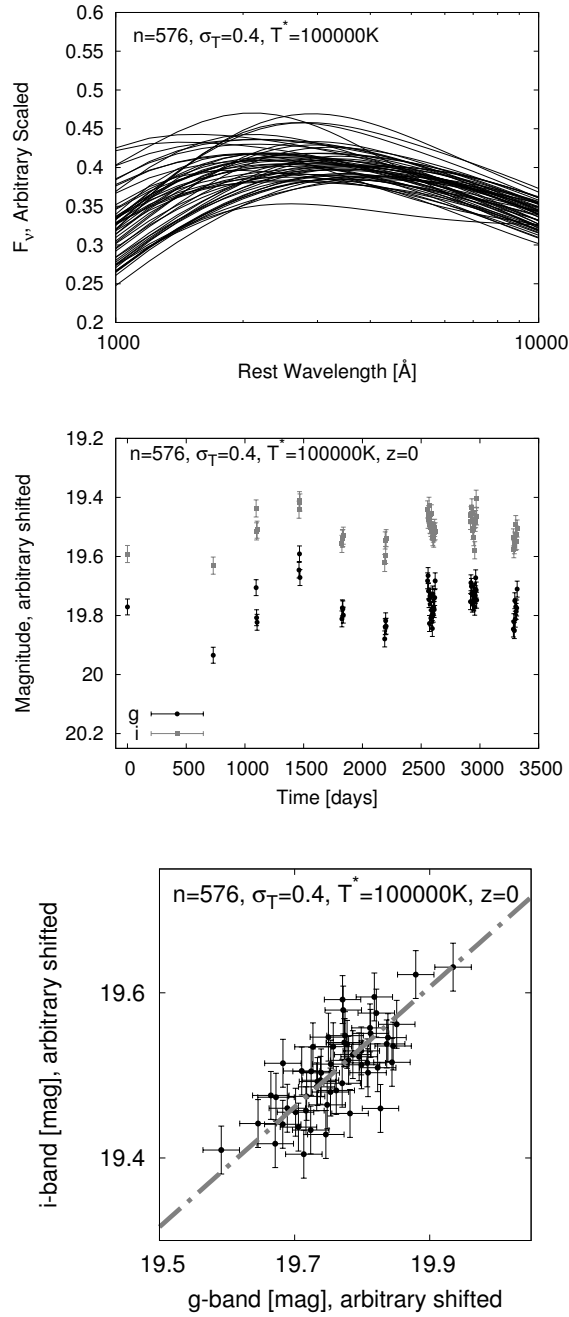


Figure 3.6: Top: A single realization of the 10-yr model spectral time series, assuming $\sigma_T = 0.40$, $n = 576$ and $T^* = 100000$ K. Middle: g - and i -band model light curves obtained from the spectral time series shown in the top panel, assuming $z = 0$, $\sigma_g = 0.027$ mag and $\sigma_i = 0.029$ mag. Bottom: Model magnitude–magnitude plot of the g - i band pair light curve shown in the middle panel. The straight line indicates the linear regression line drawn using `LINMIX_ERR`.

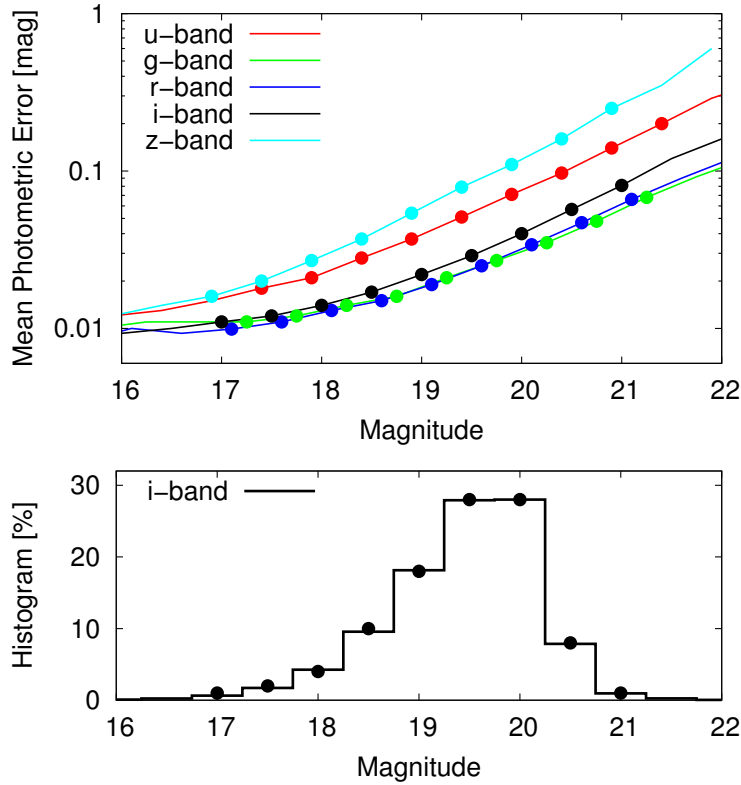


Figure 3.7: Mean photometric errors of the SDSS Stripe 82 quasar light curves as a function of the magnitude (upper panel), and a histogram of the *i*-band magnitudes of the quasar light curves (lower panel). The photometric errors and the percentages of the assignment into nine groups assumed in the model calculations (listed in Table 3.2) are shown as points in the upper and the lower panels, respectively (see Section 3.4.2 for details).

pairs; $z < 3.5$ for *r*-*i* and *r*-*z* band pairs; and $z < 4.5$ for the *i*-*z* band pair (see Section 3.3).

For a fair comparison between the Dexter & Agol inhomogeneous disk model and the SDSS Stripe 82 quasar light curves, we have to calculate mock light curves that adequately model the actual SDSS Stripe 82 data. The number of measurement points and their sampling intervals assumed in the model light curves are determined to make them similar to the average SDSS Stripe 82 light curve; i.e., we assume that we have 10 yr of light curves with 1, 0, 1, 3, 3, 4, 4, 17, 14 and 9 measurement points in each of the 10 yr (56 points in total), and the sampling interval within each of the years is fixed to 4 d (see the middle panel of Figure 3.6) (e.g., Sako et al., 2014). In the actual SDSS Stripe 82 data, the first 7 yr are the runs obtained as part of the SDSS-I Legacy survey (Adelman-McCarthy et al., 2007), and the last 3 yr correspond to the SDSS-II Supernovae project runs (Frieman et al., 2008).

Moreover, for a fair comparison between the model and the data, Gaussian photometric errors are added to the model light curves and the same linear regression method (i.e., LINMIX_ERR) is applied to the photometric error-added model magnitude–magnitude plots. We calculate the 100 realizations

of the model five-band light curves for each of the parameter sets (n, σ_T, T^*, z) , and then divide them into nine groups and assign the Gaussian photometric errors to each of the nine groups as tabulated in Table 3.2. The photometric errors and the percentages of the assignment into nine groups are determined to make them comparable to the histogram of the photometric errors of the SDSS Stripe 82 quasar light curves. Figure 3.7 shows the mean photometric errors of the SDSS Stripe 82 quasar light curves as a function of the magnitude. First, nine representative values of the photometric errors for the i -band (black points in the upper panel of Figure 3.7) are sampled according to the histogram of the i -band magnitudes of the quasar light curves rounded to a whole number (black points in the lower panel of Figure 3.7). The percentages of the assignment into nine groups are fixed to those of the i -band values (black points in the lower panel of Figure 3.7), as listed in the last row of Table 3.2. Then, the i -band magnitude histogram is shifted in the magnitude direction assuming the mean quasar spectral index of $f_\nu \propto \nu^{-0.5}$ (Vanden Berk et al., 2001), and the photometric errors for the u -, g -, r - and z -bands are sampled according to the shifted histograms (upper panel of Figure 3.7)⁵. The values of the photometric errors assumed in the model light curves for each of the nine groups are listed in Table 3.2. Each of the light curves is assumed to have fixed values of photometric errors; i.e., we ignore the changes in photometric errors within each of the light curves. Finally, we apply the same exclusion criteria for the simulated light curves as those for the SDSS Stripe 82 data described in Section 3.3.

It should be noted that the assumed values of the sampling numbers and the sampling intervals described above do not have significant impacts on the regression results, since the detailed information of the sampling cadence is essentially abandoned in the linear regression analyses in magnitude–magnitude space. Moreover, since LINMIX_ERR includes the proper models of the Gaussian photometric errors, the exact values of the assumed photometric errors also do not significantly affect the regression results.

The top panel of Figure 3.6 shows a single realization of the 10 yr model spectral time series, assuming $\sigma_T = 0.40$, $n = 576$ and $T^* = 100\,000$ K. As expected, the superposition of independent temperature fluctuations on the accretion disk makes the spectral shape of the model spectra highly variable. The middle panel of Figure 3.6 shows the g - and i -band model light curves obtained from the spectral time series shown in the top panel of Figure 3.6, assuming $z = 0$, $\sigma_g = 0.027$ mag and $\sigma_i = 0.029$ mag, where σ_g and σ_i are the assumed photometric errors. The bottom panel of Figure 3.6 shows the resulting regression line for the g - i band pair magnitude–magnitude plot of the two-band light curves of the middle panel. A quantitative discussion on the linear regression results for various values of model parameters are given in the next section.

⁵The mean photometric errors of the SDSS Stripe 82 data derived here (Figure 3.7) are roughly consistent with those derived by, e.g., Ivezić et al. (2007); Kozłowski (2016b,a).

3.5 Comparison of the Inhomogeneous accretion disk Model with Observational Data

Figure 3.8 shows the intrinsic scatter σ_{int} versus variability amplitude V for the Dexter & Agol inhomogeneous accretion disk model for the g - i band pair, for various values of σ_T in 0.1 increments (upper panel), and for various values of $n = 16, 144, 1024$ and 4096 (bottom panel). Since large temperature fluctuations lead to large flux variability, the variability amplitude V becomes larger when σ_T becomes larger. On the other hand, since the sum of a large number of independent fluctuations lessens the stochastic behaviour, the variability amplitude becomes smaller when n becomes larger [see equation (1) of Dexter & Agol (2011); Dexter & Quataert (2012)]. In the upper panel of Figure 3.8, it is apparent that there are fewer points for smaller values of σ_T ; this is because we have excluded the model light curves whose flux variability is smaller compared to the assumed photometric errors (see Sections 3.3 and 3.4.2).

In Figure 3.8, the intrinsic scatter σ_{int} is only slightly smaller than the variability amplitude V (i.e., $\sigma_{\text{int}} \lesssim V$), which means that the Dexter & Agol inhomogeneous accretion disk model predicts a weak magnitude–magnitude correlation. Moreover, as we can see in Figure 3.8, the σ_{int} - V relation for various values of σ_T and n follows a linear track from left bottom to top right, which indicates that the weakness of the magnitude–magnitude correlation is kept for the whole of the model parameter space considered here. Since (as shown in Figure 3.8) the model values of σ_{int} and V for various model parameters are confined within a certain locus in σ_{int} - V space, and we are not interested in the details of the model parameter dependence of them, hereafter we refer to the σ_{int} - V relation of the Dexter & Agol inhomogeneous accretion disk model as the region in the σ_{int} - V space defined by all the model values of σ_{int} and V for all the values of the model parameters, as described below.

Figure 3.9 shows the intrinsic scatter σ_{int} versus variability amplitude V for the Dexter & Agol inhomogeneous accretion disk model and the SDSS Stripe 82 data for all of the band pairs, expressed as contours; the solid red lines are the 1σ (68.2 per cent, inner dashed line) and the 2σ (95.4 per cent, outer dashed line) contours of the model σ_{int} - V relation for the whole of the parameter space: $0.1 \leq \sigma_T \leq 0.6$ (in 0.1 increments), $16 \leq n \leq 4096$, $T^* = 50\,000, 100\,000$ and $200\,000$ K, and the specific redshift range for each of the band pairs. The solid green lines are the same as the red lines but for the restricted parameter space comparable with Dexter & Agol’s constraints on σ_T and n : $0.35 \leq \sigma_T \leq 0.50$ (in 0.05 increments) and $144 \leq n \leq 1024$. The black dashed lines are the same as Figure 3.2; i.e., the 1σ and the 2σ contours of the σ_{int} - V relation of the SDSS Stripe 82 data.

As expected, the inhomogeneous accretion disk model predicts that a tighter magnitude–magnitude correlation (i.e., smaller values of σ_{int}) can be achieved if we take band pairs with shorter separations of the wavelengths (see $\Delta\lambda_{\text{rest}}$ listed in Table 3.1), namely u - g , g - r , r - i and i - z . Actually, if we only focus on the band pairs u - g , g - r , r - i and i - z , the model σ_{int} - V relation seems to be consistent with the observed σ_{int} - V relation. However, we should note the discrepancy in σ_{int} between the model and the data gets clearer for band pairs with longer separations of the effective wavelengths; in particular, for

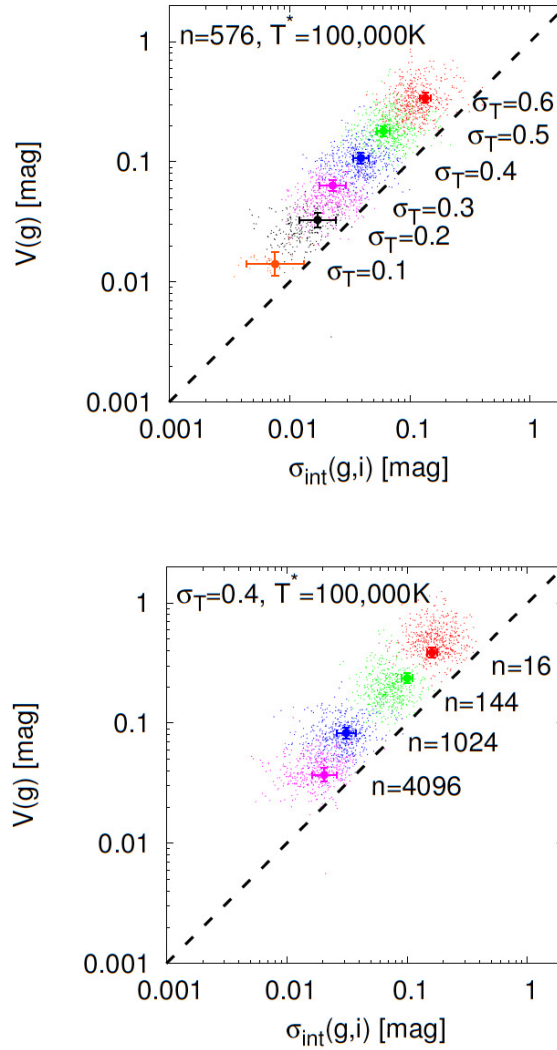


Figure 3.8: Intrinsic scatter σ_{int} versus variability amplitude V for the Dexter & Agol inhomogeneous accretion disk model for $g-i$ band pairs (dots in different colours). Coloured points with error bars are the randomly selected points of σ_{int} and V to indicate the typical values of uncertainty in the point estimates. Top: $\sigma_{\text{int}}-V$ relation for various values $0.1 \leq \sigma_T \leq 0.6$ (in 0.1 increments; in different colours). All redshifts, $z = 0.0, 0.5, 1.0, 1.5$ and 2.0 , are plotted simultaneously, and the other model parameters are fixed to $n = 576$ and $T^* = 100\,000$ K. There are fewer points for smaller values of σ_T because we have excluded the model light curves whose flux variability is smaller compared to the assumed photometric errors (see Sections 3.3 and 3.4.2 for details). Bottom: The same as the top panel, but for various values $n = 16, 144, 1024$ and 4096 (in different colours). The other model parameters are fixed to $\sigma_T = 0.4$ and $T^* = 100\,000$ K. A thin straight line in each of the panels indicates $\sigma_{\text{int}} = V$.

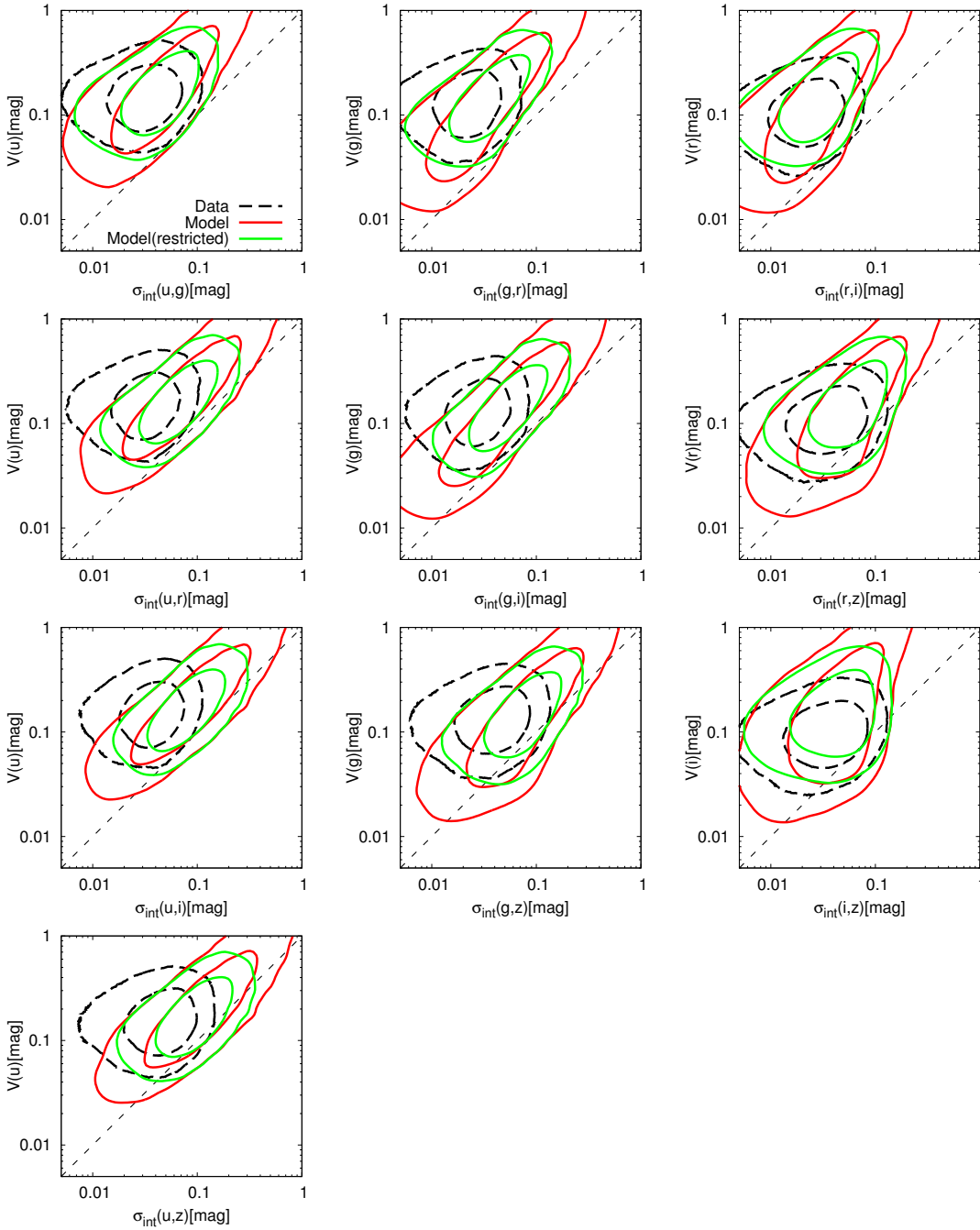


Figure 3.9: Intrinsic scatter σ_{int} versus variability amplitude V for the Dexter & Agol inhomogeneous accretion disk model and the SDSS Stripe 82 data for all of the band pairs. The solid red lines are the 1σ (68.2 per cent) and the 2σ (95.4 per cent) contours of the model $\sigma_{\text{int}}-V$ relation for the whole of the parameter space: $0.1 \leq \sigma_T \leq 0.6$ (in 0.1 increments), $16 \leq n \leq 4096$, $T^* = 50\,000, 100\,000$ and $200\,000$ K, and the specific redshift range for each of the band pairs. The solid green lines are the same as the red lines but for the restricted parameter space comparable with Dexter & Agols constraints on σ_T and n : $0.35 \leq \sigma_T \leq 0.50$ (in 0.05 increments) and $144 \leq n \leq 1024$. The black dashed lines are the same as Figure 3.2; i.e., the 1σ and the 2σ contours of the $\sigma_{\text{int}}-V$ relation of the SDSS Stripe 82 data. A thin dashed straight line in each of the panels indicates $\sigma_{\text{int}} = V$.

the $u-i$, $u-z$ and $g-z$ band pairs, the model-predicted regions cover only a part of the data regions, and the data generally show smaller values of σ_{int} than those of the model for comparable values of V .

To see the discrepancy more clearly, in Figure 3.10 we show the 1σ ranges of V and σ_{int} for the SDSS Stripe 82 data and for the Dexter & Agol inhomogeneous accretion disk model as a function of the filter combination, obtained by projecting the two-dimensional distributions of σ_{int} and V (shown in Figure 3.9) on to the V - and σ_{int} -axes, respectively. Since in Figure 3.9 and the upper panel of Figure 3.10 we can see that the variability amplitudes V of the SDSS Stripe 82 quasars are well reproduced by the inhomogeneous accretion disk model with restricted model parameter space comparable with Dexter & Agol's constraints [this verifies the consistency between model calculations by us and Dexter & Agol (2011)], in Figure 3.10 we show only the results of the model calculations with the restricted model parameters. As mentioned above, we can clearly see in Figure 3.10 that the difference for σ_{int} between the data and the model predictions becomes larger when the wavelength separation becomes larger, and the data show smaller values of σ_{int} than those of the model. For the band pairs $u-i$, $u-z$ and $g-z$, $\sigma_{\text{int}}(\text{model}) > \sigma_{\text{int}}(\text{data})$ is satisfied for about half of the SDSS Stripe 82 quasars, and this discrepancy cannot be reduced by simply adjusting the model parameters in the Dexter & Agol inhomogeneous accretion disk model. A Kolmogorov–Smirnov test reveals that the difference between the data and the model distributions of σ_{int} for the $u-z$ band pair is statistically significant, and confirms that the null hypothesis (the data are drawn from the model distribution) is rejected even at the level of significance $\alpha = 0.001$. It should be noted that, as mentioned in Section 3.2, $\sigma_{\text{int}}(\text{data})$ evaluated by the broad-band quasar light curves is contaminated by the flux variation of the broad emission lines and the Balmer continuum emission, thus the true values of σ_{int} (i.e., the intrinsic scatter of the magnitude–magnitude correlation of the pure accretion disk continuum emission) must be much smaller than those observed.

These results verify the intuition mentioned in Section 3.1; i.e., Dexter & Agol's inhomogeneous accretion disk model cannot explain the coherent flux variation within the UV-optical wavelength range often observed in quasar light curves.

3.6 Discussion and Conclusions of Chapter 3

In this work, we have examined the validity of the inhomogeneous accretion disk model presented by Dexter & Agol (2011) in the light of the quasar UV-optical spectral variability. As assumed in the Dexter & Agol inhomogeneous accretion disk model, because the quasar accretion disks have a large physical size, the several years' temperature fluctuations occurring at different radii of the quasar accretion disks must be causally unconnected. Observationally, this property of the inhomogeneous accretion disk model ought to result in a weak inter-band magnitude–magnitude correlation within the UV-optical wavelength range (see, e.g., Pereyra et al., 2006; Gaskell, 2011). We have used a large sample of long-term (approximately several years), simultaneous five-band light curves of quasars in the SDSS Stripe 82 region to evaluate intrinsic scatter $\sigma_{\text{int}}(\text{data})$ in magnitude–magnitude space,

and compared $\sigma_{\text{int}}(\text{data})$ with the Dexter & Agol inhomogeneous accretion disk model predictions of the intrinsic scatter $\sigma_{\text{int}}(\text{model})$. We have shown that, especially for the two-band light curves for the u - i , u - z and g - z band pairs, $\sigma_{\text{int}}(\text{model})$ is generally larger than $\sigma_{\text{int}}(\text{data})$ for comparable values of variability amplitude V (Figure 3.9 and Figure 3.10), which indicates that the Dexter & Agol inhomogeneous accretion disk model cannot explain the tight inter-band correlation often observed in the quasar light curves within the UV-optical wavelength range. This result indicates that the local temperature fluctuations in the accretion disks are not the main driver of the several years' UV-optical variability of quasars, and the assumption of a strongly inhomogeneous accretion disk is not preferred from the viewpoint of UV-optical spectral variability.

This conclusion seems to be inconsistent with that obtained by Ruan et al. (2014), in the sense that they concluded that the Dexter & Agol inhomogeneous accretion disk model accounted well for the spectral variability of SDSS quasars. However, as we have already mentioned in Section 3.1, the difference between our result and that of Ruan et al. (2014) is the expected one: Ruan et al. (2014) compared a geometric mean composite difference spectrum of the SDSS quasars with geometric mean composite difference model spectra, thus the model-predicted incoherent inter-band flux variations were smeared out. Because in our analyses the coherence of inter-band flux variations for each individual quasar is compared with each individual time series realization of the model, we can confidently confirm that it is difficult to explain the coherent flux variation within the UV-optical wavelength range in each individual quasar by the Dexter & Agol inhomogeneous accretion disk model.

Moreover, it should be noted that employing unexpectedly higher-temperature flares than considered here cannot settle the problem. If the blackbody flares always have a very high temperature ($\gg 100\,000$ K), the resulting UV-optical spectral variability would show a strong inter-band correlation because the Rayleigh–Jeans tail (i.e., a power-law spectrum with $\alpha_{\nu} = 2$) would dominate the whole of the UV-optical wavelength range. However, as shown in Chapter 2, the observed color of the quasar variable components ($\alpha_{\nu}^{\text{diff}} \sim 1/3$) is, generally, significantly redder than that of the Rayleigh–Jeans spectrum (see also Pereyra et al., 2006; Ruan et al., 2014), which indicates that high-temperature blackbody flares also cannot be the main driver of the quasar UV-optical variability.

Our study clarifies the importance of exploring the variability models, which can simultaneously explain the general properties of the several years' AGN variability, namely, the large variability amplitude and the tight inter-band correlation within the UV-optical wavelength range. As has already been noted in Section 2.7, one of the possibilities is the reprocessing model, which assumes the AGN UV-optical variability is caused by reprocessing of X-ray or extreme UV emission (e.g., Krolik et al., 1991). Since the fluctuations of this higher-energy photon flux, originating from the innermost region of the accretion disk, propagate from inner to outer radii in the light-crossing time, the reprocessing model can explain the several years' tight inter-band correlation within the UV-optical wavelength range (see Uttley & Casella, 2014, for review).

The reprocessing model predicts that the flux variation occurs at the UV wavelengths prior to the optical wavelengths with a time lag of a few hours (depending on the size of the accretion disk) (e.g.,

Collier et al., 1999; Cackett et al., 2007). On the other hand, mass accretion fluctuations propagate from outer to inner radii in the accretion disk, which means that the flux variations caused by the mass accretion fluctuations occur at the optical (longer) wavelengths prior to the UV (shorter) wavelengths (e.g., Arévalo et al., 2008; Uttley & Casella, 2014). Within the UV-optical wavelength range, the inter-band time delay of the AGN continuum for several AGNs are reported to be as expected in the reprocessing model (e.g., Collier et al., 1999; Sergeev et al., 2005; Suganuma et al., 2006; Czerny & Janiuk, 2007; Cackett et al., 2007; Goicoechea et al., 2012; Chelouche, 2013; Lohfink et al., 2014; Shappee et al., 2014; McHardy et al., 2014; Edelson et al., 2015; Jiang et al., 2016b), although results from different observing campaigns are conflicting (see, e.g., Nandra et al., 1998; Uttley, 2006). Moreover, several authors have pointed out that the X-ray luminosity of AGNs is insufficient to power the large UV-optical variability amplitude (e.g., Antonucci et al., 1996; Gaskell, 2008; Edelson et al., 2014; Uttley & Casella, 2014). Obviously, further observational studies are needed to test these models.

Finally, we should note that in this work we only focus on the long-term (i.e., several years) spectral variability of quasars. It is possible that the long-term and the short-term (several days) variabilities are driven by totally different physical mechanisms; there remains a possibility that the short-term AGN variability (with small variability amplitude) may be caused by some kind of local activity in AGN accretion disks (e.g., Collier & Peterson, 2001; Czerny et al., 2008; Voevodkin, 2011; Ai et al., 2013; Choi et al., 2014; Graham et al., 2014; Sun et al., 2014; McHardy et al., 2014; Edelson et al., 2014; Cai et al., 2016; Liu et al., 2016; Zhu et al., 2016, and references therein). To clarify the true nature of the AGN accretion disks, it is crucial to obtain the multi-epoch dense-time sampling and multi-wavelength light curve data for a large sample of AGN/quasars. Ongoing and future wide and deep time-domain surveys, such as the Palomar Transient Factory, the Panoramic Survey Telescope & Rapid Response System, the Dark Energy Survey, SDSS-IV Time-Domain Spectroscopic Survey and Large Synoptic Survey Telescope (Ivezic et al., 2008), will motivate the multi-epoch and multi-wavelength monitoring campaigns for AGN/quasars. These observations will clarify the nature of the short- and long-term X-ray-UV-optical-near-infrared correlations, and consequently, of the AGN/quasar accretion disk physics.

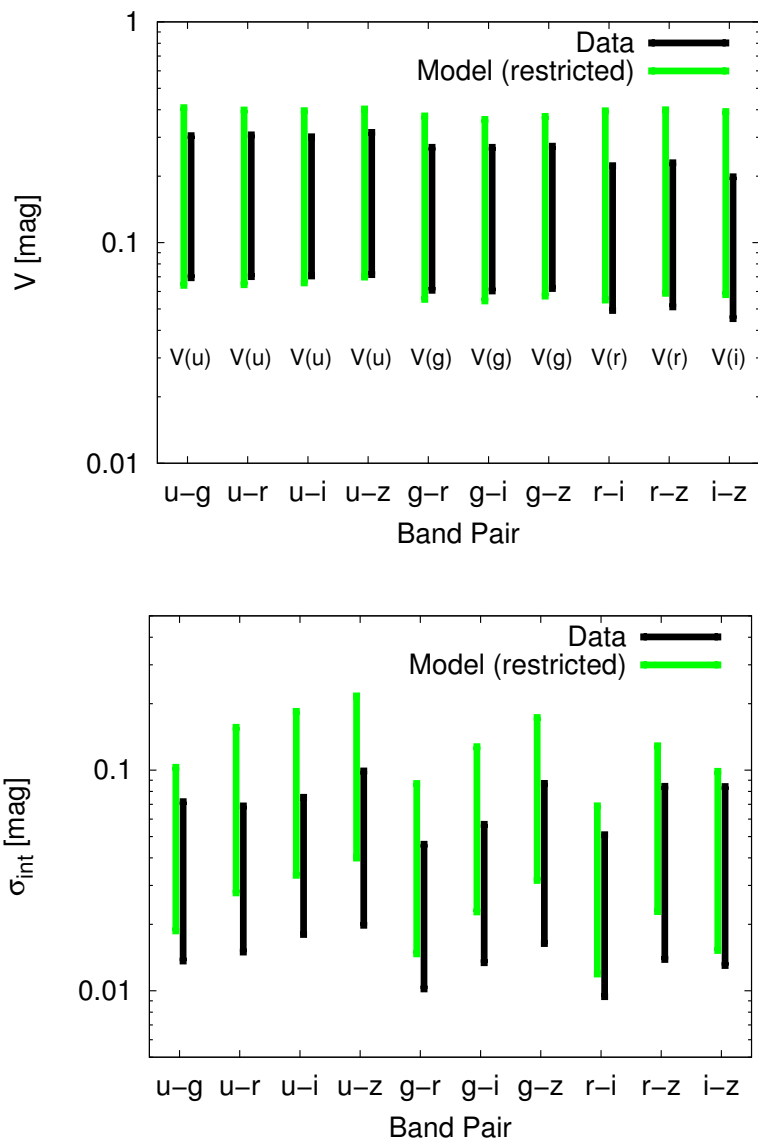


Figure 3.10: 1σ ranges of V (upper panel) and σ_{int} (lower panel) for the SDSS Stripe 82 data (black) and for the Dexter & Agol inhomogeneous accretion disk model with the restricted parameter space (green) as a function of the filter combination, obtained by projecting the two-dimensional distributions of σ_{int} and V (shown in Figure 3.9) on to the V - and σ_{int} -axes, respectively.

Chapter 4

The Relationship between Variable and Polarized Optical Spectral Components of Luminous Type 1 Non-Blazar Quasars¹

Abstract of Chapter 4

Optical spectropolarimetry carried out by Kishimoto et al. (2004) has shown that several luminous type 1 quasars show a strong decrease of the polarized continuum flux in the rest-frame near-ultraviolet wavelengths of $\lambda < 4000\text{\AA}$. In the literature, this spectral feature is interpreted as evidence of the broadened hydrogen Balmer absorption edge imprinted in the accretion disk thermal emission due to the disk atmospheric opacity effect. On the other hand, the quasar flux variability studies have shown that the variable continuum component in UV-optical spectra of quasars, which is considered to be a good indicator of the intrinsic spectral shape of the accretion disk emission, generally have significantly flat spectral shape throughout the near-ultraviolet to optical spectral range. To examine whether the disk continuum spectral shapes revealed as the polarized flux and as the variable component spectra are consistent with each other, we carry out multi-band photometric monitoring observations for a sample of four polarization-decreasing quasars of Kishimoto et al. (2004) (4C09.72, 3C323.1, Ton 202, and B2 1208+32) to derive the variable component spectra and compare the spectral shape of them with that of the polarized flux spectra. Contrary to expectation, we confirm that the two spectral components of these quasars have totally different spectral shape in that the variable component spectra are significantly bluer compared to the polarized flux spectra. This discrepancy in the spectral shape may imply either (1) the decrease of polarization degree in the rest-frame ultraviolet wavelengths is not indicating the Balmer absorption edge feature but is induced by some unknown absorption or (de)polarization mechanisms, or (2) the ultraviolet-optical flux variability is occurring preferentially at the hot inner radii of the accretion disk and thus the variable component spectra do

¹This Chapter 4, in full, is a reprint of the material as it appears in Publications of the Astronomical Society of Japan, Volume 68, Issue 4, id.52, 2016 (Kokubo, 2016). The dissertation author was the primary investigator and single author of this paper.

not reflect the whole accretion disk emission.

4.1 Contradicting results between polarimetric and variability studies on the intrinsic accretion disk continua of quasars ?

As noted in Section 1.1, one crucial difficulty in studying AGN accretion disks is that the Big Blue Bump (BBB) of the AGN accretion disk UV-optical continua is usually hidden under the so called “Small Blue Bump” (SBB) made up of Balmer continuum and Fe II lines from broad line region (BLR) (Figure 1.4; e.g., Grandi (1982)), and thus it is essentially impossible to quantify intrinsic AGN accretion disk continuum emission (e.g., Kishimoto et al. (2008b)).

In this context, as already mentioned in Section 1.4, optical spectropolarimetry offers a unique way to examine accretion disk emission in quasars; Kishimoto et al. (2003) and Kishimoto et al. (2004) have carried out deep spectropolarimetry for 16 luminous quasars using Keck/LRIS and VLT/FORS1, and confirmed that the polarization of five of these quasars (3C95, Ton 202, B2 1208+32, 3C323.1, and 4C09.72) were confined to the continua, i.e., the BLR emission is depolarized (Figure 4.1) (see also Antonucci (1988); Schmidt & Smith (2000)). Kishimoto et al. interpreted the continuum-confined polarization in these five quasars such that the polarized flux is the accretion disk continuum emission scattered into our line of sight by equatorial electron scattering region inside the BLR, and showed that the spectral shape of the polarized flux spectra of these quasars is consistent with the thermal optically-thick accretion disk model predictions of, e.g., Hubeny et al. (2000) (see Section 1.4 for details). In subsequent works (Kishimoto et al., 2005, 2008b), they further confirmed that the measurements of the near-infrared (NIR) polarized fluxes of the UV polarization-decreasing quasars were consistent with those expected from the power-law extrapolation of the optical polarized flux spectra to the NIR region with the power-law index of $\alpha_\nu = 1/3$, as predicted by the standard picture of the thermal optically-thick accretion disk models (Equation 1.11 Lynden-Bell, 1969; Pringle & Rees, 1972; Shakura & Sunyaev, 1973; Novikov & Thorne, 1973; Hubeny et al., 2000). Although it is currently unclear how common the continuum-confined polarization and its decrease at $\lambda < 4000\text{\AA}$ are for the population of luminous type 1 quasars, these results from the quasar spectropolarimetry, if confirmed, have profound implications for general understanding of the AGN accretion disk physics.

Other than the polarimetry, we should note that (as has already discussed in Chapter 2 and Chapter 3) optical flux variability is also worthy of investigation in connection with the intrinsic spectral shape of the AGN accretion disk spectra. Since the variability amplitude is enormous (typically $\sim 10\text{-}20\%$), the variable component in the AGN UV-optical spectra must be reflecting the main energy source of AGN, namely the accretion disk emission itself (Gaskell, 2008). Moreover, the strong inter-band correlations of the AGN variability indicate that the AGN UV-optical variability is not caused by localized independent fluctuations (having their own temperatures), but is a consequence of some kind of global changes in the accretion disk (Chapter 3). Therefore, it is natural to expect that the spectral shape of AGN accretion disk continuum can be obtained directly as the variable continuum

spectral component (Chapter 2; Pereyra et al. (2006); Li & Cao (2008); Schmidt et al. (2012); Ruan et al. (2014), and references therein). It should be noted that the BLR emission is less variable than the underlying continuum, known as the intrinsic Baldwin effect (Kinney et al., 1990); Wilhite et al. (2005) showed that the BLR emission lines vary at most 20%-30% as much the continuum emission, and, as noted in Chapter 2 (Section 2.6), the low ionization lines of Fe II and Mg II are even less variable than the high ionization lines. Since the flux contribution from the host galaxy and most of the BLR emission is non-variable, the spectral shape of the variable component spectra can be derived without suffering from the heavy spectral distortion by these contaminants.

In the NIR wavelength range, several spectral variability studies suggest that the accretion disk spectra revealed as the variable spectral component has spectral shape as blue as the thermal accretion disk model prediction of $\alpha_\nu = 1/3$ (Tomita et al. (2006); Lira et al. (2011); Koshida et al. (2014), and references therein). In the near-ultraviolet to optical wavelength range, thermal accretion disk models generally predict the spectral turnover to much redder spectral slope (e.g., Kishimoto et al. (2008b)). However, as we have shown in Chapter 2, the variable component spectra of SDSS Stripe82 quasars are well described by the power-law shape with $\alpha_\nu \sim 1/3$ even in the UV-optical wavelength range, and thus are systematically too blue to be explained by the existing thermal accretion disk models even after considering in the flux contamination from the (weakly) variable broad emission lines, Fe II emission lines, and the Balmer continuum emission (see also Schmidt et al. (2012); Ruan et al. (2014), and Figure 4.1). It should also be noted that the strong dip feature at $\lambda < 4000\text{\AA}$ observed in the polarized flux seems to be absent in the composite variable continuum spectrum of SDSS quasars (Wilhite et al., 2005; Pereyra et al., 2006; Ruan et al., 2014). In summary, quasar variability studies suggest that the intrinsic accretion disk spectrum revealed as the variable continuum component cannot be explained by existing accretion disk models.

As summarized above, the results from the two kinds of studies (i.e., spectro-polarimetry and variability studies) seem to be contradicting: on the one hand polarimetric studies suggest that the intrinsic accretion disk spectrum revealed by the spectropolarimetry has a spectral shape consistent with the thermal optically-thick accretion disk model predictions of , e.g., Hubeny et al. (2000), but on the other hand variability studies suggest that the intrinsic accretion disk spectrum obtained as a variable continuum component has too blue ultraviolet spectral shape to be explained by existing accretion disk models. This discrepancy, if confirmed, is a huge problem in that the basic assumptions underlying these observations are related to our fundamental understandings of quasar central engine, and thus definitely offers new insights into the nature of the quasar/AGN BBB emission.

However, we should note that the above statement is currently based on the observations for different quasar samples. Although the quasars in the Kishimoto et al. (2004)'s sample have similar optical spectra with the SDSS quasars (actually B2 1208+32, Ton 202, and 3C323.1 are contained in the spectroscopically-confirmed SDSS quasar catalog; Schneider et al. (2010)), on the one hand the variability studies are based on the general population of several thousands of SDSS quasars, but on the other hand the spectropolarimetric studies are based on the small, and probably biased, sample of quasars (see Schmidt & Smith (2000)). The purpose of this work is to examine the optical

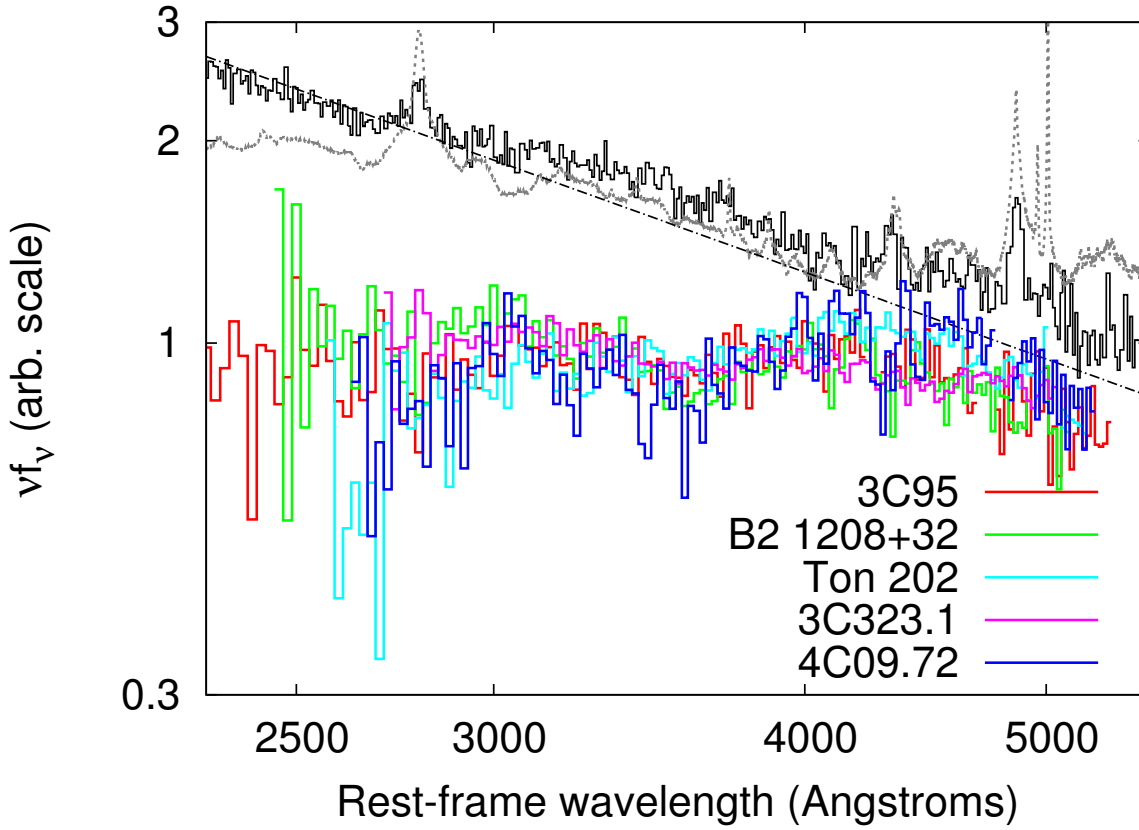


Figure 4.1: Polarized flux spectra for five quasars showing polarization decrease at $\lambda < 4000\text{\AA}$ (Figure 35 of Kishimoto et al. (2004)). For comparison, the composite difference spectrum (i.e., the composite variable component spectrum) generated by using two epoch spectra of the SDSS quasars (Ruan et al., 2014) (the black thin solid line), and the composite spectrum of the SDSS quasars (Vanden Berk et al., 2001) (the gray dashed line) are also shown. The dash-dot line indicates a power-law spectrum with $\alpha_v = +1/3$ (in the unit of $f_v \propto \nu^{\alpha_v}$).

spectral variability for the quasars showing the Balmer edge-like feature in their polarized flux spectra confirmed by Kishimoto et al. (2004), and probe whether or not these quasars also show flat variable component spectra as the other normal quasars or show. Here we present the multi-band optical light curves for four of the five quasars in Kishimoto et al. (2004)’s sample (4C09.72, B2 1208+32, Ton 202, and 3C323.1), and compare the spectral shape of the polarized flux and the variable flux components of them.

This Chapter is organized as follows. In Section 4.2, we present multi-band optical light curves of the four quasars obtained by using the 1.05-meter Kiso Schmidt telescope at the Kiso Observatory in Japan. Then, we derive the variable component spectra for the quasars from the multi-band light curves by using “flux gradient method” in Section 4.3. In Section 4.4, we compare the spectral shape of the variable and polarized component spectra of these quasars in detail (Section 4.4.1), and discuss about the possible interpretations of the relationship between these two spectral components

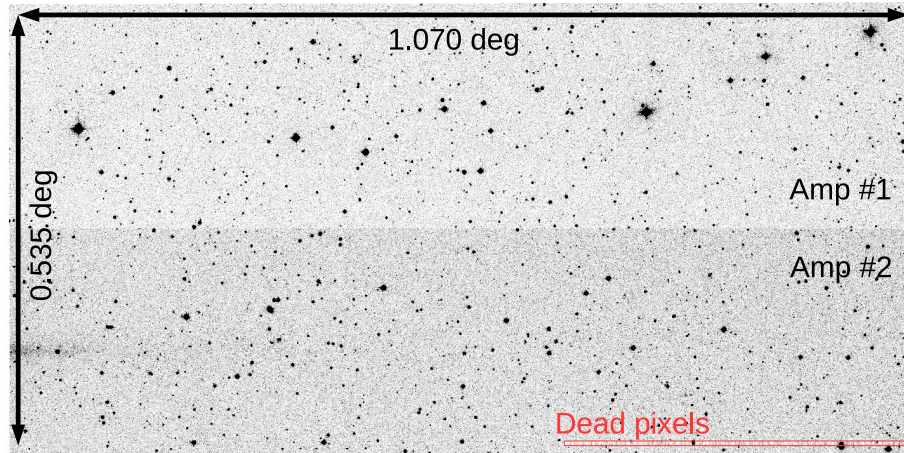


Figure 4.2: An example of the KWFC chip#3 g -band image. Overscan, master-bias, master dome-flat, and super sky-flat corrections has been applied. The difference in level of counts between upper and lower part of the image may reflect the slightly different gain values or different non-linearities associated with the different readout channels (see e.g., Sako et al., 2012; Nakao, 2015).

(Section 4.4.2). Finally, summary and conclusions of this Chapter are given in Section 4.5.

4.2 Multi-band photometric observations with the 1.05-meter Kiso Schmidt telescope

We carried out u , g , r , i , and z -bands photometric monitoring observations for four of the five quasars with polarization dip in $\lambda < 4000\text{\AA}$ in Kishimoto et al. (2004)'s sample (4C09.72, B2 1208+32, Ton 202, and 3C323.1; see Table 4.1) from April 2015 to February 2016, using the 1.05-meter Kiso Schmidt telescope being operated by the Kiso Observatory of the University of Tokyo. The 1.05-meter Kiso Schmidt telescope is equipped with Kiso Wide Field Camera (KWFC; Sako et al. (2012)), which has eight CCD chips (the field of view is 2.2 degree \times 2.2 degree) composed of four CCDs with $2k \times 4k$ pixels manufactured by Lincoln Laboratory, Massachusetts Institute of Technology (MIT) and four ST-002A CCDs with $2k \times 4k$ pixels manufactured by Scientific Imaging Technologies, Inc. (SITE). The average wavelengths of the Kiso/KWFC photometric bands are not precisely known, thus we assume them to be identical with the SDSS imaging camera, i.e., 3551, 4686, 6166, 7480, and 8932 \AA for u , g , r , i , and z -bands, respectively, taken from the SDSS web site² (see also Fukugita et al. (1996); Doi et al. (2010)). The four target quasars are located within the SDSS Legacy survey footprint (York et al., 2000; Gunn et al., 2006) and thus the photometric calibration can be done by using the SDSS photometry data of the field stars on the same frames with the targets³.

²<http://www.sdss.org/instruments/camera/>

³Although we have also been observing the other quasar 3C95 since September 2015, we do not include it in the sample of this work because it is not in the SDSS Legacy survey footprint thus currently the absolute flux calibration

Table 4.1: List of our target quasars with polarization dip in $\lambda < 4000\text{\AA}$.

Name	Coordinate	$E(B - V)$	z	P (per cent) at $2891\text{-}3600\text{\AA}$	P (per cent) at $4000\text{-}4731\text{\AA}$
B2 1208+32	12:10:37.56 +31:57:06.02	0.017	0.388	1.01 ± 0.01	1.41 ± 0.01
Ton 202	14:27:35.60 +26:32:14.55	0.019	0.366	1.25 ± 0.01	1.87 ± 0.02
3C323.1	15:47:43.53 +20:52:16.66	0.042	0.264	1.51 ± 0.01	2.19 ± 0.01
4C09.72	23:11:17.74 +10:08:15.77	0.042	0.433	0.50 ± 0.01	0.93 ± 0.01

The redshift z and polarization degree P (per cent) at two rest-frame wavelength ranges are taken from Table 6 of Kishimoto et al. (2004). The reported values of P for 4C09.72 and 3C323.1 are corrected for the inter stellar polarization effect. The Galactic selective extinction $E(B - V)$ based on Schlegel et al. (1998) is taken from NASA's Extragalactic Database (NED).

Our observations have been carried out in queue mode. In the queue mode, calibration data, i.e., dome flat frames for every filter and bias frames, are usually obtained automatically at the beginning and/or the end of each observing night. Since the dark current of the KWFC CCDs is below $5 e^- [\text{hour}^{-1} \text{pixel}^{-1}]$ at an operation temperature of 168 K (e.g., Sako et al. (2012)), we did not obtain dark frames. The five band images were normally obtained quasi-simultaneously in *giruz* order with four dithering pointing for each band, although the number of the bands and exposures was reduced in several observing nights according to the weather condition. The exposure time for each image was 30 sec for every filter in April-June 2015, and is 60 sec for *g*, *r*, and *i*-band and 120 sec for *u* and *z*-band in July 2015-February 2016.

For the observations presented in this work, we used 2×2 binning four MIT chips FAST readout mode (1.88 arcsec/pixel) to reduce the overhead time, and the targets were acquired on to the MIT chip#3 (named as MIT-4 in Figure 2 of Sako et al. (2012)). Thus, in this work we only reduce and analyse the chip#3 images. The detector temperature is kept to be 167.9-168.0 K during the observations. Each of the $2k \times 4k$ CCDs of KWFC has a dual amplifier readout. During the data reduction, we treat the two readout areas on the chip#3 (upper $1k \times 4k$ and lower $1k \times 4k$ pixels, corresponding the two amplifiers) separately (Figure 4.2). During the data reduction, the gain factor and the readout noise of the chip#3 is assumed to be 2.3 electron/ADU and 15 electrons, respectively, for both of the readout ports. Overscan subtraction for all of the calibration and object frames is carried out by using the column overscan region with the use of IRAF task `colbias`⁴. The master bias frame for each of the observing night is generated by median-combining the overscan-subtracted bias frames taken at the same or the closest night, and is used to correct for the large scale bias pattern. Master dome-flat frames for each of the observing filters are created by median-combining the dome-flat frames taken at the same or the closest night by normalizing the large scale sensitivity and/or illumination pattern with the use of the IRAF task `mkillumflat`. These master dome-flat frames are used to correct for the pixel-to-pixel sensitivity variation of the CCD detector. To correct for the global sensitivity inhomogeneity of the detector, we use super sky-flat frames created by median-combining different nights' object images by masking detected objects by the use of the IRAF task `objmasks`. During the creation of the master dome-flat and super sky-flat calibration frames, the dead pixel lines at the right bottom portion of the chip#3 ($X = 1263-2073$ and $Y = 33-41$ pixel coordinates in the 2×2 binning mode; Figure 4.2) are replaced by linear interpolation along columns by using the IRAF task `fixpix`.

Sky background subtraction, source extraction and aperture photometry for the overscan, bias, and pixel-to-pixel and global flat-fielded object frames were carried out by using SExtractor (version 2.8.6; Bertin & Arnouts (1996)), and coordinate conversion (shifts, pixel scale, and rotation) was carried out by using WCSTools `imwcs` (version 3.8.4; Mink (2006)) and USNO-B1.0 catalog (Monet et al., 2003). Automatically interpolated background-map is calculated and subtracted

cannot be performed. Further observations on this object and the construction of the reference star catalog around it are in progress and will be reported elsewhere.

⁴IRAF is distributed by the National Optical Astronomy Observatory, which is operated by the Association of Universities for Research in Astronomy (AURA) under a cooperative agreement with the National Science Foundation.

from the object frames (namely, we use the SExtractor parameters of `BACK_TYPE=AUTO`, `BACK_PHOTO_TYPE=GLOBAL`, `BACK_SIZE=64`, and `BACK_FILTERSIZE=6`). The dead pixel lines mentioned above are masked during the SExtractor runs. Considering the seeing statistics at the Kiso site (3.9 arcsec FWHM at median in *g*-band; Morokuma et al. (2014)), the extraction aperture is set to 5 pixels (~ 9.4 arcsec). The detection and analysis thresholds are set to be 3σ , where σ is defined as the sum of the photon noise and the readout noise, not including noises introduced by the overscan/bias subtraction and the flat-fielding processes. It should be noted that the target quasars are observed as point-like objects, thus the apparent flux changes due to seeing variations are cancelled by the relative photometry using field stars described below.

The magnitude zero-point shift for each frame was evaluated by taking a 3σ -clipping weighted average of the differences between the instrumental magnitudes and the SDSS model magnitudes (retrieved from the SDSS Data Release 12 (DR12) SkyServer Star view; Alam et al. (2015)) of field stars within the field of view of each of the readout area on the chip#3 (1.076 degrees \times 0.269 degrees). The field stars flagged as CLEAN in the SDSS database were used; for example, the field stars around 3C 323.1 are retrieved from the SDSS DR12 SkyServer using the following SQL (Structured Query Language) query:

```
SELECT ALL u,g,r,i,z,err_u,err_g,err_r,err_i,err_z,ra,dec,clean
FROM Star
WHERE
    ra BETWEEN 235.93142 and 237.93142 AND dec BETWEEN 19.87130 and 21.87130
    AND (clean=1)
    AND g BETWEEN 14.0 and 19.0
```

The object frames with no more than 30 position-matched field stars were excluded from the analysis. It is known that the photometric zeropoints of the SDSS magnitude system are slightly offset from those of the AB magnitude system, thus we apply the recommended offset values of $u_{AB} = u_{SDSS} - 0.04$ mag, and $z_{AB} = z_{SDSS} + 0.02$ mag to our calibrated data, following description in the SDSS website⁵. The magnitude to flux conversion is done by assuming the zero magnitude flux as 3631 Jansky (Jy). Since the color-term correction factors for the KWFC SDSS filters have not been determined, in this work we do not apply the color correction. We also decide not to combine the (mostly single-epoch) SDSS Legacy Survey photometric data for the target quasars with our light curves to avoid the possible systematic error due to the non-correction of the color-term.

The obtained light curves are shown in Table D.1 and plotted in Figure 4.3. The reported magnitude/flux values for a given filter are the weighted averaged values of the dithering images taken at the same nights. The observation epoch for each data point is expressed in the unit of Modified Julian Date (MJD) at the midpoint of the exposures. We confirm that all of the four quasars show flux variability in all five bands during our observations, although the variability amplitude in B2 1208+32 is relatively small compared to the others. The observed variability amplitudes of $\Delta g \sim 0.1$ -0.4 mag within ~ 200 days in the quasar rest-frame are consistent with the general property of the SDSS

⁵<http://www.sdss.org/dr12/algorithms/fluxcal/>

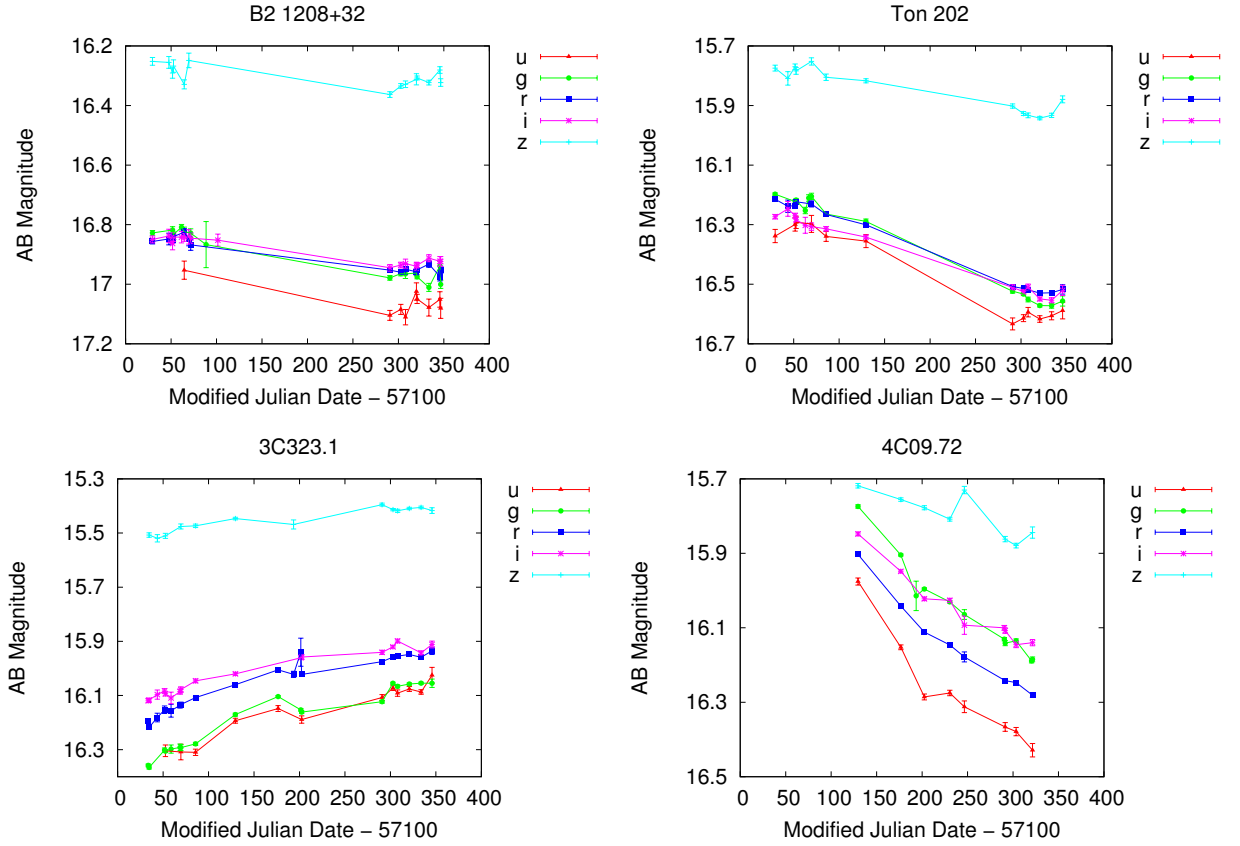


Figure 4.3: u , g , r , i , and z -band light curves of B2 1208+32, Ton 202, 3C323.1, and 4C09.72, obtained at the Kiso observatory. Galactic extinction is not corrected.

quasars (e.g., MacLeod et al. (2012)).

4.3 Deriving the variable component spectra from KWFC data

As we have already mentioned in Chapter 2 and Chapter 3, the flux-flux plots of two-band simultaneous light curves of AGNs and quasar in the UV-optical wavelength range are known to be well fitted by straight lines of $y = a + bx$, which indicates that the variable continuum component in AGNs and quasars keeps its spectral shape nearly constant over several years to several tens of years of the flux variability (Sakata et al. (2010, 2011); Ramolla et al. (2015) and references therein, although see also Sun et al. (2014)). This means that the linear regression slope (gradient) of the flux-flux plot of the quasar two-band light curves can be used as an indicator of the color of the variable component spectrum, since the flux gradient represents the flux ratio of the two-band fluxes of the variable component spectrum (“flux gradient method”; e.g., Choloniewski (1981); Winkler et al. (1992); Hagen-Thorn (1997); Winkler (1997); Glass (2004); Hagen-Thorn (2006); Cackett et al. (2007); Sakata et al. (2010, 2011); Ramolla et al. (2015)). The good point of the flux gradient method is that the regression slope is not affected by the flux contamination from the non-variable spectral components (the

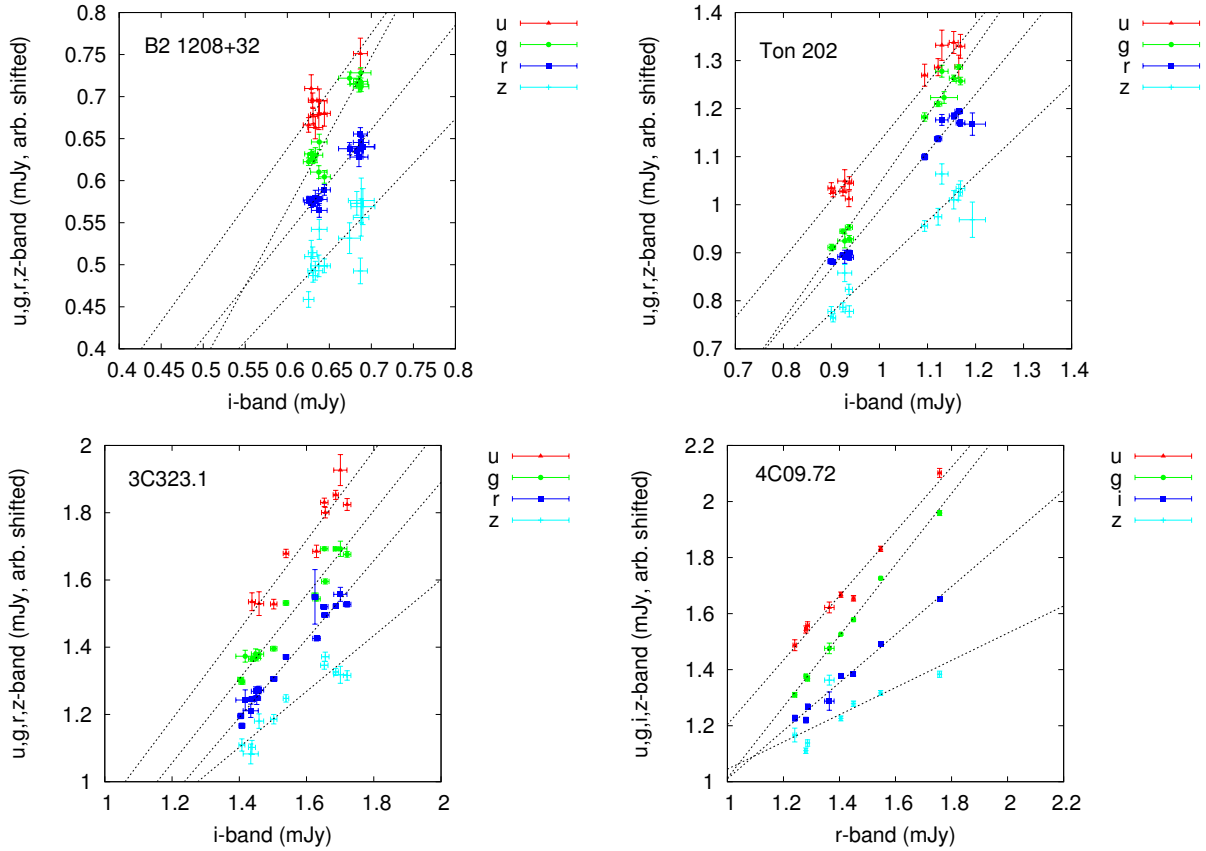


Figure 4.4: Galactic extinction-corrected flux-flux plots of the light curves of B2 1208+32, Ton 202, 3C323.1, and 4C09.72 obtained at the Kiso observatory. The flux values are arbitrarily shifted on the y-axis for clarity.

host galaxy flux and time-averaged flux level of BLR emission). Thus, by applying the flux gradient method to the multi-band light curves, we can derive the relative spectra of the variable component in quasars without suffering from the spectral distortion due to the flux contribution from the non-variable spectral components (see Section 2.3.1) Here we examine the spectral shape of the variable flux component in the four quasars by using the multi-band photometric monitoring data obtained at the Kiso observatory. The two-band simultaneous light curve for each target and for each band-pair is generated by combining the two-band measurements taken at the same nights.

Figure 4.4 shows the flux-flux plots of the light curves of B2 1208+32, Ton 202, 3C323.1, and 4C09.72, overplotted with the best-fit linear regression lines for each band-pair derived by using MPFITEXY IDL routine (Williams et al., 2010). The MPFITEXY routine depends on the MPFIT package (Markwardt, 2009), and is able to cope with the data with intrinsic scatter, which is automatically adjusted to ensure $\chi^2/(\text{degrees of freedom}) \sim 1$ (see Tremaine et al. (2002); Novak et al. (2006); Park et al. (2012) for details). Flux values in Figure 4.4 are corrected for the Galactic extinction (Galactic extinction values for the SDSS filters are taken from NED; Schlegel et al. (1998)). For B2 1208+32, Ton202 and 3C323.1, we choose to use *i*-band flux as the reference of the continuum flux variability

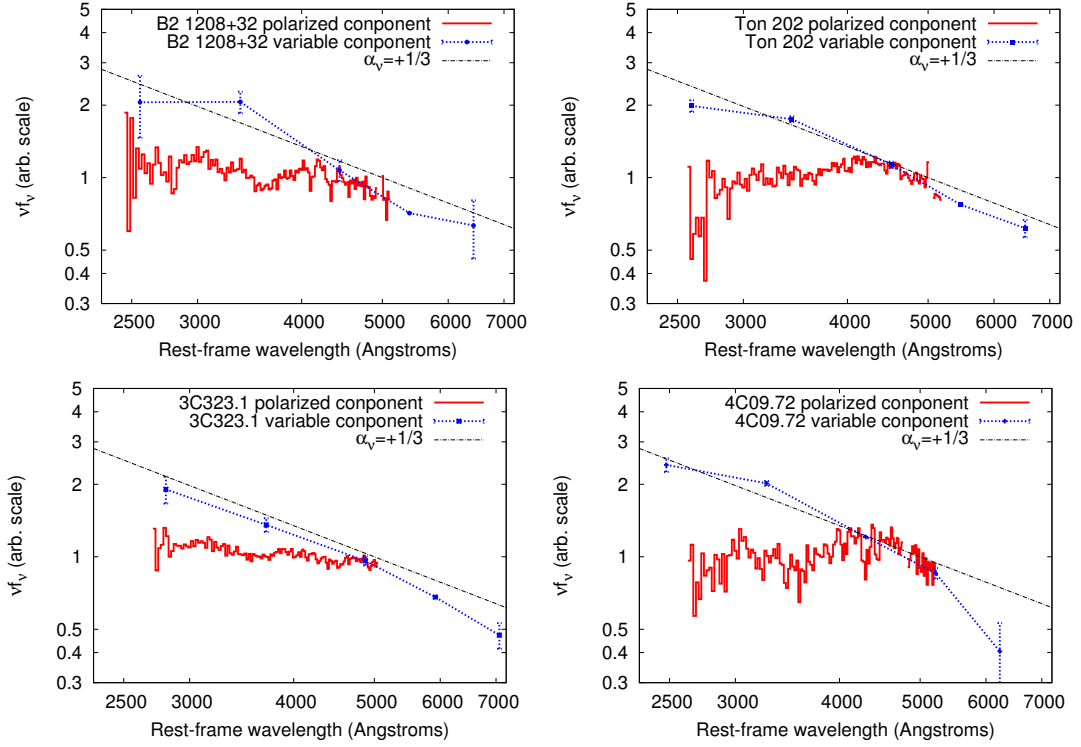


Figure 4.5: Comparison of the spectral shape of the variable and polarized components in the optical spectra of B2 1208+32, Ton 202, 3C323.1, and 4C09.72. Dotted lines indicate the variable component spectra derived in this work (see Section 4.3), and the solid lines are the polarized component spectra taken from Kishimoto et al. (2004). The polarized component spectra are the same as Figure 4.1. The two spectra in each panel are scaled to approximately match each other at the red side of the polarized component spectrum. For comparison, a power-law spectrum with $\alpha_v = +1/3$ (in the unit of $f_v \propto \nu^{\alpha_v}$) is also shown.

and as x -axis in the flux-flux plots (i.e., independent variable), since the i -band wavelength range is less contaminated by broad emission lines than the other bands. For 4C09.72, whose observed-frame i -band wavelength range contains the $H\beta$ line, r -band flux is instead used as the reference of the continuum flux variability and as x -axis in the flux-flux plots.

The best-fit linear regression parameters (regression slope and intercept) for the flux-flux plots are summarized in Table 4.2. Since the variability amplitude of B2 1208+32 is small and the sampling of the light curves is poor, the regression parameters are not well constrained for B2 1208+32, especially in the i - u band-pair. For the other quasars, the flux-flux plots are well fitted by the linear regression lines. We should also note that the regression intercepts of i - u , i - g , i - r , r - u , and r - g band-pairs (where y -axis represents shorter wavelengths) are generally negative, and conversely those of i - z , r - i , and r - z band-pairs (where y -axis represents longer wavelengths) are positive. This means that the total observed flux spectra of these quasars become bluer when they get brighter (“bluer when brighter” trend), which is a common feature observed in the light curves of the SDSS quasars (Chapter 2).

Figure 4.5 shows the relative variable component spectra of the four quasars derived from the

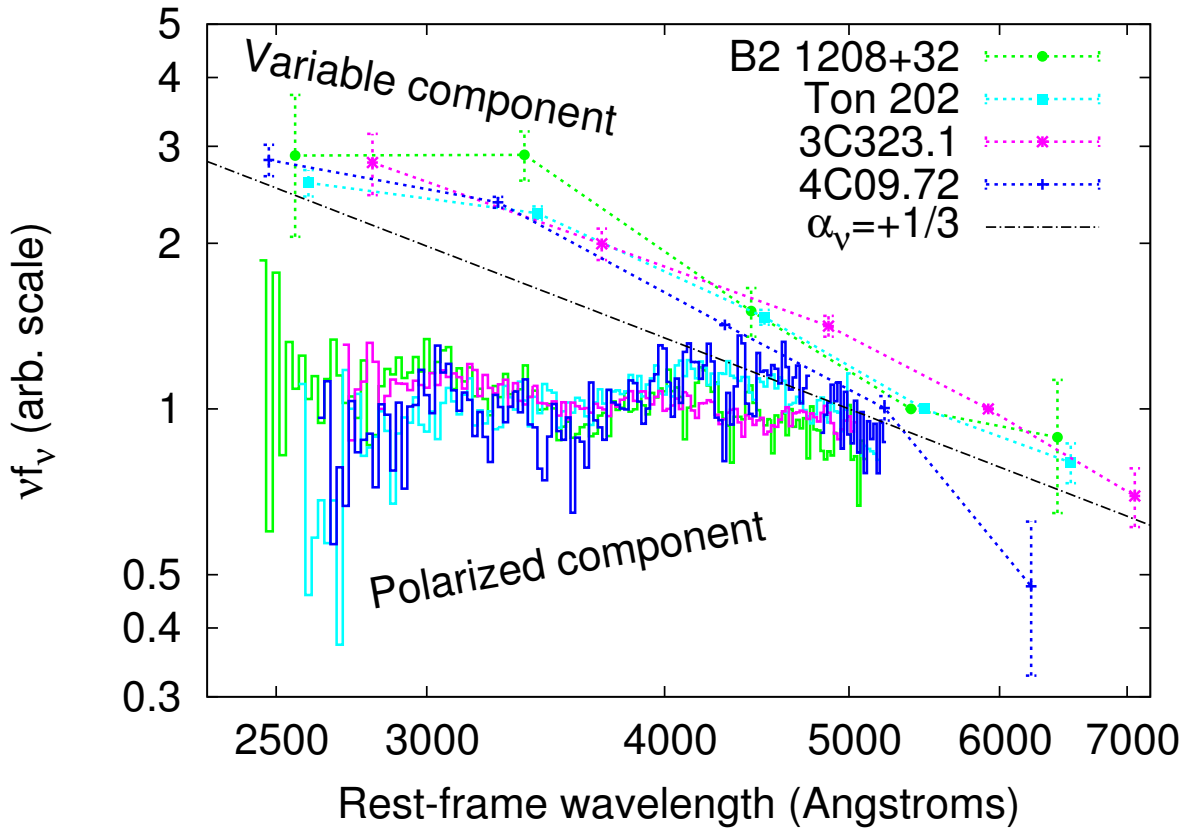


Figure 4.6: The same as in Figure 4.5, but all objects are shown simultaneously. The variable component spectra are scaled to 1 in *i* band for clarity. The spectra of B2 1208+32, Ton 202, 3C323.1, and 4C09.72 are colored green, cyan, magenta, and blue, respectively.

linear regression slopes of the flux-flux plots (Table 4.2), along with the polarized component spectra taken from Kishimoto et al. (2004). Figure 4.6 shows all of these spectra simultaneously to emphasize the similarity of the spectral shape of the variable component spectra between the target quasars. In Figure 4.5 and Figure 4.6, the uncertainty of the variable component spectra in the reference band (*r*-band for B2 1208+32, Ton 202, and 3C323.1, and *i*-band for 4C09.72) is taken to be zero. Detailed comparisons of the spectral shape of the variable component spectra and the polarized component spectra and discussion about them are given in the next section.

4.4 Discussion

4.4.1 Notes on the effect of the BLR emission variability

In Figure 4.5 and Figure 4.6, it is clearly seen that the variable component spectra of the four quasars have very blue power-law like spectral shape throughout the rest-frame near-ultraviolet to optical spectra region, which is as blue as the long-wavelength limit value of the thermal accretion disk pre-

Table 4.2: The best-fit linear regression parameters (slope and intercept) for the two-band flux-flux plots.

Name	Band-pair (x - y)	Slope	Intercept [mJy]
B2 1208+32	i - u	1.371 ± 0.395	-0.284 ± 0.251
B2 1208+32	i - g	1.814 ± 0.186	-0.523 ± 0.121
B2 1208+32	i - r	1.241 ± 0.126	-0.158 ± 0.081
B2 1208+32	i - z	1.061 ± 0.288	$+0.425 \pm 0.187$
Ton 202	i - u	1.222 ± 0.068	-0.220 ± 0.068
Ton 202	i - g	1.421 ± 0.040	-0.376 ± 0.041
Ton 202	i - r	1.210 ± 0.038	-0.172 ± 0.039
Ton 202	i - z	0.955 ± 0.079	$+0.716 \pm 0.082$
3C323.1	i - u	1.331 ± 0.169	-0.611 ± 0.272
3C323.1	i - g	1.250 ± 0.082	-0.544 ± 0.127
3C323.1	i - r	1.166 ± 0.051	-0.292 ± 0.079
3C323.1	i - z	0.830 ± 0.102	$+1.241 \pm 0.160$
4C09.72	r - u	1.148 ± 0.076	-0.244 ± 0.108
4C09.72	r - g	1.269 ± 0.029	-0.156 ± 0.042
4C09.72	r - i	0.857 ± 0.044	$+0.304 \pm 0.063$
4C09.72	r - z	0.485 ± 0.151	$+1.160 \pm 0.216$

The reported uncertainty is $\pm 1\sigma$.

diction $\alpha_v = 1/3$, in good agreement with the results in Chapter 2 and with the results of previous works on the AGN and quasar variability (e.g., Collier et al. (1999); Ruan et al. (2014); Fausnaugh et al. (2016); MacLeod et al. (2016); see Section 4.1). This means that the variable component spectra are significantly bluer than the polarized component spectra (and thus than the thermal accretion disk model predictions) in the near-ultraviolet spectral region of the four quasars. Figure 4.5 shows that the discrepancy of the spectral shape between the variable and polarized components (if these spectra are scaled to the same flux level at optical wavelengths) results in about twofold discrepancy of the emitted energy at ultraviolet wavelengths. As discussed in Section 4.1, this huge discrepancy strongly suggests that there is fundamental problems in our current understanding of the quasar ultraviolet-optical variability and/or polarization; namely, either (or both) of the two interpretations, one states that the polarized component spectrum should represent the intrinsic accretion disk continuum spectrum (e.g., Kishimoto et al. (2004, 2008b)) and the other states that the variable component spectrum well represents it (as we have assumed in Chapter 2 and Chapter 3; see also Pereyra et al. (2006); Schmidt et al. (2012); Ruan et al. (2014)), is (are) wrong.

It should first be noted that, as mentioned in Section 4.1, broad-band photometric light curves containing the rest-frame spectral regions of the broad emission lines are unavoidably (more or less)

affected by the contamination from the broad line flux variability, although the continuum variability is often larger than the broad line variability at least by a factor of a few (intrinsic Baldwin effect; e.g., Kinney et al. (1990); Wilhite et al. (2005); Bian et al. (2012)). The variable component spectra in Figure 4.5 actually show small deviations from single power-law spectra, which can possibly be attributed to the flux variability of BLR emission; z -band of Ton 202 and B2 1208+32 contains the $H\alpha$ line, i -band of 4C09.72 and r -band of Ton 202 and 3C323.1 contain the $H\beta$ line, and g -band contains blends of higher order Balmer lines and the Balmer continuum emission from the BLR, all of which are known to show flux variability as a result of reverberation of the ionizing continuum emission (Section 2.5 and Section 2.6; e.g., Maoz et al. (1993); Korista & Goad (2001, 2004); Edelson et al. (2015); Fausnaugh et al. (2016); Jiang et al. (2016b), and references therein). The dominant BLR emission in u -band is Fe II pseudo-continuum and Mg II emission, but several spectral variability studies show that the variability of these low-ionization emission lines are very weak and they do not significantly contribute to the variable spectral component (Chapter 2.6; see Goad et al. (1999a); Modzelewska et al. (2014); Sun et al. (2015), and references therein). In any case, it is very difficult to attribute the twofold flux excess in the near-ultraviolet region (u and g -band in the observed-frame) in the variable component spectra compared to the polarized component spectra (seen in Figure 4.5) to the variable BLR emission contamination considering the huge energy required to fill the gap.

More direct observational evidence against the non-accretion disk variable component contamination in near-ultraviolet region is the observed strong inter-band correlation. The flux-flux plots in Figure 4.4, especially for 4C09.72, show very strong linear correlation. Such a strong inter-band correlation is generally observed in AGNs and quasars (Chapter 3; see also Sakata et al. (2010)), and validates the use of the flux gradient method described in Section 4.3. Since the broad line region locates at a few tens or hundreds of light-days (note that our observation period is ~ 200 days in the quasar rest-frame) away from the inner region of the accretion disk in luminous quasars like those analysed in this work (according to the well-established BLR radius-optical luminosity relation; e.g., Bentz et al. (2013)), the observed strong inter-band correlation suggests that the huge flux contribution from the BLR emission is unlikely and that there exists essentially a single dominant variable continuum component throughout the near-ultraviolet to optical wavelengths.

One may think that this power-law like variable component spectra seen in Figure 4.5 and Figure 4.6 are from the variable optical synchrotron emission. However, if it was true, the optical polarized component spectra were to be dominated by the intrinsically-polarized synchrotron emission and thus had the same spectral shape with those of the variable component spectra. The similarity of the variability amplitude and the spectral shape of the variable component observed in the four quasars with the general property of the SDSS quasars, which are mostly radio-quiet quasars (e.g., Ivezić et al. (2002)), also suggests that the variable component in these luminous type 1 quasars are related with the accretion disk emission rather than the optical synchrotron emission. Inversely, it seems to be difficult to explain the observed complex spectral shape of the polarized flux spectra by the optical synchrotron emission contribution (see Kishimoto et al. (2003, 2004) for more detailed discussion).

4.4.2 Possible interpretations of the relationship between variable and polarized spectral components

Because there seems to be no explanation for the large flux deficit in the near-ultraviolet region seen in the polarized component spectra of the quasars (compared to the variable component spectra), we may have to consider that the ultraviolet-optical polarization in the luminous type 1 quasars cannot solely explained by the electron (Thomson) scattering, and there may be some unknown (de)polarization mechanisms producing the observed decrease of the polarization degree in the near-ultraviolet wavelengths, considering that the variable flux component spectra should represent the spectral shape of intrinsic accretion disk emission.

On the other hand, it can also be possible that the blue spectral shape of the variable component is not representing the shape of the total flux spectrum coming from the whole surface of the quasar accretion disk. Generally speaking, a causal argument suggests that the short-term (several days to several tens of days) flux variability observed in AGNs and quasars is caused at the disk radii smaller than several tens of light-days from the central black hole (e.g., Starling et al. (2004); Sun et al. (2014)). On the basis of this causal argument and the observational fact of the strong linear inter-band flux-flux correlation of the quasar variability in all time-scale (see e.g., Sakata et al. (2010)), it seems to be natural to consider that the quasar ultra-violet to optical flux variability is always caused by temperature fluctuations within a certain disk radius, which must result in the bluer variable component spectrum than the total flux spectrum from the disk (e.g., Lawrence, 2005). Construction of quantitative models based on the above described idea and comparison with observations are beyond the scope of this work, and these will be discussed elsewhere.

Finally, it should also be noted that, although quantitative comparisons with model spectra are currently impossible, there is still a room to consider that the observed polarization properties in the four quasars with $\lambda < 4000\text{\AA}$ polarization dip may be explained by the intrinsic polarization imprinted in the accretion disk atmosphere. By referring to the model calculations by Laor et al. (1990) (see also Shields et al. (1998); Hsu & Blaes (1998); Koratkar & Blaes (1999)), Kishimoto et al. (2003) and Antonucci et al. (2004) stated that, in a certain accretion disk model parameter space, even though the total flux (and thus the variable component) of the accretion disk spectrum has no feature around Balmer edge spectral region, the polarization degree (and thus the polarized component) spectrum can show the decreasing feature at the blueward of Balmer edge due to the increase of the absorption opacity.⁶ If this is true, our result of the discrepancy of the spectral shape between the variable component and polarized component in the four quasars can be explained so that the variable component spectrum is a scaled copy of the featureless accretion disk continuum, and the polarized component spectrum only represents the intrinsically polarized accretion disk continuum component.

⁶Although these models are generally claimed to suffer from the wrong polarization direction (i.e., polarization direction perpendicular to the disk's rotation axis, contrary to the observations), it is also suggested that absorption opacity effects can in some cases change the polarization position angle to the direction parallel to the disk's rotation axis (Nagariner effect; e.g., Gnedin & Silantev (1978); Matt et al. (1993); Agol et al. (1998)).

Although above we have listed several implications of the discrepancy between the variable component and polarized component spectra in quasars, it is definitely impossible to conclusively decide either the polarized component or variable component spectrum well represents the intrinsic accretion disk spectrum, or both of the interpretations are invalid, with the currently available data. The only way to probe the true nature of the relationship between the variable component and the polarized component in the quasar spectra is the examination of the polarimetric variability, which has rarely been investigated for AGNs and quasars (see e.g., Merkulova & Shakhovskoy (2006); Gaskell et al. (2012); Afanasiev et al. (2015)). For example, Kishimoto et al. (2003) noted that Ton 202 showed evidence of slight changes of the polarization degree at $\lambda < 4000\text{\AA}$ dip region within a year time-scale. This may indicate the presence of fast-moving absorption materials responsible for the Balmer-edge feature in the edge-on trajectory between the inner accretion disk region and the scatterer (e.g., Jiang et al., 2016a). In Section 5, we will further discuss the possibility that such equatorial absorbing region can explain photometric and spectro-polarimetric variability by examining archival polarimetric and photometric data of 3C 323.1.

Future intensive photometric and/or spectroscopic polarimetric monitoring observations will clarify the causes of the discrepancy between the spectral shapes of the polarized component and variable component in luminous type 1 non-blazar quasars.

4.5 Summary and conclusions of Chapter 4

In the literature, it is suggested that the ultraviolet-optical polarized flux spectra of the luminous type 1 quasars are representing the intrinsic spectral shape of the quasar accretion disk emission, and several quasars are showing Balmer edge features (specifically, decrease of the polarized flux at $\lambda < 4000\text{\AA}$) in their polarized flux spectra which can be interpreted as the imprint of the opacity effect in the accretion disk atmosphere (e.g., Kishimoto et al. (2003); Antonucci et al. (2004); Kishimoto et al. (2004, 2008b); Hu & Zhang (2012)). On the other hand, it is also assumed in several previous works (and in Chapter 2 and Chapter 3) that the ultraviolet-optical variable component spectra of quasars are the good indicator of the intrinsic spectral shape of the quasar accretion disk emission (e.g., Pereyra et al. (2006); Schmidt et al. (2012); Ruan et al. (2014)). In this work, we examined the consistency of the above mentioned assumptions through the investigation of whether the variable component spectra have the same spectral shape with the polarized flux component spectra in a sample of four $\lambda < 4000\text{\AA}$ polarization-decreasing quasars spectropolarimetrically confirmed by Kishimoto et al. (2004) (4C09.72, 3C323.1, Ton 202, and B2 1208+32). The result is negative, in that the variable component spectra are significantly bluer compared to the polarized flux component spectra especially in the near-ultraviolet spectral region; the variable component spectra of these quasars are confirmed to be well represented by a single power-law component with $\alpha_\nu \sim 1/3$ through the rest-frame ultraviolet-optical wavelength range, resulting in the twofold excess of the emitted energy at ultraviolet wavelengths compared to the polarized flux spectra. Although it is impossible to decide which (both) of the two

assumptions is (are) invalid only from the currently available observational constraints, we can at least say that this discrepancy in the spectral shape implies either (1) the decrease of polarization degree in the rest-frame ultraviolet wavelengths is not indicating the Balmer absorption edge feature but is induced by some unknown (de)polarization mechanisms, or (2) the ultraviolet-optical flux variability is occurring preferentially at the hot inner radii of the accretion disk and thus the variable component spectra do not reflect the whole accretion disk emission. Future photometric and/or spectroscopic polarimetric monitoring observations will be useful to clarify the causes of this discrepancy between the spectral shapes of the polarized component and variable component, and consequently the true nature of the accretion disk emission in the luminous type 1 non-blazar quasars. In Chapter 5, I will discuss the observational constraints on the optical polarization source in 3C 323.1 by collecting archival polarimetric measurements.

Chapter 5

Constraints on the Polarization Source in 3C 323.1 from the Photometric and Polarimetric Variability¹

Abstract of Chapter 5

We examine the optical photometric and polarimetric variability of the luminous type 1 non-blazar quasar 3C 323.1 (PG 1545+210). Two optical spectro-polarimetric measurements taken during the periods 1996–98 and 2003 combined with a *V*-band imaging polarimetric measurement taken in 2002 reveal that (1) as noted in the literature, the polarization of 3C 323.1 is confined only to the continuum emission, that is, the emission from the broad line region is unpolarized; (2) the polarized flux spectra show evidence of a time-variable broad absorption feature in the wavelength range of the Balmer continuum and other recombination lines; (3) weak variability in the polarization position angle (*PA*) of ~ 4 deg over a time-scale of 4–6 years is observed; and (4) the *V*-band total flux and the polarized flux show highly correlated variability over a time-scale of one year. Taking the above-mentioned photometric and polarimetric variability properties and the results from previous studies into consideration, we propose a geometrical model for the polarization source in 3C 323.1, in which an equatorial absorbing region and an axi-asymmetric equatorial electron-scattering region are assumed to be located between the accretion disk and the broad line region. The scattering/absorbing regions can perhaps be attributed to the accretion disk wind or flared disk surface, but further polarimetric monitoring observations for 3C 323.1 and other quasars with continuum-confined polarization are needed to probe the true physical origins of these regions.

¹This Chapter 5, in full, is a reprint of the material as it has been accepted for publication in Monthly Notices of the Royal Astronomical Society (Kokubo, 2017). The dissertation author was the primary investigator and single author of this paper.

5.1 What is the true nature of the optical polarization source in continuum-confined polarization quasars ?

We have shown in Chapter 4 (Figure 4.5) that the variable component and the polarized component spectra of quasars with continuum-confined polarization have totally different spectral shape, although both of which have been claimed in the literature to be reflect the spectral shape of the intrinsic accretion disk continua of quasars in the literature and thus are expected to have the same spectral shape. By assuming that the variable component spectra truly reflect the intrinsic spectral shape of the accretion disk emission, this observational fact may imply that equatorial electron scattering of the disk continua alone probably cannot explain the optical polarization properties in these quasars. Moreover, it should be noted that, before the deep spectro-polarimetric observations conducted by Kishimoto et al. (2004), Schmidt & Smith (2000) had carried out spectro-polarimetry for quasar samples overlapping with those used by Kishimoto et al. (2004) and suggested that the polarization in quasars with continuum-confined polarization may be attributed to a weak optical synchrotron component from the misdirected blazar core components. In fact, all of the five quasars (3C 323.1, Ton 202, B2 1208+32, 3C 95, and 4C09.72) confirmed as showing continuum-confined polarization by both Schmidt & Smith (2000) and Kishimoto et al. (2004) are radio-loud objects; thus, it is unsurprising that there is a flux contribution from the jet synchrotron component to the observed optical spectra (see e.g., Impey et al. 1989; Smith et al. 1993 and Afanasiev et al. 2015 for the cases of 3C 273 and 3C 390.3)².

As discussed above, the optical polarization source in quasars with continuum-confined polarization has yet to be fully understood. To probe the true nature of the optical polarization mechanism, and consequently to examine the accretion disk physics in luminous type 1 quasars, detailed studies of the quasar polarimetric variability must be a key observable to constrain the geometry of the polarization source (e.g., Stockman et al., 1979; Schmidt & Smith, 2000; Gallagher et al., 2005; Gaskell et al., 2012; Afanasiev et al., 2015; Rojas Lobos et al., 2016). In this work we examine the variability of the total flux, polarization degree, polarization PA, and the polarized flux in the luminous type 1 non-blazar quasar 3C 323.1, which is a quasar with continuum confined polarization identified by Schmidt & Smith (2000) and Kishimoto et al. (2004), by collecting archival data.

The three polarimetry data sets used in this work, including the two optical spectro-polarimetric measurements taken by Schmidt & Smith (2000) (Bok/SPOL in 1996-1998) and by Kishimoto et al. (2004) (Keck/LRIS in 2003) and a V-band imaging-polarimetry measurement by Sluse et al. (2005) (ESO3.6-m/EFOSC2 in 2002), are described in Section 5.2. The absolute V-band magnitudes at the epochs of the spectro-polarimetric measurements are carefully estimated by using broad-band light curves taken from the literature. In Section 5.3, we first examine the spectral variability of the polarimetric properties between the two spectro-polarimetric measurements, and identify the origin

²However, it should be noted that subsequent work by Kishimoto et al. (2008b) has identified two radio-quiet quasars (Q0144-3938 and CTS A09.36) with continuum-confined polarization.

of the different conclusions between Schmidt & Smith (2000) and Kishimoto et al. (2004) regarding the polarization source in the quasars with continuum-confined polarization described above. We then examine the V -band photometric and polarimetric variability of 3C 323.1 using all three polarimetric measurements in order to constrain observationally the geometry of the optical polarization source in 3C 323.1 in Section 5.4. Finally, a summary and conclusions are provided in Section 5.5.

5.2 Polarimetric and photometric data of 3C 323.1

Throughout this Chapter, we assume a cosmology of $H_0 = 73$ km/s/Mpc, $\Omega_m = 0.27$, and $\Omega_\Lambda = 0.73$ (Spergel et al., 2007). None of the data are corrected for Galactic extinction. In this study, “the total flux” (F_λ or F_ν) has the same meaning as the un-normalised Stokes parameter I expressed in units of the flux. q and u represent the normalised Stokes parameters defined as Q/I and U/I , whose polarization PA is defined using the equatorial coordinate system (a PA of 0 deg corresponds to North-South, and the PA increases from North towards East). The polarization degree $p \equiv \sqrt{q^2 + u^2}$ obtained from the observational data with finite measurement errors³ is known to be a biased estimate of the true polarization degree; therefore, the de-biased estimate of the polarization degree, $\hat{p} \equiv \sqrt{p^2 - \sigma^2}$ (e.g., Plaszczyński et al., 2014), is used throughout this study. The rotated normalised Stokes parameters q' and u' are defined in a coordinate system rotated to the systemic polarization position angle PA_c of the target; note that all of the polarization, in principle, falls in the single Stokes parameter q' when the object has a wavelength-independent PA . Details of the analysis method and the statistical properties of polarimetric data are described in Appendix E.

5.2.1 Observational properties of 3C 323.1: the variable component spectrum

3C 323.1 (PG 1545+210) is a Fanaroff-Riley II (FR II) radio-loud quasar at $z = 0.264$ (the luminosity distance $d_L = 1293.3$ Mpc; Wright, 2006). The lobe-dominant radio jet structure of 3C 323.1 has a size of ~ 300 kpc, and its position angle is ~ 20 deg (Miley & Hartsuijker, 1978; Kellermann et al., 1994; Dennett-Thorpe et al., 2000; Schmidt & Smith, 2000; Kishimoto et al., 2004). As is the case with the other quasars with the continuum-confined polarization, the radio jet axis of 3C 323.1 is known to be parallel to the direction of the optical polarization vector within $\lesssim 10$ deg (see Section 5.4; Stockman et al., 1979; Schmidt & Smith, 2000; Kishimoto et al., 2004). In the optical wavelength range, 3C 323.1 is observed as a point source with an apparent V -band magnitude of $V \sim 16$ mag. The optical multi-band colour of 3C 323.1 is within the spectroscopic target selection criteria in the Sloan Digital Sky Survey (SDSS) Legacy Survey (Richards et al., 2002), meaning that this object is “normal” in terms of its optical spectrum (see also Boroson & Green, 1992). The black hole mass (M_{BH}) and the Eddington ratio (defined as the ratio of the bolometric luminosity L to the

³For the polarimetric observations for weakly polarized objects, the measurement errors associated with q and u is essentially the same ($\sigma \equiv \sigma_q \simeq \sigma_u$).

Eddington luminosity L_E) of 3C 323.1 were estimated to be $\log(M_{\text{BH}}/M_{\odot}) = 9.07$ and $L/L_E = 0.10$, respectively, based on the single-epoch SDSS spectrum obtained at MJD=53886 (Shen et al., 2011).

As shown in Chapter 4 (Figure 4.5), the variable component spectrum in 3C 323.1 is consistent with a power-law spectrum with $\alpha_{\nu} \sim +1/3$ (in the form of $F_{\nu} \propto \nu^{\alpha_{\nu}}$). The spectral index of $\alpha_{\nu} \sim +1/3$ is commonly detected in the variable component spectra of (mostly radio-quiet) quasars (e.g., Pereyra et al., 2006; Ruan et al., 2014; Kokubo et al., 2014; MacLeod et al., 2016; Hung et al., 2016; Buisson et al., 2017), and is usually attributed to the well-known prediction of the spectral index $\alpha_{\nu} = +1/3$ of the standard thin thermal accretion disk emission (Shakura & Sunyaev, 1973; Novikov & Thorne, 1973; Frank et al., 1992). This means that it is natural to consider that the flux variability of 3C 323.1 is due to the intrinsic variations of the disk emission itself, in line with other non-blazar quasars; nevertheless, the precise mechanisms for the quasar flux variability are still under debate (see Kokubo, 2015, 2016, and references therein). The observed variability time-scale of months to years in 3C 323.1 is also consistent with the variability of the quasar accretion disk emission. As discussed in Section 5.4, the attribution of the flux variability to the intrinsic disk emission variability, combined with the observed correlated variability between the total flux and the polarized flux, implies that the polarized flux is directly related to the disk emission and does not arise from the optical synchrotron flux contribution.

5.2.2 Polarimetry data

In this work, we use the three archival polarimetric measurements for 3C 323.1 obtained at different epochs with Bok/SPOL, ESO3.6-m/EFOSC2, and Keck/LRIS. The ESO3.6-m/EFOSC2 observation is V-band imaging polarimetry (Sluse et al., 2005), and the Bok/SPOL and the Keck/LRIS observations are optical spectro-polarimetry (Schmidt & Smith, 2000; Kishimoto et al., 2004). The compilation of these polarimetric data from the literature enables to examine the two-epoch spectral variability (Section 5.3) and the three-epoch V-band variability (Section 5.4) of the polarimetric properties of 3C 323.1.

The V-band magnitudes of the total flux at the epochs of the three polarimetric measurements are also estimated (Sections 5.2.2 and 5.2.3). As discussed in Section 5.4, one of the most important subjects of this work is to examine the correlation between the total flux and the polarized flux light curves, which eventually provides strong constraints on the optical polarization source in 3C 323.1.

Following the same procedure of Kishimoto et al. (2004), we correct the three polarimetric measurements for the effects of Galactic interstellar polarization (ISP). The details of the method of the ISP correction is summarized in Section F. Throughout this Chapter, the characters with no subscript represent ISP-corrected values unless otherwise stated.

ESO3.6-m/EFOSC2 V-band imaging-polarimetry

Sluse et al. (2005) presented the results of V-band imaging-polarimetry for 3C 323.1 obtained from the 3.6-m telescope at the European Southern Observatory (ESO), La Silla, equipped with the ESO

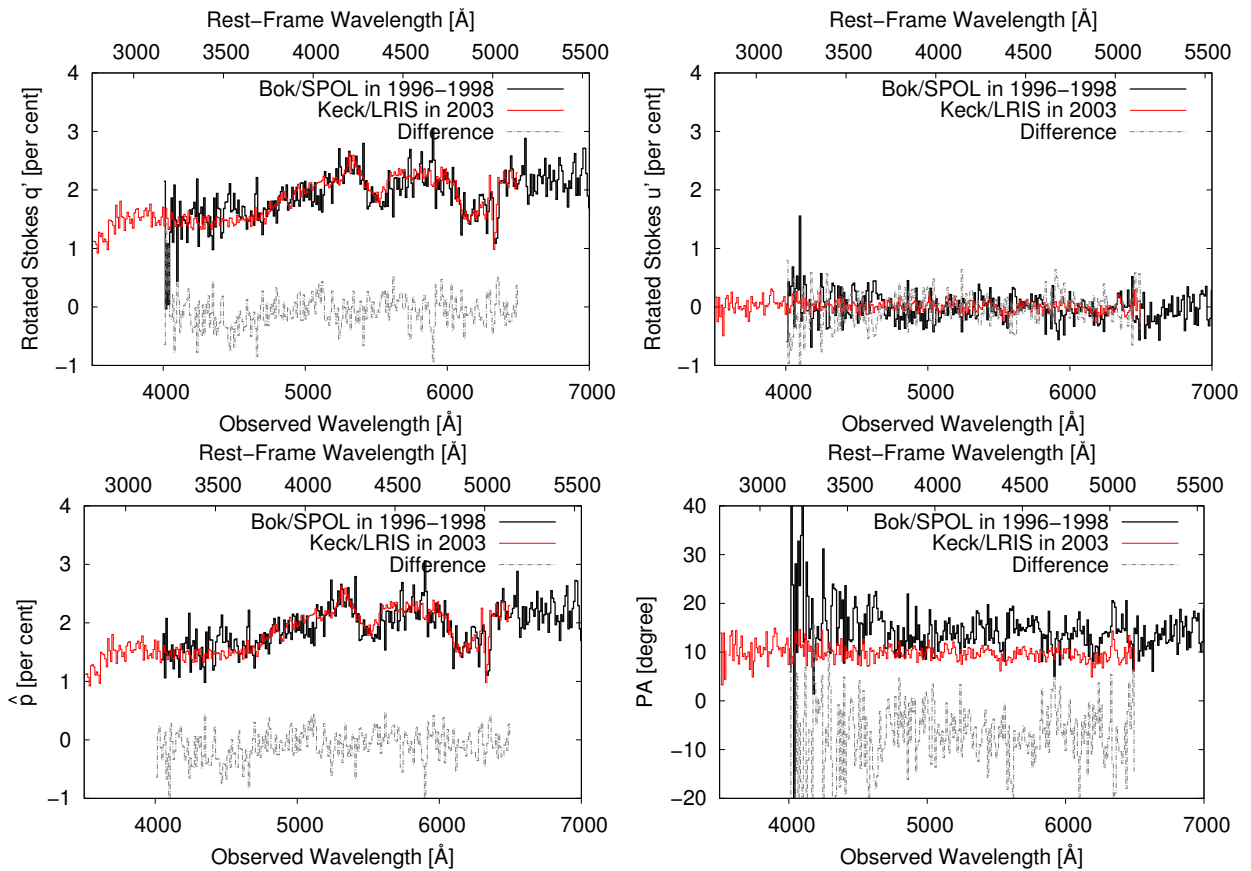


Figure 5.1: Comparison of the rotated Stokes parameters q' and u' , de-biased polarization degree \hat{p} , and the polarization position angle (PA) of 3C 323.1 between the spectro-polarimetric measurements of Bok/SPOL (Schmidt & Smith, 2000) and Keck/LRIS (Kishimoto et al., 2004). The difference spectra between the two measurements are also plotted. The spectra are binned into common wavelength bins with 10 \AA width to allow easy comparison between the two measurements. Note that q' and u' are defined by assuming the systemic PA as $PA_c = 14.2 \text{ deg}$ and 9.6 deg for Bok/SPOL and Keck/LRIS data, respectively.

Faint Object Spectrograph and Camera (v.2) (EFOSC2) on the 1st May, 2002 (MJD=52396.3; see also Hutsemékers et al., 2005). As part of this, they took a set of four 60-sec integration images with the half-wave plate position angles of 0.0 deg , 22.5 deg , 45.0 deg , and 67.5 deg .

We downloaded the ESO3.6-m/EFOSC2 imaging-polarimetry data of 3C 323.1 and the associated BIAS and FlatPolIma frames from the ESO Science Archive Facility (Program ID 68.A-0373). After applying bias and flat corrections, the V -band polarization degree \hat{p}_V and the polarization position angle PA_V of 3C 323.1 were calculated by adopting the aperture photometry and the “ratio” method (e.g., Lamy & Hutsemékers, 1999; Bagnulo et al., 2009). By subtracting the instrumental polarization using the values presented in Sluse et al. (2005), we obtained the ISP-uncorrected V -band polarization degree and polarization position angle as $p_{V,\text{uncorr}} = 1.14 \pm 0.13 \%$, $\hat{p}_{V,\text{uncorr}} = 1.13 \%$ and $PA_{V,\text{uncorr}} =$

17.88 ± 3.39 deg, which are consistent with those reported by Sluse et al. (2005)⁴. By correcting for the Galactic ISP (Section F), we obtain $\hat{p}_V = 1.94\%$ and $PA_V = 10.03$ deg (Table 5.1).

To evaluate the V -band magnitude at the epoch of the EFOSC2 polarimetry measurement, we applied differential photometry by using two field stars (SDSS J154736.44+205141.7 and SDSS J154752.41+204931.8) simultaneously imaged on the same EFOSC2 frames along with 3C 323.1 as reference stars. By using the SDSS g and r -band point spread function (PSF) photometry and the transformation equation by Jester et al. (2005) from the SDSS g and r -band magnitude to V -band magnitude, $V_{Vega} = g - 0.59(g - r) - 0.01$ mag with an uncertainty of 0.01 mag, the V -band magnitudes of SDSS J154736.44+205141.7 and SDSS J154752.41+204931.8 are estimated as $V_{Vega} = 17.0516$ mag and $V_{Vega} = 16.6971$ mag, respectively. For each image, aperture photometry was applied to combine the two orthogonally polarized fluxes of 3C 323.1 and the two reference stars. By adding the 0.01 mag error due to the transformation equation of Jester et al. (2005) to the photometric errors, we evaluated the weighted average magnitude of 3C 323.1 and its uncertainty as $V_{Vega} = 15.7779 \pm 0.0106$ mag or $V_{AB} = 15.7339 \pm 0.0113$ mag, where the AB offset and its uncertainty are taken from Frei & Gunn (1994). The polarimetric and photometric measurements for 3C 323.1 obtained with ESO3.6-m/EFOSC2 are summarised in Table 5.1.

Bok/SPOL and Keck/LRIS optical spectro-polarimetry

3C 323.1 was spectro-polarimetrically observed by Schmidt & Smith (2000) and Kishimoto et al. (2004) during 1996-1998 and 2003, respectively.

Schmidt & Smith (2000) carried out spectro-polarimetric observations of 3C 323.1 at the Steward Observatory 2.3-m Bok Telescope using the SPOL CCD Imaging/Spectropolarimeter (Schmidt et al., 1992) with a low-resolution grating. The observed wavelength range was $\lambda_{obs} = 4000 - 8000$ Å. The data presented in Schmidt & Smith (2000) comprise 10 observations from several epochs taken in June 1996 (5 observations) and April 1998 (5 observations), and thus the combined data represent the average polarization properties of 3C 323.1 at MJD~50235 and 50933. Since the raw Bok/SPOL data of 3C 323.1 are unavailable, in this work, we directly use the combined calibrated polarization spectra of 3C 323.1 presented in Schmidt & Smith (2000), which are kindly provided by G. D. Schmidt and P. S. Smith in electric form. The Galactic ISP is corrected as described in Section F. Following the definition of Kishimoto et al. (2004), the systemic polarization position angle PA_c of 3C 323.1 at the epoch of Bok/SPOL observations is evaluated to be $PA_c = 14.2$ deg as a weighted average of the PA at the rest-frame wavelength range of 4000-4731 Å; thus, the rotated Stoke parameters q' and u' are defined in a coordinate system rotated to $PA_c = 14.2$ deg.

Kishimoto et al. (2004) carried out spectro-polarimetry for 3C 323.1 on the 4th May, 2003 (MJD=52763.6), with the Low Resolution Imaging Spectrometer (LRIS) mounted on the 10-m Keck-I telescope at the W. M. Keck Observatory (Oke et al., 1995; Goodrich et al., 1995; McCarthy et al., 1998), using two

⁴Sluse et al. (2005) reported the ISP-uncorrected V -band polarization degree and the polarization position angle of 3C 323.1 as $p_{V,uncorr} = 1.15 \pm 0.13\%$, $\hat{p}_{V,uncorr} = 1.14\%$ and $PA_{V,uncorr} = 18 \pm 3$ deg.

Table 5.1: Summary of the ISP-corrected V-band polarimetric and photometric values for 3C 323.1.

Date	MJD	Instrument	\hat{p}_V [%]	PA_V [deg]	V-band AB mag. of the total flux
1996-06 and 1998-04	50235-50933	Bok/SPOL	2.06 ± 0.01	13.75 ± 0.20	15.8935 ± 0.0358
2002-05-01	52396.3	ESO3.6-m/EFOSC2	1.94 ± 0.13	10.03 ± 3.39	15.7339 ± 0.0113
2003-05-04	52763.6	Keck/LRIS	2.11 ± 0.01	9.61 ± 0.10	15.5838 ± 0.0226

grisms of 300 *l*/mm and 400 *l*/mm. The observations of 3C 323.1 (76 minutes in total) consisted of two sets of four wave-plate positions (0.0 deg, 22.5 deg, 45.0 deg, and 67.5 deg) \times 7.5 minute observations with 300 *l*/mm and a single set of four wave-plate positions \times 4 minute observations with 400 *l*/mm. As noted in Kishimoto et al. (2004), the observed spectra at the wavelength range at $\lambda_{obs} \gtrsim 6500 \text{ \AA}$ may be affected by second-order light contamination; therefore, the usable wavelength range for the analysis is $\lambda_{obs} = 3500 - 6500 \text{ \AA}$. In this work we use the calibrated polarization spectra of 3C 323.1 presented in Kishimoto et al. (2004), which are kindly provided by M. Kishimoto in electric form (see Kishimoto et al., 2004, for details of the data analysis). The ISP-corrected Keck/LRIS data used in this work are the same with those shown in Figure 9 of Kishimoto et al. (2004). As listed in Table 6 of Kishimoto et al. (2004), the systemic polarization position angle PA_c of 3C 323.1 at the epoch of the Keck/LRIS observation at the rest frame wavelength range of 4000-4731 \AA is $PA_c = 9.6 \text{ deg}$.

Figure 5.1 shows the ISP-corrected spectra of the rotated Stokes parameters q' and u' , de-biased polarization degree \hat{p} , and PA of 3C 323.1 obtained with Bok/SPOL (Schmidt & Smith, 2000) and Keck/LRIS (Kishimoto et al., 2004). A discussion of the spectral variability of the polarization properties between these two measurements is given in Section 5.3.2.

To compare the Bok/SPOL and Keck/LRIS spectro-polarimetric measurements with the ESO3.6-m/EFOSC2 *V*-band imaging-polarimetry data, the *V*-band polarization degree \hat{p}_V and the polarization position angle PA_V are calculated from the Bok/SPOL and Keck/LRIS spectro-polarimetric data by convolving the total and polarized flux spectra (F_λ , $q_\lambda \times F_\lambda$ and $u_\lambda \times F_\lambda$) with the *V*-band filter transmission curve taken from Bessell (1990). The errors on \hat{p}_V and PA_V are evaluated as the sample standard deviation of the estimates from the 1000 trials of the Monte Carlo resampling of the spectra. The *V*-band polarimetric properties of 3C 323.1 are summarized in Table 5.1.

The absolute flux calibration for the total flux (and the polarized flux) spectra of the two spectro-polarimetric measurements is discussed in Section 5.2.3.

Note on other historic polarimetric measurements for 3C 323.1

Other than the three polarimetric data described above, we can find several historic polarimetric measurements in the literature (Stockman et al., 1984; Wills et al., 2011). However, most of these measurements are obtained with white-light (no-filter) configuration, and thus, it is difficult to directly compare them with those obtained with Bok/SPOL, ESO3.6-m/EFOSC2, and Keck/LRIS because of the uncertainty of the wavelength coverage of the data; because the polarimetric properties of 3C 323.1 show wavelength dependence (see Section 5.3), it is critical for the study of the polarimetric variability to use data taken in the same wavelength range. Also, unlike the three polarimetric data used in this work, it is impossible to evaluate the magnitude values of the total flux of 3C 323.1 at the epochs of these white-light polarimetric data because of lack of referenceable photometric measurements. For these reasons, we do not include the historic white-light polarimetric measurements for 3C 323.1 in the main text; they are instead summarized and discussed in Section G.

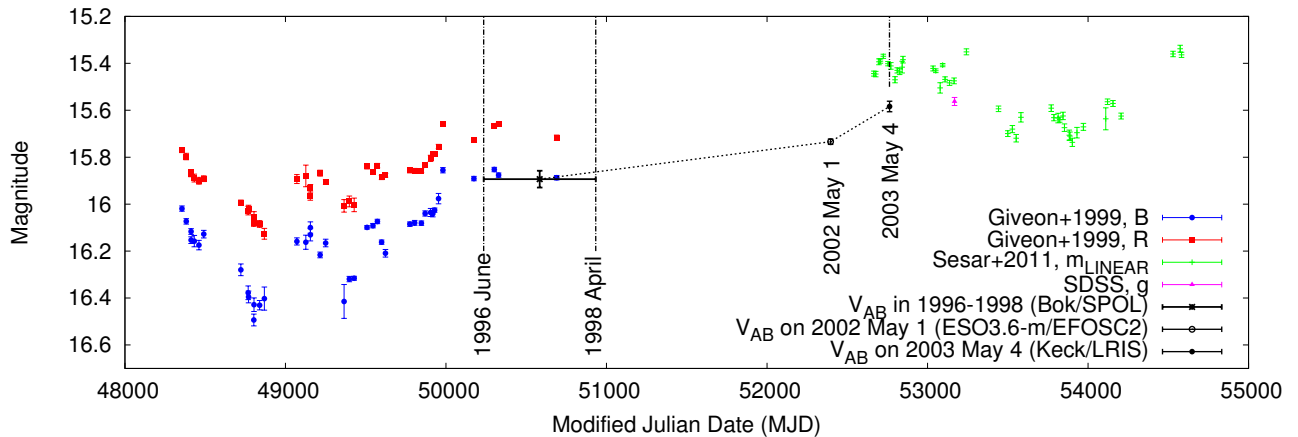


Figure 5.2: Compilation of the broad-band light curves for 3C 323.1. The B - and R -band light curves at MJD=48355-50690 are taken from Giveon et al. (1999), and the Lincoln Near-Earth Asteroid Research (LINEAR) survey recalibrated magnitudes (m_{LINEAR}) at MJD=52665-54582 are from Sesar et al. (2011). The Sloan Digital Sky Survey g -band photometry at MJD=53168.32 is also plotted. The two periods of the Bok/SPOL spectro-polarimetry and the epoch of the Keck/LRIS spectro-polarimetry are indicated by dashed-dotted vertical bars. The estimated V_{AB} magnitude at the epochs of the three polarimetric measurements (Bok/SPOL, ESO3.6-m/EFOSC2, and Keck/LRIS) is also shown (Table 5.1; see Section 5.2.2 and Section 5.2.3 for details).

5.2.3 Spectro-photometric flux calibration for the Bok/SPOL and Keck/LRIS data

The absolute flux calibration of the spectroscopic data is generally not quite as accurate as that of the broad-band photometry data. To confidently evaluate the variability of the total and polarized fluxes in 3C 323.1 at the epochs of the spectro-polarimetric observations by Bok/SPOL and Keck/LRIS described in Section 5.2.2, we collect broad-band photometric data from the literature and publicly available databases (Figure 5.2), and use them to estimate the V -band magnitude of the total flux.

B- and R-band light curves in 1991-1998

3C 323.1 was photometrically observed for seven years (1991-1998) in the Johnson-Cousins B - and R -band with the Wise Observatory 1-m telescope (see Giveon et al., 1999, for details). The B - and R -band light curves of 3C 323.1 presented by Giveon et al. (1999)⁵ are shown in Figure 5.2. In the same figure, the epoch of Schmidt & Smith (2000)'s Bok/SPOL spectro-polarimetric observations carried out in June 1996 and April 1998 is indicated by vertical bars.

Although there is no available broad-band photometric measurement obtained simultaneously with the Bok/SPOL data, we can infer the broad-band magnitude of 3C 323.1 at the periods of

⁵<http://wise-obs.tau.ac.il/givon/DATA/>

the Bok/SPOL observations from the photometry data of Giveon et al. (1999). We assume that the weighted average of the four R -band measurements of Giveon et al. (1999) from MJD=50174 to 50690, $R_{Vega} = 15.6793 \pm 0.0353$ mag or $R_{AB} = 15.7963 \pm 0.0358$ mag (the AB offset and its uncertainty are taken from Frei & Gunn, 1994), represents the magnitude value at the epoch of the observation of Schmidt & Smith (2000). Here, we assume the uncertainty in R_{Vega} as 0.0353 mag, which is derived not from the statistical error but from the sample standard deviation of the four measurements.

The Bok/SPOL total flux spectrum for 3C 323.1 is scaled so that the R_{AB} magnitude calculated by convolving the Bok/SPOL total flux spectrum with the R -band filter transmission curve taken from Bessell (1990) coincides with $R_{AB} = 15.7963$ mag. Then, the polarized flux spectra are defined as the product of the polarization degree spectra in Figure 5.1 and the scaled total flux spectrum. The V -band magnitude of the scaled total flux Bok/SPOL spectrum is calculated as $V_{AB} = 15.8935$ mag, by using the V -band filter transmission curve taken from Bessell (1990). Because the measurement errors on the Bok/SPOL total flux spectrum are negligible compared to the R -band magnitude uncertainty of 0.0358 mag, we adopt 0.0358 mag as the error of the estimated V -band magnitude. The spectral monochromatic luminosity at 5100 Å is $\lambda L_{\lambda}(5100 \text{ Å}) = 1.1499(\pm 0.0379) \times 10^{45}$ erg/s. The scaled Bok/SPOL total flux spectrum and the polarized flux spectrum are shown in Figure 5.3.

It should be noted that, since there is a time separation between the observations from the broadband measurements in Giveon et al. (1999) and the Bok/SPOL spectro-polarimetric measurements, the spectro-photometric calibration for the Bok/SPOL total and polarized flux spectra should have additional errors due to flux variability during the two Bok/SPOL observations in June 1996 and April 1998. Nevertheless, the magnitude uncertainty of the Bok/SPOL data does not affect the final result of this work in the long term because the observational constraint on the polarization source from the well-correlated total flux and the polarized flux variability (discussed in Section 5.4) can be verified even from only the two measurements of ESO3.6-m/EFOSC2 and Keck/LRIS whose magnitudes can be confidently evaluated.

SDSS photometry and LINEAR light curve during 2003-2008

3C 323.1 was photometrically observed by the SDSS Legacy Survey, using the SDSS imaging camera mounted on the Sloan Foundation 2.5-m telescope at the Apache Point Observatory (Gunn et al., 1998; York et al., 2000; Gunn et al., 2006). We use the SDSS g -band PSF magnitude of 3C 323.1, $g = 15.5606 \pm 0.0174$ mag, observed on the 12th June, 2004 (MJD=53168.3), retrieved from SDSS Data Release 12 (DR12) SkyServer (Alam et al., 2015). We checked the SDSS photometry flag, and confirmed that the g -band photometry satisfies the “clean photometry” criteria recommended on the SDSS web page⁶.

In addition, 3C 323.1 was observed between 2003 and 2008 as part of the Massachusetts Institute of Technology Lincoln Laboratory Lincoln Near-Earth Asteroid Research (LINEAR) survey using

⁶http://www.sdss.org/dr12/algorithms/photo_flags_recommend/

the 1-m LINEAR telescope (Stokes et al., 2000; Sesar et al., 2011). The LINEAR observations were carried out with an unfiltered set-up, and the magnitude values stored in the LINEAR Survey Photometric Database ⁷ are given in the LINEAR recalibrated magnitude (Sesar et al., 2011).

The SDSS photometry data and the LINEAR light curve for 3C 323.1 from MJD=52665 to 54582 are plotted in Figure 5.2. The multiple LINEAR measurements taken on the same night are binned to a weighted-average magnitude for each observation night. In the same figure, the epoch of the Keck/LRIS spectro-polarimetric observation by Kishimoto et al. (2004) on 4th May, 2003 (Section 5.2.2), is indicated by a vertical bar. As shown in Figure 5.2, since the LINEAR photometry data were taken approximately simultaneously with both the SDSS data and the Keck/LRIS spectro-polarimetry data, we are able to use the LINEAR photometry data to estimate the broad-band magnitude of 3C 323.1 at the epoch of the Keck/LRIS observation, as described below.

Because quasar spectra are significantly different from stellar spectra due to their strong broad emission lines, we do not adopt the LINEAR-to-SDSS photometric transformation equation derived by using the SDSS stellar photometry in Sesar et al. (2011). Instead, we assume that the LINEAR magnitude m_{LINEAR} is related to the SDSS g -band magnitude as $g = m_{LINEAR} + m_{g,0}$. This assumption is justified by the fact that the magnitude difference in the LINEAR measurements between the epochs of the observation of Kishimoto et al. (2004) and the SDSS observation is as small as ~ 0.07 mag, and thus the colour variability of 3C 323.1 between these epochs is also expected to be small (see e.g., Schmidt et al., 2012). The LINEAR magnitude at MJD=53165.26 is $m_{LINEAR} = 15.4747 \pm 0.0123$ mag, which can be directly compared to the SDSS photometry obtained three days later, at MJD=53168.3, with the assumption that the quasar flux variability on a time-scale of several days is essentially negligible. From these values, the magnitude shifts are calculated as

$$g = m_{LINEAR} + 0.0859 (\pm 0.0213) \text{ [mag]}. \quad (5.1)$$

Keck/LRIS spectro-polarimetry for 3C 323.1 was carried out at MJD=52763.6, and the LINEAR photometry data are available at MJD=52753.35 and MJD=52771.30 as $m_{LINEAR} = 15.4014 \pm 0.0091$ mag and $m_{LINEAR} = 15.4110 \pm 0.0140$ mag, respectively (the weighted-average is $m_{LINEAR} = 15.4043 \pm 0.0076$ mag). With the use of Equation 5.1, the g -band magnitude of 3C 323.1 at the epoch of the Keck/LRIS observation can be estimated as $g = 15.4902 \pm 0.0226$ mag.

The Keck/LRIS total flux spectrum for 3C 323.1 is scaled so that the g magnitude calculated by convolving the Keck/LRIS total flux spectrum with the g -band filter transmission curve taken from Doi et al. (2010) coincides with $g = 15.4902$ mag. Then, the polarized flux spectra are defined as the product of the polarization degree spectra in Figure 5.1 and the scaled total flux spectrum. The V -band magnitude of the scaled total flux Keck/LRIS spectrum is calculated as $V_{AB} = 15.5838$ mag, by using the V -band filter transmission curve taken from Bessell (1990). Because the measurement errors on the Bok/SPOL total flux spectrum are negligible compared to the g -band magnitude uncertainty of 0.0226 mag, we adopt 0.0226 mag as the error of the estimated V -band magnitude. The spectral

⁷The LINEAR Survey Photometric Database is available at the SkyDOT Web site (<http://skydot.lanl.gov/>)

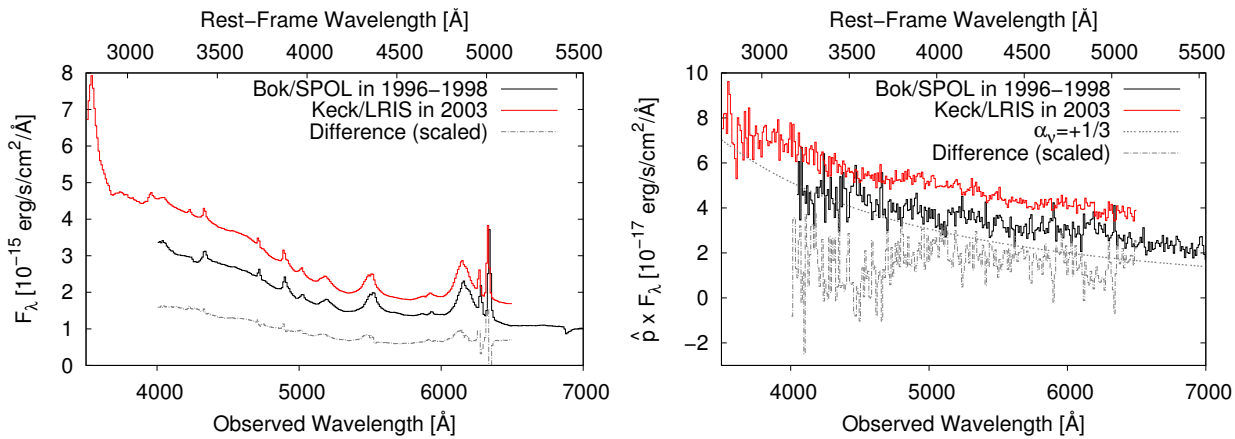


Figure 5.3: The total flux (top) and the polarized flux spectra (bottom) obtained with Bok/SPOL and Keck/LRIS. Galactic extinction is uncorrected. The arbitrarily-scaled difference spectra between the two measurements are also plotted. The spectra are binned into 10-Å-wide bins. For comparison, a power-law spectrum with $\alpha_v = +1/3$ is also plotted in the bottom panel.

monochromatic luminosity at 5100 Å is $\lambda L_\lambda(5100 \text{ Å}) = 1.7392(\pm 0.0362) \times 10^{45} \text{ erg/s}$. The scaled Keck/LRIS total flux spectrum and the polarized flux spectrum are shown in Figure 5.3.

5.3 Spectral variability of the polarimetric properties

In this section, the spectral variability between the two sets of spectro-polarimetry data obtained with Bok/SPOL and Keck/LRIS is examined.

5.3.1 Spectral variability of the polarization degree and the polarization position angle

Figure 5.1 clearly shows that, as noted by Schmidt & Smith (2000) and Kishimoto et al. (2004), the polarization degrees (q' , u' , and \hat{p}) at the wavelengths of the BLR emission are significantly diminished, making the polarization degree spectra strongly wavelength-dependent; in particular, the unpolarized “small blue bump”, which is composed of the Balmer continuum and the UV Fe II pseudo continuum from the BLR, is responsible for the decrease in the polarization degrees at $\lambda_{\text{rest}} < 4000 \text{ Å}$. Although the spectra of polarization degree do not show strong variability between the two measurements, it should be noted that the polarization degree (i.e., \hat{p}) at the rest-frame wavelength range of $\lambda_{\text{rest}} \sim 3600 \text{ Å}$ shows variations between the two spectro-polarimetric measurements (see Section 5.3.2 for details).

Each PA spectrum in the bottom panel of Figure 5.1 is nearly wavelength-independent. It is clear that, unlike the mainly time-constant polarization degrees, the PA spectra show clear evidence of variability. The difference in the PA evaluated at the rest-frame wavelength range of 4000-4731 Å is $\Delta PA_c = 4.6 \text{ deg}$, and the PA variability is nearly wavelength-independent (the bottom panel of

Figure 5.1). Because the systematic uncertainties in the grid of polarization standards are at most ~ 1 deg (e.g., Schmidt et al., 1992), the difference in the observed PA between the Bok/SPOL and Keck/LRIS measurements cannot be attributed to errors of the PA calibration by the use of different polarized standard stars, and therefore in this work the observed PA variability is assumed to be the intrinsic variability of the polarization properties of 3C 323.1.

Although PA variability is a general property of the blazar-like synchrotron emission (e.g., Ikejiri et al., 2011), Section 5.4.1 shows that synchrotron emission is not responsible for the optical polarization observed in 3C 323.1. If we assume that the optical polarization in 3C 323.1 is due to the scattering of the accretion disk continuum, the observed PA variability requires some time-variable axi-asymmetric structure in the scattering region of 3C 323.1, as discussed in detail in Sections 5.4.2 and 5.4.2.

5.3.2 Spectral variability of the polarized flux

In Figure 5.3, it is clear that the broad Balmer emission lines seen in the total flux spectra do not appear in either the Bok/SPOL or the Keck/LRIS polarized flux spectra; in other words, the BLR emission is unpolarized in 3C 323.1. As discussed by Kishimoto et al. (2004), the Keck/LRIS polarized flux spectrum ($\hat{p}_\lambda \times F_\lambda$) shows a clear broad absorption-like feature at around $\lambda_{\text{rest}} \sim 3600 \text{ \AA}$. Kishimoto et al. (2004) interpreted this feature as the Balmer continuum absorption, but they also noted the possibility that other higher-order Balmer series absorption lines and weak metal absorption lines also contribute to the absorption feature. However, this spectral feature seems to be weak or absent in the Bok/SPOL $\hat{p}_\lambda \times F_\lambda$ spectrum. Interestingly, the detailed shape of the two $\hat{p}_\lambda \times F_\lambda$ spectra also shows evidence of variability at the wavelength range of the $H\beta$ emission line ($\lambda_{\text{rest}} \sim 4861 \text{ \AA}$); there is a broad absorption-like feature at around the wavelength range of the $H\beta$ emission line in the Keck/LRIS polarized flux spectrum, but it is not clearly seen in the Bok/SPOL polarized flux spectrum. The spectral variability of $\hat{p}_\lambda \times F_\lambda$ at the wavelength ranges of the Balmer continuum and the $H\beta$ emission line can clearly be seen in the difference spectrum shown in the bottom panel of Figure 5.3.

The spectro-polarimetric variability of 3C 323.1 seen in the $\hat{p}_\lambda \times F_\lambda$ spectra (Figure 5.3) is very similar to that discovered by Kishimoto et al. (2004) in Ton 202; Kishimoto et al. (2004) have identified spectro-polarimetric variability between the two sets of Keck/LRIS data for Ton 202 obtained in 2002 and 2003 (one year apart), where the Balmer-edge absorption-like feature seen in the polarized flux spectrum in 2002 had disappeared by 2003. Kishimoto et al. (2004) suggested that the spectro-polarimetric variability of Ton 202 might be related to the time-variability of the geometry of the equatorial electron scattering region, but did not discuss how the changes in geometry resulted in the variability of the polarimetric properties around the Balmer continuum and emission lines. Apparently, if the broad absorption features in the polarized flux spectrum are assumed to be intrinsic to the disk thermal emission, it is very difficult to explain reasonably the time-variability of the absorption features by the changes in the geometry of the scattering region alone. Instead, as discussed in detail

in Section 5.4.2, we propose that the absorption features are imprinted by an absorbing region with a time-variable structure, which is assumed to be spatially separated from the UV-optical emitting regions of the accretion disk.

In the next section (Section 5.4), we focus on the V -band polarimetric and photometric variability. As can be clearly seen in Figure 5.3, the polarized flux variability in the wavelength range of the V -band [$\lambda_{obs} \sim 5000 - 5900 \text{ \AA}$ at full width at half maximum (FWHM)] is clearly detected with a high signal-to-noise ratio. It should be noted that the V -band is sampling the rest-frame wavelengths of $\lambda_{rest} \sim 4000 - 4700 \text{ \AA}$, within which the observed flux is dominated by the continuum emission. Therefore, the V -band polarimetric variability mostly reflects the variability of the polarized continuum component. This means that the final results of this work discussed in Section 5.4 are not affected by the putative changes to the polarization properties around the wavelength range of the Balmer continuum and other recombination lines discussed above.

5.4 V -band polarimetric and photometric variability and its interpretation

Figure 5.4 shows the photometric and polarimetric measurements for 3C 323.1 evaluated in the V -band summarised in Table 5.1 as a function of time. As shown in the top panel of Figure 5.4, the polarization degree \hat{p} does not show strong variability during the three observations taken during the period 1996-2003. The total flux F_ν of 3C 323.1 shows ~ 0.3 mag variability during the same period, and the small variability in \hat{p} results in the highly correlated variability between the V -band total flux and the polarized flux ($\hat{p} \times F_\nu$) (the bottom panel of Figure 5.4).

The middle panel of Figure 5.4 shows the V -band PA , compared with 3C 323.1's radio jet axis of 20 deg (Kishimoto et al., 2004). As has already been noted in Section 5.3.1, the observed PA differs between the Bok/SPOL and Keck/LRIS measurements by ~ 4 deg, although the difference between the PA and the radio axis is kept small (i.e., 3C 323.1 remains to be “parallel” polarization).

Below we discuss the geometrical constraints on the optical polarization source in 3C 323.1 derived from the polarimetric and photometric variability seen in Figure 5.4, and the possible interpretations of the optical polarization mechanism.

5.4.1 Evidence against the synchrotron origin of the optical polarization in 3C 323.1

As has already been mentioned in Section 5.3, on the one hand, the Keck/LRIS polarized flux spectrum shows clear broad absorption features, but on the other hand, the Bok/SPOL polarized flux spectrum is almost a smooth power-law spectrum. Based on the Bok/SPOL data, Schmidt & Smith (2000) have suggested that the weak flux contribution of the synchrotron emission to the optical wavelength range can explain the observed optical polarization in 3C 323.1 (see Section 5.1 for details). Even for

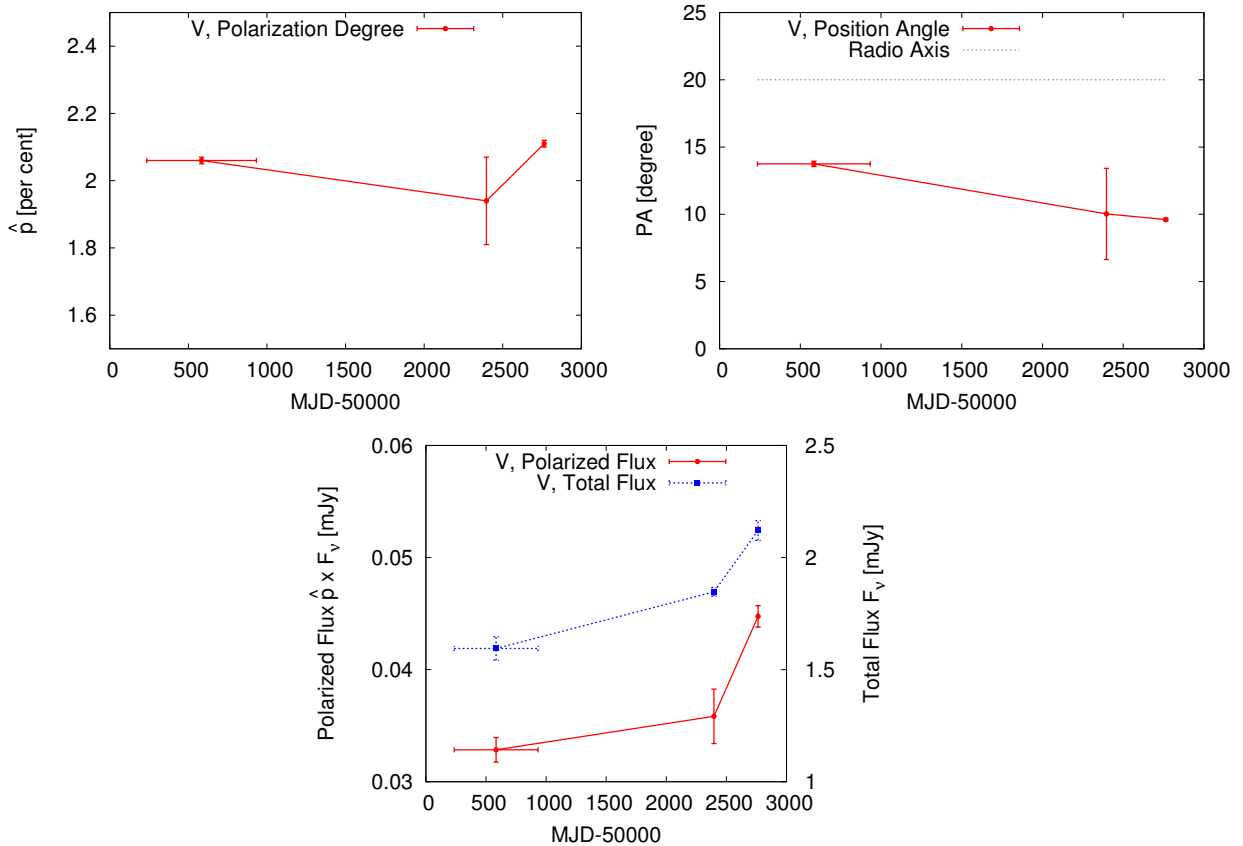


Figure 5.4: Top left and top right: light curves of polarization degree \hat{p} (top panel) and polarization position angle PA (middle panel) of 3C 323.1 given in Table 5.1. 3C 323.1's radio jet axis of 20 deg (Kishimoto et al., 2004) is indicated as a dotted line in the middle panel. Bottom: the light curves of the V-band polarized flux $\hat{p} \times F_v$ (solid line) and total flux F_v (dotted line) of 3C 323.1; Bok/SPOL in 1996-1998, ESO3.6-m/EFOSC2 on 1st May, 2002, and Keck/LRIS on 4th May, 2003.

the Keck/LRIS data, the synchrotron contribution scenario for the observed polarized flux cannot be ruled out with only the single epoch data; it is possible that the absorption features are imprinted in the intrinsically smooth synchrotron emission spectrum somewhere along the line of sight (Kishimoto et al., 2003).

However, we point out here that the observed polarimetric and photometric variability strongly suggests that the optical synchrotron emission is not the origin of the polarized flux component in 3C 323.1. As shown in Figure 5.4, the three V-band measurements reveal that both the total and the polarized fluxes vary almost simultaneously; in other words, the polarization degree is nearly time-constant (see also Figure 5.1). Because the variable component of the total flux must be dominated by the disk continuum emission as discussed in Section 5.2.1, the observed highly correlated variability between the total and polarized fluxes indicates that the polarized flux has a strong relationship with the accretion disk emission. Therefore, the observation of the polarimetric and photometric variability essentially excludes the possibility that the optical polarization source in 3C 323.1 is the optical

synchrotron emission.

In addition to the above mentioned evidence, with reference to the discussion provided in Kishimoto et al. (2003) for the case of Ton 202, we can also confirm the difficulty in attributing the observed polarized flux in 3C 323.1 solely to the flux contribution from the optical synchrotron emission in terms of its core-only radio-loudness. In general, the radio core emission of lobe-dominated quasars becomes optically thin at $\nu > 30$ GHz (Antonucci et al., 1990), and, thus, the ratio of the radio core flux to the optical synchrotron flux (measured at 5000 Å) is expected to be $\text{Flux}(\text{radio core})/\text{Flux}(\text{opt. sync.}) \sim 20,000$ by assuming $f_\nu \propto \nu^{-1}$ (Kishimoto et al., 2003). On the other hand, from 3C 323.1's radio-loudness for the core region $R_{\text{core}} = 41$ (Schmidt & Smith, 2000) and the observed optical polarization degree $p \sim 2\%$, the flux ratio of the radio core flux to the optical polarized flux is $R_{\text{core}}/p \sim 41/0.02 = 2050$. Therefore, if we assume that the optical polarized flux in 3C 323.1 originates from the synchrotron emission, the ratio of the radio core flux to the optical synchrotron flux must be $\text{Flux}(\text{radio core})/\text{Flux}(\text{opt. sync.}) \sim 2050 \times p_s < 2050$, where $p_s (< 1)$ is the fractional polarization degree of the putative optical synchrotron radiation. The discrepancy in the expected ($\sim 20,000$) and required ($\sim 2050 \times p_s$) ratio of the radio core flux to the optical synchrotron flux implies that the amount of flux contribution from the optical synchrotron in 3C 323.1 is too small (by at least an order of magnitude) to account for the observed polarized flux.

Considering the lines of evidence discussed above, we conclude that the optical synchrotron emission is not relevant for the observed optical polarization in 3C 323.1. In Section 5.4.2, we show that the observed polarimetric and photometric variability properties of 3C 323.1 are consistent with electron scattering from the equatorial scattering region, as proposed by Kishimoto et al. (2004) (see Section 5.1). However, it is apparently difficult to account for the observed PA variability seen in the middle panel of Figure 5.4 by the simple equatorial scattering scenario. We attempt to construct a geometrical model to explain all of the observed polarimetric and photometric properties of 3C 323.1 in Section 5.4.2.

5.4.2 Constraints on the geometry of the scattering region in 3C 323.1

In this section, we first obtain observational constraints on the radial extent of the scattering region inferred from the polarimetric and photometric variability via causal reasoning, and compare them with the size of the BLR and the dust torus of 3C 323.1. We then propose a geometrical model of the scattering/absorbing regions, which can potentially account for all of the observed polarimetric and photometric properties of 3C 323.1.

Radial extent of the scattering region inferred from the polarimetric and photometric variability

A robust constraint on the geometry of the scattering region can be derived from the highly correlated variability of the V -band total flux and the polarized flux. As has already been pointed out in Section 5.4.1, the two observations made by ESO3.6-m/EFOSC2 and Keck/LRIS on 1st May, 2002,

and 4th May, 2003, respectively (separated by one year, i.e., by 0.8 years in the quasar rest frame), show coordinated variability between the total and polarized fluxes. With the assumption that the polarization in 3C 323.1 is due to scattering of the disk continuum, the time lag between the total flux variation (disk continuum flux) and the polarized flux variation (scattered flux) corresponds to the light travel time across the accretion disk and the scattering region (e.g., Gaskell et al., 2012). Therefore, the observed coordinated variability of the total and polarized fluxes directly constrains the radial distance of the scattering region as

$$R_{\text{sca}}(pF \text{ var.}) < 0.8 \text{ [light years]}. \quad (5.2)$$

On the other hand, within the framework of the equatorial scattering scenario, the PA variability may possibly be interpreted as the change in geometry of the scattering region. Kishimoto et al. (2004) pointed out that the putative equatorial electron scattering region is assumed to be so small in size that its geometrical configuration can be changed within a one-year time-scale. If the putative equatorial electron scattering region in 3C 323.1 is not an axisymmetric disk-like structure but has an axi-asymmetric clumpy density distribution, the PA variability (with little variability in the polarization degree) may be a natural consequence of the orbital or bulk motion of the scattering region (see Section 5.4.2 for details). According to this interpretation, the PA variability observed in 3C 323.1 during the Bok/SPOL and Keck/LRIS observations (the two observations are 5-7 years apart, i.e. a quasar rest frame time-lag of < 6 years) implies that the maximum extent of the size of the scattering region R_{sca} is

$$\begin{aligned} R_{\text{sca}}(PA \text{ var.}) &< 6 \times \left(\frac{v_{\text{sca}}}{c} \right) \text{ [light years]} \\ &= 0.20 \times \left(\frac{v_{\text{sca}}}{10000 \text{ km/s}} \right) \text{ [light years]} \end{aligned} \quad (5.3)$$

where v_{sca} represents the typical velocity of the polarization source. If we assume that the polarization source is smaller in size than the BLR, it is reasonable to consider that the value of v_{sca} is larger than the velocity width of the broad emission lines. Since the $H\beta$ broad emission line of 3C 323.1 has an FWHM of ~ 7030 km/s (e.g., Boroson & Green, 1992), we take $v_{\text{sca}} = 10,000$ km/s to be a reference value in Equation 5.3.

Comparisons of the radial extent between the polarization source, BLR, and the dust torus

The geometrical constraints on the scattering region R_{sca} derived in Section 5.4.2 should be compared with the radial extent of the accretion disk, BLR, and the dust torus.

Under the assumption of the Shakura & Sunyaev (1973) accretion disk model, the disk radius at which the disk temperature matches the wavelength λ_{rest} as $k_B T_{\lambda_{\text{rest}}} = hc/\lambda_{\text{rest}}$ (h and k_B are the Planck constant and the Boltzmann constant, respectively) can be evaluated as (e.g., Morgan et al., 2010)

$$\begin{aligned} R_{\text{disk},\lambda_{\text{rest}}} &\simeq 0.01 \text{ [light years]} \\ &\times \left(\frac{\lambda_{\text{rest}}}{\mu\text{m}} \right)^{4/3} \left(\frac{M_{\text{BH}}}{10^9 M_{\odot}} \right)^{2/3} \left(\frac{L}{\eta L_E} \right)^{1/3}, \end{aligned} \quad (5.4)$$

where $\eta \equiv L/(\dot{M}c^2)$ indicates the radiative efficiency of the disk. The theoretical values of the radiative efficiency, including general relativistic corrections, range from 6% to 42% as a monotonically increasing function of the black hole spin (e.g., Shapiro & Teukolsky, 1983; Frank et al., 1992; Kato et al., 2008). By substituting $\log(M_{\text{BH}}/M_{\odot}) = 9.07$ and $L/L_E = 0.10$ taken from Shen et al. (2011) (see Section 5.2.1), the disk radius of $\lambda_{\text{rest}} = 5100 \text{ \AA}$ in 3C 323.1 can be calculated to be within the range

$$R_{\text{disk},5100\text{\AA}} = 0.003 - 0.005 \text{ [light years]}. \quad (5.5)$$

Recent observations of quasar microlensing events and AGN continuum reverberation mapping (e.g., Morgan et al., 2010; Edelson et al., 2015) have revealed that the actual accretion disk sizes in quasars are larger by a factor of ~ 4 than the size predicted by the Shakura & Sunyaev (1973) accretion disk model, but even considering such uncertainty, we can conclude from Equation 5.5 that the accretion disk radii responsible for the optical emission in 3C 323.1 can be regarded as a point source when viewed from the BLR or the dust torus (see below).

The $\text{H}\beta$ BLR radius has been determined by reverberation mapping of the broad $\text{H}\beta$ emission lines for several tens of AGN/quasars, and can be well expressed as a function of the continuum luminosity as (Bentz et al., 2009)

$$\log R_{\text{BLR}}[\text{light days}] = -21.3 + 0.519 \log(\lambda L_{\lambda}(5100\text{\AA}) [\text{erg/s}]) \quad (5.6)$$

By substituting the monochromatic luminosity $\lambda L_{\lambda}(5100 \text{ \AA})$ at the epochs of Bok/SPOL and Keck/LRIS (see Section 5.2.3), the BLR radius of 3C 323.1 is found to be in the range of

$$R_{\text{BLR}} = 0.33 - 0.41 \text{ [light years]}. \quad (5.7)$$

The dust reverberation radius of AGN/quasars (e.g., Barvainis, 1992; Suganuma et al., 2006; Kishimoto et al., 2011; Koshida et al., 2014, and references therein), which represents the radius of the innermost dust torus, is known to be well represented as a function of the continuum luminosity as $\log R_{\text{dust, in}} [\text{pc}] = -0.88 + 0.5 \log(\lambda L_{\lambda}(5500 \text{ \AA})/10^{44} [\text{erg/s}])$ (Koshida et al., 2014). By assuming $f_{\nu} \propto \nu^0$, this relation can be converted to

$$\log R_{\text{dust, in}}[\text{light days}] = -19.8 + 0.5 \log(\lambda L_{\lambda}(5100\text{\AA}) [\text{erg/s}]) \quad (5.8)$$

By substituting the monochromatic luminosity at the epochs of Bok/SPOL and Keck/LRIS, the innermost radius of 3C 323.1's dust torus is in the range of

$$R_{\text{dust, in}} = 1.47 - 1.81 \text{ [light years]}. \quad (5.9)$$

Figure 5.5 shows the comparison of the estimated radius of the BLR and the dust torus innermost radius of 3C 323.1 with the upper limits of the radial extent of the scattering region given in Equations 5.2 and 5.3. From this comparison, we can firmly conclude that the scattering region is located inside the dust torus. This means that scattering from regions larger than the dust torus as the dominant polarization mechanism in 3C 323.1 can be completely ruled out. Because the innermost radius

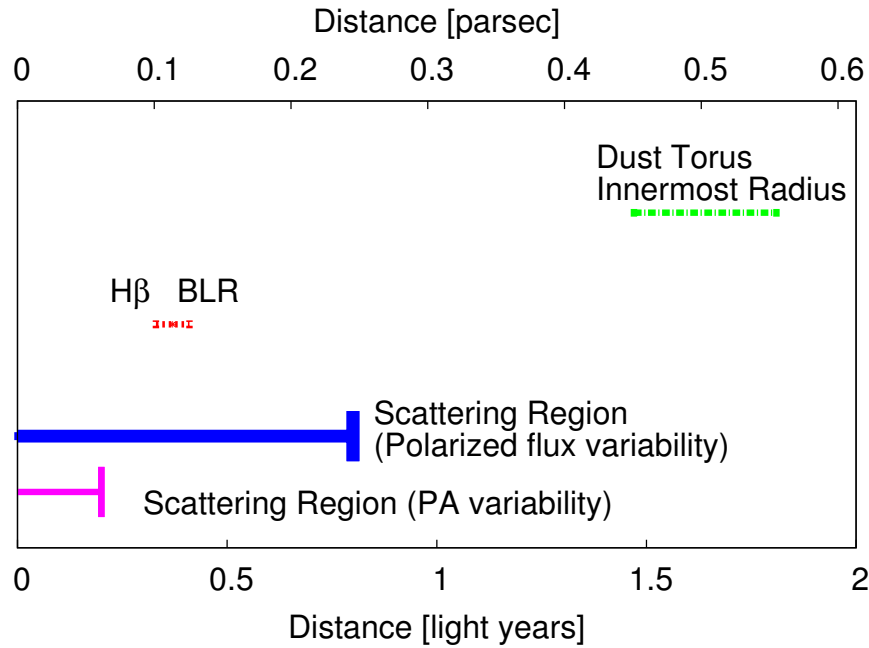


Figure 5.5: Observational constraints on the radial extent of the scattering region in 3C 323.1. Two independent upper limits on the radial extent of the scattering region are taken from the coordinated variability of the total flux and the polarized flux (Equation 5.2) and the observed time-scale of the polarization position angle variability (Equation 5.3 assuming $v_{\text{sca}} = 10,000$ km/s). The possible location of the $H\beta$ broad line region (BLR) and the radius of the innermost dust torus are also shown (see Section 5.4.2 for details). Note that the optical emitting region of the accretion disk in 3C 323.1 can be regarded as a central point source if viewed from the BLR and the dust torus (see Equation 5.5).

of the dust torus corresponds to the sublimation radius of the dust grains (e.g., Kishimoto et al., 2007; Mor & Netzer, 2012; Koshida et al., 2014; Netzer, 2015), there must be no dust grains inside the dust torus, and thus we can also conclude that electron scattering is the main contributor to the observed optical polarization in 3C 323.1. Moreover, by adopting the size constraint of $R_{\text{sca}}(\text{PA var.}) < 0.20$ light years (Equation 5.3) at face value, the scattering region should be smaller in size than the BLR, which in turn validates the assumption of the high velocity of the scattering region v_{sca} adopted to derive the constraint on R_{sca} in Equation 5.3. As has been mentioned in Section 5.1, the scattering region inside the BLR cannot produce the net polarization of the BLR emission, ensuring the null-polarization of the BLR emission of 3C 323.1. In summary, the constraints on the radial extent of the scattering region in 3C 323.1 obtained in Section 5.4.2 are consistent with the equatorial electron scattering scenario proposed by Kishimoto et al. (2003, 2004, 2008b) as the interpretation of the polarization properties of quasars with continuum-confined polarization.

A possible model for the scattering geometry in 3C 323.1

Although the constraints on the radial extent of the scattering region in 3C 323.1 obtained in Section 5.4.2 suggest that the scattering region is located inside the BLR, they do not specify the detailed geometry of the scattering region. Indeed, as was partially discussed above (Sections 5.3 and 5.4.2), several lines of evidence suggest that the simple assumption that there is an axisymmetric disk-like electron-scattering region that directly scatters accretion disk continuum photons into our line of sight cannot fully account for the observed polarimetric and photometric properties of 3C 323.1.

To infer the true geometrical structure of the inner region of 3C 323.1, we have to take the following observational properties into account:

- As noted in Section 5.4.2, the observed *PA* variability in 3C 323.1 requires the presence of some axi-asymmetric structure in the scattering region, which changes its geometry on a time-scale of several years;
- The variability of the broad absorption like features in the polarized flux spectra between the Bok/SPOL and the Keck/LRIS observations (Section 5.3.2) suggests that either (a) the broad absorption features are intrinsic to the accretion disk emission and the strength of the absorption features are time-variable, or (b) there is a high-velocity absorbing region somewhere along the line of sight whose geometry is time-variable;
- As noted in Section 5.1 (see also Section 5.2.1), Kokubo (2016) has shown that the spectral shape of the intrinsic accretion disk continuum of 3C 323.1 revealed as the variable component spectrum is inconsistent with that revealed as the polarized flux spectrum, in that the variable component spectrum is much bluer than the polarized flux spectrum (Figure 5.3). Within the equatorial scattering geometry, the discrepancy of the spectral shape between the variable and the polarized flux components can only be explained by the above-mentioned scenario (b) as long as the absorbing materials are co-spatial with the equatorial scattering region or located between the accretion disk and the scattering region.

Figure 5.6 illustrates the geometrical model that can explain the above-mentioned observational properties of 3C 323.1. In this model, an equatorial absorbing region responsible for the broad absorption features (the Balmer continuum, and possibly the Balmer and other weak metal lines, as mentioned in Section 5.3.2) is located inside (or co-spatial with) the optically-thin equatorial electron scattering region. With this geometrical configuration, the total flux spectrum, and similarly the variable component spectrum, directly reflects the spectral shape of the intrinsic accretion disk continuum, while the polarized flux spectrum shows additional broad absorption features induced by the equatorial absorbing region because the observed polarized light has once passed through the absorbing region. This also indicates that the intrinsic accretion disk continuum is featureless as observed as the variable component spectrum. The geometrical model in Figure 5.6 is essentially the same as that considered by Kishimoto et al. (2003) and Kokubo (2016) [see the model (a) in Figure 6

of Kishimoto et al. 2003], but in our model the structure of the absorbing/scattering regions is assumed to be axi-asymmetric and time-variable to account for the polarimetric variability observed in 3C 323.1. By requiring that the radial extent of the scattering region is smaller in size than the BLR (i.e., $R_{\text{sca}} \lesssim 0.33 - 0.41$ light years; Equation 5.7), the dynamical time-scale (Kepler orbital time) t_{dyn} of the scattering materials is at most $t_{\text{dyn}} \lesssim 88 - 122$ years, assuming $\log(M_{\text{BH}}/M_{\odot}) = 9.07$. Therefore, it is possible, in principle, that some dynamical motions (not only the orbital motions but also the radial motions) of the scattering materials gradually modify the net polarization PA on time-scales of several years while keeping the polarization degree nearly constant, as observed in 3C 323.1. The spectral variability of the polarized flux spectra between the Bok/SPOL and Keck/LRIS observations discussed in Section 5.3.2 can be attributed to some dynamical motions of the absorbing materials.

From the currently available observational constraints alone, it is impossible to specify the physical origins of the absorbing/scattering materials assumed in the proposed model. One promising candidate to produce time-variable inhomogeneous equatorial scattering/absorbing structures is the accretion disk wind, similar to those observed in broad absorption line (BAL) quasars (Elvis, 2000; Proga et al., 2000; Young et al., 2007; Matthews et al., 2016), especially Balmer-BAL quasars (Zhang et al., 2015, and references therein). In addition, it may be possible that the accretion disk itself is flaring up at a particular radius (e.g., Lira et al., 2011; Jiang et al., 2016a) and that the flared region absorbs some quantity of photons from the inner disk region travelling toward the equatorial direction.

Although this work deals with only a single radio-loud quasar 3C 323.1, we believe that the optical polarization source in other radio-quiet/radio-loud quasars with continuum-confined polarization must be similar to that proposed here considering the similarities of the spectral shape of the polarized flux spectra and the variable component spectra (see Kishimoto et al., 2004, 2008b; Kokubo, 2016). Further polarimetric and multi-wavelength monitoring observations for quasars with continuum-confined polarization will eventually clarify the detailed geometry and the true nature of the scattering/absorbing regions in these quasars.

5.5 Summary and conclusions of Chapter 5

We examine the polarimetric and photometric variability of 3C 323.1 by using two optical spectropolarimetric measurements taken during 1996-1998 (Bok/SPOL) and 2003 (Keck/LRIS) and a V -band imaging-polarimetric measurement taken in 2002 (ESO3.6-m/EFOSC2). The two spectropolarimetric measurements reveal that the polarimetric properties at the wavelength range of the Balmer continuum and other recombination lines are time-variable, while the polarized degree \hat{p} of the continuum emission is nearly constant (Figures 5.1 and 5.3). The V -band polarimetric and photometric measurements (where two of the three measurements are calculated from the two spectropolarimetry data sets) confirm that the polarization PA is variable on a time-scale of several years (Figure 5.4). Moreover, the light curves of the V -band total and polarized fluxes show highly correlated variability (Figure 5.4), indicating that the polarized flux is the scattered disk continuum emis-

sion because there is evidence to suggest that the variability of the total flux is due to the intrinsic variability of the accretion disk continuum emission.

The variability time-scales of the PA and the polarized flux introduce the constraint that the polarization source in 3C 323.1 is located inside the BLR (Figure 5.5), which is consistent with the equatorial electron scattering scenario suggested by Kishimoto et al. (2004). We propose a more sophisticated geometrical model to account for the polarimetric and photometric properties, as well as the variability in behaviour, observed in 3C 323.1. Our model comprises an equatorial absorbing region and an optically-thin equatorial electron-scattering region, which surrounds the UV-optical emitting regions of the accretion disk (Figure 5.6). The absorbing region is assumed to be co-spatial or smaller in size compared to the scattering region. As schematically shown in Figure 5.6, this geometrical configuration can explain the discrepancy in the spectral shape of the accretion disk continuum emission in 3C 323.1 revealed as the variable component spectrum (measured by Kokubo, 2016) and as the polarized flux spectrum. The structures of both the absorbing region and the scattering region are assumed to be axi-asymmetric and time-variable to account for the variability of the broad absorption features in the polarized flux and the variability of the PA observed in 3C 323.1.

Although the physical origins of the absorbing region and the scattering region are unclear, the accretion disk wind must be a promising candidate to produce the equatorial absorbing/scattering regions around the accretion disk. We believe that the structure of the inner regions of other quasars with continuum-confined polarization must be similar to that proposed here for 3C 323.1, considering the similarities in the spectral shape of the polarized flux spectra and the variable component spectra (see Kishimoto et al., 2004, 2008b; Kokubo, 2016). Further polarimetric and multi-wavelength monitoring observations for these quasars will enable us to probe the true nature of the internal structure of these quasars.

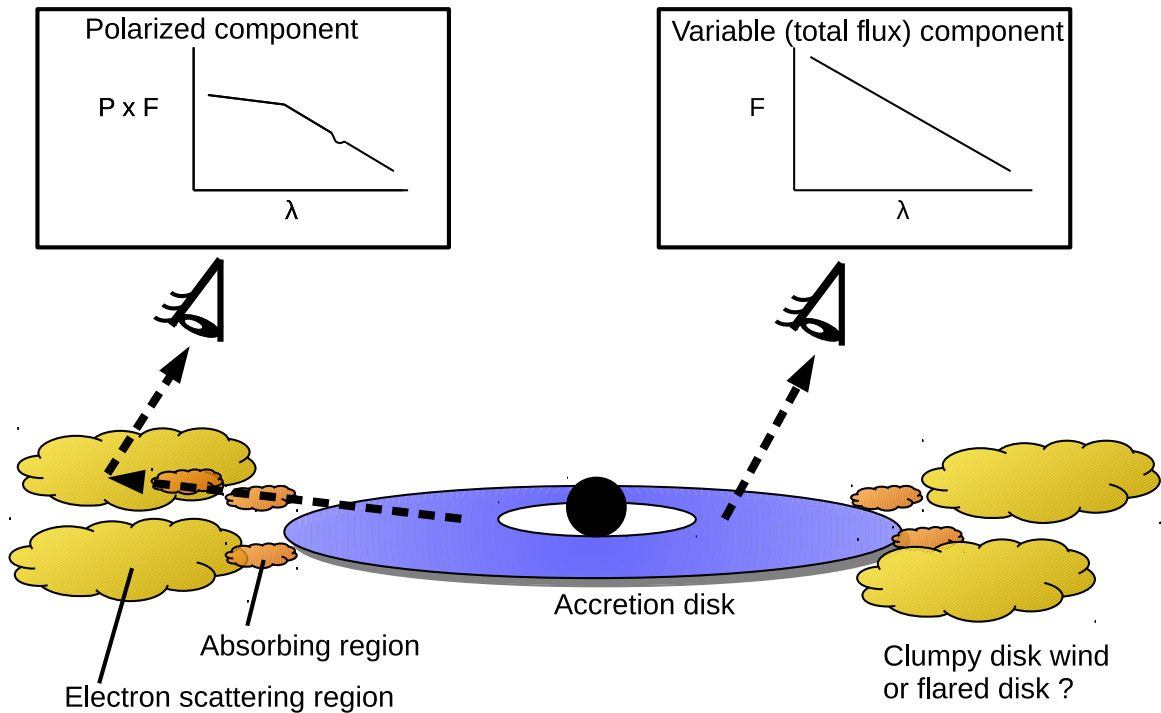


Figure 5.6: Schematic drawing of the geometrical model for the scattering region of 3C 323.1 and of other quasars with continuum-confined polarization. Note that the broad line region (BLR) is situated outside the optically-thin equatorial electron-scattering region, ensuring the null-polarization of the BLR emission. The variable component spectrum (i.e., the total flux spectrum) directly reflects the spectral shape of the disk continuum emission, while the polarized flux spectrum shows broad absorption features (the Balmer continuum and possibly the Balmer and metal lines; see Figure 5.3) due to the equatorial absorbing region, which is either co-spatial with the scattering region or located between the accretion disk and the scattering region. The geometric configurations of both the scattering and the absorbing regions are assumed to be axi-symmetric and time-variable to account for the slight variations of the polarization position angle and the absorption features in the polarized flux observed in 3C 323.1. A clumpy disk wind or flared disk surface may possibly be the physical origin of the absorbing/scattering regions.

Chapter 6

Summary and prospects for future work

In this dissertation, we study the flux variability and polarization of the UV-optical AGN/quasar emission. These two characteristic features of the AGN/quasar emission enable us to closely examine the intrinsic accretion disk continua. A brief summary of each chapter is given as follows:

- In Chapter 2, we examine the statistical properties of the spectral variability of quasars by using a large sample of multi-band light curves of quasars in the SDSS Stripe82 region (Kokubo et al., 2014). By applying the flux-flux gradient method to these quasar light curves, the 2-band color of the variable spectral components are derived (Figure 2.9). It is shown that the variable component spectra of the quasars are much bluer ($\alpha_v \sim +1/3$) than the directly-observed spectra ($\alpha_v \sim -0.5$). The comparisons of the color of the variable component spectra with that of the “variable mass accretion rate model” predictions (Figure 2.13) reveal that the variable component spectra are too blue at the rest-frame UV wavelengths to be explained by the variable mass accretion rate model. Moreover, the flatness of the quasar variable component spectra with $\alpha_v \sim +1/3$ through all the examined UV-optical wavelengths ($\lambda_{rest} > 1216\text{\AA}$) excludes the possibility that the variable component spectra are explained by existing alternative disk models because these models generally predict redder color than the standard disk model.
- In Chapter 3, we examine whether the “inhomogeneous accretion disk model” proposed by Dexter & Agol (2011) can simultaneously explain the variability amplitude and the strong inter-band correlation observed in the SDSS Stripe82 quasars (Kokubo, 2015). The variability amplitude is quantified as the standard deviation of the single-band light curves (V), and the inter-band correlation is quantified as the intrinsic scatter from the linear magnitude-magnitude relation of the two-band light curves (σ_{int}). By comparing the $V - \sigma_{\text{int}}$ plots of the observational data and the inhomogeneous accretion disk model simulations (Figure 3.9 and 3.10), we conclude that the inhomogeneous accretion disk model predict systematically larger σ_{int} (i.e., weaker inter-band correlation) compared to the real quasars. This study demonstrates that the observed inter-band correlations in AGNs/quasars impose strong constraints on the variability models involving many localized instabilities/flares over the disk surface.
- In Chapter 4, we study the relationship between the variable component and the polarized com-

ponent spectra in each of the four quasars with continuum-confined polarization (B2 1208+32, Ton 202, 3C 323.1, and 4C 09.72) (Kokubo, 2016). According to the current knowledge on the variability and polarization, both of the variable component spectra and the polarized flux spectra in these quasars should reflect the intrinsic accretion disk emission spectra. However, by comparing these two spectral components by using the archival spectropolarimetry data and the newly obtained multi-band light curves for these quasars, we show that they have totally different spectral shape (Figure 4.6), suggesting that there are fundamental problems in our current understanding of the quasar UV-optical variability and/or polarization. Two possibilities remains; one is that the polarization source in these quasars is not the simple equatorial electron (Thomson) scattering of the disk continua; second is that the variable component spectra do not reflect the whole accretion disk emission but represent the disk emission from much smaller (innermost) regions.

- In Chapter 5, we constrain the polarization source in one of the quasars with continuum-confined polarization studied in Chapter 4, 3C 323.1, by examining the polarimetric and photometric variability of this object. 3C 323.1 is spectro-polarimetrically observed in 1996-1998 (Schmidt & Smith, 2000) and in 2003 (Kishimoto et al., 2004), and is also imaging-polarimetrically observed in 2003 (Sluse et al., 2005). It is discovered that the total (\sim unpolarized) flux and the polarized flux in 3C 323.1 show strongly correlated variability during the three epochs of the polarimetric measurements (Figure 5.4), and that the polarization position angle (PA_{sky}) also show time-variability. The polarized flux spectra of Bok/SPOL and Keck/LRIS show evidence of a time-variable broad absorption feature in the wavelength range of the Balmer continuum and other recombination lines. From these observational facts, the size constraints on the polarization source can be derived; the observed coordinated variability of the total and the polarized flux constrains the size as $R_{pol}(pF \text{ var}) < 0.8$ light years (Equation 5.2); the PA_{sky} variability constrains the size as $R_{pol}(PA_{sky} \text{ var}) < 0.10 - 0.17(v_{sca}/10000 \text{ [km/s]})$ light years, where v_{sca} is (unconstrained) typical velocity of the scattering region (Equation 5.3). Both of these constrains suggest that the polarization source in 3C 323.1 is located inside the dusty torus and possibly inside the BLR, being consistent with the equatorial electron scattering scenario (Figure 5.5). We propose a geometrical model for the polarization source in 3C 323.1 (Figure 5.6), in which an equatorial absorbing region and an axi-asymmetric equatorial electron-scattering region are assumed to be located between the accretion disk and the broad line region. The scattering/absorbing regions can perhaps be attributed to the accretion disk wind or flared disk surface.

Conclusions of each chapter and the relationship between chapters of this dissertation are summarized as a block diagram in Figure 6.1. From the studies in this dissertation, we point out that the similarity of the power-law index of $\alpha_\nu \sim +1/3$ between the variable component spectra of quasars and the standard accretion disk model prediction (Equation 1.11) strongly suggests that the variable component are reflecting the intrinsic global disk continua (Chapter 2). On the other hand, the polari-

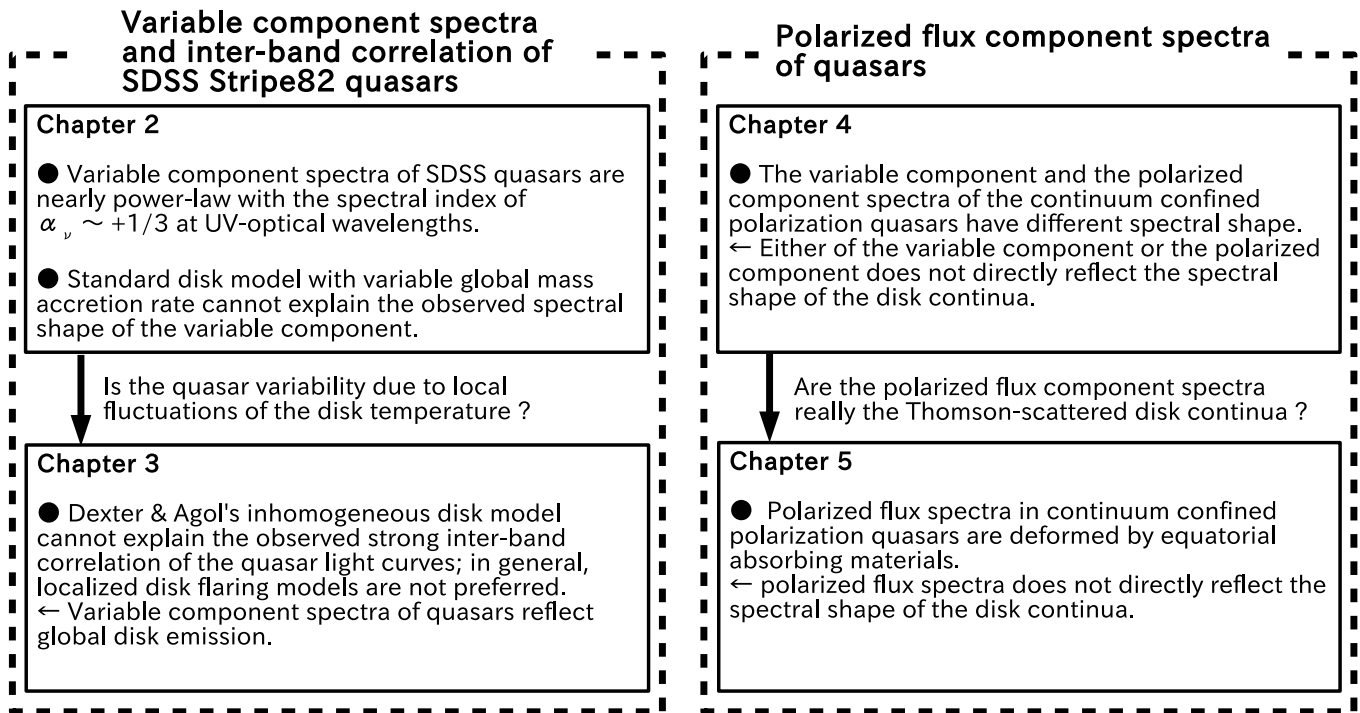


Figure 6.1: Conclusions of each chapter, and the relationship between chapters of this dissertation.

metric variability study in Chapter 5 implies that the polarized flux component spectra of quasars do not directly reflect the intrinsic disk continua, but reflect the deformed disk emission spectra affected by the equatorial absorbing materials. We also claim that the “variable mass accretion rate” model, which has been considered to be an influential model for the quasar UV-optical flux variability (e.g., Pereyra et al., 2006), can not properly account for the observed steep variable component spectra (of $\alpha_\nu \sim +1/3$).

In summary, these studies clarify that the observational properties of the UV-optical variability and polarization can strongly constrain models of the accretion disk and of the inner structure of AGNs/quasars. I emphasize that we should investigate models of quasar accretion disks which can naturally account for the general properties of the years time-scale AGN/quasar variability, namely, the large variability amplitude and the tight inter-band correlation within the UV-optical wavelength range, simultaneously. Although several clues to the origin of the variability and polarization have been taken from the results obtained in this work, it is still needed to gather additional observational constraints on the observed variability properties.

It should be noted that, as discussed in Sections 1.3.2, the X-ray reprocessing may be an important physical process determining the accretion disk structure and causing the UV-optical flux variability in AGNs/quasars (e.g., Collier et al., 1999; Cackett et al., 2007; Noda et al., 2016). In the X-ray reprocessing model, heating by the X-ray irradiation is considered to be the additional heating source of the accretion disk to the viscous heating; the viscous heating rate D_{vis} and the X-ray irradiation

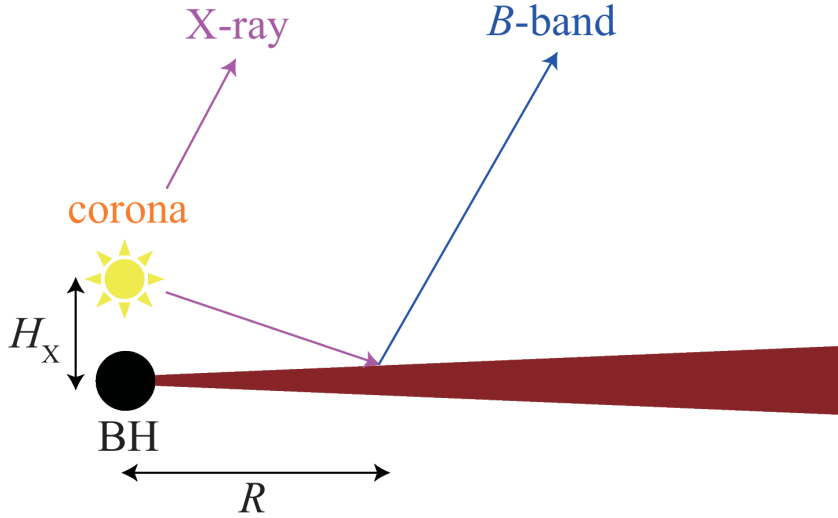


Figure 6.2: Schematic drawing of the X-ray reprocessing model with the lamp-post corona geometry (this figure is taken from Figure 12 of Noda et al., 2016).

heating rate D_{irr} at $R \gg R_{\text{in}}$ can be expressed as (Noda et al., 2016)

$$D_{\text{vis}} = \frac{3GM_{\text{BH}}\dot{M}}{8\pi R^3}, \quad (6.1)$$

$$D_{\text{irr}} = \frac{(1-A)L_X}{4\pi R_X^2} \cos \theta \quad (6.2)$$

where L_X is the X-ray luminosity, A is the disk albedo, $R_X \equiv \sqrt{R^2 + H_X^2}$, and $\cos \theta \equiv H_X/R_X$ (see Figure 6.2). By assuming $H_X \ll R$, $R_X \approx R$ and $\cos \theta \approx H_X/R$, thus

$$D_{\text{irr}} \approx \frac{(1-A)L_X H_X}{4\pi R^3}. \quad (6.3)$$

It is important to note that D_{vis} (Equation 6.1) and D_{irr} (Equation 6.3) has the same R dependence. From Stefan-Boltzmann law, $\sigma_S T_{\text{eff}}^4 = D_{\text{tot}}$ where the total heating rate D_{tot} is defined as $D_{\text{tot}} = D_{\text{vis}} + D_{\text{irr}}$, the disk effective temperature T_{eff} (Equation 1.1) is modified to

$$T_{\text{eff}}(R) = \left(\frac{3GM_{\text{BH}}\dot{M}_{\text{vis+irr}}}{8\pi\sigma_S} \right)^{1/4} R^{-3/4} \quad [R \gg R_{\text{in}}]. \quad (6.4)$$

$$\text{where } \dot{M}_{\text{vis+irr}} \equiv \dot{M} + \frac{2(1-A)L_X H_X}{3GM_{\text{BH}}} \quad (6.5)$$

Following the same discussion with Equation 1.11, $T_{\text{eff}}(R) \propto R^{-3/4}$ leads to $L_\nu \propto \nu^{+1/3}$. This means that the X-ray reprocessing increases the effective mass accretion rate $\dot{M}_{\text{vis+irr}}$, and leads to the increase of the disk temperature. As shown in the right panel of Figure 2.12), when the disk characteristic temperature T^* becomes to be larger than 200,000 K, the disk emission spectrum becomes to be $\nu^{+1/3}$ at all wavelengths in the UV-optical range. Therefore, the observed flux difference spectrum

of $\Delta L_\nu \propto \nu^{1/3}$ in quasars (Chapters 2 and 4) can be explained if the X-ray heating can increase the disk characteristic temperature to $T^* > 200,000$ K. The X-ray reprocessing model predicts that the optical light curves lag behind the X-ray light curves by several hours to days (i.e., light crossing times of the accretion disks; see Equation 1.23), and recent reverberation studies confirm that such lags are actually observed in several nearby Seyfert galaxies (Noda et al., 2016; Starkey et al., 2016, and references therein). However, as noted in Section 3.6, several authors have pointed out that the X-ray luminosity of quasars is insufficient to power the large UV-optical variability amplitude (e.g., Antonucci et al., 1996; Gaskell, 2008; Edelson et al., 2014; Uttley & Casella, 2014). Further simultaneous X-ray and optical observations for quasars are needed to examine whether the X-ray reprocessing model can be applicable not only to nearby Seyfert galaxies but also to quasars.

Finally, we point out that one promising way to directly probe the regions responsible for the variability and polarization in quasars is the observation for the microlensing events (e.g., Czerny et al., 1994; Gould & Miralda-Escudé, 1997; Yonehara et al., 1999; Agol & Krolik, 1999; Takahashi et al., 2001); it has been suggested that the multi-band monitoring observations for microlensing quasars will provide information on the regions on the disk where the intrinsic flux variability occurs (e.g., Wyithe & Loeb, 2002; Blackburne & Kochanek, 2010; Dexter & Agol, 2011). In the same way, the polarimetric monitoring observations for microlensing quasars will provide tight geometrical constraints on the polarization source in these quasars (e.g., Belle & Lewis, 2000; Chae et al., 2001; Hales & Lewis, 2007; Kedziora et al., 2011; Hutsemékers et al., 2015). We expect that future photometric/polarimetric monitoring observations for microlensing quasars, as well as for a large sample of normal quasars (i.e., extension of the study in Chapter 5) will eventually clarify the origin of the UV-optical variability and polarization in AGNs/quasars and consequently the accretion disk physics.

Acknowledgments

I would like to express my greatest thanks to Mamoru Doi for his valuable suggestions and advices. I would like to thank Tomoki Morokuma and Takeo Minezaki for guiding and supporting all of my research quite earnestly. I also acknowledge Hirofumi Noda, Makoto Kishimoto, Toshihiro Kawaguchi, Hiroaki Sameshima, Shintaro Koshida, and Makoto Kishimoto for useful discussions and comments. I thank Jason Dexter for help with understanding the inhomogeneous accretion disk model, and Gary D. Schmidt and Paul S. Smith for providing me with an electronic version of the spectropolarimetric data used in Schmidt & Smith (2000).

I thank to Shigeyuki Sako, Hidenori Takahashi, and the members of Doi's laboratory and , Hanindyo Kuncarayakti, Yasuhito Hashiba, Kazuma Mitsuda, Yuki Kikuchi, Jian Jiang, and Yuki Taniguchi. I have studied a lot about astrophysics and astronomical observations/instrumentations from the discussion with them. I would like to thank graduate students and staffs in Institute of Astronomy (IoA), the University of Tokyo. I am especially thankful to Kohei Hattori, Hideki Umehata, Hirokazu Fujii, Takaharu Shimizu, Takuma Izumi, Hiroki Minaguchi, Kazushi Okada, Yutaro Kitagawa, Masaki Yamaguchi, Ryu Makiya, Shun Ishii, and Ryou Ohsawa. I have improved my Japanese speaking skill with daily conversations with them.

I thank Yuki Sarugaku for his support during the KWFC queue mode observations at the Kiso observatory. I am grateful to all the staff in the Kiso Observatory, especially Tsutomu Aoki, Takao Soyano, Ken-ichi Tarusawa, and Hiroyuki Mito, for their efforts to maintain the observation system. I would like to thank the members of Nishi-Harima Astronomical Observatory (NHAO) for the kind hospitality during my stay at NHAO for development of Line Imager and Slit Spectrograph (LISS) (Hashiba et al., 2014; Kokubo et al., 2015).

This work was in part supported by JSPS KAKENHI Grant Number 15J10324.

This research has made use of NASA's Astrophysics Data System Bibliographic Services. This research has made use of the NASA/IPAC Extragalactic Database (NED), which is operated by the Jet Propulsion Laboratory, California Institute of Technology, under contract with the National Aeronautics and Space Administration.

Data analysis in Chapter 2 and Chapter 3 were in part carried out on common use data analysis computer system (pc08, IDL8.1) at the Astronomy Data Center, ADC, of the National Astronomical Observatory of Japan.

The work in Chapter 5 is partially based on data obtained from the ESO Science Archive Facility (ESO Programme ID 68.A-0373, PI: D. Hutsemékers). Some of the data presented in Chapter 5 were obtained at the W.M. Keck Observatory, which is operated as a scientific partnership among the California Institute of Technology, the University of California and the National Aeronautics and Space Administration. The Observatory was made possible by the generous financial support of the W.M. Keck Foundation. This research has made use of the Keck Observatory Archive (KOA), which is operated by the W. M. Keck Observatory and the NASA Exoplanet Science Institute (NExSci), under contract with the National Aeronautics and Space Administration (Keck Program ID U67L, PI: O. Blaes).

The LINEAR program is sponsored by the National Aeronautics and Space Administration (NRA No. NNH09ZDA001N, 09-NEOO09-0010) and the United States Air Force under Air Force Contract FA8721-05-C-0002.

Funding for the SDSS and SDSS-II has been provided by the Alfred P. Sloan Foundation, the Participating Institutions, the National Science Foundation, the U.S. Department of Energy, the National Aeronautics and Space Administration, the Japanese Monbukagakusho, the Max Planck Society, and the Higher Education Funding Council for England. The SDSS website is <http://www.sdss.org/>.

The SDSS is managed by the Astrophysical Research Consortium for the Participating Institutions, which are the American Museum of Natural History, Astrophysical Institute Potsdam, University of Basel, University of Cambridge, Case Western Reserve University, University of Chicago, Drexel University, Fermilab, the Institute for Advanced Study, the Japan Participation Group, Johns Hopkins University, the Joint Institute for Nuclear Astrophysics, the Kavli Institute for Particle Astrophysics and Cosmology, the Korean Scientist Group, the Chinese Academy of Sciences (LAMOST), Los Alamos National Laboratory, the Max-Planck-Institute for Astronomy (MPIA), the Max-Planck-Institute for Astrophysics (MPA), New Mexico State University, Ohio State University, University of Pittsburgh, University of Portsmouth, Princeton University, the United States Naval Observatory, and the University of Washington.

Funding for SDSS-III has been provided by the Alfred P. Sloan Foundation, the Participating Institutions, the National Science Foundation, and the U.S. Department of Energy Office of Science. The SDSS-III web site is <http://www.sdss3.org/>.

SDSS-III is managed by the Astrophysical Research Consortium for the Participating Institutions of the SDSS-III Collaboration including the University of Arizona, the Brazilian Participation Group,

Brookhaven National Laboratory, Carnegie Mellon University, University of Florida, the French Participation Group, the German Participation Group, Harvard University, the Instituto de Astrofísica de Canarias, the Michigan State/Notre Dame/JINA Participation Group, Johns Hopkins University, Lawrence Berkeley National Laboratory, Max Planck Institute for Astrophysics, Max Planck Institute for Extraterrestrial Physics, New Mexico State University, New York University, Ohio State University, Pennsylvania State University, University of Portsmouth, Princeton University, the Spanish Participation Group, University of Tokyo, University of Utah, Vanderbilt University, University of Virginia, University of Washington, and Yale University.

Appendix A

Symbols and acronyms

Symbols and acronyms used in this dissertation are summarized in Table A.1.

Table A.1: List of symbols and acronyms

Symbol/acronym	Definition
AGN	Active Galactic Nuclei
BAL	Broad absorption line quasars
BBB	Big Blue Bump
BEL	Broad emission line emitted in BLR
BH	Black hole
BLR=BELR	Broad emission line region
BWB/RWB	Bluer-When-Brighter/Redder-When-Brighter
DR	Data release
DRW	Damped random walk
EFOSC2	ESO Faint Object Spectrograph and Camera (v.2) for The ESO 3.6m Telescope
FORS	FOcal Reducer and low dispersion Spectrograph for 8-m VLT telescope
FWHM	Full Width at Half Maximum
IGM	Inter-galactic medium
ISP	Galactic inter-stellar polarization
KWFC	Kiso Wide FIeld Camera for 1.05-m Kiso Schmidt telescope
LINEAR	Lincoln Near-Earth Asteroid Research
LRIS	The Low Resolution Imaging Spectrometer for 10-m Keck telescope
LTE	Local thermodynamic equilibrium
MJD	Modified Julian Date
NIR, MIR	Near-Infrared, Mid-infrared

Table A.1: Continued

Symbol/acronym	Definition
NLR	Narrow Line Region
PSF	Point spread function
SBB	Small Blue Bump
SDSS	Sloan Digital Sky Survey
SED	Spectral Energy Distribution
SMBH	Supermassive black hole
SPOL	CCD Imaging/Spectropolarimeter for 2.3m Bok Telescope
UV	Ultra-violet
VLT	The Very Large Telescope
General	
M_{BH}	Black hole mass
M_{\odot}	The solar mass = 1.98855×10^{33} g
\dot{M}	Mass accretion rate (mass per unit time)
ISCO	The Innermost stable circular orbit
R	Radial coordinate centered at the SMBH
$R_{\text{in}}, R_{\text{out}}$	The disk inner radius, the disk outer radius
R_S	Schwarzschild radius
$T_{\text{eff}}(R)$	Disk effective surface temperature as a function of R
T^*	Disk characteristic temperature
ϵ	Mass-to-radiation conversion efficiency in accretion disks
a^*	Dimensionless black hole spin parameter
λ	Wavelength
ν	Frequency
$\lambda_{\text{rest}}, \nu_{\text{rest}}$	Rest-frame wavelength/frequency
$\lambda_{\text{obs}}, \nu_{\text{obs}}$	Observed-frame wavelength/frequency
L_{Edd}	Eddington luminosity (in the unit of erg/s)
L_{bol}	Bolometric luminosity (in the unit of erg/s)
η	Eddington ratio $\eta = L_{\text{bol}}/L_{\text{Edd}}$
$L_{2200\text{\AA}}$	Luminosity at 2200 \AA ; $L_{2200\text{\AA}} \equiv \lambda L_{\lambda}(2200\text{\AA})$ (in the unit of erg/s)
$L_{5100\text{\AA}}$	Luminosity at 5100 \AA ; $L_{5100\text{\AA}} \equiv \lambda L_{\lambda}(5100\text{\AA})$ (in the unit of erg/s)
L_{ν}	Luminosity per unit frequency (in the unit of erg/s/Hz)
F_{ν}, f_{ν}	Flux density per unit frequency (in the unit of erg/s/cm ² /Hz)
F_{λ}, f_{λ}	Flux density per unit wavelength (in the unit of erg/s/cm ² / \AA)
α_{ν}	Spectral index defined as $L_{\nu} \propto F_{\nu} \propto \nu^{\alpha_{\nu}}$
α_{λ}	Spectral index defined as $L_{\lambda} \propto F_{\lambda} \propto \lambda^{\alpha_{\lambda}}$

Table A.1: Continued

Symbol/acronym	Definition
Jy	Jansky; $1 \text{ Jy} = 10^{-23} \text{ erg/s/cm}^2/\text{Hz}$
Section 2	
A_λ	Galactic absorption at λ (in the unit of magnitude)
$b(s, l), a(s, l)$	linear regression slope and intercept ($y = b \times x + a$) in flux-flux space [$s = u, g, r, i; l = g, r, i, z$, where $\lambda(s) < \lambda(l)$]
$b^{\text{ratio}}(s, l), a^{\text{ratio}}(s, l)$	Flux ratio of the time-averaged flux at l -band to s -band [$s = u, g, r, i; l = g, r, i, z$, where $\lambda(s) < \lambda(l)$]
$c(s, l)$	$b(s, l)/b^{\text{ratio}}(s, l)$ [$s = u, g, r, i; l = g, r, i, z$, where $\lambda(s) < \lambda(l)$]
$f_v^{\text{dif}}, f_\lambda^{\text{dif}}$	Flux difference (variable component) spectrum
$\alpha_v^{\text{com}}, \alpha_\lambda^{\text{com}}$	Spectral index of the quasar composite spectrum
$\alpha_v^{\text{dif}}, \alpha_\lambda^{\text{dif}}$	Spectral index of the flux difference (variable component) spectrum
T_{sub}	Dust sublimation temperature
Section 3	
V	Variability amplitude of a broad-band light (in the unit of magnitude)
σ_{int}	Intrinsic scatter in magnitude-magnitude space
n	The number of grids on the disk
σ_T	Variability amplitude of T_{eff} [in the unit of $\log(T_{\text{eff}})$]
x	Normalized radial coordinate defined as R/R_{in}
Sections 4 and 5	
I, Q, U	Un-normalized Stokes parameters
q, u	Normalized Stokes parameters
q', u'	Normalized Stokes parameters rotated to PA_c of the target
PA	Polarization position angle
PA_c	The systemic polarization position angle evaluated at the rest-frame wavelength range of 4000-4731Å
p	Polarization degree
\hat{p}	De-biased polarization degree
R_{sca}	Radial distance of the scattering region from SMBH
$R_{\text{sca}}(PA \text{ var.})$	Radial distance of the scattering region from SMBH constrained by the observed PV variability
$R_{\text{sca}}(pF \text{ var.})$	Radial distance of the scattering region from SMBH constrained by the observed polarized flux variability

Table A.1: Continued

Symbol/acronym	Definition
R_{BLR}	Radial distance of the BLR from SMBH
$R_{\text{dust, in}}$	Radial distance of the dust inner radius from SMBH

Appendix B

Model spectra used in Section 2.5

Here we show how model spectra in Section 2.5 are calculated.

Broad emission lines $f_{\nu}^{\text{dif}}(\text{BEL})$ include $\text{H}\alpha$, $\text{H}\beta$, $\text{H}\gamma$, Mg II , $\text{C III]$, C IV , Si IV , $\text{Ly}\alpha$, which are the eight strongest BELs in the SDSS quasar composite spectrum (Vanden Berk et al., 2001), and calculated as

$$f_{\lambda}^{\text{dif}}(\text{BEL}) = R \frac{\sigma_{\lambda}(\text{Ly}\alpha)}{\sigma_{\lambda}} \exp\left(-\left(\frac{\lambda - \lambda_{\text{rest}}}{2\sigma_{\lambda}}\right)^2\right) \quad (\text{B.1})$$

where λ_{rest} (rest-frame central wavelength for an emission line), R (relative strength for each BEL), and σ_{λ} (line width) are given as Table B.1 for each emission line (Vanden Berk et al., 2001).

Balmer and Paschen continuum emission For $f_{\lambda}^{\text{dif}}(\text{BaC})$ and $f_{\lambda}^{\text{dif}}(\text{PaC})$, we assume gas clouds of uniform temperature ($T_e=15000$ K) that are partially optically thick (Dietrich et al., 2003; Kurk et al., 2007). We assume that the Balmer continuum spectrum variability below the Balmer edge $\lambda_{\text{BE}} = 3646\text{\AA}$ is described by

$$f_{\lambda}^{\text{dif}}(\text{BaC}) = R^{\text{BaC}} B_{\lambda}(T_e) \left(1 - \exp\left(-\tau_{\text{BE}} \left(\frac{\lambda}{\lambda_{\text{BE}}}\right)^3\right)\right) \quad (\text{B.2})$$

Table B.1: The Composite Spectral Property of Broad Emission Lines

Line	$\lambda_{\text{rest}}[\text{\AA}]$	$R(\text{Rel.Flux}[100 \times F/F(\text{Ly}\alpha)])$	$\sigma_{\lambda}[\text{\AA}]$
$\text{H}\alpha$	6564.61	30.832	47.39
$\text{H}\beta$	4862.68	8.649	40.44
$\text{H}\gamma$	4341.68	2.616	20.32
Mg II	2798.75	14.725	34.95
C III]	1908.73	15.943	23.58
C IV	1549.06	25.291	14.33
Si IV	1396.76	8.916	12.50
$\text{Ly}\alpha$	1215.67	100.000	19.46

References — Vanden Berk et al. (2001).

where $B_\lambda(T_e)$ is the Planck function at the electron temperature T_e , τ_{BE} is the optical depth at the Balmer edge $\lambda_{\text{BE}} = 3646\text{\AA}$, and R^{BaC} is the normalized flux density at the Balmer edge (Grandi, 1982). The optical depth is fixed at $\tau_{\text{BE}} = 1$ (Kurk et al., 2007) and R^{BaC} (with relative strength to other emission lines) is determined by the integrated flux ratio $F^{\text{BaC}}/F(\text{H}\alpha) = 1.80$ (Grandi, 1982). Note that in the actual quasar spectra, higher order Balmer lines are merging to a pseudo-continuum, yielding a smooth rise to the Balmer edge (Wills et al., 1985; Dietrich et al., 2003). In the same way as the Balmer continuum, the Paschen continuum variability is expressed by

$$f_\lambda^{\text{dif}}(\text{PaC}) = R^{\text{PaC}} B_\lambda(T_e) \left(1 - \exp\left(-\tau_{\text{PE}} \left(\frac{\lambda}{\lambda_{\text{PE}}}\right)^3\right) \right) \quad (\text{B.3})$$

where $\lambda_{\text{PE}} = 8208\text{\AA}$ the optical depth is fixed at $\tau_{\text{PE}} = 0.25$, and R^{PaC} is determined by the integrated flux ratio $F^{\text{PaC}}/F(\text{H}\alpha) = 1.17$ (Grandi, 1982).

Fe II pseudo-continuum emission The ‘‘SBB’’ is composed not only of the Balmer continuum and Mg II BEL, but also of Fe II pseudo-continuum emission. To model the Fe II pseudo-continuum emission, we adopt a UV Fe II emission template presented by Tsuzuki et al. (2006). As we do not know the relative strength of Fe II emission to the power-law continuum or the other components in the SBB, we choose to scale the peak value of the Fe II template at $\lambda = 2481.9299\text{\AA}$ to have $f_\lambda = 0.3$, then

$$f_\lambda^{\text{dif}}(\text{Fe II}) = f_\lambda(\text{Fe II template, scaled}). \quad (\text{B.4})$$

Effects of Ly α forest (IGM attenuation) In addition to the emission lines variability, we show in Figures 2.14 and 2.15 the wavelength-dependent effects by IGM attenuation. At a wavelength range shorter than 1216\AA , observed flux is attenuated due to intervening absorption systems (e.g., Madau, 1995). To describe the IGM attenuation at these wavelengths, we convolve a power-law continuum with the Meiksin (2006) optical depth, which is

$$f_\lambda^{\text{dif}}(\text{Ly}\alpha \text{ forest}) = e^{-\tau_{\text{eff}}(z, \lambda)} f_\lambda^{\text{dif}}(\text{continuum}) \quad (\text{B.5})$$

where (redshift and wavelength dependent) $\tau_{\text{eff}}(z, \lambda)$ is defined as the sum of the optical depth of resonant scattering by Lyman transitions and photoelectric absorption. The transmissivity function is shown in Figure B.1.

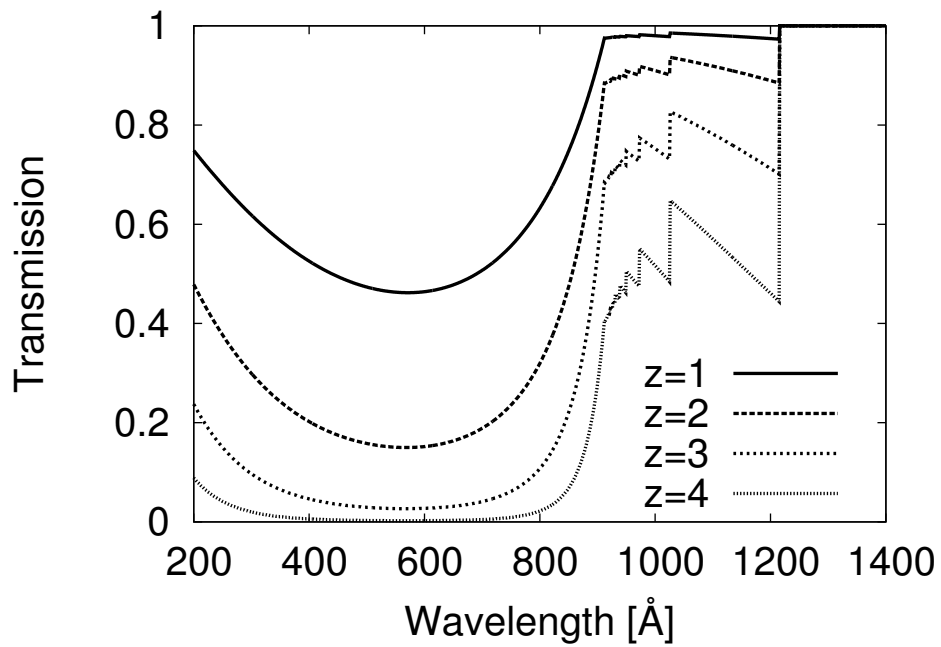


Figure B.1: Transmissivity $\exp(-\tau_{\text{eff}}(z, \lambda))$ as a function of rest-frame wavelength, where τ_{eff} is the effective optical depth of the IGM (Meiksin, 2006).

Appendix C

Regression intercepts as a function of redshift

We here consider a flux–flux plot for a quasar light curve in which the regression line has positive intercept (as the case of Figure 2.5). $a(s, l) > 0$ indicates the ratio of flux $f_v(l)/f_v(s)$, which is the slope of a straight line that passes through the origin and the observed data points at some epoch, becomes smaller when the quasar becomes brighter. In this case, the photometric color $m_s - m_l$, defined as $+2.5 \log(f_v(l)/f_v(s))$, becomes bluer-when-brighter. Similarly, if the regression intercept is negative, the color of the quasar becomes redder-when-brighter (Lyutyi & Doroshenko, 1993; Hagen-Thorn, 1997; Sakata et al., 2010, 2011). Note that, as discussed in Section 2.1, the color variability trend referenced here is that of the “observed” photometric color, which does not directly mean the spectral hardening (softening) of the AGN intrinsic continuum emission.

Thus, the sign of the regression intercept in flux–flux space can be interpreted as the indicator of the “observed” photometric color variability. We express this fact as

$$\begin{cases} \text{BWB}_{\text{obs}} & (\text{if } a(s, l) > 0) \\ \text{RWB}_{\text{obs}} & (\text{if } a(s, l) < 0) \end{cases} \quad (\text{C.1})$$

where BWB_{obs} and RWB_{obs} indicates that the “observed” color becomes bluer when brighter and redder when brighter, respectively. Figure C.1 shows the regression intercepts as a function of redshift for each quasar. Regression intercepts are generally positive, which indicates that the quasar color variability generally has BWB_{obs} trend. Note that this result is merely another expression of the result shown in Figure 2.10, as the relation of $b^{\text{ratio}}(s, l)$ and $b(s, l)$ (Equation (2.14)) is actually determined by the sign of $a(s, l)$.

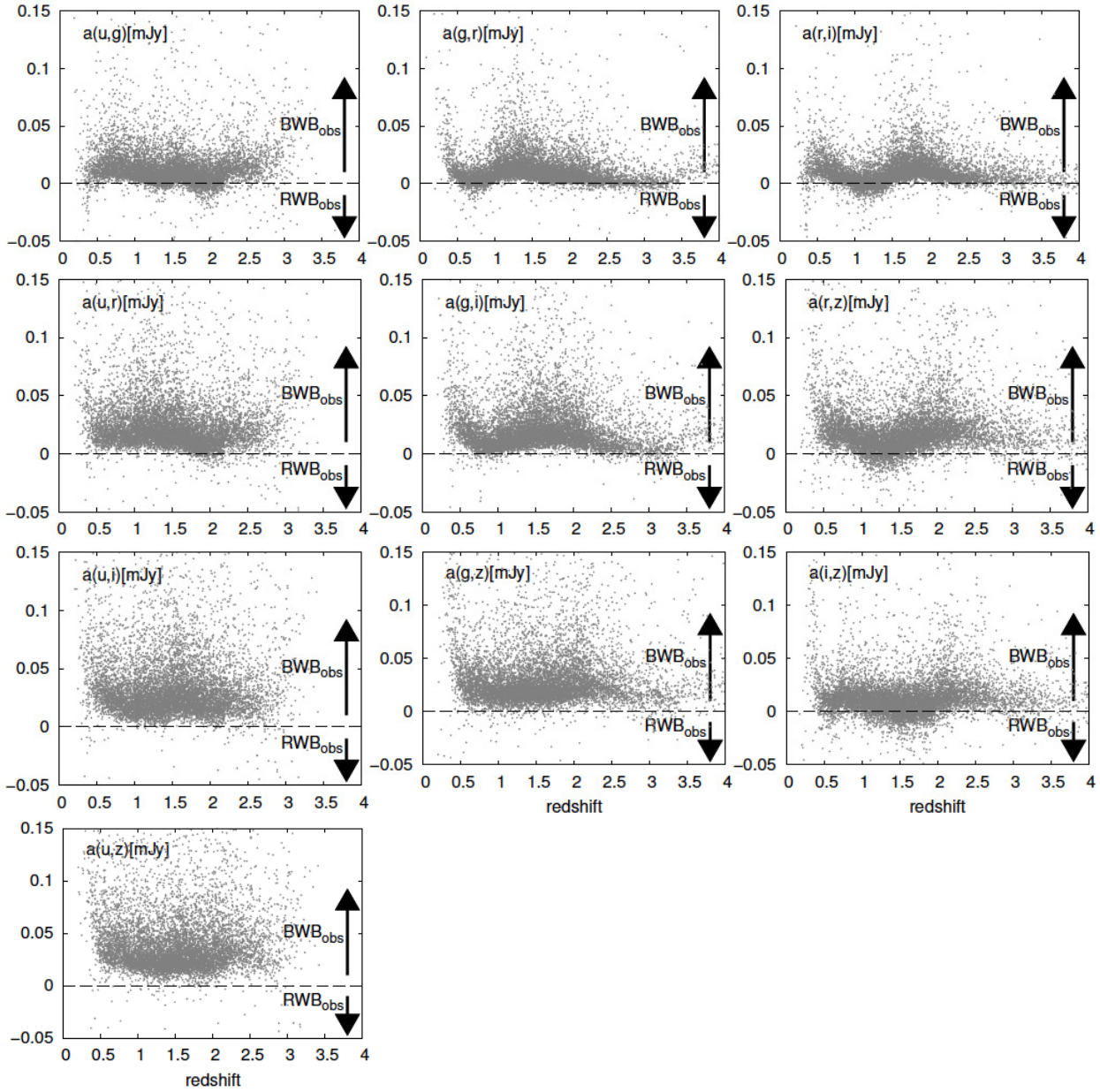


Figure C.1: Regression intercepts as a function of redshift (dots). If $a(s, l) > 0$, the “observed” color tends to become bluer when the quasar becomes brighter (BWB_{obs} in Equation (C.1)). And if $a(s, l) < 0$, the quasar has RWB_{obs} trend.

Appendix D

Kiso/KWFC Multi-band Quasar Light Curves

Table D.1: KWFC u , g , r , i , and z -band light curves for B2 1208+32, Ton 202, 3C323.1, and 4C09.72.

Object name	MJD	Magnitude	Error in magnitude	Band
B2 1208+32	57164.47822	16.9528	0.0306	u
B2 1208+32	57390.64625	17.1045	0.0167	u
B2 1208+32	57402.62973	17.0845	0.0170	u
B2 1208+32	57407.78441	17.1105	0.0258	u
B2 1208+32	57419.86152	17.0244	0.0291	u
B2 1208+32	57420.58574	17.0492	0.0155	u
B2 1208+32	57433.54302	17.0783	0.0285	u
B2 1208+32	57445.67669	17.0510	0.0259	u
B2 1208+32	57446.51312	17.0809	0.0336	u
B2 1208+32	57129.59170	16.8277	0.0081	g
B2 1208+32	57151.61124	16.8178	0.0109	g
B2 1208+32	57152.61655	16.8332	0.0088	g
B2 1208+32	57161.49397	16.8084	0.0092	g
B2 1208+32	57164.45771	16.8235	0.0154	g
B2 1208+32	57171.56550	16.8284	0.0144	g
B2 1208+32	57188.53751	16.8669	0.0773	g
B2 1208+32	57390.62650	16.9786	0.0078	g
B2 1208+32	57402.61074	16.9643	0.0075	g
B2 1208+32	57407.76236	16.9652	0.0154	g
B2 1208+32	57419.84006	16.9625	0.0092	g
B2 1208+32	57420.56788	16.9750	0.0069	g
B2 1208+32	57433.52307	17.0106	0.0135	g

Table D.1: Continued

Object name	MJD	Magnitude	Error in magnitude	Band
B2 1208+32	57445.65384	16.9384	0.0154	<i>g</i>
B2 1208+32	57446.49379	17.0004	0.0136	<i>g</i>
B2 1208+32	57129.60164	16.8564	0.0082	<i>r</i>
B2 1208+32	57147.56783	16.8481	0.0196	<i>r</i>
B2 1208+32	57151.62401	16.8520	0.0114	<i>r</i>
B2 1208+32	57152.62555	16.8404	0.0097	<i>r</i>
B2 1208+32	57164.47184	16.8248	0.0117	<i>r</i>
B2 1208+32	57169.51788	16.8488	0.0222	<i>r</i>
B2 1208+32	57171.57981	16.8679	0.0182	<i>r</i>
B2 1208+32	57390.63837	16.9526	0.0072	<i>r</i>
B2 1208+32	57402.62246	16.9599	0.0066	<i>r</i>
B2 1208+32	57407.77540	16.9495	0.0165	<i>r</i>
B2 1208+32	57419.85302	16.9583	0.0102	<i>r</i>
B2 1208+32	57420.57850	16.9519	0.0065	<i>r</i>
B2 1208+32	57433.53479	16.9322	0.0109	<i>r</i>
B2 1208+32	57445.66866	16.9745	0.0146	<i>r</i>
B2 1208+32	57446.50554	16.9519	0.0119	<i>r</i>
B2 1208+32	57129.59667	16.8495	0.0117	<i>i</i>
B2 1208+32	57147.56294	16.8380	0.0225	<i>i</i>
B2 1208+32	57151.61952	16.8633	0.0210	<i>i</i>
B2 1208+32	57152.62102	16.8415	0.0146	<i>i</i>
B2 1208+32	57161.50834	16.8420	0.0191	<i>i</i>
B2 1208+32	57164.46611	16.8427	0.0131	<i>i</i>
B2 1208+32	57169.49165	16.8410	0.0242	<i>i</i>
B2 1208+32	57171.57263	16.8454	0.0171	<i>i</i>
B2 1208+32	57201.47058	16.8520	0.0202	<i>i</i>
B2 1208+32	57390.63227	16.9447	0.0110	<i>i</i>
B2 1208+32	57402.61663	16.9356	0.0095	<i>i</i>
B2 1208+32	57407.76882	16.9310	0.0152	<i>i</i>
B2 1208+32	57419.84683	16.9394	0.0134	<i>i</i>
B2 1208+32	57420.56973	16.9364	0.0088	<i>i</i>
B2 1208+32	57433.52894	16.9126	0.0119	<i>i</i>
B2 1208+32	57445.66211	16.9229	0.0159	<i>i</i>
B2 1208+32	57446.49971	16.9238	0.0168	<i>i</i>
B2 1208+32	57129.61147	16.2518	0.0131	<i>z</i>
B2 1208+32	57147.57756	16.2554	0.0198	<i>z</i>

Table D.1: Continued

Object name	MJD	Magnitude	Error in magnitude	Band
B2 1208+32	57151.63301	16.2908	0.0175	<i>z</i>
B2 1208+32	57152.63453	16.2675	0.0208	<i>z</i>
B2 1208+32	57164.48647	16.3289	0.0152	<i>z</i>
B2 1208+32	57169.56646	16.2486	0.0246	<i>z</i>
B2 1208+32	57390.65486	16.3632	0.0095	<i>z</i>
B2 1208+32	57402.63836	16.3344	0.0079	<i>z</i>
B2 1208+32	57407.79306	16.3286	0.0111	<i>z</i>
B2 1208+32	57419.86828	16.3120	0.0188	<i>z</i>
B2 1208+32	57420.59435	16.3075	0.0066	<i>z</i>
B2 1208+32	57433.55081	16.3229	0.0081	<i>z</i>
B2 1208+32	57445.68639	16.2809	0.0112	<i>z</i>
B2 1208+32	57446.52145	16.3229	0.0127	<i>z</i>
Ton 202	57129.63296	16.3382	0.0223	<i>u</i>
Ton 202	57151.65279	16.2994	0.0224	<i>u</i>
Ton 202	57152.65318	16.2922	0.0206	<i>u</i>
Ton 202	57169.57134	16.2974	0.0285	<i>u</i>
Ton 202	57185.69187	16.3394	0.0167	<i>u</i>
Ton 202	57229.50221	16.3552	0.0218	<i>u</i>
Ton 202	57390.74597	16.6332	0.0201	<i>u</i>
Ton 202	57402.73030	16.6139	0.0117	<i>u</i>
Ton 202	57407.82143	16.5937	0.0159	<i>u</i>
Ton 202	57420.68653	16.6168	0.0111	<i>u</i>
Ton 202	57433.64743	16.6060	0.0136	<i>u</i>
Ton 202	57445.71448	16.5885	0.0279	<i>u</i>
Ton 202	57129.61581	16.1975	0.0042	<i>g</i>
Ton 202	57151.63786	16.2224	0.0068	<i>g</i>
Ton 202	57152.63260	16.2174	0.0056	<i>g</i>
Ton 202	57162.75600	16.2525	0.0108	<i>g</i>
Ton 202	57166.52074	16.2105	0.0109	<i>g</i>
Ton 202	57169.52354	16.2049	0.0105	<i>g</i>
Ton 202	57185.67310	16.2644	0.0049	<i>g</i>
Ton 202	57229.48116	16.2891	0.0080	<i>g</i>
Ton 202	57390.72878	16.5235	0.0066	<i>g</i>
Ton 202	57402.71138	16.5328	0.0053	<i>g</i>
Ton 202	57407.80132	16.5512	0.0081	<i>g</i>
Ton 202	57420.66769	16.5717	0.0048	<i>g</i>

Table D.1: Continued

Object name	MJD	Magnitude	Error in magnitude	Band
Ton 202	57433.62829	16.5723	0.0081	<i>g</i>
Ton 202	57445.69447	16.5563	0.0170	<i>g</i>
Ton 202	57129.62768	16.2148	0.0051	<i>r</i>
Ton 202	57143.66684	16.2382	0.0208	<i>r</i>
Ton 202	57151.64777	16.2359	0.0063	<i>r</i>
Ton 202	57152.64821	16.2232	0.0057	<i>r</i>
Ton 202	57169.53388	16.2304	0.0101	<i>r</i>
Ton 202	57185.68469	16.2657	0.0057	<i>r</i>
Ton 202	57229.49773	16.3006	0.0060	<i>r</i>
Ton 202	57390.74035	16.5077	0.0061	<i>r</i>
Ton 202	57402.72311	16.5142	0.0049	<i>r</i>
Ton 202	57407.81377	16.5188	0.0073	<i>r</i>
Ton 202	57420.67930	16.5297	0.0045	<i>r</i>
Ton 202	57433.64006	16.5287	0.0065	<i>r</i>
Ton 202	57445.70679	16.5174	0.0157	<i>r</i>
Ton 202	57129.62254	16.2732	0.0074	<i>i</i>
Ton 202	57143.66195	16.2470	0.0248	<i>i</i>
Ton 202	57151.64276	16.2699	0.0084	<i>i</i>
Ton 202	57152.64333	16.2830	0.0087	<i>i</i>
Ton 202	57162.75973	16.3021	0.0268	<i>i</i>
Ton 202	57169.52871	16.3066	0.0125	<i>i</i>
Ton 202	57185.67889	16.3140	0.0074	<i>i</i>
Ton 202	57229.49224	16.3416	0.0062	<i>i</i>
Ton 202	57390.73455	16.5105	0.0086	<i>i</i>
Ton 202	57402.71724	16.5250	0.0075	<i>i</i>
Ton 202	57407.80757	16.5094	0.0101	<i>i</i>
Ton 202	57420.67348	16.5493	0.0064	<i>i</i>
Ton 202	57433.63421	16.5538	0.0085	<i>i</i>
Ton 202	57445.70058	16.5206	0.0171	<i>i</i>
Ton 202	57129.63807	15.7744	0.0098	<i>z</i>
Ton 202	57143.67660	15.8089	0.0226	<i>z</i>
Ton 202	57151.65777	15.7697	0.0093	<i>z</i>
Ton 202	57152.65819	15.7838	0.0114	<i>z</i>
Ton 202	57169.57657	15.7520	0.0123	<i>z</i>
Ton 202	57185.70015	15.8051	0.0107	<i>z</i>
Ton 202	57229.51437	15.8170	0.0068	<i>z</i>

Table D.1: Continued

Object name	MJD	Magnitude	Error in magnitude	Band
Ton 202	57390.75660	15.9018	0.0072	<i>z</i>
Ton 202	57402.73898	15.9270	0.0065	<i>z</i>
Ton 202	57407.83050	15.9329	0.0080	<i>z</i>
Ton 202	57420.69511	15.9422	0.0058	<i>z</i>
Ton 202	57433.65610	15.9330	0.0071	<i>z</i>
Ton 202	57445.72362	15.8793	0.0117	<i>z</i>
3C323.1	57152.60449	16.3042	0.0215	<i>u</i>
3C323.1	57169.58268	16.3087	0.0288	<i>u</i>
3C323.1	57185.72664	16.3099	0.0117	<i>u</i>
3C323.1	57229.53120	16.1932	0.0091	<i>u</i>
3C323.1	57276.45946	16.1482	0.0108	<i>u</i>
3C323.1	57302.43283	16.1887	0.0135	<i>u</i>
3C323.1	57390.81315	16.1075	0.0109	<i>u</i>
3C323.1	57402.79654	16.0724	0.0089	<i>u</i>
3C323.1	57407.85700	16.0913	0.0118	<i>u</i>
3C323.1	57420.76717	16.0759	0.0090	<i>u</i>
3C323.1	57433.71224	16.0871	0.0085	<i>u</i>
3C323.1	57445.75129	16.0250	0.0290	<i>u</i>
3C323.1	57133.69661	16.3582	0.0053	<i>g</i>
3C323.1	57134.63122	16.3657	0.0060	<i>g</i>
3C323.1	57151.66308	16.3017	0.0081	<i>g</i>
3C323.1	57152.58978	16.3053	0.0056	<i>g</i>
3C323.1	57158.76580	16.2978	0.0151	<i>g</i>
3C323.1	57168.63109	16.2919	0.0125	<i>g</i>
3C323.1	57169.53946	16.2926	0.0108	<i>g</i>
3C323.1	57185.70844	16.2787	0.0059	<i>g</i>
3C323.1	57229.47736	16.1705	0.0055	<i>g</i>
3C323.1	57276.44243	16.1038	0.0034	<i>g</i>
3C323.1	57301.42832	16.1530	0.0050	<i>g</i>
3C323.1	57302.40406	16.1613	0.0050	<i>g</i>
3C323.1	57390.79408	16.1230	0.0055	<i>g</i>
3C323.1	57402.77770	16.0548	0.0039	<i>g</i>
3C323.1	57407.83790	16.0661	0.0058	<i>g</i>
3C323.1	57420.73072	16.0577	0.0043	<i>g</i>
3C323.1	57433.69325	16.0546	0.0039	<i>g</i>
3C323.1	57445.73129	16.0548	0.0155	<i>g</i>

Table D.1: Continued

Object name	MJD	Magnitude	Error in magnitude	Band
3C323.1	57133.70679	16.1937	0.0065	<i>r</i>
3C323.1	57134.67736	16.2175	0.0065	<i>r</i>
3C323.1	57143.69210	16.1814	0.0159	<i>r</i>
3C323.1	57151.67197	16.1525	0.0139	<i>r</i>
3C323.1	57152.59959	16.1546	0.0053	<i>r</i>
3C323.1	57158.77473	16.1563	0.0236	<i>r</i>
3C323.1	57168.64057	16.1362	0.0103	<i>r</i>
3C323.1	57169.54962	16.1332	0.0086	<i>r</i>
3C323.1	57185.71945	16.1078	0.0049	<i>r</i>
3C323.1	57229.52412	16.0602	0.0045	<i>r</i>
3C323.1	57276.45406	16.0052	0.0035	<i>r</i>
3C323.1	57293.44652	16.0220	0.0114	<i>r</i>
3C323.1	57301.44058	15.9401	0.0518	<i>r</i>
3C323.1	57302.41855	16.0222	0.0051	<i>r</i>
3C323.1	57390.80566	15.9751	0.0045	<i>r</i>
3C323.1	57402.78935	15.9582	0.0034	<i>r</i>
3C323.1	57407.84958	15.9545	0.0050	<i>r</i>
3C323.1	57420.75988	15.9485	0.0036	<i>r</i>
3C323.1	57433.70500	15.9589	0.0035	<i>r</i>
3C323.1	57445.74304	15.9353	0.0132	<i>r</i>
3C323.1	57133.70170	16.1195	0.0069	<i>i</i>
3C323.1	57134.63607	16.1167	0.0069	<i>i</i>
3C323.1	57143.68701	16.0967	0.0170	<i>i</i>
3C323.1	57151.66822	16.0832	0.0085	<i>i</i>
3C323.1	57152.59467	16.0940	0.0078	<i>i</i>
3C323.1	57158.77029	16.1091	0.0214	<i>i</i>
3C323.1	57168.63661	16.0856	0.0095	<i>i</i>
3C323.1	57169.54450	16.0782	0.0102	<i>i</i>
3C323.1	57185.71343	16.0460	0.0070	<i>i</i>
3C323.1	57229.50736	16.0200	0.0058	<i>i</i>
3C323.1	57301.43415	15.9609	0.0060	<i>i</i>
3C323.1	57302.41151	15.9579	0.0074	<i>i</i>
3C323.1	57390.80047	15.9405	0.0073	<i>i</i>
3C323.1	57402.78350	15.9204	0.0049	<i>i</i>
3C323.1	57407.84370	15.8987	0.0070	<i>i</i>
3C323.1	57433.69916	15.9425	0.0073	<i>i</i>

Table D.1: Continued

Object name	MJD	Magnitude	Error in magnitude	Band
3C323.1	57445.73719	15.9116	0.0126	<i>i</i>
3C323.1	57134.64100	15.5073	0.0082	<i>z</i>
3C323.1	57143.70212	15.5194	0.0135	<i>z</i>
3C323.1	57152.60951	15.5106	0.0093	<i>z</i>
3C323.1	57169.58816	15.4758	0.0094	<i>z</i>
3C323.1	57185.73522	15.4734	0.0062	<i>z</i>
3C323.1	57229.54058	15.4467	0.0047	<i>z</i>
3C323.1	57293.46063	15.4685	0.0167	<i>z</i>
3C323.1	57390.82173	15.3951	0.0056	<i>z</i>
3C323.1	57402.80516	15.4136	0.0043	<i>z</i>
3C323.1	57407.86596	15.4180	0.0058	<i>z</i>
3C323.1	57420.77584	15.4094	0.0045	<i>z</i>
3C323.1	57433.72091	15.4054	0.0049	<i>z</i>
3C323.1	57445.75992	15.4171	0.0105	<i>z</i>
4C09.72	57229.58331	15.9757	0.0096	<i>u</i>
4C09.72	57276.65023	16.1523	0.0064	<i>u</i>
4C09.72	57302.46231	16.2857	0.0079	<i>u</i>
4C09.72	57330.44826	16.2751	0.0073	<i>u</i>
4C09.72	57346.52437	16.3121	0.0158	<i>u</i>
4C09.72	57391.39393	16.3663	0.0117	<i>u</i>
4C09.72	57403.39828	16.3788	0.0111	<i>u</i>
4C09.72	57421.40847	16.4288	0.0179	<i>u</i>
4C09.72	57229.56485	15.7741	0.0047	<i>g</i>
4C09.72	57276.56819	15.9044	0.0028	<i>g</i>
4C09.72	57293.46705	16.0142	0.0396	<i>g</i>
4C09.72	57302.44352	15.9959	0.0034	<i>g</i>
4C09.72	57330.41384	16.0303	0.0028	<i>g</i>
4C09.72	57346.50540	16.0643	0.0131	<i>g</i>
4C09.72	57390.47603	16.1306	0.0046	<i>g</i>
4C09.72	57391.37494	16.1411	0.0070	<i>g</i>
4C09.72	57403.38318	16.1350	0.0053	<i>g</i>
4C09.72	57420.41671	16.1889	0.0055	<i>g</i>
4C09.72	57421.39121	16.1848	0.0064	<i>g</i>
4C09.72	57229.57618	15.9030	0.0040	<i>r</i>
4C09.72	57276.58061	16.0414	0.0032	<i>r</i>
4C09.72	57302.45512	16.1116	0.0038	<i>r</i>

Table D.1: Continued

Object name	MJD	Magnitude	Error in magnitude	Band
4C09.72	57330.44056	16.1459	0.0033	<i>r</i>
4C09.72	57346.51708	16.1782	0.0135	<i>r</i>
4C09.72	57391.38666	16.2420	0.0054	<i>r</i>
4C09.72	57403.38501	16.2470	0.0042	<i>r</i>
4C09.72	57421.39744	16.2811	0.0057	<i>r</i>
4C09.72	57229.57050	15.8478	0.0052	<i>i</i>
4C09.72	57276.57442	15.9484	0.0042	<i>i</i>
4C09.72	57302.44931	16.0221	0.0048	<i>i</i>
4C09.72	57330.43425	16.0263	0.0055	<i>i</i>
4C09.72	57346.51123	16.0929	0.0247	<i>i</i>
4C09.72	57390.48183	16.1000	0.0064	<i>i</i>
4C09.72	57391.38074	16.1077	0.0071	<i>i</i>
4C09.72	57403.39033	16.1453	0.0081	<i>i</i>
4C09.72	57421.39160	16.1399	0.0083	<i>i</i>
4C09.72	57229.59182	15.7185	0.0061	<i>z</i>
4C09.72	57276.65914	15.7556	0.0048	<i>z</i>
4C09.72	57302.47097	15.7775	0.0056	<i>z</i>
4C09.72	57330.45773	15.8083	0.0051	<i>z</i>
4C09.72	57346.53310	15.7300	0.0098	<i>z</i>
4C09.72	57391.40255	15.8618	0.0073	<i>z</i>
4C09.72	57403.41184	15.8791	0.0063	<i>z</i>
4C09.72	57421.41588	15.8442	0.0151	<i>z</i>

Appendix E

Analysis of linear polarimetry data

We follow the standard definition of the Stokes parameters (e.g., Kishimoto et al., 2004; Fossati et al., 2007; Landi Degl’Innocenti et al., 2007; Bagnulo et al., 2009, and references therein). We adopt the “ratio” method (e.g., Lamy & Hutsemékers, 1999; Bagnulo et al., 2009) to derive the estimates of normalized Stokes parameters of $q = Q/I$ and $u = U/I$. By defining $r(\alpha)$ as

$$r(\alpha) = \frac{f_{\alpha}^{ord}}{f_{\alpha}^{ext}}, \quad (\text{E.1})$$

where $f_{\alpha}^{ord/ext}$ represents the measured flux of the ordinary/extraordinary ray with the half-wave plate position angle of $\alpha = 0.0^{\circ}, 22.5^{\circ}, 45.0^{\circ}$, or 67.5° , q and u can be written as

$$q = \frac{\sqrt{r(0.0^{\circ})/r(45.0^{\circ})} - 1}{\sqrt{r(0.0^{\circ})/r(45.0^{\circ})} + 1} \quad (\text{E.2})$$

$$u = \frac{\sqrt{r(22.5^{\circ})/r(67.5^{\circ})} - 1}{\sqrt{r(22.5^{\circ})/r(67.5^{\circ})} + 1} \quad (\text{E.3})$$

Note that quasars are generally not circularly-polarized (Hutsemékers et al., 2010), thus the cross talk from the Stokes $v = V/I$ to the Stokes q due to a possible small deviation from the ideal phase retardance of the half-wave plate (Equation 42 of Bagnulo et al., 2009) can be neglected. In this work the circular polarization is assumed to be zero ($v = 0$), thus the polarization degree p is defined as the ratio of the linearly polarized intensity $\sqrt{Q^2 + U^2}$ to the total intensity I .

Considering the high signal-to-noise ratio of the flux measurements presented in this work, the Stokes q and u estimates can be assumed to have Gaussian distributions with the standard deviations of σ_q and σ_u , respectively (e.g., Clarke et al., 1983), and σ_q and σ_u can be derived as (Equation A10 of Bagnulo et al., 2009):

$$\sigma_q^2 = \frac{r(0.0^{\circ})/r(45.0^{\circ})}{\left(\sqrt{r(0.0^{\circ})/r(45.0^{\circ})} + 1\right)^4} \times \left[\left(\frac{\sigma_{f_{0.0^{\circ}}^{ord}}}{f_{0.0^{\circ}}^{ord}}\right)^2 + \left(\frac{\sigma_{f_{0.0^{\circ}}^{ext}}}{f_{0.0^{\circ}}^{ext}}\right)^2 + \left(\frac{\sigma_{f_{45.0^{\circ}}^{ord}}}{f_{45.0^{\circ}}^{ord}}\right)^2 + \left(\frac{\sigma_{f_{45.0^{\circ}}^{ext}}}{f_{45.0^{\circ}}^{ext}}\right)^2 \right] \quad (\text{E.4})$$

$$\sigma_u^2 = \frac{r(22.5^{\circ})/r(67.5^{\circ})}{\left(\sqrt{r(22.5^{\circ})/r(67.5^{\circ})} + 1\right)^4} \times \left[\left(\frac{\sigma_{f_{22.5^{\circ}}^{ord}}}{f_{22.5^{\circ}}^{ord}}\right)^2 + \left(\frac{\sigma_{f_{22.5^{\circ}}^{ext}}}{f_{22.5^{\circ}}^{ext}}\right)^2 + \left(\frac{\sigma_{f_{67.5^{\circ}}^{ord}}}{f_{67.5^{\circ}}^{ord}}\right)^2 + \left(\frac{\sigma_{f_{67.5^{\circ}}^{ext}}}{f_{67.5^{\circ}}^{ext}}\right)^2 \right], \quad (\text{E.5})$$

where $\sigma_{f_\alpha^{ord/ext}}$ indicates the measurement error of $f_\alpha^{ord/ext}$.

It is well known that the polarization degree p estimated from the measured q and u as

$$p = \sqrt{q^2 + u^2} \quad (\text{E.6})$$

$$\sigma_p^2 = \frac{q^2 \sigma_q^2 + u^2 \sigma_u^2}{p^2} \quad (\text{E.7})$$

is a biased estimate of the true polarization degree (see Clarke, 2010, for a review). In the case where the signal-to-noise ratio of the polarization measurements are $\gtrsim 2$, we can estimate the true polarization \hat{p} as (Plaszczynski et al., 2014):

$$\hat{p} = \frac{1}{2} \left(p + \sqrt{p^2 - 2b^2} \right) \quad (\text{E.8})$$

where

$$b^2 = \frac{q^2 \sigma_u^2 + u^2 \sigma_q^2}{p^2}. \quad (\text{E.9})$$

The estimate of polarization position angle

$$PA_{\text{inst}} = \frac{1}{2} \arctan \left(\frac{u}{q} \right) \quad (\text{E.10})$$

is unbiased (e.g., Plaszczynski et al., 2014), and its estimation error can be evaluated as (e.g., Naghizadeh-Khouei & Clarke, 1993; Fossati et al., 2007)

$$\sigma_{PA} = \frac{1}{2} \frac{b}{p}. \quad (\text{E.11})$$

Note that when the polarization degree of the target is small (e.g., $p < 1\%$), the statistical errors of q and u are almost the same ($\sigma_q \simeq \sigma_u \equiv \sigma$), and Equation E.7 becomes $\sigma_p = \sigma$, and from Equation E.11 a well known formula for the statistical error of the PA_{inst} can be derived as $\sigma_{PA} = \frac{1}{2} \frac{\sigma}{p} \text{ rad} = 28.65 \frac{\sigma}{p} \text{ deg}$ (Serkowski, 1974; Wardle & Kronberg, 1974).

Then, the instrumental coordinate system, in which q and u are measured, is transformed to the sky (celestial) coordinate system by rotating the coordinates by

$$\theta_c = \theta_\lambda - \theta_{\text{inst}}, \quad (\text{E.12})$$

where θ_λ is the wavelength-dependent instrumental correction angle, and θ_{inst} is the instrumental rotator position angle recorded in the fits header of each image. θ_λ is calibrated by observing the polarized standard stars. The coordinate rotation by θ_c results in

$$q_{\text{sky}} = q \cos(2\theta_c) + u \sin(2\theta_c) \quad (\text{E.13})$$

$$u_{\text{sky}} = -q \sin(2\theta_c) + u \cos(2\theta_c) \quad (\text{E.14})$$

$$PA = PA_{\text{inst}} - \theta_c = \frac{1}{2} \arctan \left(\frac{u_{\text{sky}}}{q_{\text{sky}}} \right) \quad (\text{E.15})$$

Appendix F

Correcting for the effects of the Galactic ISP

Kishimoto et al. (2004) pointed out that the observed optical polarization of 3C 323.1 is affected by a non-negligible amount of the Galactic ISP. The wavelength dependence of the ISP linear polarization can be described by the empirical formula (e.g., Serkowski et al., 1975)

$$p_{\text{ISP}} = p_{\text{ISP, max}} \exp \left[-K \ln^2 \left(\frac{\lambda_{\text{max}}}{\lambda} \right) \right], \quad (\text{F.1})$$

where $K = 0.01 + 1.66\lambda_{\text{max}}$ (Whittet et al., 1992). In this work, we adopt the ISP parameters of $p_{\text{ISP, max}} = 0.90\%$ and $\lambda_{\text{max}} = 5570\text{\AA}$, and the ISP position angle of $PA_{\text{ISP}} = 90$ deg derived by Kishimoto et al. (2004) for 3C 323.1. $PA_{\text{ISP}} = 90$ deg means that the ISP vector in the direction of 3C 323.1 is parallel to the q -axis in the $q - u$ plane, and thus, the ISP correction for q and u can be described as $q = q_{\text{uncorr}} + p_{\text{ISP}}$ and $u = u_{\text{uncorr}}$, where q_{uncorr} and u_{uncorr} represent the ISP-uncorrected values (see Figure F.1).

Figure F.1 shows the ISP-uncorrected $q - u$ (i.e., $q_{\text{uncorr}} - u_{\text{uncorr}}$) diagram of the Bok/SPOL and Keck/LRIS spectro-polarimetry data, and the ESO3.6-m/EFOSC2 V -band imaging-polarimetry data for 3C 323.1. In Figure F.1, the ISP vector of $p_{\text{ISP}} = 0.9\%$ is shown as a representative value, but it should be noted that the actual ISP correction is slightly wavelength-dependent (Equation F.1). The ISP correction leads to a shift of the origin of the intrinsic polarization vector to $(q_{\text{uncorr}}, u_{\text{uncorr}}) = (-p_{\text{ISP}}, 0)$, and the ISP-corrected PA is defined as half the geometrical angle between the q -axis and lines passing through the shifted origin and data points. As indicated in Figure F.1, the Keck/LRIS data points are linearly aligned along the vector of $PA_c = 9.6$ deg, meaning that the ISP-corrected PA of 3C 323.1 is nearly wavelength-independent (Figure 5.1; Kishimoto et al., 2004). As we can see in Figure 5.1, the ISP-corrected PA spectrum obtained with Bok/SPOL is also nearly wavelength-independent.

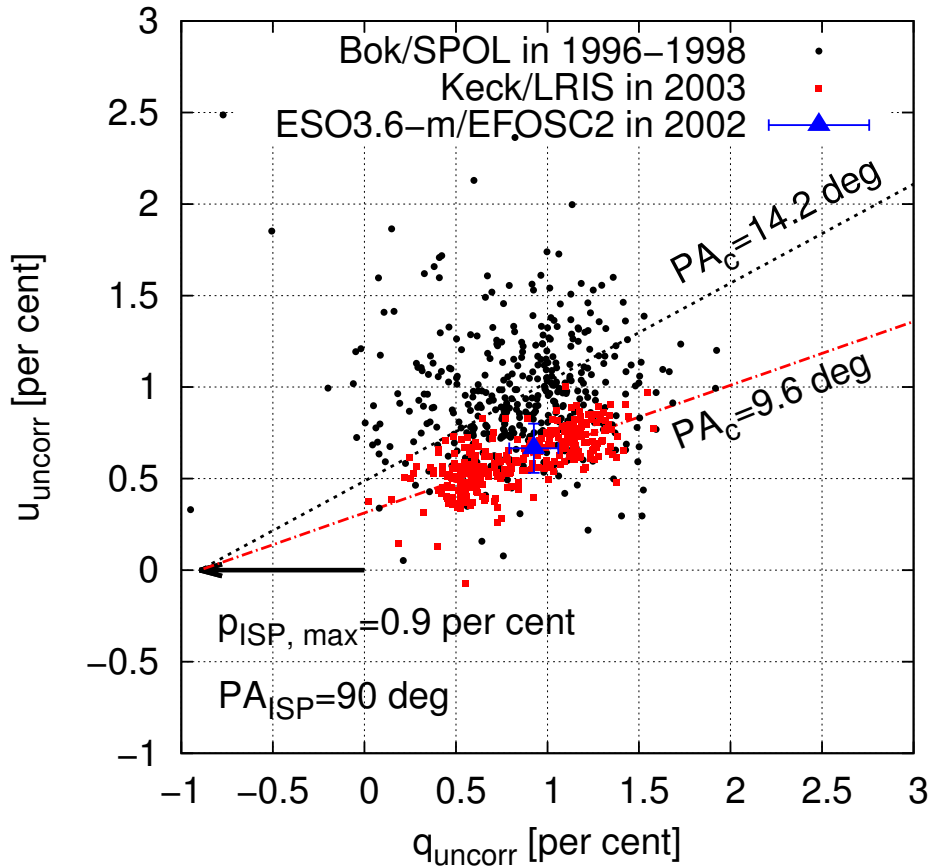


Figure F.1: The ISP-uncorrected $q-u$ diagram of the Bok/SPOL and Keck/LRIS spectro-polarimetry data, and the ESO3.6-m/EFOSC2 V -band polarimetry data for 3C 323.1. For the spectro-polarimetry data, each data point is the $q-u$ value at a wavelength bin of 10 \AA width. The thick arrow indicates the direction of the ISP polarization, and the dotted lines indicate the ISP-corrected systemic polarization position angles PA_c of the two spectro-polarimetry data evaluated at the rest-frame wavelength range of $4000\text{--}4731 \text{ \AA}$.

Appendix G

Historic white-light polarimetric measurements for 3C 323.1

Historic polarimetric measurements for 3C 323.1 presented in Stockman et al. (1984) and Wills et al. (2011) are summarized in Table G.1. It should be noted that, unlike the Bok/SPOL, ESO3.6-m/EFOSC2, and Keck/LRIS polarimetric measurements given in Table 5.1, it is impossible to estimate the V -band magnitudes of the total flux at each epoch of the polarimetric measurement summarized in Table G.1 because referenceable photometric measurements at these epochs are not available in the literature. Also, we do not correct for the Galactic ISP for these historic data, because it is difficult to evaluate the ISP strength from Equation F.1 due to the uncertainty of the wavelength coverage (see below).

In Figure G.1, the time variation of the ISP-uncorrected \hat{p} and PA of 3C 323.1 as given in Table G.1 are plotted, where different symbols indicate different filter configurations. We also plot the ISP-uncorrected \hat{p}_V and PA_V derived from the Bok/SPOL, ESO3.6-m/EFOSC2, and Keck/LRIS data in the same figure. As has already been pointed out in Section 5.2.2, the historic polarimetric measurements summarized in Table G.1 are not taken with standard photometric filter system. Considering the uncertainty of the wavelength coverage of each measurement, what we can only infer about the variability of \hat{p} in 3C 323.1 from the historic (mostly white-light) polarimetric data in Table G.1 is that there is no evidence to support the existence of strong variability of \hat{p} for the last several decades. On the other hand, since the wavelength-dependence of PA of 3C 323.1 is relatively weak, it may be valid to conclude that the PA has been showing time-variability. As discussed in Section 5.4, the variability of PA is observed even when we focus only on the V -band measurements presented in Table 5.1, and thus the historic PA data are supporting the discussion given in the main text that the PA variability has real physical origin intrinsic to the innermost scattering structure of 3C323.1.

Table G.1: Historic white-light and filtered polarimetric measurements for 3C 323.1. The Galactic ISP is uncorrected.

Date	MJD	Filter	$\hat{p}_{\text{uncorr}}[\%]$	$PA_{\text{uncorr}}[\text{deg}]$	Reference
1977-09-11	43397	None (Steward)	1.63 ± 0.24	16 ± 4	Stockman et al. (1984)
1978-05-05	43633	None (UAO)	2.01 ± 1.25	—	Stockman et al. (1984)
1979-04-02	43965	None (Steward)	1.48 ± 0.30	19 ± 6	Stockman et al. (1984)
1979-05-22	44015	None (Steward)	1.01 ± 0.20	4 ± 5	Stockman et al. (1984)
1979-05-22	44015	CuSO ₄ + B-390 (Steward)	0.78 ± 0.24	-8 ± 8	Stockman et al. (1984)
1979-05-22	44015	RG715 (Steward)	0.55 ± 0.26	-4 ± 12	Stockman et al. (1984)
1980-03-15	44313	None (Steward)	1.42 ± 0.30	8 ± 6	Stockman et al. (1984)
1990-02-26	47948	None (McDonald)	1.02 ± 0.13	28.3 ± 3.6	Wills et al. (2011)

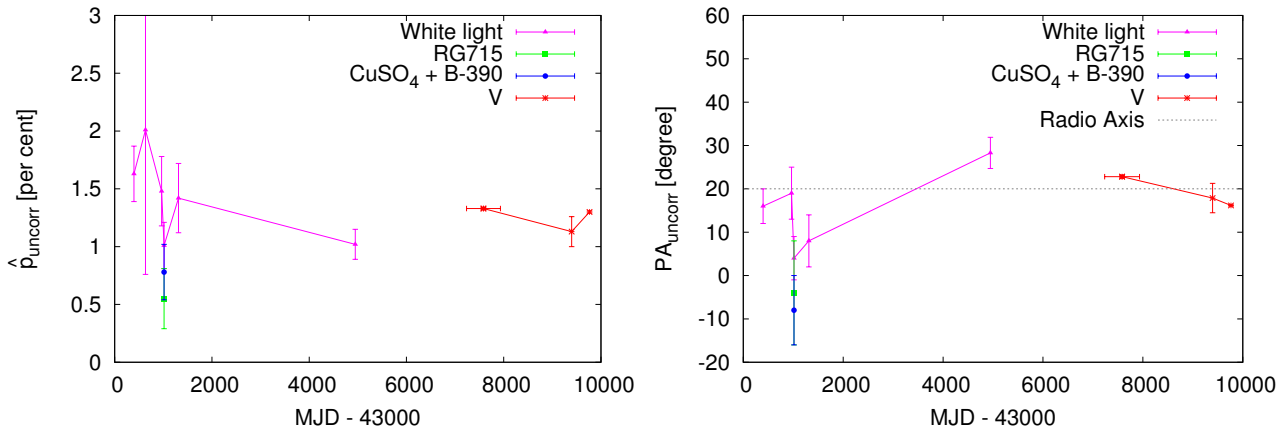


Figure G.1: The time variation of the ISP-uncorrected \hat{p} and PA of 3C 323.1 in 1977-2003. 3C 323.1's radio jet axis of 20 deg (Kishimoto et al., 2004) is indicated as a dotted line in the bottom panel.

Bibliography

- Abazajian, K., Adelman-McCarthy, J. K., Agüeros, M. A., et al. 2004, *AJ*, 128, 502, ADS
- Abazajian, K. N., Adelman-McCarthy, J. K., Agüeros, M. A., et al. 2009, *ApJS*, 182, 543, ADS
- Abramowicz, M. A., Czerny, B., Lasota, J. P., & Szuszkiewicz, E. 1988, *ApJ*, 332, 646, ADS
- Adelman-McCarthy, J. K., Agüeros, M. A., Allam, S. S., et al. 2007, *ApJS*, 172, 634, ADS
- Afanasiev, V. L., Shapovalova, A. I., Popović, L. Č., & Borisov, N. V. 2015, *MNRAS*, 448, 2879, ADS
- Agol, E., & Blaes, O. 1996, *MNRAS*, 282, 965, ADS
- Agol, E., Blaes, O., & Ionescu-Zanetti, C. 1998, *MNRAS*, 293, 1, ADS
- Agol, E., & Krolik, J. 1999, *ApJ*, 524, 49, ADS
- Ai, Y. L., Yuan, W., Zhou, H., et al. 2013, *AJ*, 145, 90, ADS
- Ai, Y. L., Yuan, W., Zhou, H. Y., et al. 2010, *ApJL*, 716, L31, ADS
- Alam, S., Albareti, F. D., Allende Prieto, C., et al. 2015, *ApJS*, 219, 12, ADS
- Alexander, D. M., & Hickox, R. C. 2012, *NewAR*, 56, 93, ADS
- Andrae, R., Kim, D.-W., & Bailer-Jones, C. A. L. 2013, *A&A*, 554, A137, ADS
- Angel, J. R. P., & Stockman, H. S. 1980, *ARA&A*, 18, 321, ADS
- Antonucci, R. 1988, in *Supermassive Black Holes*, ed. M. Kafatos, 26–38, ADS
- Antonucci, R. 1993, *ARA&A*, 31, 473, ADS
- Antonucci, R. 2002, in *Astrophysical Spectropolarimetry*, ed. J. Trujillo-Bueno, F. Moreno-Insertis, & F. Sánchez, 151–175, ADS
- Antonucci, R., Barvainis, R., & Alloin, D. 1990, *ApJ*, 353, 416, ADS
- Antonucci, R., Geller, R., Goodrich, R. W., & Miller, J. S. 1996, *ApJ*, 472, 502, ADS

- Antonucci, R., Kishimoto, M., Boisson, C., & Blaes, O. 2004, in *Astronomical Society of the Pacific Conference Series*, Vol. 311, *AGN Physics with the Sloan Digital Sky Survey*, ed. G. T. Richards & P. B. Hall, 381, ADS
- Antonucci, R. R. J. 1983, *Nature*, 303, 158, ADS
- Antonucci, R. R. J., & Miller, J. S. 1985, *ApJ*, 297, 621, ADS
- Aretxaga, I., Cid Fernandes, R., & Terlevich, R. J. 1997, *MNRAS*, 286, 271, ADS
- Aretxaga, I., & Terlevich, R. 1994, *MNRAS*, 269, 462, ADS
- Arévalo, P., Uttley, P., Kaspi, S., et al. 2008, *MNRAS*, 389, 1479, ADS
- Bachev, R., Grupe, D., Boeva, S., et al. 2009, *MNRAS*, 399, 750, ADS
- Bagnolo, S., Landolfi, M., Landstreet, J. D., et al. 2009, *PASP*, 121, 993, ADS
- Bailer-Jones, C. A. L. 2012, *A&A*, 546, A89, ADS
- Balbus, S. A., & Hawley, J. F. 1991, *ApJ*, 376, 214, ADS
- . 1998, *Reviews of Modern Physics*, 70, 1, ADS
- Baldi, R. D., Capetti, A., Robinson, A., Laor, A., & Behar, E. 2016, *MNRAS*, 458, L69, ADS
- Baldwin, J., Ferland, G., Korista, K., & Verner, D. 1995, *ApJL*, 455, L119, ADS
- Baldwin, J. A., Ferland, G. J., Korista, K. T., Hamann, F., & LaCluyzé, A. 2004, *ApJ*, 615, 610, ADS
- Barth, A. J., Pancoast, A., Bennert, V. N., et al. 2013, *ApJ*, 769, 128, ADS
- Barth, A. J., Bennert, V. N., Canalizo, G., et al. 2015, *ApJS*, 217, 26, ADS
- Barvainis, R. 1987, *ApJ*, 320, 537, ADS
- . 1992, *ApJ*, 400, 502, ADS
- Batcheldor, D., Robinson, A., Axon, D. J., et al. 2011, *ApJ*, 738, 90, ADS
- Belle, K. E., & Lewis, G. F. 2000, *PASP*, 112, 320, ADS
- Bentz, M. C., Peterson, B. M., Netzer, H., Pogge, R. W., & Vestergaard, M. 2009, *ApJ*, 697, 160, ADS
- Bentz, M. C., Denney, K. D., Grier, C. J., et al. 2013, *ApJ*, 767, 149, ADS
- Bertin, E., & Arnouts, S. 1996, *A&AS*, 117, 393, ADS

- Bessell, M. S. 1990, *PASP*, 102, 1181, ADS
- Bian, W.-H., Zhang, L., Green, R., & Hu, C. 2012, *ApJ*, 759, 88, ADS
- Blackburne, J. A., & Kochanek, C. S. 2010, *ApJ*, 718, 1079, ADS
- Blandford, R. D., & McKee, C. F. 1982, *ApJ*, 255, 419, ADS
- Borguet, B., Hutsemékers, D., Letawe, G., Letawe, Y., & Magain, P. 2008, *A&A*, 478, 321, ADS
- Boroson, T. A., & Green, R. F. 1992, *ApJS*, 80, 109, ADS
- Breedt, E., Arévalo, P., McHardy, I. M., et al. 2009, *MNRAS*, 394, 427, ADS
- Brindle, C., Hough, J. H., Bailey, J. A., et al. 1990, *MNRAS*, 244, 577, ADS
- Buisson, D. J. K., Lohfink, A. M., Alston, W. N., & Fabian, A. C. 2017, *MNRAS*, 464, 3194, ADS
- Butler, N. R., & Bloom, J. S. 2011, *AJ*, 141, 93, ADS
- Cackett, E. M., Horne, K., & Winkler, H. 2007, *MNRAS*, 380, 669, ADS
- Cagnoni, I., Fruscione, A., McHardy, I. M., & Papadakis, I. E. 1999, *MmSAI*, 70, 29, ADS
- Cai, Z.-Y., Wang, J.-X., Gu, W.-M., et al. 2016, *ApJ*, 826, 7, ADS
- Cameron, D. T., McHardy, I., Dwelly, T., et al. 2012, *MNRAS*, 422, 902, ADS
- Caplar, N., Lilly, S. J., & Trakhtenbrot, B. 2016, *ArXiv e-prints*, arXiv:1611.03082
- Cappellari, M., Scott, N., Alatalo, K., et al. 2013, *MNRAS*, 432, 1709, ADS
- Chae, K.-H., Turnshek, D. A., Schulte-Ladbeck, R. E., Rao, S. M., & Lupie, O. L. 2001, *ApJ*, 561, 653, ADS
- Chelouche, D. 2013, *ApJ*, 772, 9, ADS
- Chelouche, D., Shemmer, O., Cotlier, G. I., Barth, A. J., & Rafter, S. E. 2014, *ApJ*, 785, 140, ADS
- Choi, Y., Gibson, R. R., Becker, A. C., et al. 2014, *ApJ*, 782, 37, ADS
- Choloniewski, J. 1981, *Acta Astronomica*, 31, 293, ADS
- Clarke, D. 2010, *Stellar Polarimetry* (Weinheim: Wiley-VC), ADS
- Clarke, D., Stewart, B. G., Schwarz, H. E., & Brooks, A. 1983, *A&A*, 126, 260, ADS
- Clavel, J., Reichert, G. A., Alloin, D., et al. 1991, *ApJ*, 366, 64, ADS

- Collier, S., Horne, K., Wanders, I., & Peterson, B. M. 1999, *MNRAS*, 302, L24, ADS
- Collier, S., & Peterson, B. M. 2001, *ApJ*, 555, 775, ADS
- Collier, S. J., Horne, K., Kaspi, S., et al. 1998, *ApJ*, 500, 162, ADS
- Courvoisier, T. J.-L., & Clavel, J. 1991, *A&A*, 248, 389, ADS
- Courvoisier, T. J.-L., Paltani, S., & Walter, R. 1996, *A&A*, 308, L17, ADS
- Cristiani, S., Trentini, S., La Franca, F., & Andreani, P. 1997, *A&A*, 321, 123, ADS
- Croom, S. M., Richards, G. T., Shanks, T., et al. 2009, *MNRAS*, 392, 19, ADS
- Cutri, R. M., Wisniewski, W. Z., Rieke, G. H., & Lebofsky, M. J. 1985, *ApJ*, 296, 423, ADS
- Czerny, B. 2006, in *Astronomical Society of the Pacific Conference Series*, Vol. 360, *Astronomical Society of the Pacific Conference Series*, ed. C. M. Gaskell, I. M. McHardy, B. M. Peterson, & S. G. Sergeev, 265, ADS
- Czerny, B., Hryniewicz, K., Maity, I., et al. 2013, *A&A*, 556, A97, ADS
- Czerny, B., & Janiuk, A. 2007, *A&A*, 464, 167, ADS
- Czerny, B., Jaroszynski, M., & Czerny, M. 1994, *MNRAS*, 268, 135, ADS
- Czerny, B., Siemiginowska, A., Janiuk, A., & Gupta, A. C. 2008, *MNRAS*, 386, 1557, ADS
- D'Agostini, G. 2005, *ArXiv Physics e-prints*, physics/0511182, ADS
- Dai, X., Kochanek, C. S., Chartas, G., et al. 2010, *ApJ*, 709, 278, ADS
- Davidson, K., & Netzer, H. 1979, *Reviews of Modern Physics*, 51, 715, ADS
- Davis, S. W., Woo, J.-H., & Blaes, O. M. 2007, *ApJ*, 668, 682, ADS
- Dennett-Thorpe, J., Barthel, P. D., & van Bemmell, I. M. 2000, *A&A*, 364, 501, ADS
- Dexter, J., & Agol, E. 2011, *ApJL*, 727, L24, ADS
- Dexter, J., & Quataert, E. 2012, *MNRAS*, 426, L71, ADS
- di Clemente, A., Giallongo, E., Natali, G., Trevese, D., & Vagnetti, F. 1996, *ApJ*, 463, 466, ADS
- Dietrich, M., Hamann, F., Appenzeller, I., & Vestergaard, M. 2003, *ApJ*, 596, 817, ADS
- Doi, M., Tanaka, M., Fukugita, M., et al. 2010, *AJ*, 139, 1628, ADS
- Dong, X.-B., Wang, J.-G., Ho, L. C., et al. 2011, *ApJ*, 736, 86, ADS

- Edelson, R., Vaughan, S., Malkan, M., et al. 2014, *ApJ*, 795, 2, ADS
- Edelson, R., Gelbord, J. M., Horne, K., et al. 2015, *ApJ*, 806, 129, ADS
- Elvis, M. 2000, *ApJ*, 545, 63, ADS
- Fausnaugh, M. M., Denney, K. D., Barth, A. J., et al. 2016, *ApJ*, 821, 56, ADS
- Feigelson, E. D., & Jogesh Babu, G. 2012, *Modern Statistical Methods for Astronomy*, ADS
- Ferland, G. J., Hu, C., Wang, J.-M., et al. 2009, *ApJL*, 707, L82, ADS
- Ferrarese, L., & Merritt, D. 2000, *ApJL*, 539, L9, ADS
- Fossati, L., Bagnulo, S., Mason, E., & Landi Degl'Innocenti, E. 2007, in *Astronomical Society of the Pacific Conference Series*, Vol. 364, *The Future of Photometric, Spectrophotometric and Polarimetric Standardization*, ed. C. Sterken, 503, ADS
- Frank, J., King, A., & Raine, D. 1992, *Accretion power in astrophysics.*, ADS
- Frei, Z., & Gunn, J. E. 1994, *AJ*, 108, 1476, ADS
- Frieman, J. A., Bassett, B., Becker, A., et al. 2008, *AJ*, 135, 338, ADS
- Fukugita, M., Ichikawa, T., Gunn, J. E., et al. 1996, *AJ*, 111, 1748, ADS
- Gallagher, S. C., Schmidt, G. D., Smith, P. S., et al. 2005, *ApJ*, 633, 71, ADS
- Gallastegui-Aizpun, U., & Sarajedini, V. L. 2014, *MNRAS*, 444, 3078, ADS
- Gardner, E., & Done, C. 2016, *ArXiv e-prints*, arXiv:1603.09564, ADS
- Gaskell, C. M. 2008, in *Revista Mexicana de Astronomia y Astrofisica Conference Series*, Vol. 32, *Revista Mexicana de Astronomia y Astrofisica Conference Series*, 1–11, ADS
- Gaskell, C. M. 2009, in *Bulletin of the American Astronomical Society*, Vol. 41, *American Astronomical Society Meeting Abstracts #213*, 342.08, ADS
- Gaskell, C. M. 2011, *Baltic Astronomy*, 20, 392, ADS
- Gaskell, C. M., Goosmann, R. W., Merkulova, N. I., Shakhovskoy, N. M., & Shoji, M. 2012, *ApJ*, 749, 148, ADS
- Gebhardt, K., Bender, R., Bower, G., et al. 2000, *ApJL*, 539, L13, ADS
- Gelman, A., & Rubin, D. B. 1992, *Statist. Sci.*, 7, 457
- Gezari, S., Martin, D. C., Forster, K., et al. 2013, *ApJ*, 766, 60, ADS

- Gil-Merino, R., Goicoechea, L. J., Shalyapin, V. N., & Braga, V. F. 2012, *ApJ*, 744, 47, ADS
- Giveon, U., Maoz, D., Kaspi, S., Netzer, H., & Smith, P. S. 1999, *MNRAS*, 306, 637, ADS
- Glass, I. S. 2004, *MNRAS*, 350, 1049, ADS
- Glikman, E., Helfand, D. J., & White, R. L. 2006, *ApJ*, 640, 579, ADS
- Gnedin, I. N., & Silantev, N. A. 1978, *Soviet Ast.*, 22, 325, ADS
- Goad, M. R., Koratkar, A. P., Axon, D. J., Korista, K. T., & O'Brien, P. T. 1999a, *ApJL*, 512, L95, ADS
- Goad, M. R., Koratkar, A. P., Kim-Quijano, J., et al. 1999b, *ApJ*, 524, 707, ADS
- Goad, M. R., Korista, K. T., & Ruff, A. J. 2012, *MNRAS*, 426, 3086, ADS
- Goad, M. R., O'Brien, P. T., & Gondhalekar, P. M. 1993, *MNRAS*, 263, 149, ADS
- Goicoechea, L. J., Shalyapin, V. N., Gil-Merino, R., & Braga, V. F. 2012, *Journal of Physics Conference Series*, 372, 012058, ADS
- Goodrich, R. W., Cohen, M. H., & Putney, A. 1995, *PASP*, 107, 179, ADS
- Goosmann, R. W., & Gaskell, C. M. 2007, *A&A*, 465, 129, ADS
- Goosmann, R. W., Gaskell, C. M., & Marin, F. 2014, *Advances in Space Research*, 54, 1341, ADS
- Gould, A., & Miralda-Escudé, J. 1997, *ApJL*, 483, L13, ADS
- Graham, M. J., Djorgovski, S. G., Drake, A. J., et al. 2014, *MNRAS*, 439, 703, ADS
- Grandi, S. A. 1982, *ApJ*, 255, 25, ADS
- Gu, M. F., & Li, S.-L. 2013, *A&A*, 554, A51, ADS
- Gull, S. F. 1989, in *Maximum Entropy and Bayesian Methods*, ed. J. Skilling (Dordrecht: Kluwer), 511, 511
- Gunn, J. E., Carr, M., Rockosi, C., et al. 1998, *AJ*, 116, 3040, ADS
- Gunn, J. E., Siegmund, W. A., Mannery, E. J., et al. 2006, *AJ*, 131, 2332, ADS
- Guo, H., & Gu, M. 2014, *Journal of Astrophysics and Astronomy*, 35, 477, ADS
- . 2016, *ApJ*, 822, 26, ADS
- Hagen-Thorn, V. A. 1997, *Astronomy Letters*, 23, 19, ADS

- Hagen-Thorn, V. A. 2006, in *Astronomical Society of the Pacific Conference Series*, Vol. 350, *Blazar Variability Workshop II: Entering the GLAST Era*, ed. H. R. Miller, K. Marshall, J. R. Webb, & M. F. Aller, 41, ADS
- Hales, C. A., & Lewis, G. F. 2007, *PASA*, 24, 30, ADS
- Halpern, J. P., Leighly, K. M., & Marshall, H. L. 2003, *ApJ*, 585, 665, ADS
- Hao, H., Elvis, M., Civano, F., et al. 2010, *ApJL*, 724, L59, ADS
- Hashiba, Y., Doi, M., Sako, S., et al. 2014, in *Proc. SPIE*, Vol. 9147, *Ground-based and Airborne Instrumentation for Astronomy V*, 91472J, ADS
- Hawkins, M. R. S. 1993, *Nature*, 366, 242, ADS
- . 2003, *MNRAS*, 344, 492, ADS
- Heckman, T. M., & Best, P. N. 2014, *ARA&A*, 52, 589, ADS
- Hernán-Caballero, A., Hatziminaoglou, E., Alonso-Herrero, A., & Mateos, S. 2016, *MNRAS*, 463, 2064, ADS
- Hernitschek, N., Rix, H.-W., Bovy, J., & Morganson, E. 2015, *ApJ*, 801, 45, ADS
- Hewett, P. C., & Wild, V. 2010, *MNRAS*, 405, 2302, ADS
- Hirose, S., Blaes, O., & Krolik, J. H. 2009a, *ApJ*, 704, 781, ADS
- Hirose, S., Krolik, J. H., & Blaes, O. 2009b, *ApJ*, 691, 16, ADS
- Hogg, D. W., Bovy, J., & Lang, D. 2010, *ArXiv e-prints*, arXiv:1008.4686, ADS
- Hönig, S. F., & Kishimoto, M. 2010, *A&A*, 523, A27, ADS
- Hopkins, P. F., Strauss, M. A., Hall, P. B., et al. 2004, *AJ*, 128, 1112, ADS
- Hryniewicz, K., Czerny, B., Pych, W., et al. 2014, *A&A*, 562, A34, ADS
- Hsu, C.-M., & Blaes, O. 1998, *ApJ*, 506, 658, ADS
- Hu, C., Wang, J.-M., Ho, L. C., et al. 2008, *ApJ*, 687, 78, ADS
- Hu, R., & Zhang, S.-N. 2012, *MNRAS*, 426, 2847, ADS
- Hubeny, I., Agol, E., Blaes, O., & Krolik, J. H. 2000, *ApJ*, 533, 710, ADS
- Hung, T., Gezari, S., Jones, D. O., et al. 2016, *ApJ*, 833, 226, ADS
- Hutsemékers, D., Borguet, B., Sluse, D., Cabanac, R., & Lamy, H. 2010, *A&A*, 520, L7, ADS

- Hutsemékers, D., Cabanac, R., Lamy, H., & Sluse, D. 2005, *A&A*, 441, 915, ADS
- Hutsemékers, D., Sluse, D., Braibant, L., & Anguita, T. 2015, *A&A*, 584, A61, ADS
- Ikejiri, Y., Uemura, M., Sasada, M., et al. 2011, *PASJ*, 63, 639, ADS
- Impey, C. D., Malkan, M. A., & Tapia, S. 1989, *ApJ*, 347, 96, ADS
- Ivezić, Ž., Menou, K., Knapp, G. R., et al. 2002, *AJ*, 124, 2364, ADS
- Ivezić, Ž., Lupton, R. H., Anderson, S., et al. 2003, *MmSAI*, 74, 978, ADS
- Ivezić, Ž., Lupton, R. H., Schlegel, D., et al. 2004, *Astronomische Nachrichten*, 325, 583, ADS
- Ivezić, Ž., Smith, J. A., Miknaitis, G., et al. 2007, *AJ*, 134, 973, ADS
- Ivezic, Z., Tyson, J. A., Abel, B., et al. 2008, *ArXiv e-prints*, arXiv:0805.2366, ADS
- Jester, S., Schneider, D. P., Richards, G. T., et al. 2005, *AJ*, 130, 873, ADS
- Jiang, Y.-F., Davis, S. W., & Stone, J. M. 2016a, *ApJ*, 827, 10, ADS
- Jiang, Y.-F., Stone, J. M., & Davis, S. W. 2013, *ApJ*, 767, 148, ADS
- Jiang, Y.-F., Green, P. J., Greene, J. E., et al. 2016b, *ArXiv e-prints*, arXiv:1612.08747, ADS
- Jiménez-Vicente, J., Mediavilla, E., Kochanek, C. S., et al. 2014, *ApJ*, 783, 47, ADS
- Kato, S., Fukue, J., & Mineshige, S. 2008, *Black-Hole Accretion Disks — Towards a New Paradigm —*, ADS
- Kawaguchi, T., Mineshige, S., Umemura, M., & Turner, E. L. 1998, *ApJ*, 504, 671, ADS
- Kawaguchi, T., Shimura, T., & Mineshige, S. 2001, *ApJ*, 546, 966, ADS
- Kedziora, D. J., Garsden, H., & Lewis, G. F. 2011, *MNRAS*, 415, 1409, ADS
- Kellermann, K. I., Sramek, R. A., Schmidt, M., Green, R. F., & Shaffer, D. B. 1994, *AJ*, 108, 1163, ADS
- Kelly, B. C. 2007, *ApJ*, 665, 1489, ADS
- Kelly, B. C., Bechtold, J., & Siemiginowska, A. 2009, *ApJ*, 698, 895, ADS
- Kelly, B. C., Treu, T., Malkan, M., Pancoast, A., & Woo, J.-H. 2013, *ApJ*, 779, 187, ADS
- King, A. 2003, *ApJL*, 596, L27, ADS
- . 2008, *NewAR*, 52, 253, ADS

- Kinney, A. L., Rivolo, A. R., & Koratkar, A. P. 1990, *ApJ*, 357, 338, ADS
- Kishimoto, M., Antonucci, R., & Blaes, O. 2003, *MNRAS*, 345, 253, ADS
- . 2005, *MNRAS*, 364, 640, ADS
- Kishimoto, M., Antonucci, R., Blaes, O., et al. 2008a, *Journal of Physics Conference Series*, 131, 012039, ADS
- . 2008b, *Nature*, 454, 492, ADS
- Kishimoto, M., Antonucci, R., Boisson, C., & Blaes, O. 2004, *MNRAS*, 354, 1065, ADS
- Kishimoto, M., Hönig, S. F., Antonucci, R., et al. 2011, *A&A*, 536, A78, ADS
- Kishimoto, M., Hönig, S. F., Beckert, T., & Weigelt, G. 2007, *A&A*, 476, 713, ADS
- Kokubo, M. 2015, *MNRAS*, 449, 94, ADS
- . 2016, *PASJ*, 68, 52, ADS
- . 2017, *MNRAS*, arXiv:1701.03798, ADS
- Kokubo, M., Morokuma, T., Minezaki, T., et al. 2014, *ApJ*, 783, 46, ADS
- Kokubo, M., Hashiba, Y., Mitsuda, K., et al. 2015, *Bull. Cent. Astron. Univ. Hyogo*, 3, 1-20
- Koratkar, A., & Blaes, O. 1999, *PASP*, 111, 1, ADS
- Korista, K. T., & Goad, M. R. 2001, *ApJ*, 553, 695, ADS
- . 2004, *ApJ*, 606, 749, ADS
- Korista, K. T., Alloin, D., Barr, P., et al. 1995, *ApJS*, 97, 285, ADS
- Kormendy, J., & Ho, L. C. 2013, *ARA&A*, 51, 511, ADS
- Koshida, S., Minezaki, T., Yoshii, Y., et al. 2014, *ApJ*, 788, 159, ADS
- Kozłowski, S. 2016a, *ArXiv e-prints*, arXiv:1611.08248, ADS
- . 2016b, *ApJ*, 826, 118, ADS
- . 2017, *ArXiv e-prints*, arXiv:1701.00005, ADS
- Kozłowski, S., Kochanek, C. S., Udalski, A., et al. 2010, *ApJ*, 708, 927, ADS
- Krawczyk, C. M., Richards, G. T., Gallagher, S. C., et al. 2015, *AJ*, 149, 203, ADS

- Krawczyk, C. M., Richards, G. T., Mehta, S. S., et al. 2013, *ApJS*, 206, 4, ADS
- Krolik, J. H., Horne, K., Kallman, T. R., et al. 1991, *ApJ*, 371, 541, ADS
- Krolik, J. H., & Kallman, T. R. 1988, *ApJ*, 324, 714, ADS
- Kurk, J. D., Walter, F., Fan, X., et al. 2007, *ApJ*, 669, 32, ADS
- LaMassa, S. M., Cales, S., Moran, E. C., et al. 2015, *ApJ*, 800, 144, ADS
- Lamy, H., & Hutsemékers, D. 1999, *The Messenger*, 96, 25, ADS
- Landi Degl'Innocenti, E., Bagnulo, S., & Fossati, L. 2007, in *Astronomical Society of the Pacific Conference Series*, Vol. 364, *The Future of Photometric, Spectrophotometric and Polarimetric Standardization*, ed. C. Sterken, 495, ADS
- Landt, H., Elvis, M., Ward, M. J., et al. 2011, *MNRAS*, 414, 218, ADS
- Laor, A., Netzer, H., & Piran, T. 1990, *MNRAS*, 242, 560, ADS
- Lawrence, A. 2005, *MNRAS*, 363, 57, ADS
- Li, S.-L., & Cao, X. 2008, *MNRAS*, 387, L41, ADS
- Lightman, A. P., & Eardley, D. M. 1974, *ApJL*, 187, L1, ADS
- Lira, P., Arévalo, P., Uttley, P., McHardy, I., & Breedt, E. 2011, *MNRAS*, 415, 1290, ADS
- Lira, P., Arévalo, P., Uttley, P., McHardy, I. M. M., & Videla, L. 2015, *MNRAS*, 454, 368, ADS
- Liu, H., Li, S.-L., Gu, M., & Guo, H. 2016, *MNRAS*, 462, L56, ADS
- Lohfink, A. M., Reynolds, C. S., Vasudevan, R., Mushotzky, R. F., & Miller, N. A. 2014, *ApJ*, 788, 10, ADS
- Lynden-Bell, D. 1969, *Nature*, 223, 690, ADS
- Lyutyi, V. M., & Doroshenko, V. T. 1993, *Astronomy Letters*, 19, 405, ADS
- MacLeod, C. L., Ivezić, Ž., Kochanek, C. S., et al. 2010, *ApJ*, 721, 1014, ADS
- MacLeod, C. L., Ivezić, Ž., Sesar, B., et al. 2012, *ApJ*, 753, 106, ADS
- MacLeod, C. L., Ross, N. P., Lawrence, A., et al. 2016, *MNRAS*, 457, 389, ADS
- Madau, P. 1995, *ApJ*, 441, 18, ADS
- Magorrian, J., Tremaine, S., Richstone, D., et al. 1998, *AJ*, 115, 2285, ADS

- Mantz, A. B. 2016, *MNRAS*, 457, 1279, ADS
- Maoz, D., Markowitz, A., Edelson, R., & Nandra, K. 2002, *AJ*, 124, 1988, ADS
- Maoz, D., Netzer, H., Peterson, B. M., et al. 1993, *ApJ*, 404, 576, ADS
- Marin, F., & Goosmann, R. W. 2013, *MNRAS*, 436, 2522, ADS
- Marin, F., Goosmann, R. W., Gaskell, C. M., Porquet, D., & Dovčiak, M. 2012, *A&A*, 548, A121, ADS
- Markwardt, C. B. 2009, in *Astronomical Society of the Pacific Conference Series*, Vol. 411, *Astronomical Data Analysis Software and Systems XVIII*, ed. D. A. Bohlender, D. Durand, & P. Dowler, 251, ADS
- Marshall, H. L., Carone, T. E., Peterson, B. M., et al. 1997, *ApJ*, 479, 222, ADS
- Marshall, K., Ryle, W. T., & Miller, H. R. 2008, *ApJ*, 677, 880, ADS
- Matt, G., Fabian, A. C., & Ross, R. R. 1993, *MNRAS*, 264, 839, ADS
- Matthews, J. H., Knigge, C., Long, K. S., et al. 2016, *MNRAS*, 458, 293, ADS
- McCarthy, J. K., Cohen, J. G., Butcher, B., et al. 1998, in *Society of Photo-Optical Instrumentation Engineers (SPIE) Conference Series*, Vol. 3355, *Optical Astronomical Instrumentation*, ed. S. D'Odorico, 81–92, ADS
- McHardy, I. M., Koerding, E., Knigge, C., Uttley, P., & Fender, R. P. 2006, *Nature*, 444, 730, ADS
- McHardy, I. M., Cameron, D. T., Dwelly, T., et al. 2014, *MNRAS*, 444, 1469, ADS
- McHardy, I. M., Connolly, S. D., Peterson, B. M., et al. 2016, *Astronomische Nachrichten*, 337, 500, ADS
- Meiksin, A. 2006, *MNRAS*, 365, 807, ADS
- Merkulova, N. I., & Shakhovskoy, N. M. 2006, in *Astronomical Society of the Pacific Conference Series*, Vol. 360, *Astronomical Society of the Pacific Conference Series*, ed. C. M. Gaskell, I. M. McHardy, B. M. Peterson, & S. G. Sergeev, 65, ADS
- Meusinger, H., Hinze, A., & de Hoon, A. 2011, *A&A*, 525, A37, ADS
- Meusinger, H., & Weiss, V. 2013, *A&A*, 560, A104, ADS
- Miley, G. K., & Hartsuijker, A. P. 1978, *A&AS*, 34, 129, ADS
- Miniutti, G., & Fabian, A. C. 2004, *MNRAS*, 349, 1435, ADS

- Mink, D. 2006, in *Astronomical Society of the Pacific Conference Series*, Vol. 351, *Astronomical Data Analysis Software and Systems XV*, ed. C. Gabriel, C. Arviset, D. Ponz, & S. Enrique, 204, ADS
- Modzelewska, J., Czerny, B., Hryniewicz, K., et al. 2014, *A&A*, 570, A53, ADS
- Monet, D. G., Levine, S. E., Canzian, B., et al. 2003, *AJ*, 125, 984, ADS
- Mor, R., & Netzer, H. 2012, *MNRAS*, 420, 526, ADS
- Morgan, C. W., Kochanek, C. S., Morgan, N. D., & Falco, E. E. 2010, *ApJ*, 712, 1129, ADS
- Morganson, E., Burgett, W. S., Chambers, K. C., et al. 2014, *ApJ*, 784, 92, ADS
- Morokuma, T., Tominaga, N., Tanaka, M., et al. 2014, *PASJ*, 66, 114, ADS
- Mosquera, A. M., Kochanek, C. S., Chen, B., et al. 2013, *ApJ*, 769, 53, ADS
- Naghizadeh-Khouei, J., & Clarke, D. 1993, *A&A*, 274, 968, ADS
- Nakao, H. 2015, PhD thesis, Hokkaido University, Japan
- Nandra, K., Clavel, J., Edelson, R. A., et al. 1998, *ApJ*, 505, 594, ADS
- Nandra, K., George, I. M., Mushotzky, R. F., Turner, T. J., & Yaqoob, T. 1997, *ApJ*, 477, 602, ADS
- Netzer, H. 2015, *ARA&A*, 53, 365, ADS
- Noda, H., Minezaki, T., Watanabe, M., et al. 2016, *ApJ*, 828, 78, ADS
- Novak, G. S., Faber, S. M., & Dekel, A. 2006, *ApJ*, 637, 96, ADS
- Novikov, I. D., & Thorne, K. S. 1973, in *Black Holes (Les Astres Occlus)*, ed. C. Dewitt & B. S. Dewitt, 343–450, ADS
- O'Brien, P. T., Goad, M. R., & Gondhalekar, P. M. 1995, *MNRAS*, 275, 1125, ADS
- Ohsuga, K., Mineshige, S., Mori, M., & Umemura, M. 2002, *ApJ*, 574, 315, ADS
- Oke, J. B., Cohen, J. G., Carr, M., et al. 1995, *PASP*, 107, 375, ADS
- Oknyansky, V. L., Metlova, N. V., Taranova, O. G., et al. 2014, *Astronomy Letters*, 40, 527, ADS
- Pal, M., Dewangan, G. C., Connolly, S. D., & Misra, R. 2016, *ArXiv e-prints*, arXiv:1612.01369, ADS
- Palanque-Delabrouille, N., Yeche, C., Myers, A. D., et al. 2011, *A&A*, 530, A122, ADS
- Paltani, S., & Courvoisier, T. J.-L. 1994, *A&A*, 291, 74, ADS

- Paltani, S., & Walter, R. 1996, *A&A*, 312, 55, ADS
- Park, D., Kelly, B. C., Woo, J.-H., & Treu, T. 2012, *ApJS*, 203, 6, ADS
- Penna, R. F., Sądowski, A., & McKinney, J. C. 2012, *MNRAS*, 420, 684, ADS
- Pereyra, N. A., Vanden Berk, D. E., Turnshek, D. A., et al. 2006, *ApJ*, 642, 87, ADS
- Peterson, B. M. 1997, *An Introduction to Active Galactic Nuclei*, ADS
- Peterson, B. M., & Horne, K. 2004, *Astronomische Nachrichten*, 325, 248, ADS
- Pezzulli, E., Valiante, R., Orofino, M. C., et al. 2016, *ArXiv e-prints*, arXiv:1612.04188, ADS
- Phillips, K. C., & Meszaros, P. 1986, *ApJ*, 310, 284, ADS
- Plaszczynski, S., Montier, L., Levrier, F., & Tristram, M. 2014, *MNRAS*, 439, 4048, ADS
- Pooley, D., Blackburne, J. A., Rappaport, S., & Schechter, P. L. 2007, *ApJ*, 661, 19, ADS
- Pringle, J. E., & Rees, M. J. 1972, *A&A*, 21, 1, ADS
- Proga, D., Stone, J. M., & Kallman, T. R. 2000, *ApJ*, 543, 686, ADS
- Rakshit, S., Petrov, R. G., Meilland, A., & Hönig, S. F. 2015, *MNRAS*, 447, 2420, ADS
- Ramolla, M., Pozo Nuñez, F., Westhues, C., Haas, M., & Chini, R. 2015, *A&A*, 581, A93, ADS
- Richards, G. T., Fan, X., Schneider, D. P., et al. 2001, *AJ*, 121, 2308, ADS
- Richards, G. T., Fan, X., Newberg, H. J., et al. 2002, *AJ*, 123, 2945, ADS
- Richards, G. T., Hall, P. B., Vanden Berk, D. E., et al. 2003, *AJ*, 126, 1131, ADS
- Richards, G. T., Lacy, M., Storrie-Lombardi, L. J., et al. 2006, *ApJS*, 166, 470, ADS
- Richards, G. T., Myers, A. D., Gray, A. G., et al. 2009, *ApJS*, 180, 67, ADS
- Rojas Lobos, P. A., Goosmann, R. W., & Marin, F. 2016, *ArXiv e-prints*, arXiv:1610.05149, ADS
- Ruan, J. J., Anderson, S. F., Dexter, J., & Agol, E. 2014, *ApJ*, 783, 105, ADS
- Rybicki, G. B., & Press, W. H. 1992, *ApJ*, 398, 169, ADS
- Sakata, Y., Morokuma, T., Minezaki, T., et al. 2011, *ApJ*, 731, 50, ADS
- Sakata, Y., Minezaki, T., Yoshii, Y., et al. 2010, *ApJ*, 711, 461, ADS
- Sako, M., Bassett, B., Becker, A. C., et al. 2014, *ArXiv e-prints*, arXiv:1401.3317, ADS

- Sako, S., Aoki, T., Doi, M., et al. 2012, in Society of Photo-Optical Instrumentation Engineers (SPIE) Conference Series, Vol. 8446, Society of Photo-Optical Instrumentation Engineers (SPIE) Conference Series, 6, ADS
- Sądowski, A. 2016, MNRAS, 459, 4397, ADS
- Schlegel, D. J., Finkbeiner, D. P., & Davis, M. 1998, ApJ, 500, 525, ADS
- Schmidt, G. D., Elston, R., & Lupie, O. L. 1992, AJ, 104, 1563, ADS
- Schmidt, G. D., & Smith, P. S. 2000, ApJ, 545, 117, ADS
- Schmidt, K. B., Marshall, P. J., Rix, H.-W., et al. 2010, ApJ, 714, 1194, ADS
- Schmidt, K. B., Rix, H.-W., Shields, J. C., et al. 2012, ApJ, 744, 147, ADS
- Schmidt, M. 1963, Nature, 197, 1040, ADS
- Schneider, D. P., Richards, G. T., Hall, P. B., et al. 2010, AJ, 139, 2360, ADS
- Scott, J. E., Kriss, G. A., Brotherton, M., et al. 2004, ApJ, 615, 135, ADS
- Scranton, R., Johnston, D., Dodelson, S., et al. 2002, ApJ, 579, 48, ADS
- Sereno, M. 2016, MNRAS, 455, 2149, ADS
- Sergeev, S. G., Doroshenko, V. T., Golubinskiy, Y. V., Merkulova, N. I., & Sergeeva, E. A. 2005, ApJ, 622, 129, ADS
- Serkowski, K. 1974, Polarization techniques., ed. N. P. Carleton, 361–414, ADS
- Serkowski, K., Mathewson, D. S., & Ford, V. L. 1975, ApJ, 196, 261, ADS
- Sesar, B., Stuart, J. S., Ivezić, Ž., et al. 2011, AJ, 142, 190, ADS
- Sesar, B., Svlković, D., Ivezić, Ž., et al. 2006, AJ, 131, 2801, ADS
- Sesar, B., Ivezić, Ž., Lupton, R. H., et al. 2007, AJ, 134, 2236, ADS
- Shakura, N. I., & Sunyaev, R. A. 1973, A&A, 24, 337, ADS
- . 1976, MNRAS, 175, 613, ADS
- Shang, Z., Brotherton, M. S., Green, R. F., et al. 2005, ApJ, 619, 41, ADS
- Shapiro, S. L., & Teukolsky, S. A. 1983, Black holes, white dwarfs, and neutron stars: The physics of compact objects, ADS
- Shappee, B. J., Prieto, J. L., Grupe, D., et al. 2014, ApJ, 788, 48, ADS

- Shemmer, O., Uttley, P., Netzer, H., & McHardy, I. M. 2003, MNRAS, 343, 1341, ADS
- Shen, Y., Richards, G. T., Strauss, M. A., et al. 2011, ApJS, 194, 45, ADS
- Shen, Y., Horne, K., Grier, C. J., et al. 2016, ApJ, 818, 30, ADS
- Shields, G. A., Wobus, L., & Husfeld, D. 1998, ApJ, 496, 743, ADS
- Shields, J. C. 2007, in *Astronomical Society of the Pacific Conference Series*, Vol. 373, *The Central Engine of Active Galactic Nuclei*, ed. L. C. Ho & J.-W. Wang, 355, ADS
- Silant'ev, N. A., Gnedin, Y. N., Piotrovich, M. Y., Natsvlshvili, T. M., & Buliga, S. D. 2016, ArXiv e-prints, arXiv:1606.09050, ADS
- Silant'ev, N. A., Piotrovich, M. Y., Gnedin, Y. N., & Natsvlshvili, T. M. 2009, A&A, 507, 171, ADS
- Silk, J., & Rees, M. J. 1998, A&A, 331, L1, ADS
- Sluse, D., Hutsemékers, D., Lamy, H., Cabanac, R., & Quintana, H. 2005, A&A, 433, 757, ADS
- Smith, H. J., & Hoffleit, D. 1963, Nature, 198, 650, ADS
- Smith, J. E., Robinson, A., Alexander, D. M., et al. 2004, MNRAS, 350, 140, ADS
- Smith, J. E., Robinson, A., Young, S., Axon, D. J., & Corbett, E. A. 2005, MNRAS, 359, 846, ADS
- Smith, J. E., Young, S., Robinson, A., et al. 2002, MNRAS, 335, 773, ADS
- Smith, P. S., Schmidt, G. D., & Allen, R. G. 1993, ApJ, 409, 604, ADS
- Spergel, D. N., Bean, R., Doré, O., et al. 2007, ApJS, 170, 377, ADS
- Sredzinska, J., Czerny, B., Hryniewicz, K., et al. 2016, ArXiv e-prints, arXiv:1602.01975, ADS
- Starkey, D., Horne, K., Fausnaugh, M. M., et al. 2016, ArXiv e-prints, arXiv:1611.06051, ADS
- Starling, R. L. C., Siemiginowska, A., Uttley, P., & Soria, R. 2004, MNRAS, 347, 67, ADS
- Stockman, H. S., Angel, J. R. P., & Miley, G. K. 1979, ApJL, 227, L55, ADS
- Stockman, H. S., Moore, R. L., & Angel, J. R. P. 1984, ApJ, 279, 485, ADS
- Stokes, G. H., Evans, J. B., Viggh, H. E. M., Shelly, F. C., & Pearce, E. C. 2000, Icarus, 148, 21, ADS
- Suganuma, M., Yoshii, Y., Kobayashi, Y., et al. 2006, ApJ, 639, 46, ADS
- Sun, M., Trump, J. R., Shen, Y., et al. 2015, ApJ, 811, 42, ADS
- Sun, Y.-H., Wang, J.-X., Chen, X.-Y., & Zheng, Z.-Y. 2014, ApJ, 792, 54, ADS

- Takahashi, R., Yonehara, A., & Mineshige, S. 2001, PASJ, 53, 387, ADS
- Tanaka, Y., Nandra, K., Fabian, A. C., et al. 1995, Nature, 375, 659, ADS
- Terlevich, R., Tenorio-Tagle, G., Franco, J., & Melnick, J. 1992, MNRAS, 255, 713, ADS
- Thorne, K. S. 1974, ApJ, 191, 507, ADS
- Tomita, H., Yoshii, Y., Kobayashi, Y., et al. 2006, ApJL, 652, L13, ADS
- Torricelli-Ciamponi, G., Foellmi, C., Courvoisier, T. J.-L., & Paltani, S. 2000, A&A, 358, 57, ADS
- Tremaine, S., Gebhardt, K., Bender, R., et al. 2002, ApJ, 574, 740, ADS
- Trèvese, D., & Vagnetti, F. 2002, ApJ, 564, 624, ADS
- Troyer, J., Starkey, D., Cackett, E. M., et al. 2016, MNRAS, 456, 4040, ADS
- Tsuzuki, Y., Kawara, K., Yoshii, Y., et al. 2006, ApJ, 650, 57, ADS
- Turner, N. J., Blaes, O. M., Socrates, A., Begelman, M. C., & Davis, S. W. 2005, ApJ, 624, 267, ADS
- Ulrich, M.-H., Maraschi, L., & Urry, C. M. 1997, ARA&A, 35, 445, ADS
- Urry, C. M., & Padovani, P. 1995, PASP, 107, 803, ADS
- Uttley, P. 2006, in Astronomical Society of the Pacific Conference Series, Vol. 360, Astronomical Society of the Pacific Conference Series, ed. C. M. Gaskell, I. M. McHardy, B. M. Peterson, & S. G. Sergeev, 101, ADS
- Uttley, P., & Casella, P. 2014, SSRv, 183, 453, ADS
- Vagnetti, F., Turriziani, S., Trevese, D., & Antonucci, M. 2010, A&A, 519, A17, ADS
- Vanden Berk, D. E., Richards, G. T., Bauer, A., et al. 2001, AJ, 122, 549, ADS
- Vanden Berk, D. E., Wilhite, B. C., Kron, R. G., et al. 2004, ApJ, 601, 692, ADS
- Vanden Berk, D. E., Shen, J., Yip, C.-W., et al. 2006, AJ, 131, 84, ADS
- Vaughan, S., Edelson, R., Warwick, R. S., & Uttley, P. 2003, MNRAS, 345, 1271, ADS
- Vestergaard, M., & Wilkes, B. J. 2001, ApJS, 134, 1, ADS
- Voevodkin, A. 2011, ArXiv e-prints, arXiv:1107.4244, ADS
- Wall, J. V., & Jenkins, C. R. 2012, Practical Statistics for Astronomers, ADS
- Walsh, J. L., Minezaki, T., Bentz, M. C., et al. 2009, ApJS, 185, 156, ADS

- Wamsteker, W., Rodriguez-Pascual, P., Wills, B. J., et al. 1990, *ApJ*, 354, 446, ADS
- Wanders, I., Peterson, B. M., Alloin, D., et al. 1997, *ApJS*, 113, 69, ADS
- Wardle, J. F. C., & Kronberg, P. P. 1974, *ApJ*, 194, 249, ADS
- Webb, W., & Malkan, M. 2000, *ApJ*, 540, 652, ADS
- Whittet, D. C. B., Martin, P. G., Hough, J. H., et al. 1992, *ApJ*, 386, 562, ADS
- Wilhite, B. C., Vanden Berk, D. E., Kron, R. G., et al. 2005, *ApJ*, 633, 638, ADS
- Williams, M. J., Bureau, M., & Cappellari, M. 2010, *MNRAS*, 409, 1330, ADS
- Wills, B. J., Netzer, H., & Wills, D. 1985, *ApJ*, 288, 94, ADS
- Wills, B. J., Wills, D., & Breger, M. 2011, *ApJS*, 194, 19, ADS
- Winkler, H. 1997, *MNRAS*, 292, 273, ADS
- Winkler, H., Glass, I. S., van Wyk, F., et al. 1992, *MNRAS*, 257, 659, ADS
- Woo, J.-H. 2008, *AJ*, 135, 1849, ADS
- Woo, J.-H., Treu, T., Malkan, M. A., Ferry, M. A., & Misch, T. 2007, *ApJ*, 661, 60, ADS
- Wright, E. L. 2006, *PASP*, 118, 1711, ADS
- Wu, X.-B., Wang, F., Fan, X., et al. 2015, *Nature*, 518, 512, ADS
- Wyithe, J. S. B., & Loeb, A. 2002, *ApJ*, 577, 615, ADS
- Yip, C. W., Connolly, A. J., Vanden Berk, D. E., et al. 2004, *AJ*, 128, 2603, ADS
- Yonehara, A., Mineshige, S., Fukue, J., Umemura, M., & Turner, E. L. 1999, *A&A*, 343, 41, ADS
- York, D. G., Adelman, J., Anderson, Jr., J. E., et al. 2000, *AJ*, 120, 1579, ADS
- Young, S., Axon, D. J., Robinson, A., Hough, J. H., & Smith, J. E. 2007, *Nature*, 450, 74, ADS
- Yu, Q., & Tremaine, S. 2002, *MNRAS*, 335, 965, ADS
- Zakamska, N. L., Schmidt, G. D., Smith, P. S., et al. 2005, *AJ*, 129, 1212, ADS
- Zhang, S., Zhou, H., Shi, X., et al. 2015, *ApJ*, 815, 113, ADS
- Zhang, X.-G. 2013, *MNRAS*, 435, 2141, ADS
- Zheng, W., Kriss, G. A., Telfer, R. C., Grimes, J. P., & Davidsen, A. F. 1997, *ApJ*, 475, 469, ADS

Zhu, F.-F., Wang, J.-X., Cai, Z.-Y., & Sun, Y.-H. 2016, ArXiv e-prints, arXiv:1609.07136, ADS

Zu, Y., Kochanek, C. S., Kozłowski, S., & Udalski, A. 2013, ApJ, 765, 106, ADS

Zubko, V. G., & Laor, A. 2000, ApJS, 128, 245, ADS

Zuo, W., Wu, X.-B., Liu, Y.-Q., & Jiao, C.-L. 2012, ApJ, 758, 104, ADS